DEVELOPMENT OF HIGH FUNCTION IN-FIBRE TILTED GRATINGS AND THEIR APPLICATIONS

DANIEL ADEBAYO

Doctor of Philosophy

JUNE 2015

ASTON UNIVERSITY

ASTON UNIVERSITY
DEVELOPMENT OF HIGH FUNCTION IN-FIBRE TILTED GRATINGS AND THEIR APPLICATIONS
DANIEL ADEBAYO
Doctor of Philosophy
JUNE 2015

Summary

This thesis presents a detailed description of the fabrication process, spectral characteristics and applications of in-fibre gratings of normal structures, such as fibre Bragg gratings and long period gratings, and tilted structures of small, large and 45 angle tilted fibre gratings. All these in-fibre gratings were fabricated by UV-laser inscription in standard telecom single mode fibres.

The key part of this research work is the fabrication and systematic spectral and sensitivity characterisation of the fibre Bragg gratings (FBGs) and long period gratings (LPGs). Their temperature sensitivities were compared for different wavelength ranges from near-IR to mid-IR. The LPGs, which have multiple transmission loss peaks were characterised for temperature and refractive index sensitivities for each transmission loss peak, obtaining the correlation between the cladding mode order and sensitivity. The results of this investigation have enabled to select the best LPGs for two bio sensing applications: (i) investigation of Foetal Bovine Degradation due to change in temperature and (ii) sensing different haemoglobin concentrations.

The other major contribution of this Ph.D research is the systematic approach used in fabricating and characterising tilted fibre gratings (TFGs) with small, large and 45°angle tilted structures. All these types of TFG have been investigated in terms of inscription methods, spectral characteristics, polarisation properties and thermal responses. The three fabrication techniques used to inscribe TFG structures, two-beam holographic, phase-mask and amplitude-mask, have been fully discussed. The TFGs were subjected to various temperature sensing experiments to evaluate their responses and how the temperature change could affect their performance in real environment. In addition, for the small and large angle TFGs, their refractive index (RI) sensing characteristics have been investigated to show their unique RI sensing capability to the surrounding medium. And due to the unique polarisation property of large angle TFG, it was employed in an all fibre twist sensor. Finally, a chemical sensing application was evaluated using a pair of large angle TFGs forming a high sensitivity interferometer.

Based on their unique optical properties, a power tapper working at 800nm wavelength region has been demonstrated using 45°-TFGs. The in-fibre tapper system was characterised for its dispersion, side-tapped beam width and side-tapped power variation along the grating length. This system was then used as a temperature sensor, showing side-tapping functionality.

Finally, as another major contribution, the 800nm 45°-TFG combined with CCD array were developed into an optical fibre signal interrogation system and evaluated for FBG temperature sensing, which clearly demonstrated the design concept of an in-fibre spectrometer of low cost, compact structure and high function. In collaboration with Bern University of Applied Sciences, Bangor University and Jiangnan University, the 800nm 45°-TFG was first used to develop an OCT system for bio sensing applications.

Keywords: *fibre Bragg grating, long period grating, tilted fibre grating, optical fibre sensor, in-fibre polariser, power tapping, spectrometer*

Acknowledgments

This research would not have been possible without the gracious and essential support of many individuals. The personal support from my supervisor Prof Lin Zhang was vital in completing this project. Her passion and enthusiasm for science and research work gave me great motivation throughout the course of my research programme. Her unwavering faith and encouragement to ensure the success of this project. I will also like to appreciate the support I received over the years from Dr Zhijun Yan. He showed me around the grating fabrication laboratories during the first year of my project. I want to also thank other members of the Aston Institute of Photonics Technology (AIPT); Dr Thomas Allsop, Dr Chengbo Mou, Dr Mykhaylo Dubov and Dr Steve Grice (former member of the research group).

My time here in AIPT was made interesting due to the many friends and colleagues that became part of my life. These networks have been a backbone to the successful completion of my project. I will also like to add that the non-academic staffs have been fabulous; Mrs Helen Yard (who gave me a good support and found me an office space) and Mr Andy Abbot (who hydrogenated all the fibres I used and a friendly person too).

Special thanks also go to Dr Xianfeng Chen and Dr Kaiming Zhou, who showed me some experimental skills and help me in understanding some theories of optical fibre gratings. They were not only colleagues but also good friends. Overall, I would like to celebrate everyone in AIPT who made such a pleasant and great place to carry out my research. In addition to this, I thank Prof David Webb for his great leadership of the Engineering and Applied Science department and also Professor Sergei who has managed to keep the AIPT together in aspiration and great pursuit.

Particularly, I want to appreciate the CASE studentship awarded to me from the Engineering and Physical Sciences Research Council (EPSRC) and Arden Photonics Ltd, which supported my Ph.D. programme. Big thanks to all the staff at Arden photonics who have been so kind to me: most importantly David Robinson.

A final thanks goes to my parents, siblings, and my loving wife and thanks to GOD.

To my supportive mum and dad who patiently supported me through the years and waiting for this big moment. To my loving wife who encouraged me and was always by my side.

Contents

Summary **2**

Acknowledgments **3**

List of Figures **8**

List of Tables **15**

List of Acronyms **16**

1 INTRODUCTION AND THESIS STRUCTURE **17**

1.1 *INTRODUCTION* . . . 17
1.2 *OVERVIEW OF THESIS* . . . 18
1.3 References . . . 20

2 OPTICAL FIBRE GRATING THEORY, FABRICATION METHODS AND APPLICATIONS **21**

2.1 *INTRODUCTION* . . . 21
2.2 *PHOTOSENSITIVITY IN OPTICAL FIBRE* . . . 21
2.2.1 Photosensitivity Mechanisms . . . 22
2.2.1.1 *Compaction densification model* . . . 22
2.2.1.2 *Colour centre model* . . . 23
2.2.1.3 *Stress relief model* . . . 24
2.2.2 Optical Fibre Photosensitisation Techniques . . . 25
2.2.2.1 *Co-doping technique* . . . 25
2.2.2.2 *Flame brushing technique* . . . 26
2.2.2.3 *Hydrogen loading technique* . . . 26
2.2.3 UV-Induced Index Change Stabilisation . . . 27
2.2.3.1 *Hydrogen diffusion* . . . 27
2.3 *COUPLED MODE THEORY* . . . 28
2.3.1 Forward Propagation . . . 30
2.3.2 Backward Propagation . . . 31
2.3.3 Phase Matching Conditions . . . 33
2.4 *GRATING FABRICATION TECHNIQUES* . . . 37
2.4.1 Two Beam Holographic Inscription Technique . . . 38
2.4.2 Phase Mask Inscription Technique . . . 39
2.4.3 Point By Point Inscription Technique . . . 41
2.5 *APPLICATIONS* . . . 43
2.6 *CHAPTER CONCLUSION* . . . 45
2.7 References . . . 47

3 FIBRE GRATINGS WITH NORMAL PERIODIC STRUCTURES **54**

3.1 *INTRODUCTION* . . . 54
3.2 *FIBRE BRAGG GRATING (FBG)* . . . 55

3.2.1 Fabrication Techniques . . . 55
3.2.1.1 *Two beam holographic technique* . . . 55
3.2.1.2 *Phase mask technique* . . . 60
3.2.2 FBG Stability . . . 65
3.2.3 FBG Temperature Sensing . . . 67
3.2.4 Cryogenic Sensing and Experimental Result . . . 69
3.3 *LONG PERIOD GRATINGs (LPGs)* . . . 72
3.3.1 LPG Fabrication . . . 72
3.3.2 LPG Spectral Response . . . 73
3.3.3 LPG Temperature Sensing . . . 77
3.3.3.1 *Experiment and results* . . . 77
3.3.4 LPG Refractive Index Sensing . . . 80
3.3.4.1 *RI measurement and results* . . . 81
3.3.5 LPG Bio-Sensing Application . . . 84
3.3.5.1 *Experiment and results* . . . 85
3.4 *CHAPTER CONCLUSION* . . . 87
3.5 References . . . 91

4 FIBRE GRATINGS WITH TILTED STRUCTURES AT SMALL AND LARGE ANGLE 95
4.1 *INTRODUCTION* . . . 95
4.2 *TFG CLASSIFICATION AND FABRICATION METHODS* . . . 96
4.2.1 Classification Of Mode Coupling Range Of TFGs . . . 96
4.2.2 TFG Phase Matching Condition and Radiation Profile . . . 98
4.2.3 Relationship between the Internal and External Angles and the Period Of a Tilted Fibre Grating Structure . . . 100
4.3 *FABRICATION METHOD* . . . 102
4.4 *FABRICATION AND SPECTRAL CHARACTERISATION OF SMALL ANGLE TFGS* . . . 103
4.4.1 Polarisation Characteristics Of Small Angle Tilted Fibre Gratings . . . 106
4.4.2 Small Angle TFG Thermal Response . . . 109
4.5 *FABRICATION AND CHARACTERISATION OF LARGE ANGLE TFGS* . . . 111
4.5.1 Fabrication and Set Up . . . 111
4.5.2 Large Angle TFG Thermal Response . . . 115
4.6 *SENSING APPLICATIONS OF LARGE ANGLE TFGS* . . . 117
4.6.1 Twist Sensor Based On 81°TFG . . . 117
4.6.1.1 *Experimental set up and measurements* . . . 117
4.6.1.2 *Power based measurements* . . . 119
4.6.2 Large Angle TFG Based Mach-Zehnder Interferometer . . . 121
4.6.2.1 *Fabrication and spectral characteristics* . . . 121
4.6.2.2 *Refractive index sensing and sugar concentration measurement* . . . 124
4.6.2.3 *Bio sensing application – HgB measurement* . . . 127
4.7 *CHAPTER CONCLUSION* . . . 129
4.8 References . . . 131

5 45°TILTED FIBRE GRATINGS AT 800NM RANGE 134
5.1 *INTRODUCTION* . . . 134
5.2 *STRUCTURE AND MODE COUPLING MECHANISM* . . . 135
5.3 *FABRICATION OF 800NM 45°- TILTED FIBRE GRATING* . . . 137
5.3.1 Introduction . . . 137
5.3.2 Fabrication Set-Up and Configuration . . . 139
5.3.3 Phase Mask Efficienncy . . . 141
5.3.4 800NM 45°- TFG Fabrication . . . 145
5.4 *SPECTRAL CHARACTERISTICS OF 800NM 45°- TFGS* . . . 146

5.4.1 The Entire PER Profile . . . 146
5.4.2 The Annealing Effect and Effect of Temperature on Grating Profile . . . 148
5.4.3 Effect of Grating Length On PER . . . 149
5.4.4 Ultra Broadband PER By Concatenating Detuned 45°-TFGs . . . 151
5.4.5 Polarisation Distribution Measurement . . . 153
5.5 *POWER TAPPING FUNCTION AND MEASUREMENT* . . . 155
5.5.1 Introduction . . . 155
5.5.2 Side Tapped Power Distribution Measurement . . . 156
5.5.3 Side Tapped Beam Characterisation And Dispersion Measurement . . . 158
5.6 *CHAPTER CONCLUSION* . . . 162
5.7 References . . . 164

6 45°TFB BASED SPECTROMETER 166
6.1 *INTRODUCTION* . . . 166
6.2 *45°- TFG BASED INTERROGATION SYSTEM* . . . 167
6.2.1 Principle And System Set-Up Of The Interrogation System . . . 167
6.2.1.1 *Spectral property of the sensing FBG and 45°-TFGs* . . . 169
6.2.1.2 *Set-up of the 800nm TFG-CCD interrogation system* . . . 170
6.2.1.3 *System alignment* . . . 171
6.2.1.4 *CCD detected signal – bandwidth and resolution* . . . 173
6.2.1.5 *Transfer function of the interrogation system* . . . 176
6.3 *APPLICATION OF 45°- TFG BASED INTERROGATION SYSTEM* . . . 177
6.3.1 Temperature Sensing . . . 177
6.3.1.1 *Experimental set up* . . . 177
6.3.1.2 *Experiment result and discussion* . . . 178
6.4 *BIOLOGICAL APPLICATION* . . . 180
6.4.1 Application In Optical Coherence Tomography (OCT) . . . 180
6.4.1.1 *System design* . . . 181
6.4.1.2 *OCT system* . . . 183
6.4.1.3 *OCT sensitivity measurement* . . . 185
6.5 *CHAPTER CONCLUSION* . . . 187
6.6 References . . . 188

7 THESIS CONCLUSION, FUTURE WORK AND PUBLICATIONS 189
7.1 *THESIS CONCLUSION* . . . 189
7.1.1 Theoretical, Literature Review And Fabrication Techniques . . . 189
7.1.2 Spectral Characteristics Of Normal Periodic Structure Gratings And Their Applications . . . 190
7.1.3 Spectral Characteristics Of Small And Large Angle Tilted Grating Structures And Their Applications . . . 190
7.1.4 45°-TFG Structures In Near-IR 800nm And Their Applications . . . 191
7.2 *SUGGESTED FUTURE WORK* . . . 191
7.2.1 Dual Parameter Grating Sensor . . . 191
7.2.2 LPG In 2µm Region For Chemical And Bio Sensing . . . 192
7.2.3 OCT Spectrometer Optimisation . . . 192
7.2.4 Dual Wavelength 45°-TFG Based Spectrometer . . . 193
7.3 *PUBLICATIONS* . . . 194
7.4 References . . . 195

List of Figures

2.1 Photo-induced refractive index change mechanism: Ge-Si wrong bonds break and release free electrons to diffuse into the lattice network. The resulting molecular change results into change in the refractive index ([22]) 24
2.2 Schematic diagram of backward-mode coupling in FBG. 34
2.3 Schematic diagram of forward-mode coupling in LPG. 35
2.4 Schematic diagram of forward-mode coupling in TFG. 35
2.5 Schematic diagram of backward-mode coupling in TFG. 35
2.6 Schematic diagram of a standard fibre with a tilted fibre grating structure. 36
2.7 Laboratory set up for the two-beam holographic fabrication system. 38
2.8 The Schematic diagram of phase mask grating inscription technique. 40
2.9 Laboratory set up of UV inscription of fibre Bragg grating inscription by the phase mask method. 41
2.10 Schematic set up of a point-by-point inscription technique. 42

3.1 The Schematic diagram of the two-beam holographic inscription technique (refer to figure 2.7 for the actual set-up). 55
3.2 (a) Bragg wavelength against the two-beam interferometer arm-length L_x for L_0 =522mm, n_{eff} =1.446, θ_0 = 45° and λ_{uv} =244nm. (b) Schematic diagram of optical set-up for changing the Bragg wavelength by varying the arm-lengths (moving mirrors M2 and M3 to position M2' and M3'). 56
3.3 Spectra growth of holographically inscribed FBGs in SMF-28 monitored for about 1 minute. 58
3.4 Typical transmission spectra of holographically inscribed FBGs in SMF-28 fibre with Bragg wavelengths ranging from near-IR (800nm) to mid-IR (2µm). 59
3.5 Images of the UV diffraction pattern: (a) with a bare phase mask; (b) with phase mask and optical fibre; (c) the laboratory set up showing the viewing screen, the phase mask, the fibre and the scanning stage; (d) another diffraction pattern with both the phase mask and the fibre. 60
3.6 (a) Schematic of UV diffraction beams by phase mask and (b) five selected points of phase mask for measurement. 61
3.7 The fabrication set up with the QPS phase mask mounted on a tilt stage on a 3D translation stage. 63
3.8 The microscope with $\times$ 100 objective lens used to view the inscribed FBG, showing a uniform period across the length of the grating. 64
3.9 The transmission spectrum of the fabricated FBGs using the QPR phase mask; at wavelengths (a) 1536nm, (b) 1544nm, (c) 1552nm, (d) 1560nm and (e) 1568nm respectively; (f) a plot showing the effect of change in period on grating wavelength. 65
3.10 Graph showing the annealing result of an FBG inscribed in SMF-28 fibre. 66
3.11 FBG temperature sensing experimental setup, showing the FBG on a heat controlled peltier and the OSA for observing and capturing the wavelength shift using a LabView program. 68
3.12 Comparison FBG thermal response Vs Wavelength shift for three different wavelength ranges. 69

3.13 Experimental set up of FBG cryogenic sensing. 70
3.14 (a) Comparison FBG response for both the cryogenic and elevated temperatures: (b) Comparison FBG thermal response Vs wavelength. 71
3.15 Transmission spectra of six LPGs inscribed in SMF-28 fibre by point-by-point method with periods of 290μm (a), 295μm (b), 300μm (c), 305μm (d), 310μm (e) and 315μm (f). 73
3.16 Combined transmission spectra of the selected two LPGs with periods of 290μm and 315μm, showing the wavelength shifts for each coupled peak. 74
3.17 Analysis of the change in transmission peak intensity observed when the LPG period changes of 290μm to 315μm, for LP_{03} - LP_{05}. 75
3.18 Comparison of transmission loss peaks fabricated for LPGs with different grating lengths, while all other parameters are kept the same. 76
3.19 Transmission spectra of four LPGs inscribed in SMF 28 fibre by point-by-point method with periods of 300μm, 330μm, 360μm and 440μm. 78
3.20 Comparison of thermal responses of LP_{05} cladding modes of four LPGs with different periods (300μm, 330μm, 360μm and 440μm). 78
3.21 Comparison of thermal response of different cladding modes of an LPG with a period of 440μm. 79
3.22 A schematic representation of an LPG as a RI sensor. 81
3.23 Experimental set up of the RI sensing, with the LPG secured to the glass slide and the two ends connected to the BBS and an OSA. 82
3.24 Plot of (a) the central wavelength shift at RI from RI = 1.3 to RI = 1.4; (b) LPG response to RI from 1.46 to 1.70. 83
3.25 (a) Plot of the overall RI induced wavelength shift of the LP_{05} mode from the LPG with 360μm period when surrounding RI changed from 1.46 to 1.70; (b) The effect of each change in RI on the transmission peak strength. 83
3.26 The experimental results showing RI induced wavelength shift of the LP_{05} of four LPGs of different periods at around 300μm, 330μm, 360μm and 440μm. 84
3.27 Sensing LPG calibration for RI versus Wavelength shift; showing about 5nm wavelength shift for RI change from 1.35 to 1.40 (Cargille Index Gels). 85
3.28 Plots of (a) LPG wavelength shift with immersion in FBS for about 240 seconds, (b) LPG wavelength shift with immersion in FBS showing what happens when the Serum sample dry out, (c) Captured trace of LPG central wavelength response per 20 seconds interval and (d) LPG transmission peak intensity at different wavelengths before the Serum sample dry out. 86

4.1 Diagram showing the three mode coupling regimes for a TFG: (a) Phase matching condition for when $\theta < \theta_{1c}$ showing a backward cladding mode coupling, (b) Phase matching condition for when $\theta_{1c} < \theta < \theta_{2c}$ showing a radiation mode coupling and (c) Phase matching condition for when $\theta > \theta_{2c}$ showing a forward cladding mode coupling. 97
4.2 Phase matching condition for tilted angles (a) when θ <45°and (b) for when θ >45°[7]. 98
4.3 Diagram of a TFG showing the difference between the internal tilt (θ_{int}) and external tilt angles (θ_{ext}) [3]. 100
4.4 (a) Phase mask tilted with respect to the optical fibre, (b) phase mask with tilted pitches and (c) rotating the fibre about the axis normal to the plane defined by the two interfering UV beams from the two-beam holographic system. 102

4.5 The laboratory set up used to fabricate small and large angle TFGs. The grating growth can be monitored in-situ by connecting to a BBS and an OSA. The phase mask is mounted on a goniometer, which facilitates the rotation of the mask for lunching the light into the fibre, the fibre holder which holds the fibre in place, the tilt stage enables the tilting of the phase mask, the OSA for interrogating the grating during fabrication and a LabView programme for capturing the data from the OSA. . . . 103
4.6 Transmission-loss spectra of TFGs with small tilted angles varying tilted angles from 0° to 10° (2° increment) fabricated on standard SMF-28 fibre, measured when the TFG fibres were exposed in air. . . . 104
4.7 (a) Plot showing the relationship between cladding modes profile central wavelength Vs the internal tilt angle and (b) the relationship between the Bragg wavelength Vs the internal tilt angle. . . . 105
4.8 The spectral profile of a 4°-TFG with a resonance feature when the grating is surrounded by air and the smooth spectral profile when the grating is immersed in an index matching gel. . . . 106
4.9 The set up for characterising the polarisation responses of small angle TFGs, with a BBS, a polariser, polarisation controller, the 8°-TFG, the OSA and a LabView capture programme. . . . 107
4.10 The transmission spectra of an 8°-TFG, showing the two sets of cladding modes of orthogonal polarisation states (P1 and P2) in four different wavelength ranges: (a)1500nm – 1509nm, (b)1511nm – 1520nm,(c)1522nm – 1531nm and (d)1533 – 1542nm. . . . 108
4.11 The transmission spectra of (a) a 4°-TFG and (b) a 10°-TFG with two orthogonal polarisation states; zoomed transmission spectra of (c) a 4°-TFG and (d) a 10°-TFG with two orthogonal polarisation (P1 in blue and P2 in red). . . . 109
4.12 (a) The thermal response of a normal FBG (0°-TFG) at 1550nm; The thermal response of P1 polarisation state peaks at wavelengths 1500.1nm and 1535nm for (b) 4°-TFG, (c) 8°-TFG and (d) 10°-TFG. . . . 110
4.13 (a) Simulation showing the internal tilt angle (θ_{int}) Vs the external tilt angle (θ_{ext}) for TFGs fabricated by the phase mask technique using equation 4.10, (b) The diffraction pattern after the tilted amplitude mask captured on a screen during the fabrication. . . . 112
4.14 Magnified microscopic images of the fringe of the TFGs with internal angles (a) 75.85° i.e. the θ_{ext} is ~69.5° and (b) 82.55° i.e. the θ_{ext} is ~79.2°, captured with a 40x objective lens. . . . 112
4.15 Transmission spectra of (a) 75.9°-TFG and (b) 83°-TFG across a wavelength range of 1500nm – 1700nm probed with un-polarised light, showing distinctive dual-peak feature. Transmission spectra of (c) 75.9°-TFG and (d) 83°-TFG across a wavelength range of 1500nm – 1700nm probed with polarised lights (P1 and P2). Zoomed transmission spectra of (e) 75.9°-TFG at ~1535nm and (f) 83°-TFG at ~1532nm. . . . 114
4.16 Transmission resonances with dual-peaks for an 83°-TFG in air (red line) and immersed in index matching gel (black line) across a wavelength range of 1500nm – 1700nm. . . . 115
4.17 Thermal responses of the selected P1 polarised peaks from the dual polarisation states at (a) 1526.1nm and 1638.2 nm for the 75.9°-TFG, and (b) at 1524.2nm and 1690.1 nm for the 83°-TFG . . . 116
4.18 The experimental set up of the spectral interrogation for the implementation of the all-fibre twist sensor based on a 45°-TFG and an 81°-TFG. . . . 117
4.19 The transmission spectra of an 81°-TFG when lunched with randomly and orthogonally polarised light. . . . 118

4.20 Spectrum evolution of 81°-TFG under twist in clockwise direction from 0° to 180° and in the anticlockwise direction. 119
4.21 The schematic diagram of the all fibre twist sensor system using a single wavelength laser and a power detector. 119
4.22 The upper plot is the transmission of spectra of dual peaks of the 81°-TFG; the wavelength of P1 is at 1539.62nm and that of the P2 is at 1545.74nm. The lower one is the output spectra of a tuneable laser set at the wavelength 1539.62nm and 1545.74nm. 120
4.23 Transmission powers for the two orthogonal polarisation modes (Red dots – 1539.62nm and Black dots – 1545.74nm) measured by using a low-cost power detection method: (a) using a power meter and (b) using a photo-detector. 120
4.24 The schematic of an in-fibre Mach-Zehnder interferometer implemented with a pair of large angle tilted fibre gratings. 122
4.25 Interference fringes of the MZI formed by a pair of 81°-TFGs with 48mm separation (Red and blue curves: core mode coupled to P1 and P2 orthogonal polarised cladding modes respectively) 123
4.26 Fringe spacing against the grating separation with individual grating length of 8mm. 124
4.27 The graph of the wavelength shift Vs the change in index matching gel ranging from 1.30 to 1.42 RIU. 124
4.28 (a) The unrefined cane sugar used for the experiment, (b) the digital weighting scale used to measure the sugar and (c) the cylindrical glass holding the diluted sugar of different sugar concentration. 125
4.29 (a) MZI wavelength shifts at (a) 0% (b) 10%, (c) 20%, (d) 30%, (e) 35% and (f) 40% sugar concentrations. Red curve (in air) and black curve in different sugar concentrations. 126
4.30 (a) Wavelength shift against the concentration of sugar and (b) Graph showing correlation calibration between RI and sugar concentration for the paired 81°-TFGs based MZI. 127
4.31 (a) Graph showing the wavelength shift of resonant peaks against the concentration of HgB in phosphate buffer solution, (b) Graph showing the wavelength shift of resonant peaks against the concentration of HgB in 20% sugar solution. 128

5.1 (a) The Transmission spectra of TFGs with 5°C, 15°C, 25°C, 35°C, 45°C, 55°C and 65°C tilted angles; showing the dashed lines (P-polarised light) and solid curves (S-polarised light). (b) Plot showing the percentage transmission losses of TFGs versus the S-polarized and P-polarised light for a 45°C tilt angle[8]. 136
5.2 (a) The phase matching of TFG < 45° (b) The phase matching of TFG = 45° (c) The phase matching of TFG > 45° (d) The Schematic of 45°-TFG structure showing the three mode coupling range. 137
5.3 Simulation showing the internal tilt angle (θ_{int}) Vs the external tilt angle (θ_{ext}) for TFGs fabricated by the phase mask technique using Equation 4.10. 139
5.4 (a) 3-D schematic diagram showing the interference area of the ± 1 UV diffraction order after a normal phase mask; the dark area represents the interference area in the xy plane (b) 2-D diagram of the UV interference region with θ = angle between the ± 1 order diffraction beam, D is area of the depth of interference and L is the UV beam in the y-axis (c) 3-D schematic diagram showing the interference area of the ± 1 UV diffraction order after a tilted phase mask (d) 3-D diagram of the volume after the tilted phase mask; with φ = tilt angle of the phase mask, H is the height of the UV beam in the z-axis and D is the distance between the interference area and the phase mask. [6] 140
5.5 The fabrication set up showing how the change in the focal length of the cylindrical lens is used to defocus the beam by 1.5mm; yielding a UV beam spot size of about 0.5mm. 141

5.6 Schematic of a tilted phase mask of length 25mm and a height of 10mm 141
5.7 Schematic of UV diffraction beams by phase mask (a) and five selected points of phase mask for measurement (b). 142
5.8 Image of UV diffraction pattern by SRK003C-1 phase mask. (a) with bare phase mask and (b) with phase mask and optical fibre; Image of UV diffraction pattern by SRK003C-2 phase mask.(c) with bare phase mask and (d) with phase mask and optical fibre; Image of UV diffraction pattern by Ibsen phase mask.(e) with bare phase mask and (f) with phase mask and optical fibre. 144
5.9 The grating fabrication set up used in the laboratory; with a LabView programme controlling the air-bearing stage. 145
5.10 The microscopic image captured from the Zeiss Axioskop 2 mot plus showing the grating structure of the 45°-TFG inscribed in the fibre core 146
5.11 (a) The broadband PER profile of a 15mm long 45°-TFG over a 180nm span using HP83437A broadband source, (b) PER measurement of a 15mm long 45°-TFG using a single wavelength laser diode 147
5.12 The PER profile of a 15mm long 45°-TFG before and after annealing over 60nm span 148
5.13 (a) Experimental measurement of the PER thermal response of the post- annealed five 45°-TFGs, showing no change with increasing temperature. 149
5.14 The linear relationship between 45°-TFG grating lengths and its PER. 150
5.15 (a) PER of a 15mm 45°-TFG at approximately 802nm wavelength showing a PER of ~13dB and (b) the PER of a concatenated 30mm long 45°-TFGs at approximately 802nm wavelength showing a PER of about 37dB. 150
5.16 (a) The PER profile of a 22mm long 45°-TFG detuned at +2° and +4° to the phase mask tilt angle of 33.7°, (b) the PER profile of a 22mm long 45°-TFG detuned at -2° and -4° to the phase mask tilt angle of 33.7°, (c) The PER profile of a 22mm long 45°-TFG detuned at -2° and +2° to the phase mask tilt angle 33.7°, (d) the PER profile of a 22mm long 45°-TFG detuned at -4° and +4° to the phase mask tilt angle of 33.7°. 152
5.17 The PER profile of a 24mm long 45°-TFG (concatenated 12mm TFGs) detuned at +2°and -2°to the phase mask tilt angle 33.7°, showing a very broad PER spectrum. . 153
5.18 Experimental set-up for measuring the polarization distribution of 45°-TFG 154
5.19 (a) The Polarization distribution in a plain fibre with 0dB PER; (b) the polarization distribution of an 800nm 45°-TFG (15mm in length) with ~13dB PER. 154
5.20 Experimental set-up used for the power tapping measurement; comprising of an 800nm butterfly laser diode, power meter, polarization controller, silicon photodetector, an oscilloscope, fibre holder, a 3D stage and a 45°-TFG at 800nm 156
5.21 (a) the relationship showing the amount of side tapped power and PDL (b) Captured image of white light through the 45°-TFG grating and (c) captured image of red light through the 45°-TFG grating. 157
5.22 (a) Side tapped power distribution along the TFG length (b) measured power distribution in azimuthal direction along a 9mm 45°-TFG, showing a Gaussian profile . 157
5.23 Gaussian profile generated from the measurement seen in Figure 5.22 (b) using Matlab 158
5.24 Schematic diagram of the experimental set-up for the side tapped beam characterizing and dispersion measurement. 158
5.25 (a) Measurement of the side tapped beam width of a 1mm 45°-TFG, (b) measurement of the side tapped beam width of a 10mm 45°-TFG 159
5.26 (a) Measurement of the side tapped beam dispersion of a 10mm 45°-TFG with 2D camera at 1mm from TFG, (b) measurement of the side tapped beam dispersion of a 10mm 45°-TFG with 2D camera at 5mm from TFG, (c) measurement of the side tapped beam dispersion of a 10mm 45°-TFG with 2D camera at 10mm from TFG and (d) measurement of the side tapped beam dispersion of a 10mm 45°-TFG with 2D camera at 15mm from TFG. 160

5.27 (a) Azimuthal dispersion measurement of the 1mm 45°-TFG sample, (b) Azimuthal dispersion measurement of the 10mm 45°-TFG sample 161
5.28 Dispersion rate comparison between the 1mm 45°-TFG and the 10mm 45°-TFG. . . . 161

6.1 Schematic showing the 800nm TFG-CCD interrogation system 167
6.2 Transmission spectrum of the white-light continuum laser by Fianium, measured from 600nm to 1050nm. 168
6.3 The dimensions and arrangement of the 800nm TFG interrogation system as used in the set up shown in Figure 6.1. 168
6.4 (a) The transmission spectrum of an 800nm 45°-TFG, measured in air. (b) The reflection spectrum of the sensing FBG sensor. 169
6.5 The photograph of the experimental setup using the CCD, cylindrical lens, cylindrical rod and TFG. 170
6.6 The manufacturers stated relative sensitivity from 400nm to 1000nm radiation range (Sony ILX511 datasheet). 171
6.7 The photographic images projected on the screen from the 633nm He-Ne laser; (a) without the cylindrical rod and cylindrical lens, (b) without the cylindrical rod and with the cylindrical lens, (c) using Fianium BBS without cylindrical lens and rod, (d) with the cylindrical rod and without the cylindrical lens and (e) with both the cylindrical rod and cylindrical lens. 172
6.8 The separated colours from Figure 6.7 (c), showing individual colours green, yellow, orange and red corresponding to wavelengths 530nm, 600nm, 630nm and 670nm respectively. 173
6.9 (a) Signal captured from an 800nm laser diode by the CCD-array, (b) Signal captured from an 800nm laser diode by an OSA, (c) Signal captured from a 633nm He-Ne laser by the CCD-array and (d) Signal captured from a 633nm He-Ne laser by an OSA. . . 174
6.10 (a) The CCD array captured signal when the focal length of the cylindrical lens was changed by ±10mm in steps of 1mm, (b) The CCD array captured signal when the focal length of the cylindrical lens was kept at 155mm and the 800nm laser diode current changed from 30mA to 50mA in steps of 2mA. 175
6.11 The relationship between the CCD pixel reading and the Bragg wavelength shift of the 800nm interrogation system; showing a linear correlation. 176
6.12 The schematics of the 800nm interrogation system based on 45°- TFG and CCD for temperature sensitivity. 178
6.13 (a)-(g) The intensity profiles of FBG captured by the 800nm 45°- TFG and CCD based interrogation unit under temperature change from 10°C to 70°C; (h) Converted wavelength shift against temperature for the FBG sensor. 179
6.14 (a) The reflection spectra for all temperatures captured by the OSA system; (b) the plot of wavelength shift against temperature. 180
6.15 Simplified sketch of a TFBG displaying the emission geometry. Left: Divergence output characteristics in the radial plane of the fiber. Right: Wavelength dependent refraction of the tilted Bragg grating in the axio-lateral plane. 182
6.16 Optical design illustrated in different planes as a printout of the Zemax simulation. 184
6.17 The opto-mechanical design of the TFG spectrometer. 184
6.18 Schematic overview of the OCT system with the implemented TFG spectrometer: SLED - superluminescence diode, FC – 50:50 fibre coupler, PC1-PC3 – Polarization controller, Ref – reference arm, L1-L6 – lenses, Dim – screw to dim the reference signal, Mirr – silver mirror, Sam – Sample arm, Galvo – galvanometric scanner, Spec – TFG Spectrometer, TFG – tilted fibre grating, CCD – CCD line camera, USB – USB interface, Comp – computer, DAQ – data acquisition card. 184

6.19 Measured sensitivity over the half depth range acquired with an integration time of 100µs and an optical power of 0.98 mW on the sample. The maximum sensitivity reaches 108 dB and falls-off by -34 dB over 3.23 mm. 186
6.20 (a) Single tomogram of lemon pulp: lateral scan range of 18 mm, acquired at 100µs integration time sampled at 1024×4096 pixels. (b) In-vivo OCT image of a fingertip with 400×1200 pixels from a volunteer acquired on an integration time of 100µs over a scan range of 11 mm. (c) Anterior segment images of a pig-eye made with an integration time of 100µs; cross-sectional OCT image of the cornea, scan range of 12.5 mm, 1024×1400 pixels (d) averaging of 18 frames shows lens and the iris, scan range 11.5 mm, 667×1096 pixels. 186

List of Tables

2.1 Comparison of the different grating fabrication techniques 43

3.1 Diffraction efficiency of QPS Phase Mask at Λ = 1060.85nm 62
3.2 Diffraction efficiency of QPS Phase Mask at Λ = 1066.39nm 62
3.3 Diffraction efficiency of QPS Phase Mask at Λ = 1071.92nm 62
3.4 Diffraction efficiency of QPS Phase Mask at Λ = 1077.45nm 62
3.5 Diffraction efficiency of QPS Phase Mask at Λ = 1082.98nm 62
3.6 Temperature sensitivity of LPGs of different LP_{05}. 79
3.7 Temperature sensitivity of different modes (LP_{01} - LP_{05}) of a LPG with 440μm period. 79

4.1 The table showing the thermal sensitivity result comparison for the 4°-TFG, 8°-TFG and 10°-TFG: 110
4.2 The table showing the thermal sensitivity result comparison for the 75.9°-TFG and 83.0°-TFG: 116

5.1 Tilted phase mask diffraction efficiency of SKR003C-1 143
5.2 Tilted phase mask diffraction efficiency of SKR003C-2 143
5.3 Tilted phase mask diffraction of Ibsen Phase Mask 143

List of Acronyms

BBS	Broadband Light Source
B/Ge	Boron/Germanium Codoped
CCD	Charge-Coupled Device
CDA	Centroid Detection Algorithm
CMT	Coupled Mode Theory
EMI	Electromagnetic Interference
FBG	Fibre Bragg Grating
FBS	Fetal Bovine Serum
GODC	Germanium Oxygen Defeciency Centre
IR	Infrared Ray
LPG	Long-period Grating
MVCD	Modified Chemical Vapour Deposition
NBOHC	Non Bonding Oxygen Hole Centre
OSA	Optical Spectrum Analyser
PDL	Polarisation Dependent Loss
PER	Polarisation Exctinction Ratio
PM	Polarisation Maintaining
RIU	Refractive Index Unit
SMF	Single-Mode Fibre
SRI	Surrounding-medium Refractive Index
TIR	Total Internal Reflection
TFG	Tilted Fibre Grating
UV	Ultraviolet
VCM	Volume Current Method
WDM	Wavelength Division Multiplexing

1 INTRODUCTION AND THESIS STRUCTURE

1.1 *INTRODUCTION*

In today's technological revolution and since the realisation of low loss optical fibre 1970's [1], optical fibre has found its application in the day to day living without people appreciating the extent of its impact. Some of these applications are optical communications, bio-medical detection and diagnostic function and other various optical sensing applications. The fibre optic properties such as: immunity to electromagnetic interference, flexibility, high temperature tolerance, low insertion loss, small size and lightweight, high coupling efficiency, multiplexing capability, and low-cost have helped to tackle the high demands been placed on global communication systems, which in effect affects vital services like; internet access, audio and video transmissions. As consumer demands and expectation increases, fibre optics have proven to have greater advantages over the already existing technologies as they can be directly integrated into other systems and in some cases they can replace bulk optical components.

Hill et al. at the Canadian Communications Research Centre (CRC) [2] reported the first in-fibre grating in 1978. Subsequently, scientists have developed devices for various applications based on the fibre Bragg grating (FBG), long period grating (LPG) and tilted fibre grating (TFG) structures. Due to the great potential of these grating structures and their coupling mechanism [2, 3] researchers have been working to design customised grating devices for applications in optical communications, signal processing and sensing [4–6].

Normal axis fibre gratings can be classed into two categories: FBGs and LPGs. These usually are created by exposing a given length of a fibre to an Ultraviolet laser (UV) light source, which causes a refractive index (RI) modulation in the fibre core. This process can be carried out using a variety of techniques, such as the two-beam holographic, phase mask and point-to-point method.

In recent years, the other type of gratings, TFGs, which have non-normal axis as the UV inscribed refractive index fringes in the fibre core are tilted, have sparked great interest due to their distinctive optical properties. The ability to couple light from the core to cladding and radiation modes demonstrated by TFGs was first revealed in 1990 by Meltz et al [7]. Due to advances in UV inscription technology and greater demands for applications, 45°-TFG structures have been explored in applications such as polarisation-dependent-loss (PDL) equalizer [8], in-line polarimeter [9] and in-line polarizer [10]. In an initial experiment by Zhou et al [10], it was shown that the maximum polarisation dependent loss (PDL) of 33dB was obtained at a 45° tilt grating compared to other tilted grating angles, which supports the theory of the Brewster angle.

This thesis will review optical fibre grating devices with different structures, including FBG, LPG and TFG, and their various applications in optical sensing, bio-medical sensing and power monitoring. The increasing demand for high function in-fibre devices and systems and their commercialisation for a range of applications are the motivation of the work reported in this thesis.

1.2 *OVERVIEW OF THESIS*

This thesis gives a summary of the work carried out in the fabrication of fibre grating structures and their application as optical fibre sensors. Various grating fabrication methods have been used and explored. The three main grating structures examined in this thesis are FBG, LPG and TFG. In addition to these, a systematic characterisation work was carried out on these different grating structures. This thesis is made up of 7 chapters and the details of each chapter are highlighted below:

Chapter 1 contains a brief introduction and an overview of the thesis. It also includes the motivation for this Ph.D. research.

Chapter 2 gives a theoretical background and an introduction to the optical fibre gratings in terms of the theories, optical fibre photosensitivity mechanisms, fabrication methods, grating structures and spectral characteristics. The theoretical analysis using the coupled mode theory for the different types of grating structure is presented in detail. This will enable the reader to comprehend the concept of fibre grating structures and their applications in subsequent chapters.

Chapter 3 introduces the design, fabrication and characterisation of normal-axis periodic grating structures, i.e. FBGs and LPGs. Then a review on their sensing applications is presented. The

FBGs have been characterised for their temperature responses, while the LPGs were also used in refractive index (RI) sensing and bio-medical sensing applications.

Chapter 4 explores the mode coupling mechanisms, fabrication and characterisation of non-normal-axis gratings, i.e. TFGs with small and large tilt angle structures. Their sensitivity to temperature, polarisation status and surrounding refractive index (SRI) have also been characterised. In order to further analyse the potential application, the large angle TFGs have been implemented as an all-fibre twist sensor and furthermore as an interferometer used for sensing bio-samples.

Chapter 5 presents the design, fabrication and characterisation of 45°-TFG particularly at the shorter wavelength range, 800nm. It explores the implementation of 45°-TFG as an in-line polariser. This work systematically explored the maximum polarisation dependent loss (PDL), PDL profile, annealing effect on PDL, thermal effect on PDL, polarisation distribution and the relationship between the external and the internal angle of the 45°-TFGs. Another application investigated in this section is the power tapping ability of the 45°-TFG at 800nm, which was further explored for its ultra-broadband capability. And this 45°-TFG based power tapper has been used to monitor the temperature of an FBG sensor.

Chapter 6 reports on the utilisation of the unique radiation profile of 45°-TFGs working at 800nm to build a versatile interrogation systems (spectrometers). The interrogation system has been evaluated for an FBG sensor subjected to the changes in temperature. In collaboration with Stefan et al (Bern University of Applied Science), this work has been extended into an optical coherence tomography (OCT) for bio-medical sensing application.

Chapter 7 concludes the work and gives some suggestions for future work.

1.3 References

[1] D. Kato, "Fused-silica-core glass fiber as a low-loss optical waveguide," *Applied Physics Letters*, vol. 22, no. 1, pp. 3–4, 1973.

[2] K. Hill, Y. Fujii, D. Johnson, and B. Kawasaki, "Photosensitivity in optical fiber waveguides: Application to reflection filter fabrication," *Applied Physics Letters*, vol. 32, pp. 647–649, 1978.

[3] T. Erdogan, "Fiber grating spectra," *Journal of Lightwave Technology*, vol. 15, no. 8, pp. 1277–1294, 1997.

[4] R. A. Bergh, H. C. Lefevre, and H. J. Shaw, "Single-mode fiber-optic polarizer.," *Optics letters*, vol. 5, pp. 479–481, 1980.

[5] R. B. Dyott, J. Bello, and V. A. Handerek, "Indium-coated D-shaped-fiber polarizer.," *Optics letters*, vol. 12, pp. 287–289, 1987.

[6] W. Eickhoff, "In-line fibre-optic polariser," *Electronics Letters*, vol. 16, no. 20, pp. 762–764, 1980.

[7] G. Meltz, W. Morey, and W. Glenn, "In-fiber Bragg grating tap," in *Optical Fiber Communication Conference*, vol. 1169, p. 6108, 1990.

[8] D. Williams, B. Ainslie, J. Armitage, R. Kashyap, and R. Campbell, "Enhanced UV photosensitivity in boron codoped germanosilicate fibres," 1993.

[9] P. Lemaire, R. Atkins, V. Mizrahi, and W. Reed, "High pressure H2 loading as a technique for achieving ultrahigh UV photosensitivity and thermal sensitivity in GeO2 doped optical fibres," 1993.

[10] K. Zhou, X. Chen, L. Zhang, and I. Bennion, "High extinction ratio in-fiber polarizer based on a 45deg-tilted fiber bragg grating," *OFC/NFOEC Technical Digest. Optical Fiber Communication Conference, 2005.*, vol. 1, 2005.

2 OPTICAL FIBRE GRATING THEORY, FABRICATION METHODS AND APPLICATIONS

2.1 *INTRODUCTION*

This chapter contains the fundamental theories and principle of optical fibre gratings. The historical perspective of photosensitivity mechanisms in optical fibres is examined discussion on various photosensitisation techniques. Later in this chapter, the mode coupling mechanisms using mode coupling theory are used to examine the behaviours of FBGs, LPGs and TFGs. This is followed by the detailed description on various optical fibre grating fabrication techniques: two-beam holographic, phase-mask and point-by-point methods. This section briefly reviewed the main applications of optical fibre gratings, which explains the motivation of my research work. Finally, conclusion is given.

2.2 *PHOTOSENSITIVITY IN OPTICAL FIBRE*

Photosensitivity is a term that generally refers to material sensitivity to electromagnetic radiation, usually light. The photosensitivity of optical fibres shows itself as a change in the refractive index following the exposure to UV radiation. In 1978, Hill was the first researcher to discover the photosensitivity of optical fibres when his group launched light from an Argon-ion laser into a germania-doped fibre. They observed an increase in the intensity of the reflected light after several minutes, which then continued until all the light has reflected out of the fibre [1]. Since this discovery, there has been wide academic interests in optical fibre photosensitivity to explain the different photosensitivity mechanisms. Despite this great interest, there is still no single theory that can explain the photosensitivity in all cases. However, there is consensus that optical fibre photosensitivity depends on a number of factors: core material, fibre type, the wavelength and intensity of radiating light and fibre treatment (flame brushing, hydrogenation, etc.). In the earlier stage, researchers once believed that only germanium-doped fibres are photosensitive [2], but later studies showed that some fibres such as cerium [3] and europium [4] doped have also shown photosensitivity.

Overall, silicate fibres with germanium dopant have attracted the most interests due to their wide use in telecommunication and optical sensing.

2.2.1 Photosensitivity Mechanisms

The photosensitivity models that were reported over the years include: compaction [5], ionic migration [6], colour centre [7], electron charge migration [8], stress relief [7], Soret effect [9] and permanent electric charge dipole [10].

Defect points in silicate glass have been regarded as the cause of photosensitivity in optical fibres and this has been investigated using the electron spin resonance (ESR) technique. Three main defects found are: the E' centre, the nonbonding oxygen hole centre (NBOHC) and the peroxy centre [11].

The two stable oxides of germanium occur as GeO and GeO_2. The germanium-oxygen deficiency centres (GODCs) created during the UV absorption in a germane-silicate fibre are the elements responsible for their refractive index change. During the fibre drawing process, the modified chemical vapour deposition (MVCD) process occurs at high temperatures which cause the GeO_2 molecules to break into a more stable GeO molecule, which itself changes to Ge+. When the Ge+ gets into the glass material, they can form oxygen vacant Ge-Si or Ge-Ge bonds which are both oxygen deficient [12]. These deficiency centres are linked to the 240nm absorption band of silica glass. This thesis will only be looking at three main mechanisms of photosensitivity in germanium-doped fibres: compaction densification model, colour centre model and stress relief model.

2.2.1.1 *Compaction densification model*

The densification model considers that the laser irradiation of the glass causes density increase resulting in the increase in the refractive index of the glass. Researchers Fiori & Devine [5] carried out an experiment in which an amorphous silica thin film was grown on Si wafers and irradiated by a KrF excimer laser. An increase of about 16% in the film thickness has been reported and an increase in refractive index. The sample was then annealed at 950°C for about 1 hour and the film thickness returned to its original state. The further exposure of the sample to radiation above the threshold leads to permanent densification. Chiang et al [13] annealed the sample at an even higher temperature 1200°C; their result shows that at this temperature the photosensitivity of the germane-silicate fibre was completely removed and irreversible. It was later experimentally shown that changes in refractive index of a non-hydrogen loaded fibre is mainly due to the densification of the silica [14].

2.2.1.2 *Colour centre model*

The fibre drawing process [15] and ionisation radiation [16] can cause defect points which are also called colour centres and are very important for optical fibres due to their absorption bands centred at 240nm. Understanding the nature of these defects in germane-silicate fibres will help us in understanding the colour centre model. Germanium has +2 and +4 stable oxidation states, therefore it can form either GeO or GeO_2 molecules in glass despite the Si. The rule of thermodynamics requires that there is a balance between GeO_2 and the GODCs concentrations. GeO has also been found to be more stable than GeO_2 at high temperatures, which gives rise to wrong bond Ge-Si formation in glass. These wrong bonds are known to be precursors to defects. The Ge dopant of the fibre core is directly related to the defect centres, labelled as Ge (n) [11] during a radiation study on the paramagnetic defect centres in germano-silicate fibres. Ge (n) centres change to Ge(n)- centres by trapping an electron. Also called the GeE' centre is the Ge (0)/Ge (3) damage centres which have the deepest electron trap depth.

Hand and Russell [17] originally proposed the colour centre model as shown in Figure 2.1. They examined the photo-induced refractive index change in a germano-silicate fibre exposed to a 488nm Argon-ion laser and linked it to a two-photon absorption process. Oxygen deficient bonds; Si-Ge, Si-Si and Ge-Ge are produced in the fibre core due to the presence of Ge atoms, which acts as a defect within the silica. The energy required to break this bond could be single-photon (absorption of the 244nm radiation of an excimer laser) or double-photon (absorption of the 488nm radiation of an Argon ion laser). However, recapturing of free electrons occurs at the hole-defect sites to form colour centres as Ge $(1)^-$ and Ge $(2)^-$ in the absorption bands 281nm and 213nm respectively. Illuminating the fibre by a wavelength coinciding with the 240nm band results in bleaching of the 240nm band and the formation of a new band with central peaks at 195nm [18]. Following Kramers-Kroning relationship (equation 2.1), the new absorption band formed will induce the refractive index change [19].

$$\Delta n_{eff}(\lambda) = \frac{1}{2\pi^2} p \int_0^{\infty} \frac{\Delta\alpha_{eff}(\lambda)}{1-(\frac{\lambda}{\lambda'})^2} d\lambda \tag{2.1}$$

Where P is the principal part of the integral; λ is the wavelength and $\Delta\alpha_{eff}$ is the effective change in the absorption coefficient of the defect. The relationship reflects that between the infrared to visible range, any refractive index change is a result of the absorption spectrum change in silica from UV to far-UV spectrum [7][12][20, 21]

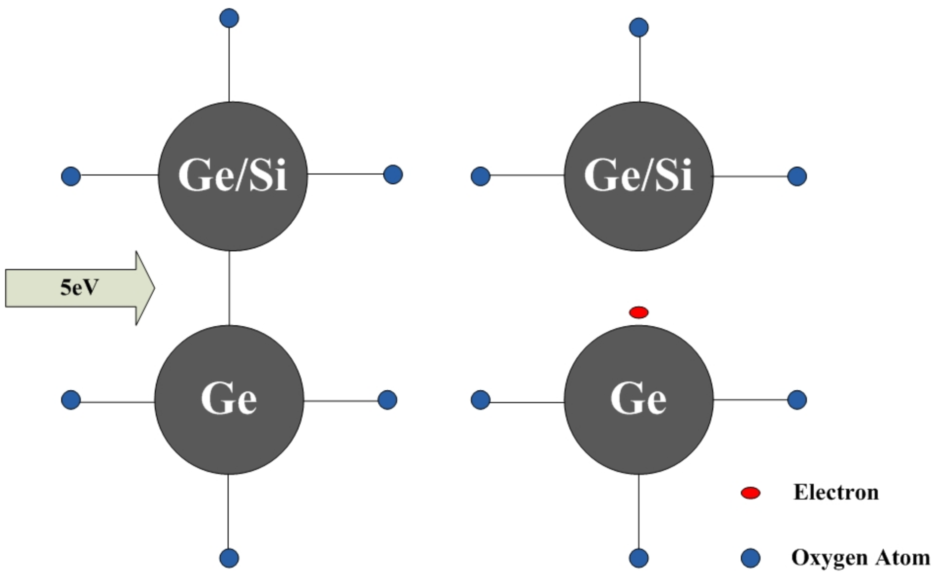

Figure 2.1: Photo-induced refractive index change mechanism: Ge-Si wrong bonds break and release free electrons to diffuse into the lattice network. The resulting molecular change results into change in the refractive index ([22])

The GeE' centres have been known to be responsible for the original Hill grating due to two photon beam absorption at 240nm band [23, 24]. Even though this model is widely supported by researchers and believed to be a source of photosensitivity in germane-silicate and hydrogen loaded germane-silicate fibres, it has not been able to fully explain the higher value refractive index changes induced by UV exposure [25–28].

2.2.1.3 *Stress relief model*

The fibre drawing process occurs at a very high temperature. Due to the difference in the thermal expansion between the core and the cladding, there is an inner tension induced as the glass is cooling down. The stress relief model considers that the refractive index of the fibre increases due to the release of the built-in thermo-elastic stress [20, 21]. It is proposed that the breakage of the wrong bonds due to UV irradiation promotes the relaxation in the tensioned glass and therefore increases the refractive index of the core due to stress-optic effect [20].

2.2.2 Optical Fibre Photosensitisation Techniques

After the discovery of FBG formation and fibre core photosensitivity by Hill et al, great efforts have gone into enhancing the photosensitivity of optical fibres. Various photosensitising techniques have been developed including co-doping the fibre core [29], flame brushing [30] and hydrogen loading [31]. These methods have been shown to increase the photo-induced index modulation of the fibre core up to 10^{-3} or higher.

2.2.2.1 *Co-doping technique*

Adding co-dopants such as boron (B) [29] and tin (Sn) [30] into the fibre can enhance the photosensitivity of germane-silicate fibre. Williams et al reported in 1993 [21] the systematic investigation of the corresponding photosensitivity of differently B co-doped fibre types. This result shows that B co-doped fibre has a saturated index change 4 times higher than that in pure germane-silicate fibre. Three fibres were selected for the experiment: standard telecom fibre (3 mol% GeO_2), high Ge concentrated fibre (20 mol% GeO_2) and B co-doped fibre (15 mol% GeO_2). After subjecting all three samples to UV radiation, the saturated index modulation results were approximately 3×10^{-5}, 2.5×10^{-4} and 7×10^{-4} respectively. The experiment also showed that it took about 10 minutes for B co-doped fibre to reach a saturated index modulation, whilst it took about 2 hours for the other two samples to reach a saturated index modulation. This result makes B co-doped fibre a much better choice in photosensitivity response, however, due to its extra loss of about 0.4dB per km at 1550nm, it may not be so desirable.

Another alternative to B co-doping is the use of Tin (Sn) as a co-dopant in increasing the photosensitivity of germane-silicate fibre. An experiment carried out by Don et al [32, 33] showed that the saturated refractive index change of Sn co-doped fibre was 3 times larger than that of the pure germane-silicate fibre. This result has undoubtedly placed Sn co-doped fibre over the B co-doped fibre due to the grating ability to survive at high temperature and no loss in the 1550nm window.

2.2.2.2 *Flame brushing technique*

Although germane-silicate optical fibres have intrinsic photosensitivity, the photosensitivity can be further enhanced through the flame brushing technique. It was reported that a flame of hydrogen was repeatedly brushed over a desired region of the optical fibre for almost 20 minutes with a small amount of oxygen at about 1700°C [31]. During this process, the H_2 diffused quickly into the fibre core (cladding properties remained unaffected) and reacted with the germane-silicate glass, forming GODCs [11]. It was reported that using this method on a standard telecom fibre increases its photosensitivity by a factor greater than 10 and a refractive index change greater than 10^{-3} in the core of a 1540nm fibre was achieved [31].

2.2.2.3 *Hydrogen loading technique*

Another method to enhance fibre photosensitivity without dramatically altering the physical properties of the glass is the fibre hydrogenation technique. This is a highly effective and simple technique and widely used to increase the photosensitivity of germane-silicate fibres. This process of pressurising the optical fibre in H_2 usually takes place at 150bar before being exposed to the UV. Lemaire et al [31][33] were the first to report this technique in 1993, based on the Ge, Si and H_2 molecule interactions in combination with UV exposure conditions. During the experiment, fibres were soaked in H_2 gas at temperatures from 20°C to 75°C and pressures approximately from 20atm to over 750atm. The fibre was then exposed to a pulsed UV radiation at 241nm. For a hydrogen loaded fibre with 3 mol%GeO_2 and 3.3 mol%H_2, the peak-to-peak index modulation was about 6×10^{-3} and an increment of about 3.4×10^{-3} to the average core index.

During hydrogenation, the fibre is loaded into a high-pressured hydrogen tube. The H_2 molecules diffuse through the cladding of the fibre into the core over a period of time. The H_2 is later dissolved to thermally react with the Si-O-Ge glass sites when exposed to UV or intense heat (including flame or CO_2 laser). Also during this exposure, the formation of Si-OH and Ge-OH bonds occur in addition to the GODCs which causes permanent change in the refractive index of the core. The amount of OH absorption bands at 1.4μm is proportional to the level of hydrogen in the fibre [34]. The UV exposure creates an OH band which has an absorption band at ~1.4μm and also comprises of two closely space absorption peaks at 1.39μm corresponding to Si-OH bonds and 1.49μm corresponding to Ge-OH bonds. The presence of these two closely spaced absorption peaks is not desirable to some telecommunication network systems, but by immersing the fibre into deuterium instead of hydrogen, no UV-induced absorption peaks appears at the communication band (1.3μm-1.6μm).

2.2.3 UV-Induced Index Change Stabilisation

The study of the stability of UV-induced index change in optical fibre is essential for real application purposes. Unreacted or dissolved H_2 diffuses slowly out of the fibre after UV exposure, which means that the UV induced index change is not a permanent phenomenon. Williams et al [35] showed and concluded in a study that the thermal stability of fibre gratings may be stable at room temperature for 25 years after annealing treatment. Further work was carried out by Kannan et al [36] to confirm the work by Williams et al.

2.2.3.1 *Hydrogen diffusion*

The unit of measurement of hydrogen diffusion (i.e. its diffusion coefficient or diffusivity) is cm ^{2} s^{-1} and given by [37, 38]:

$$D = D_0 e^{\left(-\frac{E}{RT}\right)} \tag{2.2}$$

where D_0 is a constant (given as 5.65 $\times$ 10^{-4} cm^2 s^{-1}) independent of temperature and ambient pressure, E is the diffusion activation energy (given as 43.55 KJ^{-1} mol^{-1}), R is the gas constant 8.3 JK^{-1} mol^{-1} and T is the absolute temperature. The values for D_0 and E are almost identical for both the pure and doped silica fibre, with the diffusion rate increasing more rapidly at high temperatures.

Hydrogen diffusion in optical fibres (which begins as soon as the sample is removed from a high pressure atmosphere) causes a Bragg resonance wavelength shift. The fibre structural factors such as its geometry, core and cladding thickness determines the rate at which the diffusion takes place. As the temperature increases, the rate of hydrogen diffusion increases, which means a process (annealing) needs to be undertaken to ensure fibre-grating stability. The annealing of these fibre gratings takes place at elevated temperatures to outgas the unreacted or residual hydrogen. Patrick et al [39] also carried out a study on the grating stability of fibre gratings in hydrogenated and non-hydrogenated fibre after 10 hours at 176°C, which showed that the gratings in non-hydrogenated fibres were more stable at elevated temperatures. The result indicated a 40% UV induced index modulation reduction in hydrogen-loaded fibres and 5% UV induced index modulation in non-hydrogen loaded fibres [39]. However, this model does not agree with Erdogan's model.

The "power law", a model proposed by Erdogan et al, describes the decay of the UV induced index change in non-hydrogen loaded fibre and also explains the thermal degradation of FBGs written in germanium doped silica fibre [40]. Baker et al [41] later confirmed that Erdogan's model is only well suited for non-hydrogenated fibres and does not apply to hydrogenated fibres. An extension of their work includes the proposed long-time model for predicting the decay characteristics of gratings inscribed in hydrogen-loaded fibres. Their model was also extended to fibres (B-doped, Sn-doped and fluorine-doped fibres) in need of thermally stable FBGs [42–44]. Pre-sensitisation [45] of the fibre was earlier proposed to give more stability to fibre gratings, but a report by Niay et al [28] showed that the use of either the Continuous Wave (CW) or pulsed UV sources in the grating fabrication process does not make any difference to the stability of the grating inscribed.

Now as a standard procedure, after fibre grating fabrication, a thermal annealing is usually carried out at 80°C for 48 hours. This is done to accelerate the H_2 diffusion and create stability in the fibre grating [46]. FBGs' reflectivity has been recorded to decrease about 1%-2% over the annealing process with a blue-wavelength shift of 0.2-0.5nm [35, 36].

2.3 *COUPLED MODE THEORY*

Coupled mode theory describes the propagation of electromagnetic waves in periodic layered medium. Due to its simplicity and modelling capabilities of the optical properties of fibre gratings, it has been the most widely used theory in explaining the light coupling operation of fibre gratings. This section will not show the detailed derivation of this theory, but Yariv [47], Kogelnik [48] and Erdogan [49, 50] have produced the derivation. Erdogan mentioned that the couple mode theory is a superposition of ideal modes of an ideal waveguide, and there is no grating perturbation. If modes are labelled with index j, we will have:

$$\overrightarrow{E}_t(x,y,z) = \sum_j [A_j(z)\exp(i\beta_j z) + B_j(z)\exp(-i\beta_j z)].\overrightarrow{e}_{jt}(x,y) \tag{2.3}$$

where the coefficients $Aj(z)$ and $Bj(z)$ are the slowly varying amplitudes of the jth mode travelling in the $+z$ and $-z$ directions, respectively. $\overrightarrow{e}_{jt}(x,y)$ is the transverse mode field, which might describe; bound-core, cladding or radiation mode. The propagation constant β is given by:

$$\beta = \frac{2\pi}{\lambda} n_{eff} \tag{2.4}$$

where n_{eff} represents the refractive index of the jth modes. The coupling between the various modes happens when there is a dielectric perturbation which causes the amplitudes $A_i(z)$ and $B_j(z)$ of the jth modes to evolve along the z direction. This can be seen in the following equations:

$$\frac{dA_j(z)}{dz} = i \sum_k A_k(K^t_{kj} + K^z_{kj}) \exp[i(\beta_k - \beta_j)z] + i \sum_k B_k(K^t_{kj} - K^z_{kj}) \exp[-i(\beta_k + \beta_j)z] \tag{2.5}$$

$$\frac{dB_j(z)}{dz} = -i \sum_k A_k(K^t_{kj} - K^z_{kj}) \exp[i(\beta_k + \beta_j)z] - i \sum_k B_k(K^t_{kj} + K^z_{kj}) \exp[-i(\beta_k - \beta_j)z] \tag{2.6}$$

where K^t_{kj} is the transverse coupling coefficient and K^z_{kj} is the longitudinal coupling coefficients between the k and j modes.

The transverse coupling coefficient between the k and j modes can be expressed as:

$$K^t_{kj}(z) = \frac{w}{4} \iint [\Delta\varepsilon(x, y, z) \overrightarrow{e}^t_k(x, y). \overrightarrow{e}^{t*}_k(x, y)] dxdy \tag{2.7}$$

The longitudinal coefficient $K^z_{kj}(z)$ has similar expression as $K^t_{kj}(z)$, but $K^z_{kj}(z)$ modes are usually neglected ($K^t_{kj}(z)$ « $K^z_{kj}(z)$) since it is half the magnitude of $K^t_{kj}(z)$ for fibre modes. The permittivity perturbation $\Delta\varepsilon(x, y, z)$ in equation 2.7 for δn_{eff} « n_{eff} is approximately;

$$\Delta\varepsilon(x, y, z) = 2n\delta n_{eff}(x.y.z) \tag{2.8}$$

where δn_{eff} is the effective refractive index variation and small compared with the local index n. For instance, in an ideal waveguide (no perturbations) $\Delta\varepsilon$ = 0, the coupling coefficient $K^t_{kj}(z)$ = 0 and the transverse modes are orthogonal; hence there is no exchange of energy. When photosensitive fibres are exposed to a UV-light source, refractive index modulation occurs and this can be expressed as:

$$\Delta n_{eff}(z) = \bar{\delta} n_{eff}(z)[1 + v\cos(\frac{2\pi}{\Lambda}z + \phi(z))] \tag{2.9}$$

where v is the fringe visibility of the index change, Λ is the grating period, $\phi(z)$ is the grating chirp and $\bar{\delta} n_{eff}(z)$ is the "dc" index change spatially averaged over a grating period. The index change $\delta n_{eff}\,(x, y, z)$ induced by the UV in most fibre gratings is uniform across the core and non-existent outside the core. Therefore, by using similar expressions as in equation 2.9 and replacing $\bar{\delta} n_{eff}(z)$ by $\bar{\delta} n_{co}(z)$, the core index change can be described. Also, using equation 2.8 and 2.9, the general coupling coefficient equation 2.7 can be re-written as:

$$K^t_{kj}(z) = \sigma_{kj}(z) + 2K_{kj}(z)\cos\left[\frac{2\pi}{\Lambda}z + \phi(z)\right] \tag{2.10}$$

where $\sigma_{kj}(z)$ is the "dc" coupling coefficient and $K_{kj}(z)$ is the "ac' coupling coefficient and can be expressed as:

$$\sigma_{kj}(z) = \frac{\omega n_{eff}\bar{\delta} n_{eff}(z)}{2}\iint_{core}\overrightarrow{e}^{t}_{k}(x,y).\overrightarrow{e}^{t*}_{k}(x,y)]dxdy \tag{2.11}$$

and

$$K_{kj}(z) = \frac{v}{2}\sigma_{kj}(z) \tag{2.12}$$

2.3.1 Forward Propagation

In this case, the forward propagating mode of amplitude $A_1(z)$ is coupled strongly into the co-propagating mode of amplitude $A_2(z)$. Equation 2.5 and 2.6 can be modified by keeping the terms that involve the amplitudes of these two modes and by synchronous approximation thus:

$$\frac{dR}{dz} = i\hat{\sigma}R(z) + ikS(z) \tag{2.13}$$

$$\frac{dR}{dz} = -i\hat{\sigma}R(z) + ikR(z) \tag{2.14}$$

The new amplitudes are R and S and are expressed as:

$$R(z) = A_1 \exp\left[-i(\sigma_{11} + \sigma_{22})\frac{z}{2}\right] \exp\left(i\delta z - \frac{\phi}{2}\right) \tag{2.15}$$

$$S(z) = A_2 \exp\left[-i(\sigma_{11} + \sigma_{22})\frac{z}{2}\right] \exp\left(-i\delta z + \frac{\phi}{2}\right) \tag{2.16}$$

The "dc" components σ_{11} (and) σ_{22} are described in equation 2.11 and the "ac"- coupling coupling coefficient (k = K_{21} = K_{12}^*) is described in equation 2.12. Also, $\hat{\sigma}$ is the "dc" self-coupling coefficient and can be shown as:

$$\hat{\sigma} = \delta + \frac{\sigma_{11} - \sigma_{22}}{2} - \frac{1}{2}\frac{d\phi}{dz} \tag{2.17}$$

The detuning δ is assumed to be constant along the axis, this becomes:

$$\delta = \frac{1}{2}(\beta_1 - \beta_2) - \frac{\pi}{\Lambda} = \pi\Delta n_{eff}\left[\frac{1}{\lambda} - \frac{1}{\lambda_d}\right] \tag{2.18}$$

where λ_d = $\Delta n_{eff}\Lambda$ is the design wavelength for a grating near zero index modulation. In Bragg gratings, the grating conditions correspond to δ = 0 or λ = λ_d = $\Delta n_{eff}\Lambda$. The forward coupling equations in equation 2.13 and equation 2.14 relates to the first-order ordinary differential equation with constant coefficients for FBGs. In the case of a uniform forward coupling grating, $\hat{\sigma}$ and k are constants and with the appropriate boundary conditions, the closed-form solutions can be obtained.

2.3.2 Backward Propagation

In this case, the dominant interaction is close to the wavelength for which the reflection of a mode of amplitude A(z) is similar to the counter-propagating mode of amplitude B(z). Therefore, this simplifies equation 2.5 and equation 2.6 to the following [51]:

$$\frac{dR}{dz} = i\hat{\sigma}R(z) + ikS(z) \tag{2.19}$$

$$\frac{dR}{dz} = -i\hat{\sigma}R(z) + ik^{*}R(z) \tag{2.20}$$

The amplitude R and S are:

$$R(s) = A(z)\exp\left(i\delta z - \frac{\phi(z)}{2}\right) \tag{2.21}$$

$$S(s) = B(z)\exp\left(-i\delta z + \frac{\phi(z)}{2}\right) \tag{2.22}$$

In equation 2.19 and 2.20, the "ac" component is k. The "dc" self-coupling coefficient is $\hat{\sigma}$ and it can be expressed as:

$$\hat{\sigma} = \delta + \sigma - \frac{1}{2}\frac{d\phi(z)}{dz} \tag{2.23}$$

The detuning δ is independent of z and can be expressed as;

$$\delta = \beta - \frac{\pi}{\lambda} = \beta - \beta_d = 2\pi\Delta n_{eff}\left[\frac{1}{\lambda} - \frac{1}{\lambda_d}\right] \tag{2.24}$$

where λ_d = Δn_{eff} λ is the design wavelength for Bragg scattering by a very weak grating (i.e. δ n_{eff} $\longrightarrow$ 0). For a single-mode Bragg grating, σ and k can be further simplified;

$$\sigma = \frac{2\pi}{\lambda}\bar{\delta}n_{eff} \tag{2.25}$$

$$k = k^{*} = \frac{\pi}{\lambda}\nu\bar{\delta}n_{eff} \tag{2.26}$$

For a uniform grating along z direction, $\bar{\delta}n_{eff}$, k, σ and $\hat{\delta}$ are constants and $\frac{d\phi(z)}{dz}$ = 0 (no grating chirp). This simplifies equation 2.21 and equation 2.22 into first order-coupled differential equations with constant coefficients. When the appropriate boundary conditions are satisfied, the closed-form solutions may be found.

2.3.3 Phase Matching Conditions

The existence of perturbation in the fibre makes it possible for the coupling of the bound-wave to the counter-propagating or co-propagating modes. Due to the direction of grating coupling (forward-coupled or backward-coupled), fibre gratings can be classed into forward-coupled grating: FBGs with uniform, chirped and small-tilt angle structures and backward-coupled grating: LPGs and large angle TFGs. For the coupled modes, the phase mismatch factor $\Delta\beta$ also referred to as detuning is expressed as [49]:

$$\Delta\beta = \beta_i \pm \beta_d - \frac{2\pi}{\Lambda_g} N \cos\theta \tag{2.27}$$

where β_i and β_d are the propagation constants for the incident and diffracted modes respectively, Λ_g is the grating period, θ is the grating tilt angle and N represents an integer number. When there is significant transfer of energy, $\Delta\beta$ = 0 and equation 2.27 becomes [47]:

$$\beta_i \pm \beta_d = \frac{2\pi}{\Lambda_g} N \cos\theta \tag{2.28}$$

If both β_i and β_d have identical signs, then the phase will be matched for counter-propagating modes; if they have opposite signs, the interaction is matched for co-propagating modes. Most cases have shown that the first-order diffraction is dominant, hence N = 1 [47]. The resonant wavelength is therefore:

$$\lambda = \left(n_i^{eff} \pm n_d^{eff}\right) \frac{\Lambda_g}{\cos\theta} \tag{2.29}$$

For Bragg gratings (θ = 0°), the core mode is coupled to the counter-propagating mode (backward coupling) and the Bragg wavelength (λ_β) is expressed as;

$$\lambda_\beta = 2n_{eff}\Lambda \tag{2.30}$$

where n_{eff} is the core effective refractive index. Figure 2.2 below shows a diagram of this coupling;

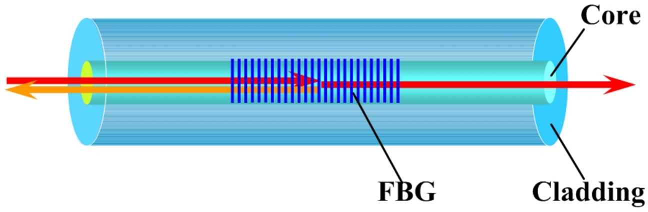

Figure 2.2: Schematic diagram of backward-mode coupling in FBG.

For Long period gratings (θ = 0°),the core mode is coupled to the co-propagating cladding mode (forward coupling) and the resonant wavelength is expressed as:

$$\lambda_{co-cl} = (n_{co} - n_{cl,m}).\Lambda \tag{2.31}$$

where n_{co} and $n_{cl,m}$ are the effective indices of the core and m^{th} cladding mode respectively. Therefore the period of the LPG becomes larger than the FBG as the difference between the core and the cladding mode increases. Long period gratings couple light from the core to the forward propagating cladding modes, where the wavelengths of the coupled modes are decided by the period of the core refractive index modulation. The phase-matching condition for the resonant wavelength of LPGs can be given as;

$$\beta_{co} - \beta_{cl,m} = \frac{2\pi}{\Lambda}(m = 1, 2, 3, 4) \tag{2.32}$$

where β_{co} is the propagation constant of the LP_{01} fundamental core mode, $\beta_{cl,m}$ is the propagation constant of the cladding mode, m is the order of the cladding mode and Λ is the period of the grating. The coupling of the light into the cladding modes generates a series of resonant bands centred at λ_m (equation 2.31). From equation 2.31, it can be deduced that as the grating period increases, the resonant wavelength of the m^{th} cladding mode increases. In comparison, the periods of LPGs (few hundred microns) are much larger than in FBGs (less than one micron) [52, 53]. Figure 2.3 shows the diagram of mode coupling by LPGs:

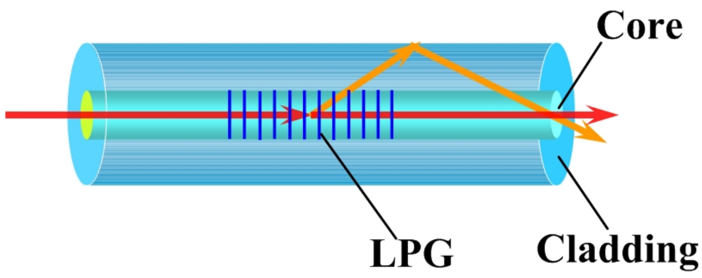

Figure 2.3: Schematic diagram of forward-mode coupling in LPG.

For Tilted fibre gratings, For Tilted fibre gratings, the mode coupling is more complex (i.e. the core mode can be coupled to the counter propagating modes or to the co-propagating modes) coupling to either the forward mode or the backward mode. The resonant wavelength is expressed as [54, 55];

$$\lambda_{co,cl} = (n_{co} \pm n_{cl,m}) \frac{\Lambda_g}{\cos\theta} \tag{2.33}$$

The $\pm$ shows the direction of the mode propagation towards the $\mp$ Z direction respectively. The schematics of mode coupling by TFGs are shown in Figure 2.4 and 2.5:

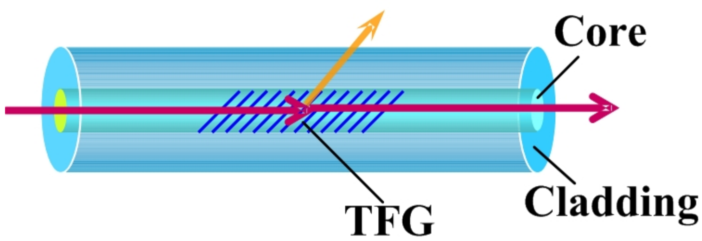

Figure 2.4: Schematic diagram of forward-mode coupling in TFG.

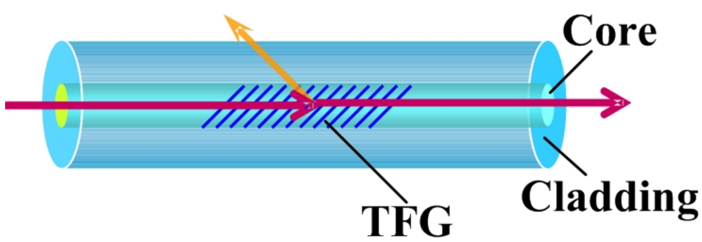

Figure 2.5: Schematic diagram of backward-mode coupling in TFG.

For a tilted grating, the grating structure is rotated by an angle θ. The period of the fibre grating structure is as stated in equation 2.34:

$$\Lambda = \frac{\Lambda_g}{\cos\theta} \tag{2.34}$$

Below is a diagram showing the core of a standard fibre with a tilted fibre grating structure:

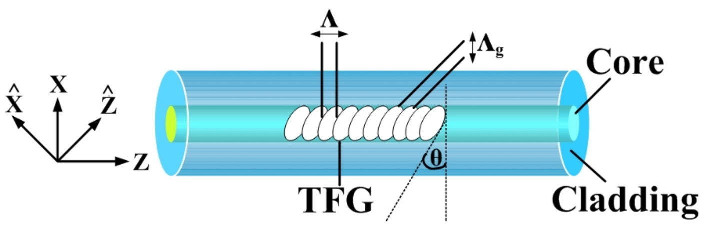

Figure 2.6: Schematic diagram of a standard fibre with a tilted fibre grating structure.

In a single mode fibre, the induced index change (δn_{co}) in the fibre core can be expressed as:

$$\delta n_c(x,z) = \bar{\delta} n_{co}(\hat{z})\left[1 + s\cos\left(\frac{2\pi}{\Lambda_g}\hat{z} + \phi(\hat{z})\right)\right] \tag{2.35}$$

where the $\hat{z}$ (as seen in Figure 2.6) axis follows the relationship: $\hat{z} = xsin\theta + zcos\theta$. However, for a small varying $\bar{\delta}\ n_{co}\ (\hat{z})$ and $\phi(\hat{z})$, it can be said that $\bar{\delta} \cong zcos\ \theta$. The general coupling coefficeint expression (equation 2.10) can be re-written by taking into consideration the projection along the fibre axis as:

$$K^t_{\mp\pm}(z) = \sigma(z) + 2K_{\mp\pm}(z)\cos\left[\frac{2\pi}{\Lambda}z + \phi(z\cos\theta)\right] \tag{2.36}$$

The "k" and "j" in equation 2.10 are related to the backward propagation mode (-) and the forward propagation mode (+) respectively. The equation 2.37 and equation 2.38 shows the expression for the modified self-coupling and cross coupling coefficients:

$$\sigma(z) = \frac{\omega n_{eff}\bar{\delta}n_{eff}(z\cos\theta)}{2}\iint_{core}\overrightarrow{e}^{t}_{\mp}(x,y).\overrightarrow{e}^{t*}_{\pm}(x,y)dxdy \tag{2.37}$$

$$K_{\mp\pm}(z,\theta) = \frac{\nu}{2}\frac{\omega n_{eff}\bar{\delta}n_{eff}(z\cos\theta)}{2}\iint_{core}\left(\pm i\frac{2\pi}{\Lambda}x\tan\theta\right).\overrightarrow{e}^{t*}_{\pm}(x,y)dxdy \tag{2.38}$$

In this case, $K_{\mp\pm} = K^{*}_{\pm}$ and the "effective fringe visibility" $V_{\mp\pm}(\theta)$ corresponding to the effect of the fibre grating tilting structure is given as:

$$\frac{V_{\mp\pm}(\theta)}{\nu} = \frac{\iint_{core}(\pm i\frac{2\pi}{\Lambda}x\tan\theta).\overrightarrow{e}^{t}_{\mp}(x,y).\overrightarrow{e}^{t*}_{\pm}(x,y)dxdy}{\iint_{core}\overrightarrow{e}^{t*}_{\pm}(x,y)dxdy} \tag{2.39}$$

Therefore equation 2.36 can be rewritten as:

$$K_{\mp\pm}(z,\theta) = \frac{V_{\mp\pm}(\theta)}{\nu}\sigma(z) \tag{2.40}$$

This shows the effectiveness of grating perturbation in backward propagation modes and also indicates that the effective fringe visibility is reduced (by the amount in equation 2.40) when the fibre grating structure is tilted.

2.4 *GRATING FABRICATION TECHNIQUES*

Hill et al reported the first Bragg grating inscribed in a photosensitive optical fibre in 1978 from the Canadian Communication Research Centre (CRC) [1]. They used a 488nm (blue light) Ar^{+} laser as the light source in their experiment. Due to the interference caused by Fresnel reflection (approx. 4%) from the cleaved end of the fibre and the incident beam, a standing wave was created in the fibre core, bringing about the formation of a grating (also known as Hill Grating or Internally fabricated grating) due to the fibre photosensitivity. The Hill Grating formed had a 90% reflectivity and bandwidth of less than 200MHz. After this discovery, researchers Lam and Garside [56] carried out an experiment that showed the magnitude of the grating strength increased as the square of the UV power from the Ar^{+} laser.

However, due to the limitation in variable Bragg wavelength of this technique, other techniques that overcome the limitation of internally inscribed gratings have been proposed and developed [1][51, 56–59]. This thesis will examine in more detail in the following sections the three main grating fabrication techniques: two-beam holographic, phase mask inscription and point-by-point inscription technique.

2.4.1 Two Beam Holographic Inscription Technique

The two-beam holographic technique was first demonstrated by Meltz et al [51]. The disadvantages in the original Hill gratings were overcome by Meltz work due to improved writing efficiency and the ability to write gratings with arbitrarily designed Bragg wavelength (typically from 600nm to 2000nm) by the angle adjustment of the interfering beams. This fabrication technique has been developed over the years (with new set ups) and extended to different fibre types [58] [60–64]. Figure 2.7 shows the image of the two-beam holographic set up in Aston photonics laboratory.

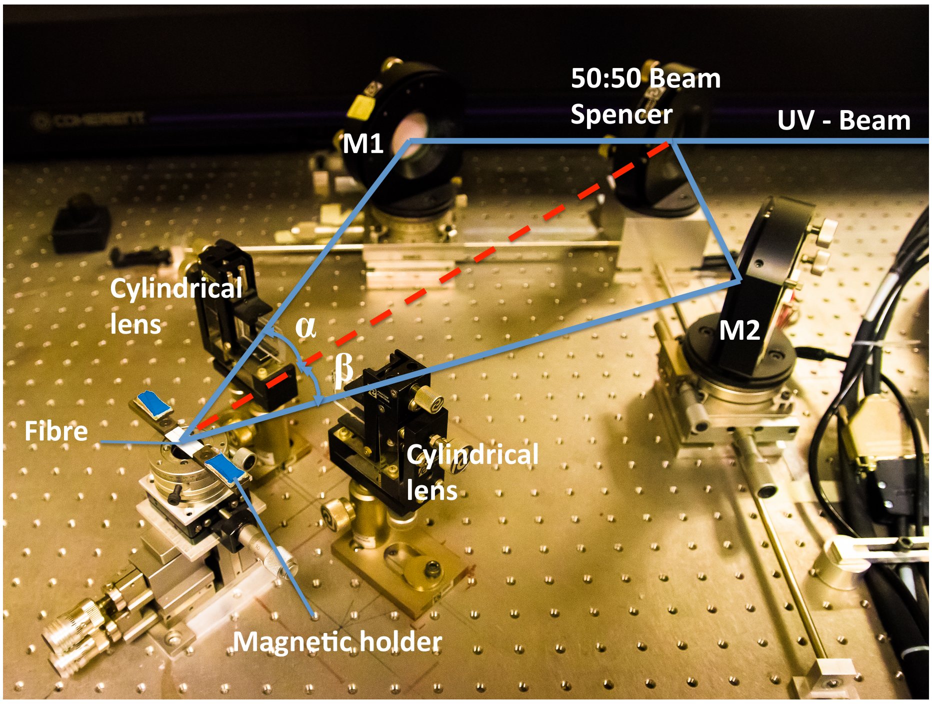

Figure 2.7: Laboratory set up for the two-beam holographic fabrication system.

It can be seen from the set up in Figure 2.7 that the incident UV beam is split (50%) with equal power. The two highly reflective mirrors (M1 and M2) then reflect the two beams in a symmetric manner to meet on the photosensitive fibre, creating interfering beams. The two beams are also passed through two similar cylindrical lenses (C1 and C2) to focus the power intensity of the two beams on the fibre core region, thus inducing a refractive index modulation in the fibre core.

High power density is achieved in the core by the use of the cylindrical lens to focus the beam down to the size of the fibre core, thus enabling strong FBG inscription. The fringe pattern or grating period depends on the irradiation wavelength and the angle between the interfering beams (α and β). This can be expressed as;

$$\Lambda = \frac{\lambda_{uv}}{\sin\alpha + \sin\beta} \tag{2.41}$$

where $\lambda_{u\nu}$ is the UV wavelength. Given that the Bragg condition is satisfied, the Bragg wavelength can be expressed as in equation 2.30. In equation 2.41 and 2.30, the Bragg wavelength can be varied by changing the angle between the interfering beams (α and β) or the UV wavelength ($\lambda_{u\nu}$). However the main disadvantages of this technique are: the grating length is limited by the size of the two interfering beams, susceptibility to mechanical vibrations during the fabrication process and the need for a good coherent laser source. A number of different wave-front splitting interferometer based fabrication systems have been developed over the years to reduce the mechanical vibration sensitivity of the system and to simplify the optical setup, such as prism interferometer [61] [63] and Lloyd interferometer [65].

2.4.2 Phase Mask Inscription Technique

The phase-mask technique was first demonstrated by Anderson et al and Hill et al [57, 58]. It has been widely reported as the most effective grating inscription technique due to the simplicity of the optical system and its stability compared to the two-beam holographic technique. The phase mask is a one-dimensional periodic surface relief pattern with period Λ_{pm} etched into the fused silica. The incident beam is diffracted into several orders. It works by suppressing the light energy of 0 order (to less than 5% of the transmitted light intensity) and maximizing the energy in the $\pm$ 1 order (to about 40% of the transmitted light intensity). A near-field fringe pattern is thereby produced on the fibre core due to the interference of the $\pm$ 1 order diffracted beams. The schematic diagram of FBG inscription using the phase mask technique is shown below:

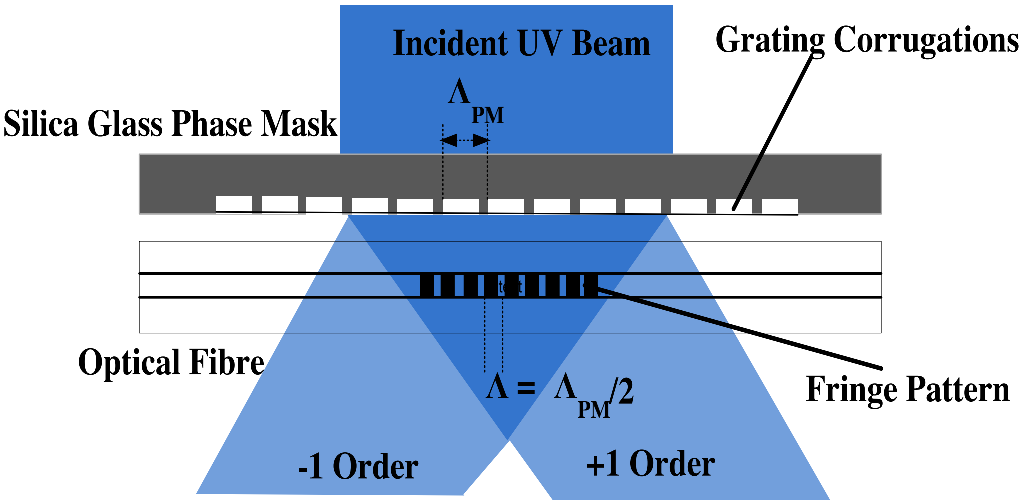

Figure 2.8: The Schematic diagram of phase mask grating inscription technique.

The period of the grating inscribed by this method can be expressed as;

$$\Lambda = \frac{\Lambda_{pm}}{2} \tag{2.42}$$

where Λ_{pm} is the phase mask period.

The stability of the phase mask inscription technique is due to the minimal space alignment required (i.e. there is no need to align the two beams relative to each other as in the case of the two-beam holographic method), but the incident UV beam is aligned perpendicularly to the fibre and phase mask. Another advantage of phase mask inscription technique is the ability to inscribe gratings with sophisticated structures and angles. Examples are: chirped gratings [66], apodized gratings [67, 68], phase-shifted gratings [69, 70] and Moiré gratings [71, 72].

The typical laboratory set up for this technique is shown below.

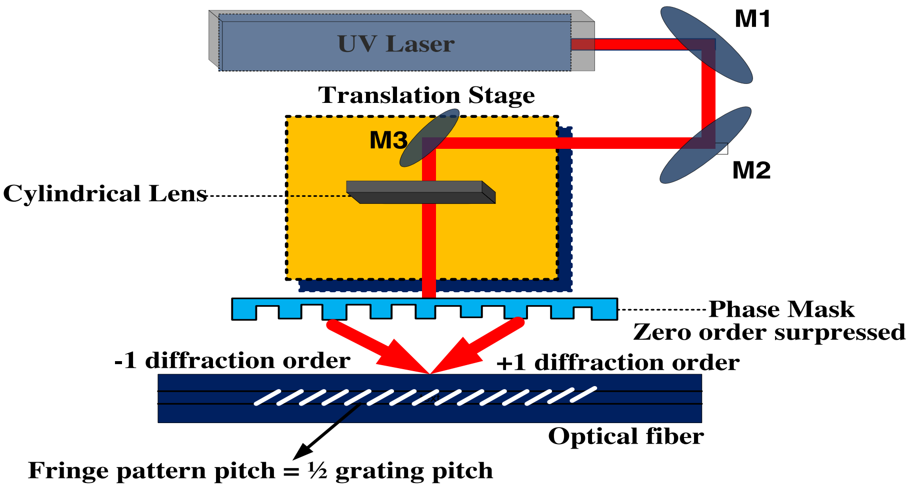

Figure 2.9: Laboratory set up of UV inscription of fibre Bragg grating inscription by the phase mask method.

The drawback in using this technique is the requirement of different phase-masks for inscription at different wavelengths, but methods such as placing a magnifying lens before the mask by Prohaska et al. [73] and pre-stretching the fibre demonstrated by Zhang et al. [64] and Byron et al. [74] have been demonstrated to tune the wavelength from 0.5nm to 7nm using a single phase mask.

2.4.3 Point By Point Inscription Technique

Point-by-point technique is a non-interferometry method of grating inscription, which was first demonstrated by Malo et al. and Hill et al. [75, 76]. It was also explored here in Aston using the femtosecond laser [77] [78]. It involves the periodic exposure of a small section of fibre to UV beam. Since the UV spot size is larger than the period of normal Bragg gratings (~0.5μm at 1.5μm), this technique is mostly suitable for fabricating LPGs. The refractive index of only the UV exposed fibre area changes at a time. The UV beam is later translated to expose other sections of the fibre. The diagram below shows the set-up for this inscription technique:

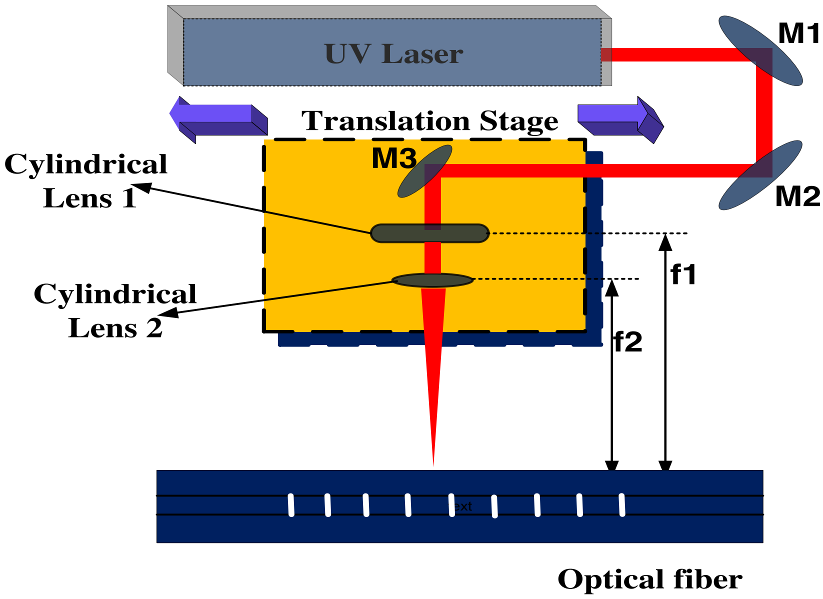

Figure 2.10: Schematic set up of a point-by-point inscription technique.

Since these gratings are inscribed on the fibre section by section, it is not an efficient technique of writing long gratings that require large index perturbation. This technique cannot be used for inscribing the TFG structures, but is usually used for LPGs with the period ranging from 10μm to 600μm [79–81]. Recently there have been great interests in LPGs and their applications as bio-sensors [82], refractive index and temperature sensors [83], liquid level sensor [84], chemical sensor [85] and bend sensor [86]. In the point-by-point LPG fabrication, a cylindrical lens is used to focus the UV beam onto the fibre axis, which is similar to the phase-mask inscription system in Figure 2.9 but without the phase mask. Since the translation stage is electronically controlled, being fed with the desired parameters like period, duty cycle and grating length, only high order Bragg gratings may be written using point-by-point technique. There are some advantages to this technique; the changing of grating period and strength is easy and flexible, because the grating structure is fabricated a point at a time; it also allows for the fabrication of gratings used in complex grating designs [78] [87]; it makes possible the fabrication of polarisation mode converters [88] for sensing applications. The disadvantage of the point-by-point fabrication technique is its susceptibility to errors due to inaccurate movement of the axis core direction. Below is a summary of the different fabrication techniques:

Table 2.1: Comparison of the different grating fabrication techniques

Fabrication techniques	Advantages	Disadvantages
Two-beam holographic	Very flexible for making gratings with different Bragg wavelengths	Susceptible to mechanical vibrations and not very simple to align. It can only be used to write short grating length and can sometimes be unstable
Phase Mask	Makes inscription easier, gives more stability and not susceptible to vibrations and air currents. It can also be used for the fabrication of sophisticated grating structures	Expensive as each different wavelength requires a different phase mask and the grating length can also be limited by the length of the phase mask
Point by point	Makes the changing of period flexible and makes it possible to write long period gratings	High accuracy is required in aligning the fibre core axis and its often a longer process . Also,thermal effect and variations in fibre strain can affect grating period.

2.5 *APPLICATIONS*

In telecommunication FBGs are mostly used as filters in optical communication networks [11]. They are used in; ultra long haul (ULH), long haul (LH), wavelength division multiplexing (WDM) and dense wavelength division multiplexing (DWDM) telecommunication networks. In these networks, the FBG is usually situated: in the erbium-doped fibre amplifiers (EDFA) as pump stabilizers (through the feedback provided by the grating, the laser oscillates at the reflected wavelength) and for gain flattening (especially for LH and ULH where a low optical signal to noise ratio is desired at all wavelengths during amplification); in the communication channel as band dispersion compensator. Its function as a band rejection filter comes in various configurations: Sagnac [89], Michelson [90, 91], Mach-Zhender [92, 93], interferometry configurations. Another major issue with telecommunication is chromatic dispersion; which limits the transmission distance of 10 and 40 Gbit/s optical systems. The use of chirped FBGs are commonly used to solve this problem through phase compensation [63].

FBGs have also been used for structural health monitoring in the civil engineering industry. In 2004, the Iowa department of transportation completed the construction of the Iowa's first high performance Steel Bridge. This bridge incorporates the use of FBGs interrogation to monitor the local and global bridge performance, help with fatigue evaluation and also to generate baseline data for identifying structural performance changes [94]. The 30 installed FBGs were predominantly used to measure strain, as it is a parameter that can be used in civil engineering to describe deformation, detect slip and bonding, and to study a crack opening. The approach of using FBG as a structural monitor has now taken off well in China (Binzhou Yellow River Bridge in Shandong Province and Songhuaijiang River Bridge in Heilongjiang province) [94] for monitoring the structural health of bridges. Pete et al and his team at Cranfield university have now extended this application unto the structural health monitoring of aircraft wings [95].

The coastal areas is an area of great biodiversity, changes like the salinity of water can greatly change the dynamics/health of the ecosystem. The method used to measure salinity in the past was based on the mobility of ions in water [96], which is inherently electrical and can be influenced by electromagnetic interference (EMI). Silva et al [97] designed and tested a system based on LPG for measuring the salinity changes in the coastal areas. Optical technology in the form of LPG was used for this application due to its mode coupling mechanism, sensitivity to the change in the refractive index of the environment and immunity to EMI. The result of there experiment showed a blue shift in wavelength (~2nm) for 0% - 19% salt concentration. The same device was also used to sense the changes in environmental temperature (25°C to 100°C) of the coastal areas, there result showed a linear shift of ~46pm/°C up to 40°C and non-linear for the region from 40°C - 100°C due to possible tension in the mechanical design of the sensor.

The need for liquid level measurement will usually take place in the petroleum industry, steel industry, and pharmaceutical industry and in day-to-day life. Optical sensors in the form of TFGs (small or large) are a good choice for this application as mentioned by Liu et al [98]. This is possible for the small and large TFGs due to their mode coupling mechanism that allows them to be sensitive to changes in external environment. Xiaoyi et al [99] during this experiment found out that length of immersion of the TFGs affects their transmission power and transmission peaks. The transmission loss peaks gradually looses power as the length of the grating in the liquid increases.

Due to the robustness of these gratings, they have been used to make hybrid sensors. In 2010, Shao et al [100] made a bend sensor using a hybrid LPG and TFG fabricated in a photosensitive fibre. The bend sensor utilises the advantages of the different mode coupling mechanism that exist between the LPG and a TFG, but it has a slight issue of temperature cross sensitivity (similar temperature sensitivity) which can be eliminated by using LPGs fabricated in photonic crystal fibre (PCF) [101, 102]. Other devices making use of hybrid gratings are: all fibre twist sensor [103], temperature and refractive index sensor [104, 105] and wearable sensors [106].

2.6 *CHAPTER CONCLUSION*

The chapter has looked extensively into the concept of photosensitivity of in-fibre gratings, which is the key factor for UV induced refractive index modulation in the optical fibre. The photosensitivity mechanisms discussed were colour centre, compaction densification and stress relief models. The hydrogenation technique (amongst other enhancing photosensitivity techniques like co-doping, flame brushing) is used to enhance the photosensitivity of the fibres and have been used throughout this thesis. This photosensitivity technique has been reviewed and found to increase the UV-induced refractive index modulation to around 10^{-3} to 10^{-2}. This high index modulation makes it possible to write strong, complex and quality gratings. In order to then stabilise the fabricated gratings for real applications, the unreacted hydrogen needs to the removed through the process of annealing at the temperature to which the grating will be used.

The way light (electromagnetic waves) travels in the different grating structures made in this thesis can be analysed and explained through the use of the coupled mode theory. The two form of electromagnetic propagation described are the forward propagation (co-propagating) and the backward propagation (counter propagating). The different gratings structures have phase matching conditions are follows: FBGs couples the core propagating mode to the counter propagating core mode, LPGs couples the core mode to the co-propagating cladding modes and the TFGs couples to either the co-propagating or the counter – propagating modes depending on the internal tilt angle of the grating.

Fibre grating inscription techniques including two-beam holographic technique, point-by-point inscription technique and phase mask technique have been discussed and the various limitations of the different techniques were mentioned. Out of all the three fabrication techniques, the phase mask fabrication technique has proven to be the most stable and repeatable but has its own limitations of cost (phase masks, air-bearing stage and computerised controls) and grating length limitation due to the length of the mask used. However the holographic set up enables us to fabricate FBGs of desired wavelength, by the changing the distance of the mirrors from the 50:50 beam splitter (thereby changing the angle of the interfering beams). This technique also suffers from instability, unrepeatability, and short grating length. These fabrication techniques have been used to fabricate the gratings (FBGs, LPGs and TFGs) used throughout the work reported in this thesis.

Finally, few applications of amongst many of the applications of fibre gratings as sensors were mentioned. For example; FBGs used as filters in telecommunication networks, FBGs used in structural health monitoring in civil and aerospace industries, LPGs used in salinity testing of coastal environments, TFGs used as liquid level sensors in the petroleum industries and applications based on the hybrid of the different grating types.

2.7 References

[1] K. Hill, Y. Fujii, D. Johnson, and B. Kawasaki, "Photosensitivity in optical fiber waveguides: Application to reflection filter fabrication," *Applied Physics Letters*, vol. 32, pp. 647–649, 1978.

[2] J. Stone, "Photorefractivity in GeO2-doped silica fibers," *Journal of Applied Physics*, vol. 62, no. 11, pp. 4371–4374, 1987.

[3] M. M. Broer, R. L. Cone, and J. R. Simpson, "Ultraviolet-induced distributed-feedback gratings in Ce(3+) -doped silica optical fibers.," *Opt. Lett.*, vol. 16, pp. 1391–1393, 1991.

[4] K. O. Hill, B. Malo, F. Bilodeau, D. C. Johnson, J. F.Morse, A. Kilian, L.Reinhart and K. Oh, "Photosensitivity in Eu2+ : Al2O3 doped core fiber: preliminary results and application to mode converters," *Optical Fiber Communication Conference*, vol. 14, 1991.

[5] C. Fiori and R. A. B. Devine, "Evidence for a wide continuum of polymorphs in a-SiO2," *Physical Review B*, vol. 33, pp. 2972–2974, 1986.

[6] N. Lawandy, "Light induced transport and delocalization in transparent amorphous systems," *Opt. Commun.*, vol. 74, pp. 180–184, 1989.

[7] D. Hand and P. Russell, "Photoinduced refractive index changes in germanosilicate fibres," *Proceedings SPIE*, vol. 1516, pp. 47–54, 1991.

[8] A. E. Attard, "Fermi level shift in Bi12SiO20 via photon-induced trap level occupation," *Journal of Applied Physics*, vol. 71, no. 2, pp. 933–937, 1992.

[9] A. Miotello and R. Kelly, "Laser irradiation effects in Si+-implanted SiO 2," *Nuclear Instruments and Methods in Physics Research Section B: Beam Interactions with Materials and Atoms*, vol. 65, no. 1, pp. 217–222, 1992.

[10] D. L. Williams, B. J. Ainslie, R. Kashyap, G. D. Maxwell, J. R. Armitage, R. J. Campbell, and R. R. Wyatt, "Photosensitive index changes in germania-doped silica glass fibers and waveguides," in *Optics Quebec*, pp. 55–68, International Society for Optics and Photonics, 1993.

[11] A. Othonos and K. Kalli, *Fiber Bragg gratings: fundamentals and applications in telecommunications and sensing.* Artech House, 1999.

[12] K. D. Simmons, S. Larochelle, V. Mizrahi, G. I. Stegeman, and D. L. Griscom, "Correlation of defect centers with a wavelength-dependent photosensitive response in germania-doped silica optical fibers.," *Optics Letters*, vol. 16, no. 3, pp. 141–143, 1991.

[13] K. S. Chiang, M. G. Sceats, and D. Wong, "Ultraviolet photolytic-induced changes in optical fibers: the thermal expansion coefficient.," *Optics Letters*, vol. 18, no. 12, pp. 965–967, 1993.

[14] P. W. Levy, "Reactor and Gamma-Ray Induced Coloring in Crystalline Quartz and Corning Fused Silica," *The Journal of Chemical Physics*, vol. 23, no. 4, pp. 764–765, 1955.

[15] P. Kaiser, "Drawing-induced coloration in vitreous silica fibers," 1974.

[16] E. J. Friebele, C. G. Askins, M. E. Gingerich, and K. J. Long, "Optical fiber waveguides in radiation environments, II," *Nuclear Instruments and Methods in Physics Research Section B: Beam Interactions with Materials and Atoms*, vol. 1, no. 2, pp. 355–369, 1984.

[17] D. A. Parthenopoulos and P. M. Rentzepis, "Three-dimensional optical storage memory.," *Science (New York, N.Y.)*, vol. 245, no. 4920, pp. 843–845, 1989.

[18] R. Atkins, V. Mizrahi, and T. Erdogan, "248 nm induced vacuum UV spectral changes in optical fibre preform cores: support for a colour centre model of photosensitivity," *Electron. Lett.*, vol. 29, no. 4, pp. 385, 1993.

[19] P. S. Russell, D. P. Hand, Y. T. Chow, and L. J. Poyntz-Wright, "Optically induced creation, transformation, and organization of defects and color centers in optical fibers," in *International Workshop on Photoinduced Self-Organization Effects in Op*, pp. 47–54, International Society for Optics and Photonics, 1991.

[20] D. Wong, S. B. Poole, and M. G. Sceats, "Stress-birefringence reduction in elliptical-core fibers under ultraviolet irradiation.," *Optics Letters*, vol. 17, no. 24, pp. 1773–1775, 1992.

[21] D. Williams, B. Ainslie, J. Armitage, R. Kashyap, and R. Campbell, "Enhanced UV photosensitivity in boron codoped germanosilicate fibres," *Electronics Letters*, vol. 29, pp. 45, 1993.

[22] B. Malo, J. Albert, D. Johnson, F. Bilodeau, and K. Hill, "Elimination of photoinduced absorption in Ge-doped silica fibres by annealing of ultraviolet colour centres," *Electronics Letters*, vol. 28, pp. 1598, 1992.

[23] T.-E. Tsai, E. J. Friebele, and D. L. Griscom, "Thermal stability of photoinduced gratings and paramagnetic centers in Ge-and Ge/P-doped silica optical fibers," *Optics Letters*, vol. 18, no. 12, pp. 935–937, 1993.

[24] T. E. Tsai, G. M. Williams, and E. J. Friebele, "Index structure of fiber Bragg gratings in Ge-SiO(2) fibers.," *Optics Letters*, vol. 22, no. 4, pp. 224–226, 1997.

[25] B. Leconte, W. X. Xie, M. Douay, P. Bernage, P. Niay, J. F. Bayon, E. Delevaque, and H. Poignant, "Analysis of color-center-related contribution to Bragg grating formation in Ge:SiO 2 fiber based on a local Kramers -Kronig transformation of excess loss spectra.," *Applied optics*, vol. 36, no. 24, pp. 5923–5930, 1997.

[26] W. Xie, P. Niay, P. Bernage, M. Douay, J. Bayon, T. Georges, M. Monerie, and B. Poumellec, "Experimental evidence of two types of photorefractive effects occuring during photoinscriptions of Bragg gratings within germanosilicate fibres," *Optics Communications*, vol. 104, pp. 185–195, 1993.

[27] P. Cordier, J. Doukhan, E. Fertein, P. Bernage, P. Niay, J. Bayon, and T. Georges, "TEM characterization of structural changes in glass associated to Bragg grating inscription in a germanosilicate optical fibre preform," *Optics Communications*, vol. 111, no. 3-4, pp. 269–275, 1994.

[28] P. Niay, P. Bernage, S. Legoubin, M. Douay, W. Xie, J. Bayon, T. Georges, M. Monerie, and B. Poumellec, "Behaviour of spectral transmissions of Bragg gratings written in germania-doped fibres: writing and erasing experiments using pulsed or CW UV exposure," *Optics Communications*, vol. 113, pp. 176–192, 1994.

[29] P. Lemaire, R. Atkins, V. Mizrahi, and W. Reed, "High pressure H2 loading as a technique for achieving ultrahigh UV photosensitivity and thermal sensitivity in GeO2 doped optical fibres," *Electronics Letters*, vol. 29, no. 13, pp. 1191, 1993.

[30] L. Dong, J. L. Cruz, L. Reekie, M. G. Xu, and D. N. Payne, "Enhanced photosensitivity in tin-codoped germanosilicate optical fibers," *Photonics Technology Letters, IEEE*, vol. 7, no. 9, pp. 1048–1050, 1995.

[31] F. Bilodeau, B. Malo, J. Albert, D. C. Johnson, K. O. Hill, Y. Hibino, M. Abe, and M. Kawachi, "Photosensitization of optical fiber and silica-on-silicon/silica waveguides.," *Optics Letters*, vol. 18, no. 12, pp. 953–955, 1993.

[32] L. Dong, J. L. Cruz, J. A. Tucknott, L. Reekie, and D. N. Payne, "Strong photosensitive gratings in tin-doped phosphosilicate optical fibers," *Optics Letters*, vol. 20, no. 19, pp. 1982–1984, 1995.

[33] R. M. Atkins, P. J. Lemaire, T. Erdogan, and V. Mizrahi, "Mechanisms of enhanced UV photosensitivity via hydrogen loading in germanosilicate glasses," *Electronics Letters*, vol. 29, no. 14, pp. 1234–1235, 1993.

[34] J. Canning, M. Aslund, and P. F. Hu, "Ultraviolet-induced absorption losses in hydrogen-loaded optical fibers and in presensitized optical fibers.," *Optics Letters*, vol. 25, no. 22, pp. 1621–1623, 2000.

[35] D. Williams and R. Smith, "Accelerated lifetime tests on UV written intra-core gratings in boron germania codoped silica fibre," *Electronics Letters*, vol. 31, pp. 2120, 1995.

[36] S. Kannan, J. Guo, and P. Lemaire, "Thermal stability analysis of UV-induced fiber Bragg gratings," *Journal of Lightwave Technology*, vol. 15, pp. 1478–1483, 1997.

[37] R. W. Lee, R. C. Frank, and D. E. Swets, "Diffusion of hydrogen and deuterium in fused quartz," *The Journal of Chemical Physics*, vol. 36, no. 4, pp. 1062–1071, 1962.

[38] J. Stone, "Interactions of hydrogen and deuterium with silica optical fibers: A review," *Lightwave Technology, Journal of*, vol. 5, no. 5, pp. 712–733, 1987.

[39] H. Patrick, S. L. Gilbert, A. Lidgard, and M. D. Gallagher, "Annealing of Bragg Gratings in Hydrogen-Loaded Optical-Fiber," *Journal of Applied Physics*, vol. 78, pp. 2940–2945, 1995.

[40] T. Erdogan, V. Mizrahi, P. J. Lemaire, and D. Monroe, "Decay of ultraviolet-induced fiber Bragg gratings," *Journal of Applied Physics*, vol. 76, no. 1, pp. 73–80, 1994.

[41] S. R. Baker, H. N. Rourke, V. Baker, and D. Goodchild, "Thermal decay of fiber bragg gratings written in boron and germanium codoped silica fiber," *Journal of Lightwave Technology*, vol. 15, pp. 1470–1477, 1997.

[42] S. Pal, J. Mandal, T. Sun, and K. T. V. Grattan, "Analysis of thermal decay and prediction of operational lifetime for a type I boron-germanium codoped fiber Bragg grating.," *Applied optics*, vol. 42, no. 12, pp. 2188–2197, 2003.

[43] G. Brambilla and H. Rutt, "Fiber Bragg gratings with enhanced thermal stability," vol. 80, pp. 3259–3261, 2002.

[44] M. Fokine, "Formation of thermally stable chemical composition gratings in optical fibers," *Journal of the Optical Society of America B*, vol. 19, no. 8, pp. 1759, 2002.

[45] M. Aslund and J. Canning, "Annealing properties of gratings written into UV-presensitized hydrogen-outdiffused optical fiber.," *Optics Letters*, vol. 25, no. 10, pp. 692–694, 2000.

[46] B. Malo, J. Albert, K. Hill, F. Bilodeau, and D. Johnson, "Effective index drift from molecular hydrogen diffusion in hydrogen-loaded optical fibres and its effect on Bragg grating fabrication," *Electronics Letters*, vol. 30, pp. 442, 1994.

[47] A. Yariv, "Coupled-mode theory for guided-wave optics," *Quantum Electronics, IEEE Journal of*, vol. 9, no. 9, pp. 919–933, 1973.

[48] H. Kogelnik and C. V. Shank, "Coupled wave theory of distributed feedback lasers," *J.Appl.Phys*, vol. 43, p. 2327, 1972.

[49] T. Erdogan, "Fiber grating spectra," *Journal of Lightwave Technology*, vol. 15, no. 8, pp. 1277–1294, 1997.

[50] T. Erdogan, “Cladding-mode resonances in short-and long-period fiber grating filters,” *JOSA A*, vol. 14, no. 8, p. 1760, 1997.

[51] G. Meltz, W. W. Morey, and W. H. Glenn, “Formation of Bragg gratings in optical fibers by a transverse holographic method.,” *Optics Letters*, vol. 14, no. 15, pp. 823–825, 1989.

[52] A. M. Vengsarkar, J. R. Pedrazzani, J. B. Judkins, P. J. Lemaire, N. S. Bergano, and C. R. Davidson, “Long-period fiber-grating-based gain equalizers.,” *Optics Letters*, vol. 21, no. 5, pp. 336–338, 1996.

[53] V. Bhatia and A. M. Vengsarkar, “Optical fiber long-period grating sensors.,” *Optics Letters*, vol. 21, no. 9, pp. 692–694, 1996.

[54] T. Erdogan and J. Sipe, “Tilted fiber phase gratings,” *Journal of the optical society of America A-Optics Image Science and Vision*, vol. 13, pp. 296–313, 1996.

[55] K. S. Lee and T. Erdogan, “Fiber mode coupling in transmissive and reflective tilted fiber gratings.,” *Applied Optics*, vol. 39, no. 9, pp. 1394–1404, 2000.

[56] D. K. Lam and B. K. Garside, “Characterization of single-mode optical fiber filters.,” *Applied Optics*, vol. 20, no. 3, pp. 440–445, 1981.

[57] D. Z. Anderson, V. Mizrahi, T. Erdogan, and A. E. White, “Production of in-fibre gratings using a diffractive optical element,” *Electronics Letters*, vol. 29, no. 6, pp. 566–568, 1993.

[58] K. O. Hill, B. Malo, F. Bilodeau, D. C. Johnson, and J. Albert, “Bragg gratings fabricated in monomode photosensitive optical fiber by UV exposure through a phase mask,” *Applied Physics Letters*, vol. 62, no. 10, pp. 1035–1037, 1993.

[59] G. Meltz, W. Morey, and W. Glenn, “In-fiber Bragg grating tap,” in *Optical Fiber Communication Conference*, vol. 1169, p. 6108, 1990.

[60] R. Kashyap, J. R. Armitage, R. J. Campbell, D. L. Williams, G. D. Maxwell, B. J. Ainslie, and C. A. Millar, “Light-sensitive optical fibres and planar waveguides: Advances in optical technology,” *BT technology journal*, vol. 11, no. 2, pp. 150–160, 1993.

[61] R. Kashyap, J. Armitage, R. Wyatt, S. Davey, and D. Williams, “All-fibre narrowband reflection gratings at 1500 nm,” *Electronics Letters*, vol. 26, pp. 730, 1990.

[62] H. Patrick and S. L. Gilbert, “Growth of Bragg gratings produced by continuous-wave ultraviolet light in optical fiber.,” *Optics Letters*, vol. 18, no. 18, p. 1484, 1993.

[63] B. J. Eggleton, P. A. Krug, L. Poladian, K. A. Ahmed, and H. F. Liu, “Experimental demonstration of compression of dispersed optical pulses by reflection from self-chirped optical fiber Bragg gratings.,” *Optics Letters*, vol. 19, no. 12, pp. 877–879, 1994.

[64] Q. Zhang, D. A. Brown, L. Reinhart, T. F. Morse, J. Q. Wang, and G. Xiao, “Tuning Bragg wavelength by writing gratings on prestrained fibers,” *Photonics Technology Letters, IEEE*, vol. 6, no. 7, pp. 839–841, 1994.

[65] H. G. Limberger, P.-Y. Fonjallaz, P. Lambelet, R.-P. Salathe, C. Zimmer, and H. H. Gilgen, “Optical low-coherence reflectometry (OLCR) characterization of efficient Bragg gratings in optical fiber,” in *Optics Quebec*, pp. 272–283, International Society for Optics and Photonics, 1993.

[66] K. Byron, T. Bricheno, I. Bennion, and K. Sugden, “Fabrication of chirped Bragg gratings in photosensitive fibre,” *Electronics Letters*, vol. 29, no. 18, pp. 1659, 1993.

[67] J. Albert, K. Hill, B. Malo, S. Theriault, F. Bilodeau, D. Johnson, and L. Erickson, "Apodisation of the spectral response of fibre Bragg gratings using a phase mask with variable diffraction efficiency," *Electronics Letters*, vol. 31, no. 3, pp. 222, 1995.

[68] J. Albert, K. Hill, D. Johnson, F. Bilodeau, and M. Rooks, "Moire phase masks for automatic pure apodisation of fibre Bragg gratings," *Electronics Letters*, vol. 32, no. 24, pp. 2260, 1996.

[69] R. Kashyap, P. Mckee, and D. Armes, "UV written reflection grating structures in photosensitive optical fibres using phase-shifted phase masks," *Electronics Letters*, vol. 30, pp. 1977, 1994.

[70] J. Canning and M. G. Sceats, "pi-phase-shifted periodic distributed structures in optical fibres by UV post-processing," *Electronics Letters*, vol. 30, pp. 1344–1345, Aug. 1994.

[71] L. Zhang, K. Sugden, I. Bennion, and A. Molony, "Wide-stopband chirped fibre moire grating transmission filters," *Electronics Letters*, vol. 31, no. 6, pp. 477, 1995.

[72] S. Legoubin, E. Fertein, M. Douay, P. Bernage, P. Niay, F. Bayon, and T. Georges, "Formation of moire grating in core of germanosilicate fibre by transverse holographic double exposure method," *Electronics Letters*, vol. 27, no. 21, pp. 1945–1947, 1991.

[73] J. Prohaska, E. Snitzer, S. Rishton, and V. Boegli, "Magnification of mask fabricated fibre Bragg gratings," *Electronics Letters*, vol. 29, pp. 1614, 1993.

[74] K. Byron and H. Rourke, "Fabrication of chirped fibre gratings by novel stretch and write technique," *Electronics Letters*, vol. 31, no. 1, pp. 60, 1995.

[75] B. Malo, K. Hill, F. Bilodeau, D. Johnson, and J. Albert, "Point-by-point fabrication of micro-Bragg gratings in photosensitive fibre using single excimer pulse refractive index modification techniques," *Electronics Letters*, vol. 29, pp. 1668, 1993.

[76] K. Hill, B. Malo, K. Vineberg, F. Bilodeau, D. Johnson, and I. Skinner, "Efficient mode conversion in telecommunication fibre using externally written gratings," *Electronics Letters*, vol. 26, pp. 1270, 1990.

[77] A. Martinez, M. Dubov, I. Khrushchev, and I. Bennion, "Point by point FBG inscription by a focused NIR femtosecond laser," in *Lasers and Electro-Optics, 2004. (CLEO). Conference on*, vol. 1, pp. 2 pp. vol.1–, May 2004.

[78] Y. Lai, K. Zhou, K. Sugden, and I. Bennion, "Point-by-point inscription of first-order fiber Bragg grating for C-band applications," *Optics express*, vol. 15, no. 26, pp. 18318–18325, 2007.

[79] H. Patrick, C. Askins, R. McElhanon, and E. Friebele, "Amplitude mask patterned on an excimer laser mirror for high intensity writing of long period fibre gratings," *Electronics Letters*, vol. 33, no. 13, pp. 1167, 1997.

[80] D. Davis, T. Gaylord, E. Glytsis, S. Kosinski, S. Mettler, and A. Vengsarkar, "Long-period fibre grating fabrication with focused CO2 laser pulses," *Electronics Letters*, vol. 34, no. 3, pp. 302, 1998.

[81] X. Shu, L. Zhang, and I. Bennion, "Sensitivity characteristics near the dispersion turning points of long-period fiber gratings in B/Ge codoped fiber.," *Optics Letters*, vol. 26, no. 22, pp. 1755–1757, 2001.

[82] M. P. DeLisa, Z. Zhang, M. Shiloach, S. Pilevar, C. C. Davis, J. S. Sirkis, and W. E. Bentley, "Evanescent wave long period fiber Bragg grating as an immobilized antibody biosensor," *Analytical Chemistry*, vol. 72, no. 13, pp. 2895–2900, 2000.

[83] B. A. L. Gwandu, X. Shu, T. D. P. Allsop, W. Zhang, L. Zhang, D. J. Webb, and I. Bennion, “Simultaneous refractive index and temperature measurement using cascaded long-period grating in double-cladding fibre,” *Electronics Letters*, vol. 38, no. 14, pp. 695–696, 2002.

[84] S. Khaliq, S. W. James, and R. P. Tatam, “Fiber-optic liquid-level sensor using a long-period grating.,” *Optics Letters*, vol. 26, no. 16, pp. 1224–1226, 2001.

[85] X. J. Gu, “Wavelength-division multiplexing isolation fiber filter and light source using cascaded long-period fiber gratings.,” *Optics Letters*, vol. 23, no. 7, pp. 509–510, 1998.

[86] Y. Liu, L. Zhang, J. A. R. Williams, and I. Bennion, “Optical Bend Sensor Based on Measurement of Resonance Mode Splitting of Long-Period Fiber Grating,” *IEEE Photonics Technology Letters*, vol. 12, no. 2000, pp. 531–533, 2000.

[87] D. Nikogosyan, M. Dubov, H. Schmitz, V. Mezentsev, I. Bennion, P. Bolger, and A. Zayats, “Point-by-point inscription of 250-nm-period structure in bulk fused silica by tightly-focused femtosecond UV pulses: experiment and numerical modeling,” *Open Physics*, vol. 8, no. 2, pp. 169–177, 2010.

[88] J. P. Carvalho, A. Anuszkiewicz, G. Statkiewicz-barabach, J. M. Baptista, O. Frazão, and P. Mergo, “Long period gratings and rocking filters written with a CO2 laser in highly-birefringent boron-doped photonic crystal fibers for sensing applications,” *Optics Communications*, vol. 285, no. 3, pp. 264–268, 2012.

[89] D. P. Hand and P. S. J. Russell, “Single-mode fibre grating written into Sagnac loop using photosensitive fibre: transmission filters,” *7th International Conference of Integrated Optics Optical Fiber Communication*, vol. 4, pp. 64–65, 1989.

[90] K. O. Hill, D. C. Johnson, F. Bilodeau, and S. Faucher, “Narrow-bandwidth optical waveguide transmission filters,” *Electronics Letters*, vol. 23, no. 9, pp. 465–466, 1987.

[91] F. Bilodeau, K. O. Hill, B. Malo, D. C. Johnson, and J. Albert, “High-return-loss narrowband all-fiber bandpass Bragg transmission filter,” *IEEE photonics technology letters*, vol. 6, no. 1, pp. 80–82, 1994.

[92] D. C. Johnson, K. O. Hill, F. Bilodeau, and S. Faucher, “New design concept for a narrowband wavelength-selective optical tap and combiner,” *Electronics Letters*, vol. 23, no. 13, pp. 668–669, 1987.

[93] T. J. Cullen, H. N. Rourke, C. P. Chew, S. R. Baker, T. Bricheno, K. C. Byron, and A. Fielding, “Compact all-fibre wavelength drop and insert filter,” *Electronics Letters*, vol. 30, no. 25, pp. 2160–2162, 1994.

[94] J. D. Doornink, B. M. Phares, Z. Zhou, J. Ou, and T. W. Graver, “Fiber Bragg grating sensing for structural health monitoring of civil structures,” in *International Symposium on Advances and Trends in Fiber Optics and Applications*, vol. 11, pp. 41–44, 2004.

[95] P. D. Foote, I. J. Read, T. J. Slack, A. Ball, P. Jackson, Y. J. Rao, D. A. Jackson, I. Bennion, and L. Zhang, “‘Optical fibre Bragg sensors systems: a basis for aircraft health and usage monitoring,” *submitted to J. Smart Mater. Struct*, 1996.

[96] Y. Zhao, Y. Liao, B. Zhang, and S. Lai, “Monitoring technology of salinity in water with optical fiber sensor,” *Journal of lightwave technology*, vol. 21, no. 5, p. 1334, 2003.

[97] C. Silva, J. A. M. P. Coelho, P. Caldas, and P. Jorge, *Fibre Sensing System Based on Long-Period Gratings for Monitoring Aqueous Environments.* INTECH Open Access Publisher, 2012.

[98] B. Liu, Y. Miao, J. Liu, H. Sun and H. Zhang, "Temperature-independent liquid level sensor based on tilted fiber Bragg grating," pp. 28–30, 2010.

[99] X. Dong, H. Zhang, B. Liu, and Y. Miao, "Tilted fiber Bragg gratings: principle and sensing applications," *Photonic Sensors*, vol. 1, no. 1, pp. 6–30, 2011.

[100] L.-Y. Shao, A. Laronche, M. Smietana, P. Mikulic, W. J. Bock, and J. Albert, "Highly sensitive bend sensor with hybrid long-period and tilted fiber Bragg grating," *Optics Communications*, vol. 283, no. 13, pp. 2690–2694, 2010.

[101] T. Allsop, K. Kalli, K. Zhou, Y. Lai, G. Smith, M. Dubov, D. J. Webb, and I. Bennion, "Long period gratings written into a photonic crystal fibre by a femtosecond laser as directional bend sensors," *Optics Communications*, vol. 281, no. 20, pp. 5092–5096, 2008.

[102] C.-L. Zhao, J. Zhao, W. Jin, J. Ju, L. Cheng, and X. Huang, "Simultaneous strain and temperature measurement using a highly birefringence fiber loop mirror and a long-period grating written in a photonic crystal fiber," *Optics Communications*, vol. 282, no. 20, pp. 4077–4080, 2009.

[103] X. F. Chen, K. Zhou, L. Zhang, and I. Bennion, "In-fibre twist sensor based on a fibre Bragg grating with 81° tilted structure," vol. 18, pp. 2596–2598, 2006.

[104] H. Guo, G. Xiao, N. Mrad, and J. Yao, "Simultaneous interrogation of a hybrid FBG/LPG sensor pair using a monolithically integrated echelle diffractive grating," *Journal of Lightwave Technology*, vol. 27, no. 12, pp. 2100–2104, 2009.

[105] X. Chen, K. Zhou, L. Zhang, and I. Bennion, "Simultaneous measurement of temperature and external refractive index by use of a hybrid grating in D fiber with enhanced sensitivity by HF etching.," *Applied Optics*, vol. 44, no. 2, pp. 178–182, 2005.

[106] S. Ghosh, C. Amidei, and K. Furrow, "Development of a sensor-embedded flexible textile structure for apparel or large area applications," *Indian J. Fibre & Textile Res*, vol. 30, pp. 42–48, 2005.

3 FIBRE GRATINGS WITH NORMAL PERIODIC STRUCTURES

3.1 *INTRODUCTION*

Fibre Bragg gratings (FBGs) can be inscribed using the two-beam holographic (as described in section 2.4.1) and phase mask techniques (section 2.4.2). Years after the development of these two techniques, potential applications have surfaced which have required researchers to devise methods to improve stability and spectral response of FBGs during the writing process (in the case of holographic inscription) and the introduction of the phase mask technique in 1993 by Hill et al allowed FBGs to be fabricated in production conditions with high quality and reproducibility. Due to advantages like lightweight and robustness, low cost fabrication and electromagnetic interference (EMI) immunity, interest is increasing in its use over bulk optical components. This Chapter will report on the experimental work on the UV-inscription, characterisation and sensing capabilities of fibre gratings with normal periodic structures, including FBGs and long period gratings (LPGs). The major inscription techniques used to produce all FBGs and LPGs discussed in this thesis are: two-beam holographic, phase mask and point-by-point writing techniques.

FBG structures have become very useful in various applications due to their ability to couple light between the forward and the backward propagating core modes, while LPGs make use of their ability to couple light propagating through the core to the cladding modes, generating a range of filtering functions. After the fibre-grating inscription, the FBGs were characterised for temperature sensitivity at different wavelength; the LPGs were characterised for temperature and refractive index sensitivities and later used for sensing changes in bio-samples (FBS).

3.2 *FIBRE BRAGG GRATING (FBG)*

3.2.1 Fabrication Techniques

The aim of this section is to give a detailed analysis of the fabrication techniques employed in the inscription of the normal periodic FBGs described in this section. Two main techniques were used for fabricating these FBGs: two-beam holographic technique and phase mask technique. The laboratory set up for the holographic technique (Figure 2.7) and the phase mask technique (Figure 2.9) have been shown in Chapter 2 of this thesis. However, these two techniques will be discussed in more detail.

3.2.1.1 *Two beam holographic technique*

The schematic of fibre Bragg grating inscription using the two beam holographic technique is shown in Figure 3.1, in which all system geometrical parameters are labelled [1].

Figure 3.1: The Schematic diagram of the two-beam holographic inscription technique (refer to figure 2.7 for the actual set-up).

When using two-beam holographic technique to induce refractive index fringes in the fibre core, the UV-beam intensity distribution along the fibre can be given as:

$$I(z) = [A(x,z)]^2 = 2 + 2\cos\left[\frac{2\pi z}{\Lambda}\right] \tag{3.1}$$

where A(x, z) is the composed amplitude, Λ is the fibre grating period , x and z are unit vector of the x -axis and z -axis respectively. The fibre-grating period is dependant on the interference angles, α and β, and can be illustrated as seen in equation 2.41 (Chapter 2) and the Bragg wavelength of a FBG as seen in equation 2.30 (Chapter 2). Since the grating has normal structure, the irradiated photosensitive fibre is perpendicular to the two UV writing beams bisector, so $\alpha = \beta$

$$\alpha = \beta = \tan^{-1}\left[\frac{L_x \sin(\theta_0)}{L_0 - L_x\cos(\theta_0)}\right] = \sin^{-1}\left[\frac{n_{eff}\lambda_{uv}}{\lambda_B}\right] \tag{3.2}$$

where L_x is the interferometer arm length, λ_{uv} is 244nm (from a frequency doubled Ar^+ ion laser) and L_0 is ~522mm in our set-up for 1550nm FBGs. Using equation 2.41 and equation 2.30, for a grating at 1550nm, Λ is 0.540µm and $\alpha = \beta = 13.6°$ respectively. The Bragg wavelength can also be expressed in terms of the interferometer arm length L_x taking into account equation 3.2:

$$\lambda_B = \frac{n_{eff}\lambda_{uv}}{\sin\left[\tan^{-1}\left(\frac{L_x\sin(\theta_0)}{L_0 - L_x\cos(\theta_0)}\right)\right]} \tag{3.3}$$

Using equation 3.3, a graph of the interferometer arm length (L_x) was plotted against the Bragg wavelength (λ_B) as shown in figure 3.2 (a).

Aston University

Illustration removed for copyright restrictions

Figure 3.2: (a) Bragg wavelength against the two-beam interferometer arm-length L_x for L_0 =522mm, n_{eff} =1.446, θ_0 = 45° and λ_{uv} =244nm. (b) Schematic diagram of optical set-up for changing the Bragg wavelength by varying the arm-lengths (moving mirrors M2 and M3 to position M2' and M3').

The relationship between the Bragg wavelength and the arm-length L_x in Figure 3.2(a) with a fixed L_0 makes it possible to predict the grating wavelength by using the appropriate reference arm-length value L_{ref} (Figure 3.2(b)). The L_{ref} and a grating of wavelength λ_{ref} can be initially measured, and then by rearranging equation 3.2, we have;

$$L_0 = \frac{L_{ref}}{\sqrt{2}} + \frac{L_{ref}}{\sqrt{2}\tan\left[\sin^{-1}\left(\frac{n_{eff}\lambda_{uv}}{\lambda_{ref}}\right)\right]} \tag{3.4}$$

By moving the mirrors M2 and M3 to new positions M2' and M3' as seen in Figure 3.2(b), this gives new arm lengths L_x = L_{ref} + x, where x is the measure of displacement using a micrometer. With the new arm lengths in Figure 3.2(b), the Bragg wavelength can be re-written as:

$$\lambda_B = \frac{n_{eff}\lambda_{uv}}{\sin\left[\tan^{-1}\left(\frac{L_{ref}+x}{\sqrt{2}L_0-(L_{ref}+x)}\right)\right]} \tag{3.5}$$

where L_0 is given in Equation 3.4

This technique has since proven to be a useful tool in fabricating FBGs with arbitrary wavelengths by simply adjusting the angle of the two interfering beams. However the main disadvantages of this technique are that the grating length is limited by the size of the two interfering beams, susceptibility to mechanical vibrations during the fabrication process and the need for a good coherent laser source. Also self-chirping is observed usually on the short wavelength side of the Bragg resonance, which is caused by the non-uniformity of the beam profile over the exposed length of the grating. In the use of the holographic system as a fabrication technique, various parameters can be altered in order to change the strength and bandwidth of the Bragg peak, including the laser beam power and exposure time. The Spectra growth of holographically inscribed FBG in SMF-28 was monitored for about 1 minute and the observed result (showing the effect of exposure time whilst keeping other conditions the same) is shown below in Figure 3.3.

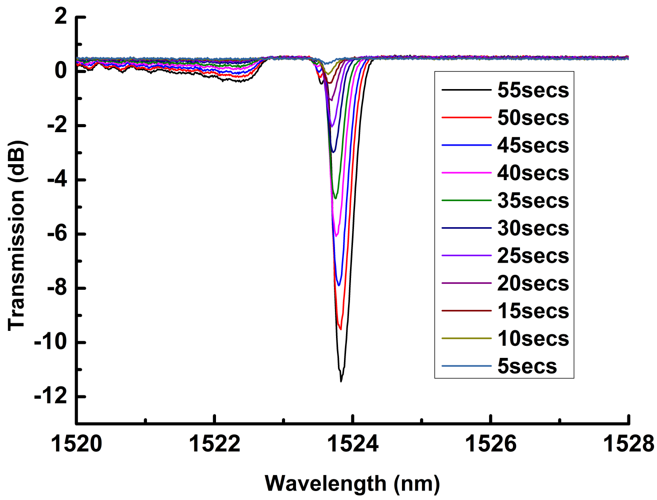

Figure 3.3: Spectra growth of holographically inscribed FBGs in SMF-28 monitored for about 1 minute.

The growth of the reflectivity (or transmission loss) of an FBG increases over a period of UV exposing time, as shown in Figure 3.3. The more the fibre is exposed to the UV beam, the stronger the index modulation that takes place in the fibre core. It can be deduced from the results shown in Figure 3.3 that the change in wavelength over a period of approximately 1 minute of exposure time is ~0.43nm, while the reflectivity growth of the grating approximately 1 minute is 11.5dB. Figure 3.3 also shows a slow start of reflectivity, but the more noticeable change in transmission loss begins at about 15secs into the fibre exposure. When the grating grows, a red shift in Bragg wavelength is also observed. This is due to the increased change in effective refractive index of the fibre core. The transmission evolution stops increasing as the photosensitivity of the hydrogenated SMF-28 fibre reaches saturation point.

The maximum reflectivity of a uniform Bragg grating is however governed by [2]

$$R_{peak} = \tan h^2(kL) \tag{3.6}$$

and

$$k = \frac{\pi \delta n \eta(v)}{\lambda} \tag{3.7}$$

where L is the grating length and $\eta(v)$ is a function of the fibre V parameter and is given by:

$$\eta(v) = 1 - \frac{1}{v^2} \tag{3.8}$$

and the detuning δ is given by:

$$\delta = 2n_{eff}\left(\frac{1}{\lambda} - \frac{1}{\lambda_B}\right) \tag{3.9}$$

where n_{eff} is the effective mode index and λ_B is the Bragg wavelength.

Most of the gratings in this session are fabricated using the phase mask techniques but the holographic method has been used when some specific wavelengths are required. Figure 3.4 shows typical transmission spectra of four FBGs fabricated in standard Corning SMF fibre with Bragg wavelength ranging from near-IR 800nm to mid-IR 2µm

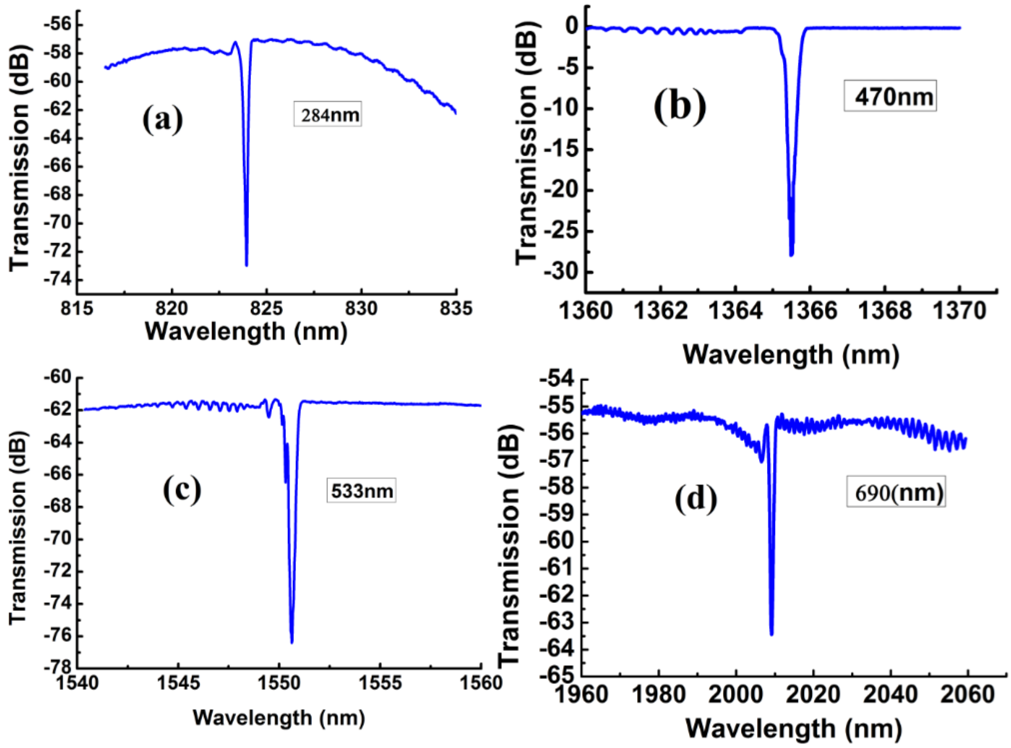

Figure 3.4: Typical transmission spectra of holographically inscribed FBGs in SMF-28 fibre with Bragg wavelengths ranging from near-IR (800nm) to mid-IR (2µm).

The spectra in Figure 3.4 clearly shows that as the period change occurs (284nm, 470nm, 533nm and 690nm respectively) during the fibre exposure to UV (using the experimental set up in Figure 2.7), there is a corresponding Bragg wavelength shift (823nm, 1365nm, 1552nm and 2009nm respectively). The transmission strengths of these four FBGs are about 12dB, 25dB, 14dB and 7dB respectively. Factors that would affect the strength of the grating during fabrication using the holographic system are: the UV laser power, the exposure time and the grating length (determined by the length of the effective interference region of the two beams).

3.2.1.2 *Phase mask technique*

The phase mask technique is known to be the most robust FBG fabrication technique, due to its grating repeatability and system stability. The phase mask is a one-dimensional periodic surface relief pattern, which can diffract incident light into several orders (m = 0, ± 1, ± 2)[3] [4]. The diagram in Figure 2.8 and 2.9 (Chapter 2) illustrates the beam diffraction from a phase mask. Most of the fabrications discussed in this thesis used phase masks with m = ± 1 orders optimised, while other orders were suppressed to allow for better visibility of the interference pattern. The diffraction caused by the phase mask shows the ± 1 orders (Figure 3.5(a)) with the strongest intensity while the other orders are suppressed. The gap between successive orders also increases outwards across the phase mask.

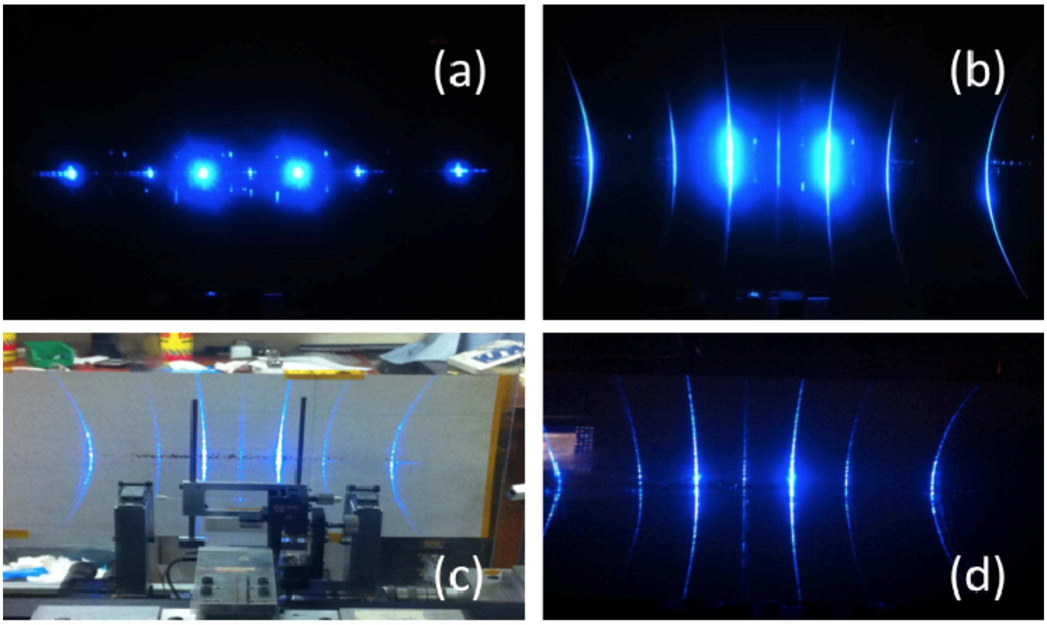

Figure 3.5: Images of the UV diffraction pattern: (a) with a bare phase mask; (b) with phase mask and optical fibre; (c) the laboratory set up showing the viewing screen, the phase mask, the fibre and the scanning stage; (d) another diffraction pattern with both the phase mask and the fibre.

To ensure quality-grating fabrication, further analysis was carried out to compare the diffraction efficiency of the 0 and ±1 orders) of a commercial phase mask. This commercial phase mask (manufactured by QPS (S/N 9018H-17-50-3-D)) can be used to fabricate FBGs at five different wavelengths and the phase mask attributes are shown in Figure 3.6.

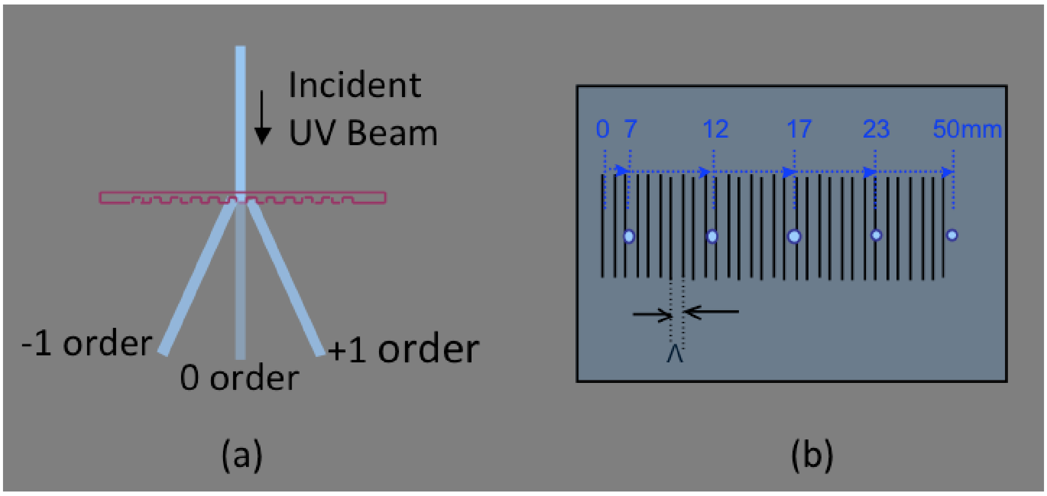

Figure 3.6: (a) Schematic of UV diffraction beams by phase mask and (b) five selected points of phase mask for measurement.

As shown in Figure 3.6, the diffraction power intensity of 0 order and ± 1 order at five different positions along the 50mm long phase mask were measured. In tables 3.1-3.5 below, the detail characterisation of the QPS phase mask is shown. The diffraction efficiency experiment was carried out by lunching an incident UV beam (Frequency doubled argon ion laser at 244nm wavelength) with a spot size of approximately 0.5 mm to the phase mask. The mask structure results in diffraction beams of 0, ±1, ±2 orders which were viewed clearly on a screen placed behind the mask (as the image shown in Figure 3.5(a-d)).

Point Location (mm)	Diffraction Efficiency (%)		
	-1 order	0 order	+1 order
7	38	0.9	38
12	38.1	0.1	38.1
17	38	0.1	38
23	39	0.1	39
50	39.2	0.2	39.2

Table 3.1: Diffraction efficiency of QPS Phase Mask at Λ = 1060.85nm

Point Location (mm)	Diffraction Efficiency (%)		
	-1 order	0 order	+1 order
7	39	0.9	39
12	39	0.1	39
17	40.1	0.2	40.1
23	39	0.2	39
50	40.1	0.2	40.1

Table 3.2: Diffraction efficiency of QPS Phase Mask at Λ = 1066.39nm

Point Location (mm)	Diffraction Efficiency (%)		
	-1 order	0 order	+1 order
7	38	1.1	38
12	38.1	0.2	38.1
17	38	0.2	38
23	39	0.3	39
50	39.2	0.3	39.2

Table 3.3: Diffraction efficiency of QPS Phase Mask at Λ = 1071.92nm

Point Location (mm)	Diffraction Efficiency (%)		
	-1 order	0 order	+1 order
7	39	1.1	39
12	39	0.3	39
17	40.1	0.3	40.1
23	39	0.3	39
50	40.1	0.3	40.1

Table 3.4: Diffraction efficiency of QPS Phase Mask at Λ = 1077.45nm

Point Location (mm)	Diffraction Efficiency (%)		
	-1 order	0 order	+1 order
7	38	1.0	38
12	38.1	0.3	38.1
17	38	0.2	38
23	39	0.3	39
50	39.2	0.2	39.2

Table 3.5: Diffraction efficiency of QPS Phase Mask at Λ = 1082.98nm

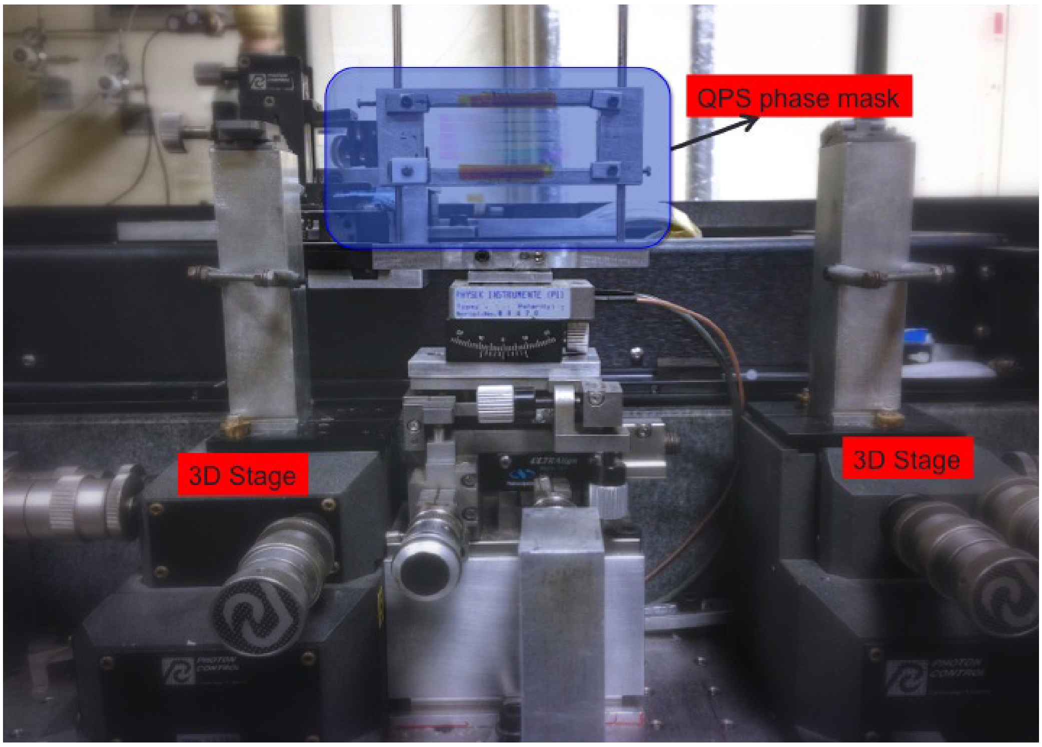

Figure 3.7: The fabrication set up with the QPS phase mask mounted on a tilt stage on a 3D translation stage.

The intensities of three order beams (0 order, ± 1 order) were measured using a UV detector. The experimental results from testing on the phase mask with five different periods show a diffraction efficiency $> 35\%$ for the ± 1 orders and $< 5\%$ for the 0 order. The suppression of the 0 order diffraction can usually be controlled through the corrugation depth and the choice of the amplitude of the surface-relief pattern. For a minimum 0 order, the depth of corrugation can be expressed as:

$$d_c = \frac{\lambda_{uv}}{2(n_s(\lambda_{uv}) - 1)} \tag{3.10}$$

where λ_{uv} is the wavelength of the UV beam and $n_s(\lambda_{uv})$ is the refractive index of the fused silica substrate at the incident wavelength of the UV beam. The period of the grating fabricated is always half the period of the phase mask used (equation 2.42 in Chapter 2). A stronger than 5% 0 order will erase the grating fringes induced by ± 1 order diffraction, so a well suppressed 0 order gives the best FBG fabrication condition.

In order to fabricate FBG grating, the stripped fibre must be placed at the effective interference region (with the fibre almost in close-contact with the phase mask corrugations) of the ± 1 orders of the UV beam (Figure 2.8 and 2.9 in chapter 2), so that refractive index modulation can be induced in the core of the fibre. A microscopic image (Carl Zeiss Microscope) of an FBG inscribed using phase mask technique is shown in Figure 3.8, where the periodic fringe pattern with designed FBG period can be clearly seen:

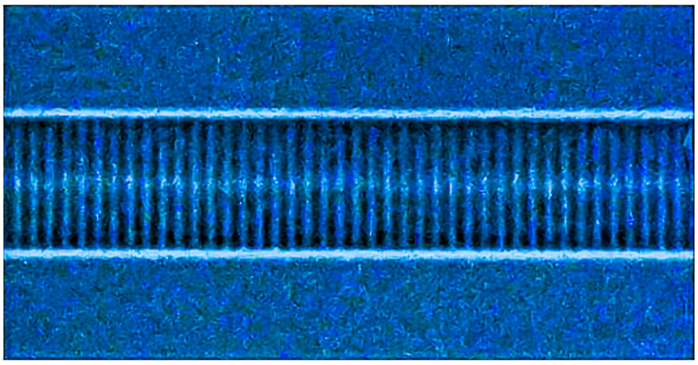

Figure 3.8: The microscope with $\times$ 100 objective lens used to view the inscribed FBG, showing a uniform period across the length of the grating.

The QPR phase mask (Figure 3.5 and 3.7) with five different periods of 1060.85nm, 1066.39nm, 1071.92nm, 1077.45nm and 1082.98nm has been used to inscribe five FBGs, showing Bragg wavelengths at 1536.5nm, 1544.6nm, 1552.9nm, 1560.6nm and 1568.2nm, respectively, with reflectivity around 16dB, as shown in Figure 3.9(a-e)

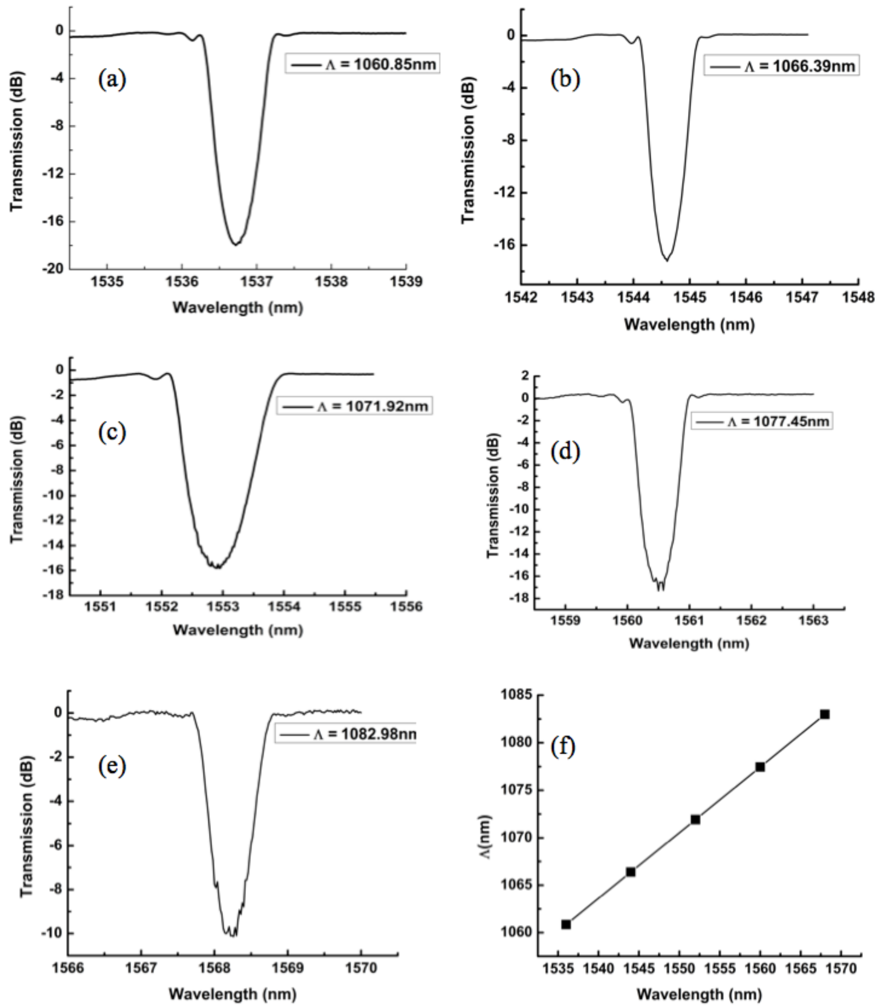

Figure 3.9: The transmission spectrum of the fabricated FBGs using the QPR phase mask; at wavelengths (a) 1536nm, (b) 1544nm, (c) 1552nm, (d) 1560nm and (e) 1568nm respectively; (f) a plot showing the effect of change in period on grating wavelength.

Figure 3.9 (f) shows a red shift in wavelength as the period of the phase mask used increases, showing also a linear correlation when the fabrication condition is kept the same.

3.2.2 FBG Stability

Since the FBGs are widely used in optical fibre communications and sensor systems, their stability in wavelength and reflectivity over a time period is therefore crucial. Erdogan et al [5] mentioned that grating decay is caused by the thermal depopulation of trapped states that the grating fabrication process produces. Most systems have 25 years design lifetime and gratings are not expected to decay in this time period. Considerable efforts have taken place in the photonics community over the issue of thermal stability and its consequent effect on performance [6–10]. For example, FBGs written in Sn-doped silica fiber sustain temperatures as high as 800°C [11], but FBGs written in Boron/Germanium (B/Ge) co-doped silica fiber can sustain much lower temperature of 300°C [6].

In order for the FBGs to function as temperature sensors, they are usually thermally annealed at the required temperature, because the thermal annealing treatment removes the portion of traps that will decay quickly and leave behind stable traps that can survive long term, thus increasing FBG stability. However, there is link between the annealing time, long-term stability and operating temperature. For example, if an FBG will be used for sensing temperature of up to 100°C, it must be annealed for 24 hours at 120°C. If the lifetime requirement or operating temperature is increased, the annealing temperature of the grating should also be increased.

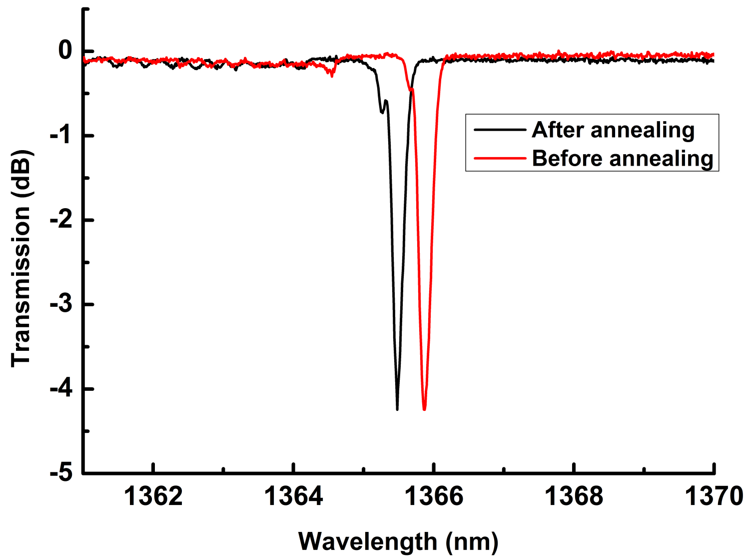

Figure 3.10: Graph showing the annealing result of an FBG inscribed in SMF-28 fibre.

The FBGs fabricated and reported in this thesis have been annealed to remove the unreacted hydrogen in SMF-28 fibre and to stabilize the structure. This process of annealing treatment was conducted over 48 hours at 80°C. Figure 3.10 shows the result of an FBG inscribed in a hydrogen loaded SMF-28 telecom fibre, before and after annealing.

In 1993, Douay et al [6] described that when the grating is heated from a temperature 80°C to 425°C, the Bragg wavelength shows thermal hysteresis due to an annealing effect. The increase in temperature causes the fibre to thermally expand thereby increasing the grating period causing the Bragg wavelength to increase. But, when the grating is restored to its initial temperature, a permanent Bragg wavelength shift to the shorter wavelength is still observed. This depends on the fibre and the condition of exposure. The wavelength shift of the FBG shown in Figure 3.10 after annealing at 80°C for 48 hours and returned to room temperature is ~0.5nm and the reflectivity stayed almost the same. This annealing process will make the FBG stable in sensing applications operating below 80°C.

3.2.3 FBG Temperature Sensing

The sensing capability of FBG works by monitoring the shift in the Bragg wavelength (equation 2.30 in Chapter 2) as the grating condition changes with external perturbation. The thermal response of an FBG is due to the inherent thermal expansion of the fibre and the refractive index temperature dependence of the fibre. Using the chain rule of derivatives, the wavelength shift per unit temperature $\frac{d\lambda_B}{dT}$ for a particular temperature change ΔT can be derived as [12]:

$$\frac{d\lambda_B}{dT} = \frac{d\lambda_B}{dn_{eff}}\frac{dn_{eff}}{dT} + \frac{d\lambda_B}{d\Lambda}\frac{d\Lambda}{dT} \tag{3.11}$$

Equation 3.11, suggests that the thermal induced Bragg wavelength shift is due to the change in the effective index of the fibre and the change in the grating period. The first part of the equation is the material effect on wavelength shift and the second part is the waveguide effect as it causes a change in length due to thermal expansion. Since the slope of the wavelength versus grating period of a silica fibre is constant and approximated as $\frac{d\lambda_B}{d\Lambda} = 2n_{eff}$ [13], equation 3.11 can then be re-written as:

$$\frac{d\lambda_B}{dT} = 2\Lambda\left(\frac{dn_{eff}}{dT} + n_{eff}\frac{1}{\Lambda}\frac{d\Lambda}{dT}\right) \tag{3.12}$$

Therefore, by approximating the effective index with the index of refraction of pure silica, equation 2.30 and equation 3.12 can be combined to form:

$$\frac{d\lambda_B}{dT} = \lambda_B\left(\frac{1}{n_{si}}\frac{dn_{si}}{dT} + \frac{1}{L}\frac{dL}{dT}\right) \tag{3.13}$$

were n_{si} is the index of refraction of pure silica and L is the grating length ($\frac{1}{\Lambda}\frac{d\Lambda}{dT}$ = $\frac{1}{L}\frac{dL}{dT}$). Using n_{si} = 1.458, $\frac{dn_{si}}{dT}$ = 7.8 $\times$ 10^{-6}/ °C and $\frac{1}{L}\frac{dL}{dT}$ = 4.1 $\times$ 10^{-7}/ °C [14],equation 3.13 can be rewritten as:

$$\Delta\lambda_B = 5.76 \times 10^{-6}\lambda_B\Delta T \tag{3.14}$$

where ΔT is the change in temperature and $\Delta\lambda_B$ is the Bragg wavelength shift. The changes in n_{eff} temperature lead to changes in the thermo-optic coefficient and the change in period occurs through the thermal expansion and contraction of the fibre. In the following described experiment, three FBGs fabricated using the two-beam holographic inscription method with three distinctive wavelength ranges were evaluated for temperature sensing and their temperature sensitivities were then compared. The temperature sensing experimental set-up used is shown in Figure 3.11.

Aston University

Illustration removed for copyright restrictions

Figure 3.11: FBG temperature sensing experimental setup, showing the FBG on a heat controlled peltier and the OSA for observing and capturing the wavelength shift using a LabView program.

The FBGs used in this experiment were fabricated holographically to generate wavelengths in three regions: 800nm, 1550nm and 2000nm and they were first annealed in a heat chamber at 80°C for 24 hours. The FBG section of the fibre was placed in the heating device that was controlled by a Lightwave LDT-5910B temperature controller and the temperature was explored for range 10°C to 70°C (with a stability of between $\pm$0.08°C). The gratings are 24mm each in length, a BBS (Broad Band Source) was used as a light source and the HP86142A OSA (optical spectrum analyser) was used to observe the transmission spectrum. The set up (Figure 3.11) involves fixing (using a thermal tape) both sides of the FBG sensor unto the v-grove of the heating unit (peltier). The temperature controller was then used to control the temperature of the v-grove (50mm long aluminium plate) plate to which the 24mm FBG region was placed.

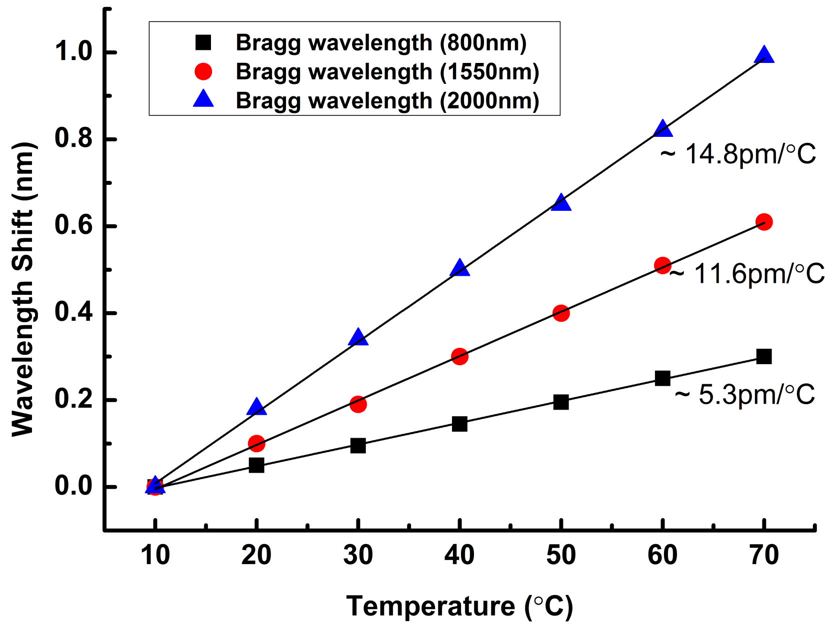

Figure 3.12: Comparison FBG thermal response Vs Wavelength shift for three different wavelength ranges.

It can be seen from the plot (Figure 3.12) that the temperature responses for all three different wavelength ranges have a linear fit. The temperature sensitivity for the 800nm FBG is ~5.3 pm/°C, for the 1550nm FBG is ~11.6 pm/°C and for the 2000nm FBG is ~14.8 pm/°C, showing that the temperature sensitivity increases with Bragg wavelength and satisfies equation 3.14. The measured temperature sensitivity in 1550nm range is in agreement with the theoretical and reported values, which lie between 10.0 pm/°C and 13.0 pm/°C.

3.2.4 Cryogenic Sensing and Experimental Result

There are several sensors available in the market capable of measuring low temperatures but with great limitations in their use in harsh environments [15]. However, the uses of optical sensors for low temperature applications, like storage or transport of cryogens and liquid hydrogen fuel tanks [16–21] are now becoming more appealing. In this continued effort to use FBGs as sensors in cryogenic conditions, scientist have embedded FBGs in substrates like Teflon or Poly(methyl methacrylate) (PMMA) to enhance their sensitivity due to having a greater thermal expansion than that of a silica fibre [16][18]. In 2002, White showed that the thermal expansion of Silica glass is negative at temperatures below 150K (-123°C) [22]. The experiment described here was looking at low temperature measurements up to -40°C.

The FBG used for the cryogenic testing experiment had been previously annealed to improved stability. The set up for this experiment is shown in Figure 3.13.

Aston University

Illustration removed for copyright restrictions

Figure 3.13: Experimental set up of FBG cryogenic sensing.

The environmental chamber (ESPEC Platinous series ESX-3CA) consists of a brass body housing which has the capability to measure both humidity and temperature. It is capable of varying environmental conditions (temperature and humidity) over hourly, seasonal, and annual time scales through touchscreen and remote programming. The chamber runs off a dedicated circuit and utilizes ultra-pure compressed air from an SF-8 Atlas Co. compressor.

A FBG centred at 1550.93 nm at room temperature was bonded on an aluminium v-groove plate with an epoxy adhesive and placed in the chamber after the chamber was initialised to 0°C. With the help of the programmable temperature input, the chamber was programmed to increase the temperature for every 10°C (up to 35°C) at 20 minutes interval, allowing for the temperature reading to stabilise before changing to the next temperature. The two fibre ends were connected to a BBS (Ando AQ-6310B) and an OSA (HP86142A) respectively. The observed spectral shift from the OSA was auto-captured throughout the course of the experiment by using a LabViiew program. Similar experiment was then carried out for temperatures from -5°C to -40°C and programmed using the same interval. The experimental results are shown in Figure 3.14.

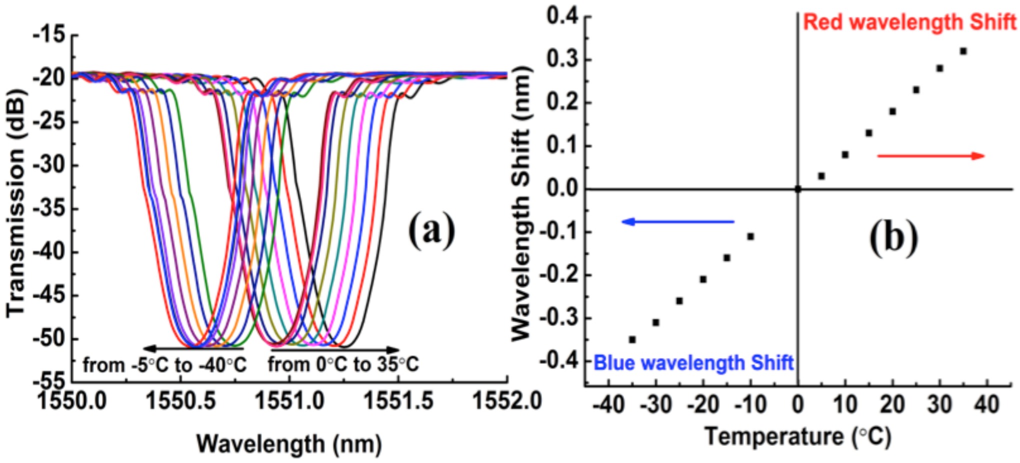

Figure 3.14: (a) Comparison FBG response for both the cryogenic and elevated temperatures: (b) Comparison FBG thermal response Vs wavelength.

showed that as the programmed temperature of the environmental chamber increases from 0°C to 35°C, the FBG transmission spectrum experiences a red shift towards the longer wavelength (from 1550.93nm to 1551.25nm). The temperature sensitivity for the elevated temperature sensing is ~9.5pm/°C (Figure 3.14(a)), with the reflectivity of the FBG remaining the same throughout the elevated temperature change. The result of the cryogenic experiment (from -5°C to -40°C) shows a blue shift towards the shorted wavelength (1551.25nm to 1550.48nm) and with a temperature sensitivity of 10pm/°C. In Figure 3.14 (b), the comparison of the temperature sensitivity for both the elevated temperature and cryogenic temperature shows a linear correlation.

3.3 *LONG PERIOD GRATINGs (LPGs)*

3.3.1 LPG Fabrication

Long period grating (LPG) devices have periods in the range of 100µm to 1mm compared to FBGs with shorter periods of few hundred nanometres. The longer spacing of the period in LPGs is a result of a different waveguide coupling mechanism. LPGs couple light from the guided core mode to forward propagating cladding modes generating attenuation peaks in the transmission spectrum associated with each coupling. Due to this LPG coupling property, it has been used in applications like strain, bend, temperature, and refractive index change sensors [13, 23, 24], band-pass and band-rejection filters [24], gain equalizers [24], mode converters [25], light diffusers for medical applications [26] and chemical sensors [27]. Historically, LPGs have been inscribed by various methods: amplitude mask method [28], femtosecond laser inscription [29], using computer-generated holographic element (HOE) [30] and point- by- point methods [28].

The aim of this section is to give a detailed analysis of the fabrication technique employed in the inscription of the LPG structures reported in this thesis. The spectral characteristics of LPGs fabricated in hydrogenated SMF 28 fibre with periods from 290µm to 440µm will be reviewed. Also, the temperature sensitivity of LPGs at different wavelengths will be examined, showing a comparison between the temperature sensitivities of different modes of the LPG. The refractive index sensitivity of LPGs at different wavelengths will also be described. Furthermore, the LPG usage as an ultra-sensitive low curvature-sensing device is also described.

The LPG fabrication was through the point-by-point method, (first reported by Malo et al [31]). The output from a UV laser (Sabre FreD frequency doubled argon ion laser, operated at 50Hz line frequency and at 100mW output power) is directed towards two sets of circular Plano-convex lens (f1 and f2 in Figure 2.10), which are used to focus the beam down (in the x and y direction) to the fibre axis. With the fibre fixed unto the v-grove holders (with a magnet) mounted on a 3D stage, the UV beam is translated for a set length through the computer controlled air bearing translation stage with maximum travel of 150mm and a resolution of 7nm. The periodic exposure and the varying of the duty cycle are controlled via the automatic (using a LabView programme) switching on/off of the acousto-optic (AO) modulator. The LabView programme also enables the parameters setting for the duty cycle, period, and fabrication speed and grating length. The transmission spectrum was monitored via the connectorised ends of the clamped fibre to the BBS and an OSA (with maximum resolution of 0.06nm).

The LPGs were inscribed in hydrogenated SMF-28 single mode fibre. The output power of the laser was set to 100mW and the measured laser power after the two focusing lenses was ~90mW. After carefully aligning the fibre axis to the focused beam (Figure 2.10 in Chapter 2), the LabView programme (with desired parameters set) was set to run and as the fibre exposed to UV beam. The fabrication conditions were set as: the grating length to 15mm, duty cycle to 0.5 and grating periods to 290µm, 295µm, 300µm, 305µm, 310µm, 315µm accordingly. After the irradiation of the fibre, transmission loss peaks (LP_{01}-LP_{05}) begin to emerge and the spectrum was captured from the OSA with a GPIB card.

3.3.2 LPG Spectral Response

Similar to FBGs, after the fabrication, the LPG devices were annealed for 48 hours at 80°C to stabilise the grating structure. Then, all fabricated LPGs were characterised for their spectral responses. As the transmission loss peaks of an LPG may cover a wavelength range of several hundred nm, a broadband light source and an optical spectrum analyser (OSA) were used to capture the spectral response of the LPG. The resolution bandwidth of the OSA usually was set to 0.06nm and the sensitivity was -75dBm.

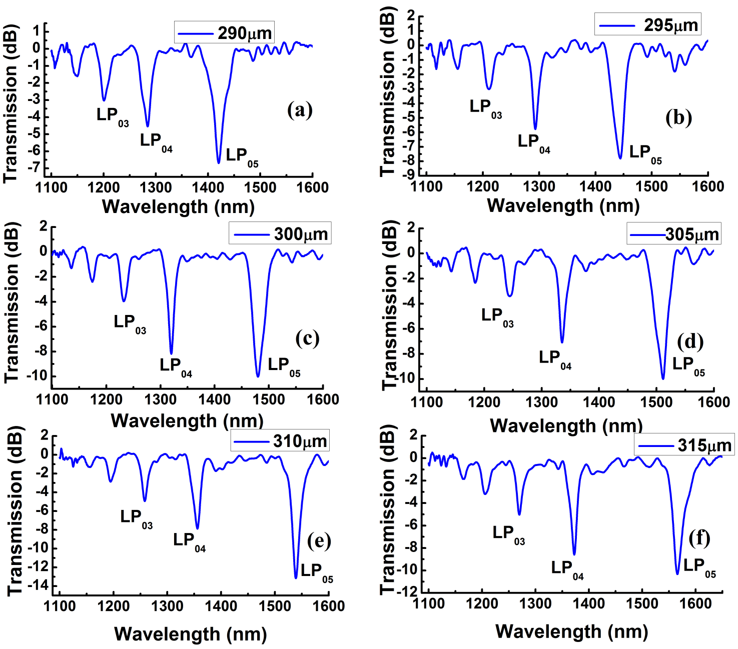

Figure 3.15: Transmission spectra of six LPGs inscribed in SMF-28 fibre by point-by-point method with periods of 290µm (a), 295µm (b), 300µm (c), 305µm (d), 310µm (e) and 315µm (f).

Figure 3.15 shows the typical spectral responses of six LPGs (15mm long) with slightly different periods: Λ = 290μm, 295μm, 300μm, 305μm, 310μm and 315μm. The coupled main cladding modes of LP_{03}-LP_{05} are all shown but shifting towards longer wavelength side with increasing period. The transmission spectra for the Λ = 290μm and Λ = 315μm have been combined for analysis in Figure 3.16 and Figure 3.17.

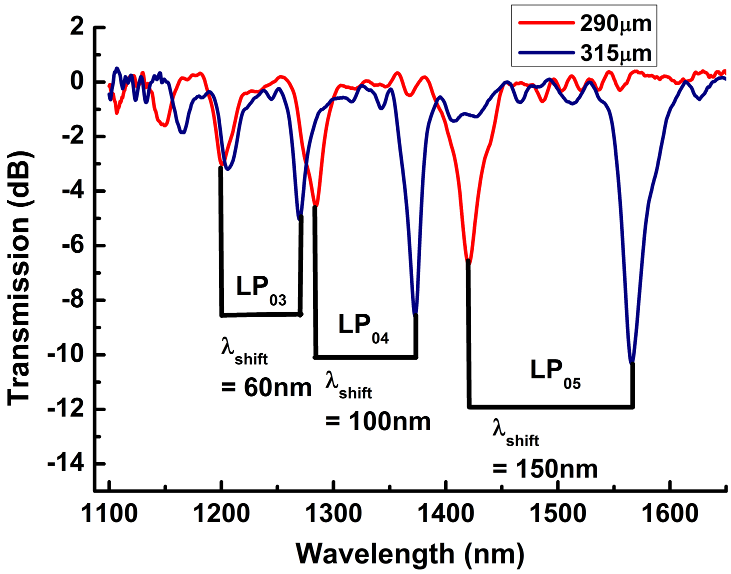

Figure 3.16: Combined transmission spectra of the selected two LPGs with periods of 290μm and 315μm, showing the wavelength shifts for each coupled peak.

In Figure 3.16, when the LPG period is changed from 290μm to 315μm, the transmission peaks of selected LP_{03} - LP_{05} showed a shift to the higher wavelength. For the LP_{03}, LP_{04}, LP_{05} , the measured wavelength shifts are ~60nm, ~100nm and ~150nm respectively; the shift of LP_{05} is almost 3 times of that of LP_{03}.

The ratio (C) of the power coupled to a cladding mode of order m to the initial power in the fundamental guided mode in the presence of a perturbation can be expressed as [32]

$$C = \frac{P^{(m)}(L)}{P_{01}(0)} = \frac{\sin^2\left[K^{(m)}L\sqrt{1+\left(\frac{\delta^{(m)}}{K^{(m)}}\right)^2}\right]}{1+\left(\frac{\delta^{(m)}}{K^{(m)}}\right)^2} \tag{3.15}$$

where L is the grating length, $\delta^{(m)}$ and $K^{(m)}$ are the detuning parameter for the corresponding cladding mode and the coupling coefficient respectively, which explains why Figure 3.15, 3.16 and 3.17 show transmission loss peaks of varying peak intensity, with change in intensity of ~2dB, ~3dB and ~3.7dB for the LP_{03} - LP_{05} modes respectively.

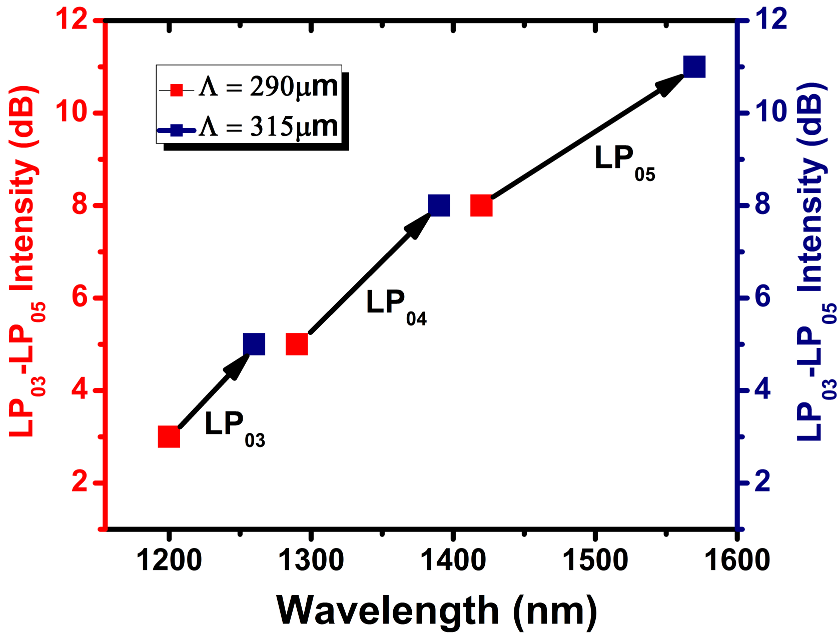

Figure 3.17: Analysis of the change in transmission peak intensity observed when the LPG period changes of 290µm to 315µm, for LP_{03} - LP_{05}.

Further analysis was carried out to investigate the effect of grating length of the fabricated LPG on transmission peaks. The coupled mode theory expressed that the transmission intensity S of any loss peak of an LPG is a function of the grating length (L) and the coupling coefficient (η) [33]:

$$S = \sin^2(\eta L) \tag{3.16}$$

where the coupling coefficient η can be expressed as:

$$\eta = \frac{\omega n_{core} \delta n_{core} I}{4} \tag{3.17}$$

where δn_{core} is the amplitude of the index modulation by UV irradiation of the fibre core, n_{core}

is the effective index of the fundamental core mode, ω is the resonant frequency and I (which determines the growth rate of each loss peaks) is the overlap integral between the core mode and the cladding modes. For this experiment, the grating period (300μm), exposure time, UV–laser power (100mW), duty cycle (50:50) and the writing speed were kept the same and the grating lengths were set at 10mm, 15mm and 20mm respectively.

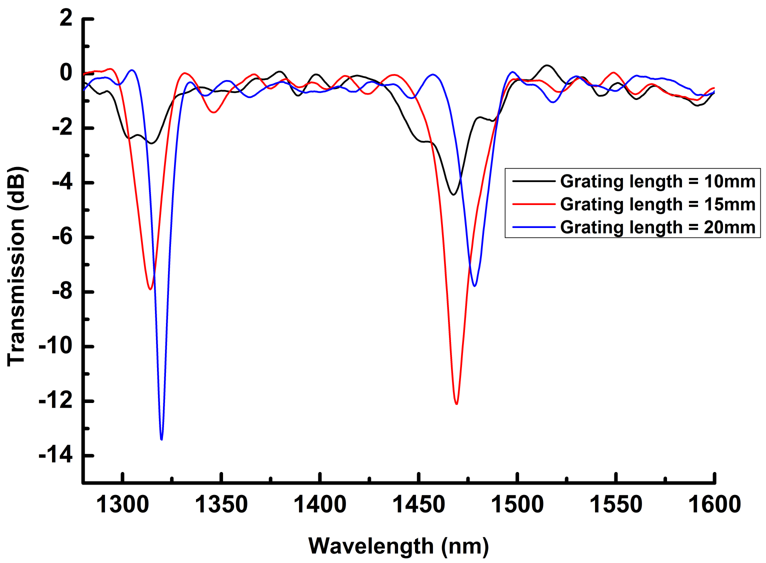

Figure 3.18: Comparison of transmission loss peaks fabricated for LPGs with different grating lengths, while all other parameters are kept the same.

The OSA span was set to 300nm, which gave the range to observe two transmission loss peaks. During UV irradiation, η increases as δn_{core} increases, thus the peak loss strength increases [34], which agrees with what was observed in Figure 3.18. At 10mm length, the two transmission loss peaks are about -2dB and -4dB respectively and about 5nm broad. As the grating length increased to 15mm, the transmission loss peaks intensity increases to 8dB & 12dB respectively with the width reduced to about 3nm and a slight wavelength shift (~2nm) to the longer wavelength. At 20mm, the transmission loss peaks intensity increased for the first peak to ~14dB (with ~2nm width) and the second peak reduced to 8db from 12dB (with ~3nm width); the second peak reached its saturated transmission strength at the grating length of 20mm and at which point the transmission intensity also reduces, satisfying the sine function expressed in equation 3.16.

3.3.3 LPG Temperature Sensing

The coupling that takes place between the fundamental core modes to the forward cladding modes makes an LPG more sensitive to the changes in its environment condition. If we consider an LPG with period Λ subjected to a temperature change ΔT , with ξ = T to give [35]

$$\frac{d\lambda}{dT} = \frac{d\lambda}{d(\delta n_{eff})}\left(\frac{d(\delta n_{eff})}{dT}\right) + \frac{d\lambda}{d\Lambda}\frac{d\Lambda}{dT} \tag{3.18}$$

In order to identify the material and the waveguide contribution to the thermally induced shift, equation 3.19 can be further modified into:

$$\frac{d\lambda}{dT} = \frac{d\lambda}{d(\delta n_{eff})}\left(\frac{dn_{eff}}{dT} - \frac{dn_{cl}}{dT}\right) + \frac{d\lambda}{d\Lambda}\frac{1}{L}\frac{dL}{dT} \tag{3.19}$$

Where λ is the central wavelength of the attenuation band, T is the temperature, n_{eff} is the effective refractive index of the core mode (expressed as n_{eff} - n_{cl}), n_{cl} is the effective refractive index of the cladding mode, L is the length of the LPG and Λ is the period of the LPG. The following section will describe the temperature sensitivity characteristics of four LPGs with different periods.

3.3.3.1 *Experiment and results*

The four LPGs used for temperature sensing were fabricated with periods of 300µm, 330µm, 360µm and 440µm, thus having the transmission loss peaks of coupled LP_{01} - LP_{06} (with labels only for the LP_{03} - LP_{06} in Figure 3.19) cladding modes distributed around the wavelength range from 1100nm to 2000nm. The captured spectra for these LPGs are shown in Figure 3.19

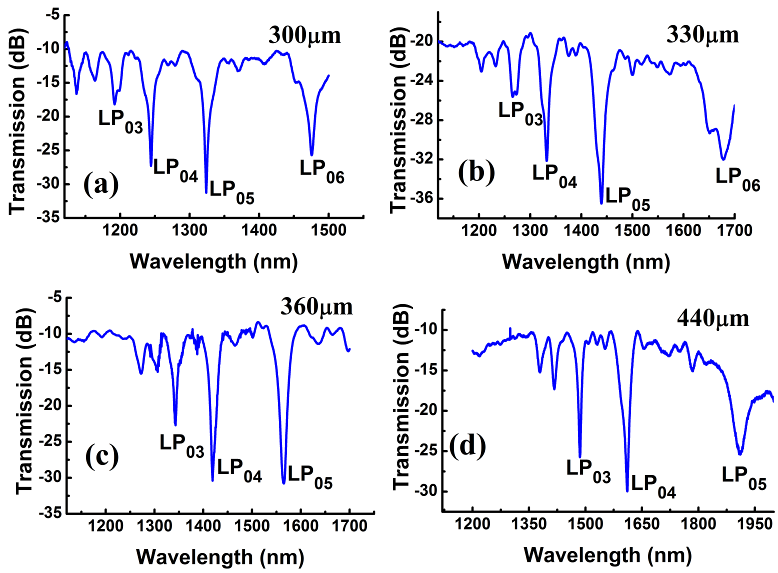

Figure 3.19: Transmission spectra of four LPGs inscribed in SMF 28 fibre by point-by-point method with periods of 300μm, 330μm, 360μm and 440μm.

The spectrum range from 1100nm to 2000nm, for the LPGs with periods of Λ = 300μm and Λ = 330μm both have LP_{03} - LP_{06} cladding modes, but by increasing the period, the LP_{06} peaks of the other two LPGs with longer periods (360μm and 440μm) have shifted beyond the OSA capture spectral span. A set up similar to Figure 3.11 was used for LPG temperature sensing. The Lightwave LDT-5910B temperature controller was used to increase the temperature of the LPG device from 10°C - 70°C with 10°C increments. The measured wavelength shifts against temperature for the LP_{05} modes of the four LPGs are plotted in Figure 3.20.

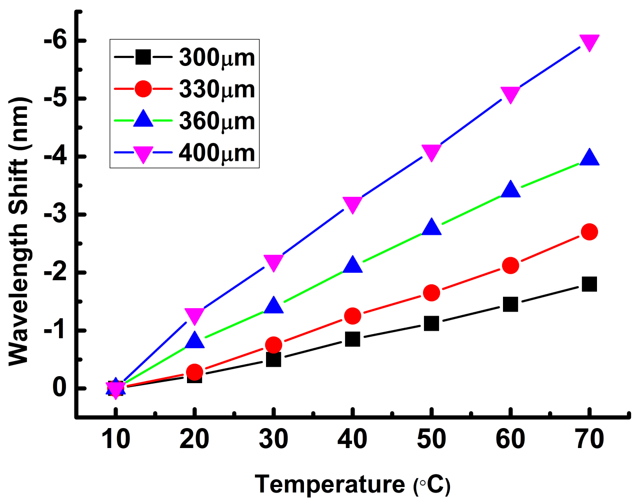

Figure 3.20: Comparison of thermal responses of LP_{05} cladding modes of four LPGs with different periods (300μm, 330μm, 360μm and 440μm).

Table 3.6 lists the temperature sensitivities for the LP_{05} modes of the four LPGs

Wavelength (nm) @LP_{05}	300µm	330µm	360µm	440µm
Temperature sensitivity	30pm/°C	45pm/°C	65pm/°C	100pm/°C

Table 3.6: Temperature sensitivity of LPGs of different LP_{05}.

Figure 3.20 and table 3.6 clearly show that for the same order of the cladding mode, the response of the LPG at larger period has higher temperature sensitivity. Quantitatively, the temperature sensitivity for the LP_{05} for the LPGs of periods of 300µm, 330µm, 36µm and 440µm is 30pm/°C, 45pm/°C, 65pm/°C and 100pm/°C respectively. The longest period LPG with LP_{05} at around 2000nm has just about tripled the temperature sensitivity of the same mode of the shortest LPG.

The temperature sensitivity was also measured for the LP_{01} to LP_{05} modes of a single LPG with a period of 440µm. During the measurement, the OSA was used to zoom into each mode and the wavelength shift was captured with LabView. These results are found in Figure 3.21 and table 3.7 below:

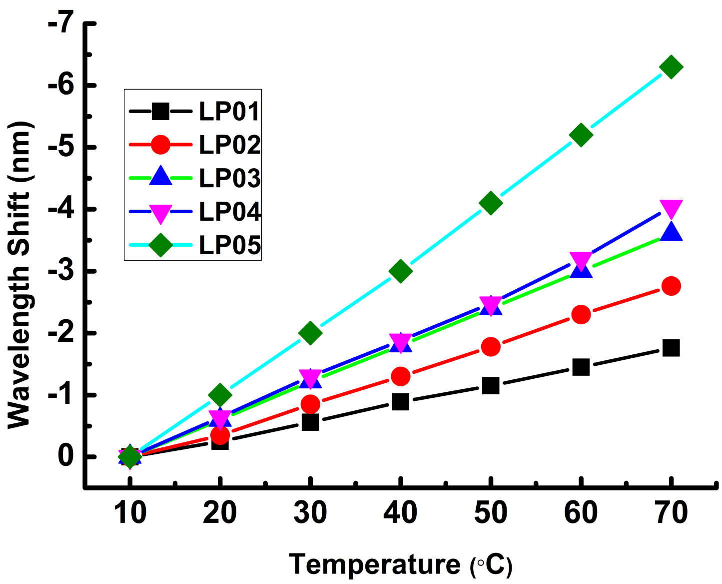

Figure 3.21: Comparison of thermal response of different cladding modes of an LPG with a period of 440µm.

440µm period LPG modes	LP_{01}	LP_{02}	LP_{03}	LP_{04}	LP_{05}
Temperature sensitivity	29pm/°C	47pm/°C	59pm/°C	66pm/°C	101pm/°C

Table 3.7: Temperature sensitivity of different modes (LP_{01} - LP_{05}) of a LPG with 440µm period.

From table 3.7, the LP_{05} cladding mode is about 4 times thermally sensitive than the LP_{01}; and in comparison to FBG, the thermal sensitivity of the LP_{05} mode of 440µm LPG is ten times higher than that of the FBG shown in Figure 3.12. The different cladding modes relates to how they interact to the changes in the grating surrounding; meaning that the higher cladding modes (in this case LP_{05}) are in this case the most sensitive to the change in surrounding temperature. From Equation 3.19, the thermal sensitivity of the grating at a particular period depends strongly on the slope of the $\frac{d\lambda}{d\Lambda}$ characteristics of the cladding mode. The non-linearity in the wavelength shift could be as a result of the temperature dependence of the thermo-optic coefficients of the core and cladding. It has been demonstrated that the wavelength shift can be enhanced by applying appropriate coating to the grating area [36] and the sensitivity can be suppressed either by coupling to specific lower cladding modes (LP_{01}) or by customising the fibre profile [35].

3.3.4 LPG Refractive Index Sensing

The light guided through a FBG is screened from the cladding due to the core-to-core mode coupling mechanism, thereby blocking out any strong interaction with the surrounding medium, thus a normal FBG cannot be used as a surrounding medium refractive index (RI) sensor. To make an FBG sensitive to surrounding medium RI, one has to modify the fibre structure to allow the interaction between the evanescent wave of the core mode and the surrounding environment. A number of methods have been used to achieve this, including polishing [37, 38] and chemical etching the fibre [39–41], but both methods reduce the mechanical strength of the fibre and make the fibre unsuitable for real applications.

In contrast to FBGs, and based on the core-cladding mode coupling mechanism, LPGs are intrinsically sensitive to changes in surrounding medium RI and can be implemented as RI sensors. In 2002, Shu et al presented a complete theoretical analysis of the RI sensitivity characteristics of LPG [42]; this analysis gives an insight into the design and application of LPG as a RI sensor. An expression for the RI sensitivity of an LPG was derived as [43, 44]:

$$\frac{d\lambda_m}{dn_{sur}} = \frac{d\lambda_m}{dn^{cl}_{eff,m}} \left[\frac{dn^{cl}_{eff,m}}{dn_{sur}} \right] \tag{3.20}$$

Where, n_{sur} is the refractive index of the surrounding, $n^{cl}_{eff,m}$ is the effective index of the mth cladding mode and λ_m is the resonant wavelength. Equation 3.20 reflects that the higher cladding modes (e.g. LP_{05}) are most sensitive to change in the environmental condition. The change in the effective index of a particular cladding mode ($dn^{cl}_{eff,m}$) is dependent on the order of the cladding mode, with each resonance band showing a distinct wavelength shift.

For most RI sensing applications, the index measurements are performed in the RI range 1.33 (water) to about 1.45 (fibre cladding index). For a situation where $n_{sur} > n_{cl}$, the propagation constant of the cladding mode becomes complex and the modes become leaky [45]. Figure 3.22 shows a schematic representation of an LPG with a surrounding medium; the cores refractive index is n_1, the claddings refractive index is n_2 and the surrounding refractive index is n_{sur}. The change in the effective index of a particular cladding mode ($dn^{cl}_{eff,m}$) is dependent on the order of the cladding mode. Changes in the surrounding medium RI will affect both the transmission intensity S (equation 3.16) and shift in resonant wavelength λ_m (equation 2.31).

Figure 3.22: A schematic representation of an LPG as a RI sensor.

3.3.4.1 *RI measurement and results*

A 15mm long LPG of period 360µm was selected for RI sensing experiment. The set up used as illustrated in Figure 3.23 shows the grating been supported on two sides by fibre holders in such a way that the fibre is kept parallel to the surface of the table. A glass slide is placed on a small laboratory jack, which is raised until the slide is touching the fibre. The portion of the fibre with the grating is fully pooled with the refractive index oils from Cargille Laboratories. The index oils are available in increments of 0.002 or 0.004, with an average temperature coefficient of 5×10^{-4}/°C [46]; the specified values of these index gels are at 589.3nm and Cauchy equation can be used to calculate the refractive index at the wavelength [46]. For the index oils in the range 1.4 – 1.46, the refractive index values at 1550nm are about 0.01 smaller that those at 589.3nm [47].

Figure 3.23: Experimental set up of the RI sensing, with the LPG secured to the glass slide and the two ends connected to the BBS and an OSA.

Light from a BBS was coupled into the fibre and the transmission spectrum was measured using an OSA. The LPG area was pooled by a series of Cargille index matching gels of varying index from 1.3−1.44 and left on the grating for about 1min for each index measurement; afterwards the spectrum was captured by the OSA. On completion of each index measurement, the small laboratory jack was lowered and the surface of the glass slide was cleaned carefully (with ethanol) to remove the residual index oils; with a reference scan taken after the cleaning to ensure the resonant peak returned to its unperturbed position (in air). As clearly described from the theory above (equation 3.20), the higher order cladding mode shows higher sensitivity to the surrounding medium RI, and this sensitivity will approach the maximum when RI is close to the refractive index of the cladding [48], hence the reason why the LP_{05} of the 360μm period LPG (Figure 3.19) was selected for the refractive index sensing.

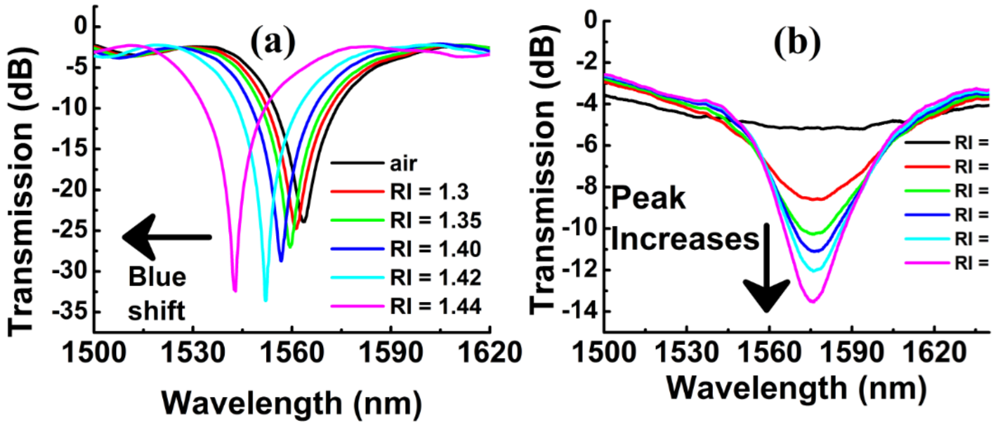

Figure 3.24: Plot of (a) the central wavelength shift at RI from RI = 1.3 to RI = 1.4; (b) LPG response to RI from 1.46 to 1.70.

Figure 3.24(a) shows a set of transmission spectra taken at several values of surrounding medium RI (1.00 – 1.44). When the LPG is surrounded by air, the resonant peak of the LP_{05} remained at the initial position, but as the RI increases, the resonant peak experienced a blue shift for each change in index gel. The RI sensitivity increased rapidly as the surrounding medium RI approaches to the index of cladding. The overall wavelength shift is about 25nm with the LP_{05} mode over the whole RI change from 1 to 1.44. As the RI increased, a small non-uniform change in the resonance peak strength was also observed (Figure 3.25(b)). The RI value was then increased from 1.44-1.46; as the RI index approached the cladding mode index, the resonant peak completely disappeared (Figure 3.24(b)); this is because the cladding appears to be infinite at this point and no co-propagating cladding modes are supported. The resonant peak later reappears as the RI value reaches 1.50; with progressive increase in amplitude (and no significant wavelength shift) as the RI value increases from 1.50 to 1.7. The overall wavelength shift of LP_{05} to surrounding RI change is shown in Figure 3.25(a)

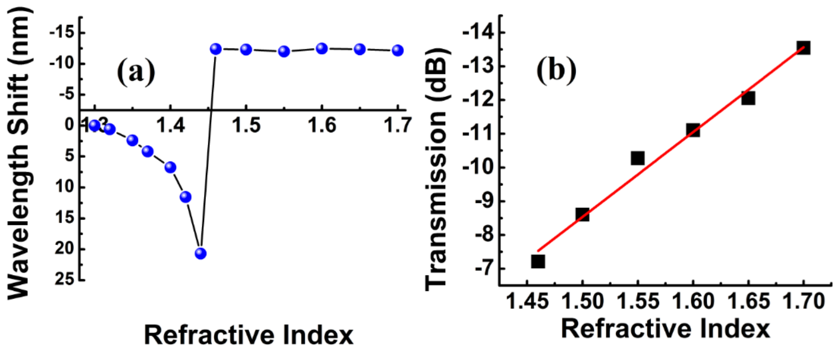

Figure 3.25: (a) Plot of the overall RI induced wavelength shift of the LP_{05} mode from the LPG with 360μm period when surrounding RI changed from 1.46 to 1.70; (b) The effect of each change in RI on the transmission peak strength.

Furthermore, the RI sensitivities of the same order (LP_{05}) cladding modes of four LPGs with different periods (300μm, 330μm, 360μm and 400μm) were also analysed and the results are shown in Figure 3.26. As the surrounding medium RI increases from 1.30 to 1.44, a non-linear and negative wavelength shift of LP_{05} mode for the four LPGs was observed since the sensitivity to index changes increases as the effective index of the cladding mode is attained. The overall wavelength shifts of LP_{05} are 375nm/RIU, 75nm/RIU, 49nm/RIU and 25nm/RIU for the four LPGs with period of 300μm, 330μm, 360μm and 440μm respectively.

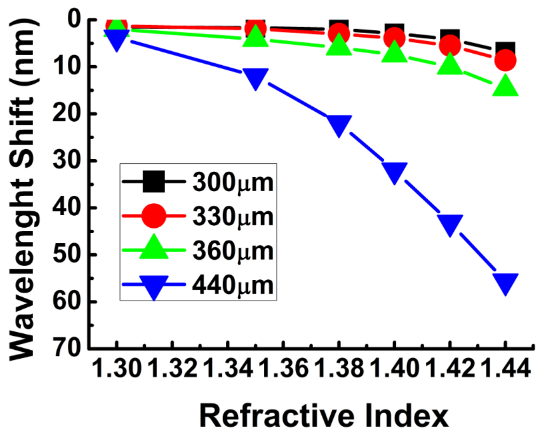

Figure 3.26: The experimental results showing RI induced wavelength shift of the LP_{05} of four LPGs of different periods at around 300μm, 330μm, 360μm and 440μm.

This therefore signifies that the wavelength shift is an increasing function of the order of the cladding mode, i.e. resonant peak at higher wavelength will give larger wavelength shifts with change in surrounding refractive index, e.g. higher RI sensitivity.

3.3.5 LPG Bio-Sensing Application

An LPG was then selected to measure the protein degradation of Fetal Bovine Serum (FBS). FBS is a part of the plasma that remains after blood coagulation. Due to its major use as a supplement in cell culture, Van der Valk et al., 2004 estimated that there are about 500,000 litres of FBS produced for the world market per year [49]. This level of production is bound to increase in the cell culture media. FBS is made up of numerous components of which some are growth factors (cytokines, fibroblast and hormones) and protein. The presence of these growth factors helps to promote cell differentiation in medical applications, for example, blood vessel differentiation using the vascular endothelial growth factor.

Due to its use, it is therefore important to be able to measure and monitor the degradation of some of the key component (proteins) that play a great part in its use for cell culture. In 1944, William Sunderman carried out work in estimating the refractive index (RI) change in FBS against different concentration of protein [50]. He concluded that as the concentration of protein increases in the serum, the RI also increases. The method proposed to measure protein degradation at room temperature, is by sensing these changes with an LPG device with the most sensitive cladding mode LP_{05} at around 1550nm. The sterile filtered FBS used was purchased from Sigma-Aldrich and has a storage temperature of -20°C.

3.3.5.1 *Experiment and results*

The FBS purchased was thawed at 4°C for 24 hours and small samples were stored in a micro-centrifuge tube for the sensing work. The LPG used was first calibrated for RI sensitivity using the refractive index oils by Cargille Laboratories. This is carried out so that an observed wavelength shift can be linked to a particular index change. The RI calibration experiment was carried out in similar way as described in section 3.3.4.1 and the result is shown in Figure 3.27:

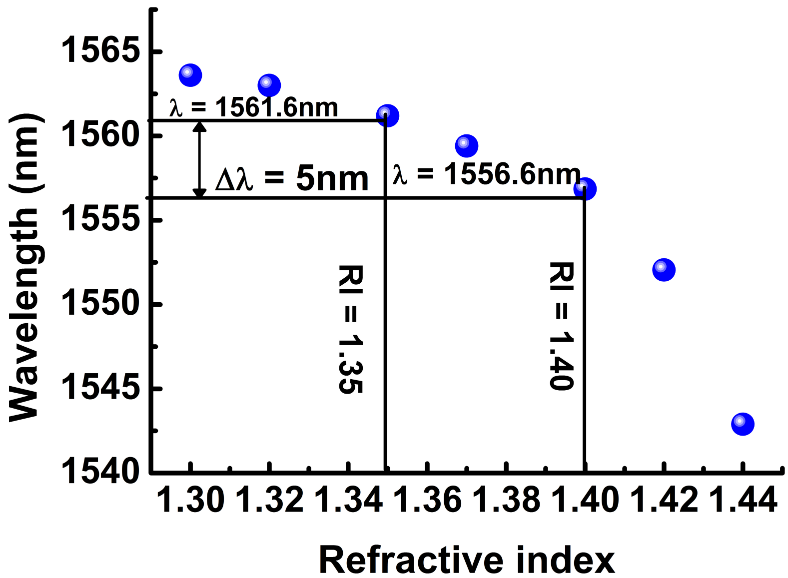

Figure 3.27: Sensing LPG calibration for RI versus Wavelength shift; showing about 5nm wavelength shift for RI change from 1.35 to 1.40 (Cargille Index Gels).

Form Figure 3.27, there is barely any shift in wavelength at the initial increase in RI from 1.30 to 1.32; significant shift in wavelength becomes apparent as the RI changed from 1.35 to 1.44 with a maximum shift observed when the RI value is 1.44. In other to carry out the bio-sensing experiment, a set up similar to Figure 3.23 was used, with the sensing LPG clamped in place. In the set up, the glass slide that is placed on the laboratory jack is adjusted accordingly to a position that the glass slide is almost touching the grating. This experiment was carried out at room temperature (24°C). A syringe was used to transfer about 0.5ml of FBS unto the LPG device and the LabView capture software was set to automatically capture the spectral shift of the sensing LPG at 20 seconds interval and the shifts monitored on an OSA set to 0.06nm resolution. The observed wavelength shift is shown in Figure 3.28:

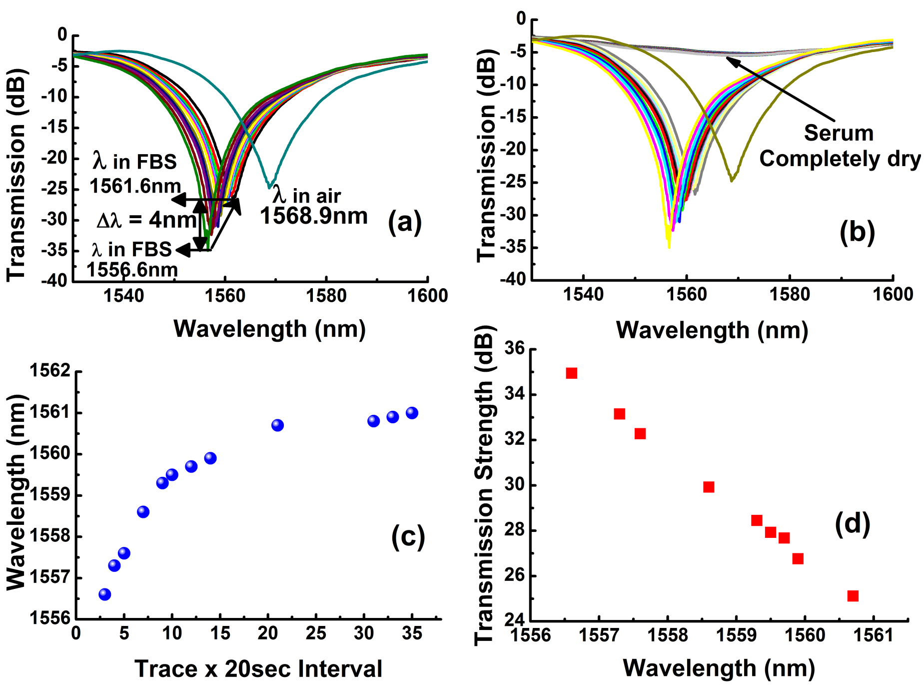

Figure 3.28: Plots of (a) LPG wavelength shift with immersion in FBS for about 240 seconds, (b) LPG wavelength shift with immersion in FBS showing what happens when the Serum sample dry out, (c) Captured trace of LPG central wavelength response per 20 seconds interval and (d) LPG transmission peak intensity at different wavelengths before the Serum sample dry out.

In air, the initial wavelength of the LPG was about 1568.9nm (Figure 3.28(a)), with transmission intensity of about 24dB. A few seconds after the LPG device was immersed in FBS, the transmission peak experienced a blue shift in wavelength (Figure 3.28(a)) to 1556.6nm (which corresponds to a RI of 1.40 from the calibration in Figure 3.27 and with increased intensity of about 34.9dB; this is due to the sudden increase in the surrounding RI. The spectral change was captured for about 15 minutes (Figure 3.28(c)) using auto-capture LabView software. It was observed that after few seconds at room temperature, the wavelength begins to show a red-shift (to about 1561.6nm corresponding to a RI of 1.35) with a gradual reduction in the transmission intensity (Figure 3.28(d)). The result shows that as the temperature of the FBS changes (from 4°C to room temperature), the RI also decreases from 1.41 to 1.35. This was supported by a research carried out by Hammett et al in 1921 [51]. The Serum sample was left longer on the LPG for over 30mins, the Serum sample gradually increased in viscosity until it completely dried out over the grating (like a coating). At this stage (Figure 3.28(b)) the transmission spectrum becomes almost flat, similar to when the external RI is at 1.46 as seen earlier in Figure 3.24(b). The change in wavelength of the LPG device immersed in FBS is due to the degradation of the component (proteins) of the FBS due to temperature and the reduction in the strength of the transmission peak reflects that as the serum is continuously exposed to room temperature, the concentration of the serum compositions degrades.

Different techniques have been used in the analyses of the composition of bio-samples (such as protein concentration in FBS); these includes: Serum protein electrophoresis (known as SPEP), used for measuring specific proteins in the blood in order to help identify some diseases like cancer, problems with kidneys, liver and immune system, refractometry and dye binding and colorimetric test using the Biuret reagent (which is made of sodium hydroxide (NaOH) and hydrated copper (II) sulphate, together with potassium sodium tartrate). All the aforementioned techniques require bulk systems and machines like: UV spectroscopes, cell counters and expensive automated analysers. This experiment has therefore provided another way of monitoring the protein degradation in a Serum sample by monitoring its RI change; which makes for a cheaper, compact, stable to calibrate and mobile test system for measuring protein concentrations.

3.4 *CHAPTER CONCLUSION*

This chapter started with the background history of fibre gratings with normal periodic structures (FBGs and LPGs) and their various applications for temperature and refractive index sensing. Their applications are a direct result of their various mode coupling mechanisms and phase matching conditions as discussed in Chapter 2, as FBGs couple light between the forward and the backward propagating core modes and LPGs couple light from the forward propagating core mode to the forward propagating cladding modes.

This Chapter has reviewed the fabrication techniques for FGB and LPG. The two-fabrication techniques used to inscribe FBG structures in a standard Corning SMF 28 fibre are the two beam holographic technique and the phase mask technique. In the two beam holographic inscription, the fibre-grating period is dependent on the interference angles of the beam from the two mirrors, which in controlled by the arm-length (the length between the mirror and the beam 50:50 beam splitter). A simulation carried out shows that as the arm length increases the grating wavelength decreases. This method has shown advantages of been able to write FBGs with different wavelengths (from ~824nm, ~1365nm, ~1551nm and ~2009nm) without the need for an expensive phase mask, but with limitations like susceptibility to mechanical vibrations and the need for a coherent laser source.

The other FBG fabrication technique employed is the phase mask technique. The set up for this technique includes: an air bearing translation stage, 3D stages, collimating cylindrical lens, fibre holders and mirrors. The phase masks used are commercially made by QPS, with periods at 1060.85nm, 1066.39nm, 1071.92nm, 1077.45nm, 1082.98nm, yielding wavelengths at 1536nm, 1552nm, 1560nm and 1568nm respectively. The phase mask diffracts the light into modes 0, ± 1, ± 2, by which the fabrication of the FBG takes place at the interference point of the ± 1 order (~40$\%$ diffraction efficiency) with 0 order suppressed to about <5$\%$.During fabrication, a LabView program sets the laser beam scanning speed and grating length at a constant laser power, usually about 100mW. All SMF 28 fibre pieces for FBG fabrication were hydrogenated at 150 bar and 80°C for 24 or 48 hours to increase the photosensitivity. All FBGs were thermally annealed at 80°C for 24-48 hours to stabilize the grating structure. The thermal annealing in general case causes a ~0.5nm blue shift to FBG Bragg resonance.

After the FBGs have been fabricated and annealed, they were characterized for temperature sensing application. The FBGs responded based on the thermal expansion that takes in the fibre at elevated temperatures and the thermal-optic coefficient of the fibre. The theoretical analysis of FBG temperature sensitivity was analysed and an expression for the wavelength shift with respect to temperature change was derived. After subject the grating area to elevated temperature of 10°C to 70°C, the temperature sensitivities for FBGs at wavelengths 800nm, 1550nm and 2000nm are 5.3pm/°C , 11.6/°C and 14.8pm/°C . The temperature sensing results also show a linear correlation between temperature change and wavelength shift for the three FBGs evaluated. To further analyse the temperature sensitivity of FBGs, their sensitivity in cryogenic environment condition was examined, as some applications such as in liquid fuel tanks and in the transport/storage of cryogens may need cryogenic temperature monitoring. The fibre was placed in an environmental chamber, with the temperature set automatically to change from -5°C to - 40°C . The overall wavelength shift experienced by the grating is about -9.5pm/°C .

However, the fabrication technique used to inscribe the LPGs is through the point-by-point exposure method. The fabrication set up includes an air bearing translation stage, two cylindrical focusing lenses, fibre holders, 3D stage and a computer controlled LabView program used to set the fabrication parameter like duty cycle, writing speed and grating length and period. The LPGs were fabricated at different periods and also at different lengths. The analysis of the spectral characteristics shows that the resonance wavelength of the same order cladding mode red shifts with increasing grating period, as the LP05 mode of LPG with the longest period 440μm occurred in the mid-IR wavelength region around 2000nm. The LPGs were then annealed at 80°C for 24hours and then characterized for temperature and refractive index sensing.

For the temperature sensing, the resonance peak LP05 from four LPGs with periods of 300μm, 330μm, 360μm and 440μm were selected and subjected to elevated temperatures 10°C-70°C. There was an increase in the wavelength shift of the LP_{05} mode for every temperature change, with the LP05 resonance peak of the 440μm period LPG showing the highest sensitive at about 100pm/°C. Then, all five modes (LP_{01}-LP_{05}) of the 440μm period LPG were evaluated for temperature responsivity. The result showed that the higher wavelength mode (LP_{05}) at 2000nm of the 440μm LPG was three times more sensitive that the mode (LP_{01}) at 1320nm wavelength, e.g. higher order cladding mode is more temperature sensitive.

The LPG was then investigated as a refractive index sensor. Similarly, the most sensitive mode LP_{05} of one of the earlier fabricated LPGs was submerged in index gels with different refractive indexes. The result shows a blue shift in the wavelength of the resonant peak, with change in intensity as index changed from 1.3 – 1.44. But as the surrounding medium index matched the cladding index, the resonant peak disappeared and re-appeared at a longer wavelength at about index 1.5. This peak shows little wavelength shift but more noticeable intensity increase when the surrounding medium index increased from 1.5 – 1.7. The selected LP_{05} modes from the four LPGs were compared, showing the LP_{05} of the 440μm LPG has higher refractive index sensitivity (375nm/RIU) than the 360μm (75nm/RIU), 330μm (49nm/RIU) and 300μm (25nm/RIU) LPGs.

Finally, the LPG was employed in a bio-sensing experiment. The change in refractive index (1.40-

1.35) of the LPG device immersed in FBS is due to the degradation of the proteins in the FBS caused by to the temperature change (from 4°C - 24°C) and the reduction in the transmission peak strength reflects that as the serum is continuously exposed to room temperature, the concentration of the serum compositions degrades.

3.5 References

[1] Y. Liu, *Advanced fibre gratings and their applications.* PhD thesis, Aston University, 2001.

[2] A. Ikhlef, R. Hedara, and M. Chikh-Bled, “Uniform Fiber Bragg Grating modeling and simulation used matrix transfer method,” *Int. J. Comput. Sci*, vol. 9, pp. 368–374, 2012.

[3] D. Z. Anderson, V. Mizrahi, T. Erdogan, and A. E. White, “Production of in-fibre gratings using a diffractive optical element,” *Electronics Letters*, vol. 29, no. 6, pp. 566–568, 1993.

[4] K. O. Hill, B. Malo, F. Bilodeau, D. C. Johnson, and J. Albert, “Bragg gratings fabricated in monomode photosensitive optical fiber by UV exposure through a phase mask,” *Applied Physics Letters*, vol. 62, no. 10, pp. 1035–1037, 1993.

[5] T. Erdogan, V. Mizrahi, P. J. Lemaire, and D. Monroe, “Decay of ultravioletinduced fiber Bragg gratings Decay of ultraviolet-induced fiber Bragg gratings,” vol. 73, no. 1, pp. 73–80, 1994.

[6] M. Douay, E. Fertein, W. X. Xie, P. Bernage, P. Niay, J. F. Bayon, and T. Georges, “Thermal hysteresis of Bragg wavelengths of intra-core fiber gratings,” *Photonics Technology Letters, IEEE*, vol. 5, no. 11, pp. 1331–1334, 1993.

[7] Z. Zhuo and B. Ham, “A temperature-insensitive strain sensor using a fiber Bragg grating,” *Optical Fiber Technology*, vol. 15, no. 5-6, pp. 442–444, 2009.

[8] P. K. C. Chan, W. Jin, K. T. Lau, L. M. Zhou, and M. S. Demokan, “Multi-point strain measurement of composite-bonded concrete materials with a RF-band FMCW multiplexed FBG sensor array,” *Sensors and Actuators, A: Physical*, vol. 87, no. 1-2, pp. 19–25, 2000.

[9] J. Jung, H. Nam, B. Lee, J. O. Byun, and N. S. Kim, “Fiber Bragg grating temperature sensor with controllable sensitivity.,” *Applied Optics*, vol. 38, no. 13, pp. 2752–2754, 1999.

[10] Z. Xiang-Kai and R. Yun-Jiang, “Simultaneous Static Strain, Temperature and Vibration Measurement Using an Integrated FBG/EFPI Sensor,” *Chinese Physics Letters*, vol. 18, no. 12, pp. 1617–1619, 2001.

[11] H. Ahmad, W. Y. C. W. Y. Chong, K. Thambiratnam, M. Zulklifi, P. Poopalan, M. Thant, and S. Harun, “High Sensitivity Fiber Bragg Grating Pressure Sensor Using Thin Metal Diaphragm,” *IEEE Sensors Journal*, vol. 9, no. 12, pp. 1654–1659, 2009.

[12] Y.-J. Rao, “In-fibre Bragg grating sensors,” *Measurement Science and Technology*, vol. 8, pp. 355–375, 1997.

[13] V. Bhatia and A. M. Vengsarkar, “Optical fiber long-period grating sensors.,” *Optics Letters*, vol. 21, no. 9, pp. 692–694, 1996.

[14] N. P. Bansal and R. H. Doremus, “Handbook of glass properties.” *Elsevier*, 1986.

[15] A. Philips, “Cryogenic Temperature Sensors,” *Lakeshore Cryogenics*, 2015.

[16] S. Gupta, T. Mizunami, T. Yamao, and T. Shimomura, “Fiber Bragg grating cryogenic temperature sensors,” *Applied Optics*, vol. 35, no. 25, pp. 5202–5205, 1996.

[17] C. Lupi, F. Felli, L. Ippoliti, M. A. Caponero, M. Ciotti, V. Nardelli, and A. Paolozzi, “Metal coating for enhancing the sensitivity of fibre Bragg grating sensors at cryogenic temperature,” *Smart materials and structures*, vol. 14, no. 6, p. N71, 2005.

[18] T. Mizunami, H. Tatehata, and H. Kawashima, "High-sensitivity cryogenic fibre-Bragg-grating temperature sensors using Teflon substrates," *Measurement Science and Technology*, vol. 12, no. 7, p. 914, 2001.

[19] S. W. James, R. P. Tatam, A. Twin, M. Morgan, and P. Noonan, "Strain response of fibre Bragg grating sensors at cryogenic temperatures," *Measurement Science and Technology*, vol. 13, no. 10, p. 1535, 2002.

[20] E. M. Dianov, A. S. Kurkov, O. I. Medvedkov, S. A. Vasiliev, D. Baykin, S. Bender, and A. Koretsky, "Erbium-Doped Fibre as a Sensitive Element of the Cryogenic Temperature Sensor," in *Lasers and Electro-Optics Europe, 1998. 1998 CLEO/Europe. Conference on*, p. 243, IEEE, 1998.

[21] B. Lee, "Review of the present status of optical fiber sensors," *Optical Fiber Technology*, vol. 9, no. 2, pp. 57–79, 2003.

[22] G. K. White, "Thermal expansion of reference materials: copper, silica and silicon," *Journal of Physics*, vol. 6, no. 17, pp. 2070–2078, 2002.

[23] A. M. Vengsarkar, P. J. Lemaire, J. Justin B., and E. Al, "Long-Period Fiber Gratings as Band-Rejection Filters," *Journal of Lightwave Technology*, vol. 14, pp. 58–65, 1996.

[24] V. Grubsky and J. Feinberg, "Long-period fiber gratings with variable coupling for real-time sensing applications.," *Optics Letters*, vol. 25, no. 4, pp. 203–205, 2000.

[25] F. Bilodeau, K. Hill, B. Malo, D. Johnson, and I. Skinner, "Efficient, narrowband LP01LP02 mode convertors fabricated in photosensitive fibre: spectral response," *Electronics Letters*, vol. 27, no. 1991, pp. 682, 1991.

[26] L. Vesselov, W. Whittington, and L. Lilge, "Design and performance of thin cylindrical diffusers created in Ge-doped multimode optical fibers.," *Applied Optics*, vol. 44, no. 14, pp. 2754–2758, 2005.

[27] X. Shu and D. Huang, "Highly sensitive chemical sensor based on the measurement of the separation of dual resonant peaks in a 100-mm-period fiber grating," *Optics Communications*, vol. 171, no. 1999, pp. 65–69, 1999.

[28] L. Zhang, W. Zhang, and I. Bennion, "In-fiber grating optic sensors," *Optical Engineering-New York-Marcel Dekker Incorporated-*, vol. 76, pp. 123–182, 2002.

[29] M. Dubov, T. D. Allsop, A. Martinez, V. Mezentsev, and I. Bennion, "Highly birefringent long period gratings fabricated with femtosecond laser," in *Optical Fiber Communication Conference*, p. OWI50, Optical Society of America, 2006.

[30] A. Sugitatsu, H. Kawano, T. Hatta, and K. Kasahara, "A novel fabrication technique of long period fiber gratings using a holographic optical element," *Optical review*, vol. 8, no. 4, pp. 267–270, 2001.

[31] B. Malo, K. Hill, F. Bilodeau, D. Johnson, and J. Albert, "Point-by-point fabrication of micro-Bragg gratings in photosensitive fibre using single excimer pulse refractive index modification techniques," *Electronics Letters*, vol. 29, pp. 1668, 1993.

[32] J. R. Pierce, "Coupling of modes of propagation," *Journal of Applied Physics*, vol. 25, no. 2, pp. 179–183, 1954.

[33] B.O. Guan, H.Y. Tam, H. L. W. Chan, C.L. Choy, and M. S. Demokan, "Growth characteristics of long-period gratings in hydrogen-loaded fibre during and after 193 nm UV inscription," *JMeasurement Science and Technology*, vol. 12, no. 2001, pp. 818–823, 2001.

[34] R. U. I. Suo, "Advanced Fibre Gratings In Normal and Infrared Glass Fibres by UV and Near Infrared Femtosecond Lasers - Doctor of Philosophy," *PhD Thesis*, Aston University, September, 2009.

[35] J. B. Judkins, J. Renee, J. David, and M. Ashish, "Temperature-insensitive long-period fiber gratings," *Optical Fiber Communication Conference*, p. PD1, Optical Society of America, 1996.

[36] A. A. Abramov, A. Hale, R. S. Windeler, and T. A. Strasser, "Temperature-sensitive long-period fiber gratings for wideband tunable filters," in *Optical Fiber Communication Conference, 1999, and the International Conference on Integrated Optics and Optical Fiber Communication. OFC/IOOC'99. Technical Digest*, vol. 3, pp. 144–146, IEEE, 1999.

[37] K. Usbeck, W. Ecke, V. Hagemann, R. Mueller, and R. Willsch, "Temperature Referenced Fibre Bragg Grating Refractometer Sensor for On-line Quality Control of Petrol Products," *Proceedings of 13th International Conference on Optical Fiber Sensors OFS-13, Kyongju, Korea, Proc. SPIE Vol.*, vol. 3746, pp. 163–166, 1999.

[38] J. Ctyroky, W. Ecke, K. Schroeder, and R. Slavik, "Separation of refractive index and temperature measurements using surface plasmon-coupled fiber grating," in *Proceedings of SPIE, the International Society for Optical Engineering*, vol. 4185, pp. 322–325, Society of Photo-Optical Instrumentation Engineers, 2000.

[39] X. Chen, K. Zhou, L. Zhang, and I. Bennion, "Optical chemsensor based on etched tilted Bragg grating structures in multimode fiber," *Photonics Technology Letters, IEEE*, vol. 17, no. 4, pp. 864–866, 2005.

[40] K. Zhou, X. F. Chen, L. Zhang, and I. Bennion, "High-sensitivity optical chemsensor based on etched D-fibre Bragg gratings," *Electronics letters*, vol. 40, no. 4, pp. 232–234, 2004.

[41] K. Zhou, X. Chen, G. Simpson, D. Zhao, L. Zhang, and I. Bennion, "Temperature-referenced high-sensitivity point-probe optical fiber chem-sensors based on cladding etched fiber Bragg gratings," in *Photonics Europe*, pp. 409–414, International Society for Optics and Photonics, 2004.

[42] X. Shu, L. Zhang, and I. Bennion, "Sensitivity characteristics of long-period fiber gratings," *Journal of Lightwave Technology*, vol. 20, no. 2, p. 255, 2002.

[43] X. Shu, T. Allsop, B. Gwandu, L. Zhang, and I. Bennion, "Room-temperature operation of widely tunable loss filter," *Electronics Letters*, vol. 37, no. 4, pp. 216–218, 2001.

[44] T. T. W. MacDougall, S. Pilevar, C. W. C. Haggans, and M. M. A. Jackson, "Generalized expression for the growth of long period gratings," *IEEE Photonics Technology Letters*, vol. 10, pp. 1449–1451, Oct. 1998.

[45] M. H. Kuhn, "Optimum Attenuation of Cladding Modes in Homogeneous Single-Mode Fibers," *AEU-INTERNATIONAL JOURNAL OF ELECTRONICS AND COMMUNICATIONS*, vol. 29, no. 5, pp. 201–204, 1975.

[46] P.R., "Specialty Optical Liquids," *Cargille Laboratories*, New Jersey, 1994.

[47] V. Bhatia, *Properties and sensing applications of long-period gratings.* PhD thesis, Virginia Tech, 1996.

[48] H. H. J. Patrick, a. A. D. Kersey, and F. Bucholtz, "Analysis of the response of long period fiber gratings to external index of refraction," *Journal of Lightwave Technology*, vol. 16, no. 9, pp. 1606–1612, 1998.

[49] J. Van Der Valk, D. Mellor, R. Brands, R. Fischer, F. Gruber, G. Gstraunthaler, L. Hellebrekers, J. Hyllner, F. H. Jonker, P. Prieto, M. Thalen, and V. Baumans, “The humane collection of fetal bovine serum and possibilities for serum-free cell and tissue culture,” in *Toxicology in Vitro*, vol. 18, pp. 1–12, 2004.

[50] F. W. Sunderman, “A rapid method for estimating serum proteins formula for calculating serum protein concentration from the refractive index of serum,” *Journal of Biological Chemistry*, vol. 153, no. 1, pp. 139–142, 1944.

[51] F. S. Hammett and I. Teller, “Changes In The Refractive Index of the Blood Serum of the Albino Rat with Temperature.,” *The Journal of Biological Chemistry*, vol. 50, p. 47, 1922.

4 FIBRE GRATINGS WITH TILTED STRUCTURES AT SMALL AND LARGE ANGLE

4.1 *INTRODUCTION*

Traditionally, bulk devices were used in optical signal processing, sensing and laser systems to provide polarization function, but recently due to the benefits of low insertion loss, light weight and high coupling efficiency, in-fibre polarizers have become an area of interest and been made available. Some in-fibre devices based on the 45° tilted fibre grating (45°-TFG) technology have been reported and employed as polarization equalizer and spectrometer [1–3]. In 2005, Zhou et al carried out the theoretical simulation on TFGs of various tilted angles [4], and realized that the highest polarization dependent loss (PDL) may be achievable with a TFG when the tilted angle is at 45°. Also in 2006, Zhou et al explored TFGs with angles larger than 45°, showing light coupling out of the forward propagating core mode and into cladding modes and radiation modes.

In this Chapter, the research work in designing, fabricating and characterizing TFGs with small (<45°) and large (>45°) tilted structures will be discussed, leaving the TFGs with tilted structure exactly at 45° to Chapter 5. Also, the temperature and refractive index sensing capability of the small and large angle tilted TFGs will be discussed. Due to the unique polarization property (two distinct set of polarization dependent modes) of large angle TFGs, it was employed in an all fibre twist sensor. Finally, an interferometer sensor using two large angle TFGs for bio-sensing applications will be discussed.

4.2 *TFG CLASSIFICATION AND FABRICATION METHODS*

4.2.1 Classification Of Mode Coupling Range Of TFGs

The TFG structure due to its phase matching condition is able to couple light from the fibre core into diverse directions as mentioned in section 2.3.3. The phase matching condition that gives the strongest out-coupled wavelength can be expressed as [5][6]:

$$\lambda_{co,cl} = (n_{co} \pm n_{cl,m}).\frac{\Lambda_g}{\cos\theta} \tag{4.1}$$

where n_{co} and $n_{cl,m}$ are the effective indices of the core and mth cladding mode respectively, "+" and "-" show the cases when the mode propagation is in the -z or +z direction respectively. By specifying the right parameters during TFG fabrication, the direction of radiation and the wave-vector of the main beam can be identified by equation 4.2:

$$\overrightarrow{K_R} = \frac{K_G}{2\cos(\delta)}(\theta = \pi - 2\delta) \tag{4.2}$$

where θ and δ are the radiation angle and the tilt angle of the grating structure. According to the total internal reflection (TIR) effect, the TFGs can be classified into three different mode coupling regimes depending on tilted angle (Figure 4.1). Due to total internal reflection, the light that encounters the cladding boundary (i.e. when the tilted angle is very small or very large) stays confined in the cladding modes. But at some specific tilted angle range, the incident angle of the cladding mode coupling is smaller than the critical angle θ_c or larger than 180-θ_c, the light will no longer stay in the cladding modes, but coupled out to radiation modes, i.e. tapped out of the fibre. The coupling regimes for air/fibre-glass interface are classified as below:

(1) θ < 23.1°- backward cladding mode coupling (-z direction);

(2) 23.1°< θ < 66.9°- radiation mode coupling;

(3) θ > 66.9°- forward cladding mode coupling (+z direction);

Figure 4.1: Diagram showing the three mode coupling regimes for a TFG: (a) Phase matching condition for when $\theta < \theta_{1c}$ showing a backward cladding mode coupling, (b) Phase matching condition for when $\theta_{1c} < \theta < \theta_{2c}$ showing a radiation mode coupling and (c) Phase matching condition for when $\theta > \theta_{2c}$ showing a forward cladding mode coupling.

Therefore, the radiation mode out-coupling of $\theta_{1c} < \theta < \theta_{2c}$ occurs when $|\varphi| < \alpha_c$, where φ is the incident angle of the radiation beam; θ_{1c} and θ_{2c} can then be calculated as:

$$\theta_{1c} = \frac{1}{2}\left(\frac{\pi}{2} - \alpha_c\right), \theta_{2c} = \frac{1}{2}\left(\frac{\pi}{2} + \alpha_c\right) \tag{4.3}$$

Thus, TFGs with tilted angle in the range of 23.1° to 66.9° (air as surrounding medium) ($\theta_{1c} < \theta < \theta_{2c}$) will have their radiation modes coupled out of the fibre cladding; and a radiation range of 11.5°- 78.5° when the surrounding medium is water. For a standard Corning SMF-28 fibre placed in air, θ_{1c} = 23.1° and θ_{2c} = 66.9°. But the critical angle (α_c) when placed in another medium can be expressed as:

$$\alpha_c = \sin^{-1}\left(\frac{n_1}{n_2}\right) \tag{4.4}$$

where n_1 is the refractive indices of the surrounding medium and n_2 is the refractive index of the cladding.

When n_1~1 (fibre placed in vacuum or air), the critical angle (α_c) is calculated as 43.8° using equation 4.4, with n_2~1.45 (cladding). Similarly, when the surrounding medium is changed from air to water (n_1 ~1.33), the critical angle (α_c) becomes 66.8°.

4.2.2 TFG Phase Matching Condition and Radiation Profile

There are two main phenomena that happen when a light source of different wavelengths (broadband light source) is lunched into the core of a fibre with TFG structure: the light is first diffracted out from the fibre core by the TFG and then propagates to the cladding until it gets to the boundary of the fibre cladding. Below is the phase matching conditions for a TFG with tilted angle θ <45°and θ >45°

Figure 4.2: Phase matching condition for tilted angles (a) when θ <45°and (b) for when θ >45°[7].

Where K_R ,K_C ,K_G, and are the wave vectors of the radiated light, the core mode and the grating; ξ, φ and θ are the radiation angle of the TFG, the incident angle of the radiation beam at the cladding boundary and the tilted angle respectively; K'_R , K'_C and ξ' are the non-phase matching condition wave vector for the radiated light, core mode and radiation angle respectively. The amplitude difference between K'_R and K'_C can be ignored due to the negligible differences between the refractive indices of the cladding and the core. Figure 4.2 shows that the optical path of the coupled light is dependent on the tilt angle of the grating. For instance: when θ <45°, the radiation angle is obtuse and the core mode is coupled to the backward propagation direction; the radiation angle ξ is acute when θ >45°and core mode coupling to the forward propagating direction. It can be concluded that K_R and K_G are related as:

$$K_R = \frac{K_G}{2\cos\theta}(\xi = 2\theta) \tag{4.5}$$

where ξ and θ are the radiation angle and the tilted angle respectively. For radiated light of other wavelengths, K_R is weakly coupled at ξ direction, with a minimal mismatch among the wave vectors $K_R^{'}$, K_C and K_G . Also from Figure 4.2, we can deduce the relationship between ξ, θ and K_G:

$$\tan \xi = \tan \theta - \frac{K_R^{'}}{K_G \sin \theta} \tag{4.6}$$

Where $K_R^{'}$ = K_C = nK_0, and n represents the refractive index of the fibre.

K_G = $\frac{2\pi}{\Lambda_G}$ and K_0 = $\frac{2\pi}{\lambda}$, using these two makes Equation 4.6 become:

$$\tan \xi = \frac{\lambda \sin \theta}{\lambda \cos \theta - n\Lambda_G} \tag{4.7}$$

Equation 4.7 shows the relationship between the radiation angle ξ and the tilted angle θ for a particular wavelength λ. The relationship above also means that TFGs will couple light out of the fibre core in different directions depending on the wavelength of the incident light. If the amplitude difference between $K_R^{'}$ and $K_C^{'}$ due to the negligible differences between the refractive indices of the cladding and the core is ignored, the radiation angle (ξ) of the phase-matched beam can be derived as ξ = 2θ and incident angle φ is related to the tilted angle (θ) as φ = $\frac{\pi}{2}$ - 2θ.

When the phase matching condition is satisfied, the strongest light is coupled out:

$$K_G \cos \theta = K_R \cos 2\theta + K_C \tag{4.8}$$

Substituting the following parameters:

K_G = $\frac{2\pi}{\Lambda_G}$, Λ_G = $\frac{\Lambda_{ext} \cos \theta}{\cos (\theta_{ext})}$, Λ_{ext} = $\frac{1}{2}$ Λ_{PM} and K_0 = $\frac{2\pi}{\lambda}$

into equation 4.8 we can then derive the wavelength of the radiated profile in equation 4.9:

$$\lambda_R = \frac{n \, \Lambda_{PM} \cos^2 \theta}{\cos (\theta_{ext})} \tag{4.9}$$

The relationship shown in equation 4.9 can help to develop a TFG into a spectrometer, designed to cover a particular wavelength range based on its radiation profile. The application of TFG based spectrometer will be discussed later in Chapter 6 and also the use of a 45°-TFG as a power-tapping device will be discussed in Chapter 5.

4.2.3 Relationship between the Internal and External Angles and the Period Of a Tilted Fibre Grating Structure

The optical fibres used in making TFGs are cylindrical in geometry, and due to this geometry, the fibre's internal grating tilt angle θ_{int} is different from the external tilt angle θ_{ext} (the angle between the mask and the fibre) on the phase mask in the fabrication using a phase mask, or different from the fibre rotated angle in a holographic fabrication set up. Using the phase mask technique, the fibre's internal grating tilt (θ_{int}) and the external phase mask tilt (θ_{ext}) are related as follows[3]:

$$\theta_{int} = \frac{\pi}{2} - \tan^{-1}\left[\frac{1}{n\tan(\theta_{ext})}\right] \tag{4.10}$$

where, n = 1.45 and it is the refractive index of the fibre at UV wavelength.

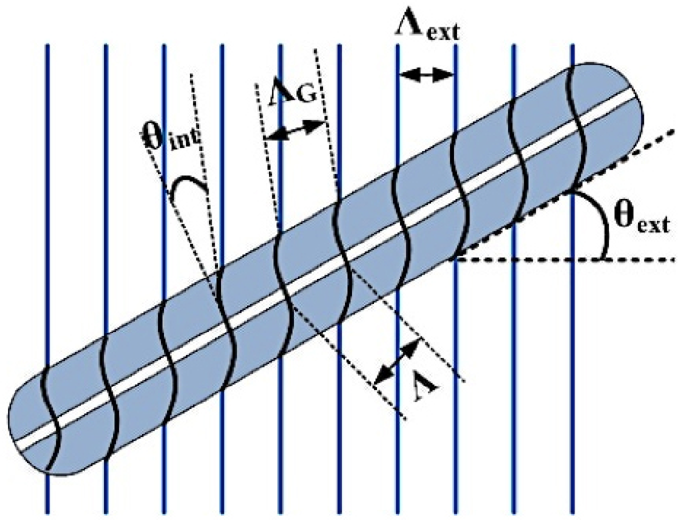

Figure 4.3: Diagram of a TFG showing the difference between the internal tilt (θ_{int}) and external tilt angles (θ_{ext}) [3].

Where by relating the diagram in Figure 4.3 to Equation 4.1, we have

$$\Lambda = \frac{\Lambda_G}{\cos(\theta_{int})} = \Lambda = \frac{\Lambda_{ext}}{\cos(\theta_{ext})} \tag{4.11}$$

The TFG internal grating period Λ_G is therefore related to the UV interference fringe period Λ_{ext} by:

$$\Lambda_G = \frac{\Lambda_{ext}\cos(\theta_{int})}{\cos(\theta_{ext})} \tag{4.12}$$

The period of the UV interference fringe Λ_{ext} can be expressed as Λ_{ext}=$\frac{\Lambda_{PM}}{2}$, where Λ_{PM} is the period of the Phase mask.

4.3 *FABRICATION METHOD*

There are three ways in which tilted structures can be fabricated in a fibre: by tilting the phase mask with respect to the optical fibre (Figure 4.4(a)); by using a phase mask with tilted pitches (Figure 4.4(b)) and by rotating the fibre about the axis normal to the plane (Figure 4.4(c)) defined by the two interfering UV beams from the two-beam holographic system (Figure 3.1)[8].

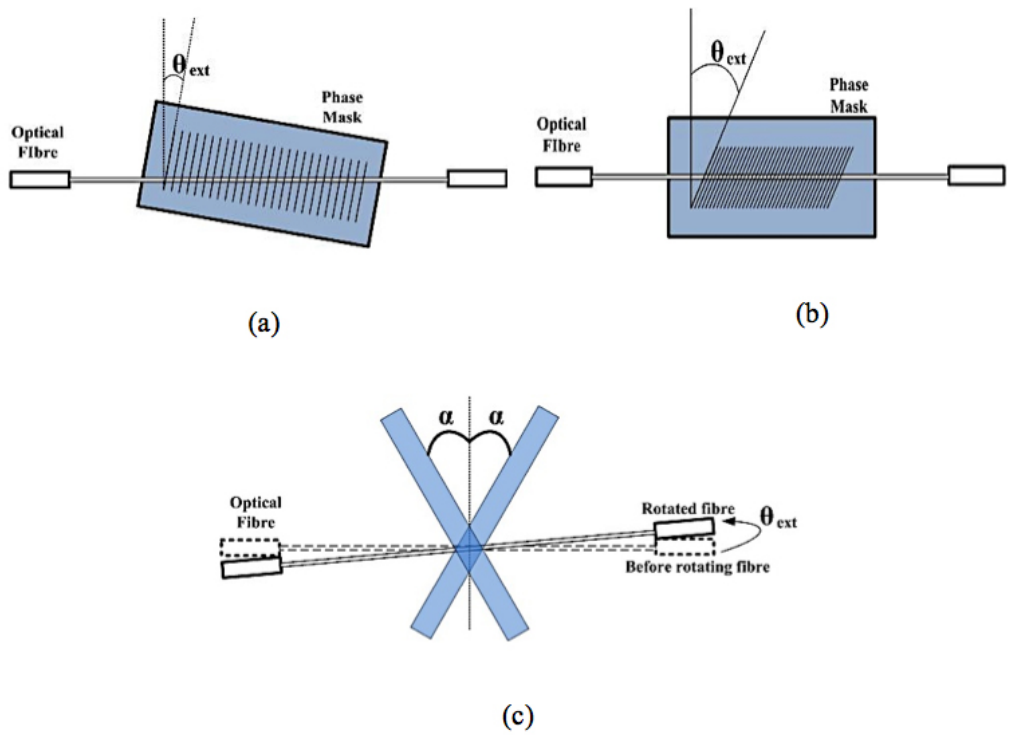

Figure 4.4: (a) Phase mask tilted with respect to the optical fibre, (b) phase mask with tilted pitches and (c) rotating the fibre about the axis normal to the plane defined by the two interfering UV beams from the two-beam holographic system.

As discussed earlier in Chapter 2, the phase mask fabrication technique makes it certain that high quality fibre gratings can be fabricated. So, the small angle TFGs and the large angle TFGs used in this research work were fabricated by tilting a normal phase mask with respect to the optical fibre. More detailed information about this technique will be discussed in the next section. The phase mask scanning set up used in our laboratory is shown below:

Aston University

Illustration removed for copyright restrictions

Figure 4.5: The laboratory set up used to fabricate small and large angle TFGs. The grating growth can be monitored in-situ by connecting to a BBS and an OSA. The phase mask is mounted on a goniometer, which facilitates the rotation of the mask for lunching the light into the fibre, the fibre holder which holds the fibre in place, the tilt stage enables the tilting of the phase mask, the OSA for interrogating the grating during fabrication and a LabView programme for capturing the data from the OSA.

The standard SMF-28 used is hydrogen loaded at 150 bars for 48 hours pre-fabrication; this is to increase the UV-photosensitivity of the fibre during exposure and also to increase the inscription efficiency. All fabricated fibre was then annealed post-fabrication in order to remove unreacted hydrogen thereby increasing the stability of the grating for sensing applications.

4.4 *FABRICATION AND SPECTRAL CHARACTERISATION OF SMALL ANGLE TFGS*

In this section, the comparative study of the characteristics of the cladding mode out-coupling of small angle TFGs is discussed. Six 12mm long small angled TFGs with internal tilted angles of 0°, 2°, 4°, 6°, 8° and 10° were UV inscribed in hydrogen loaded (at 80°C, 150 bars pressure for 48 hours) standard SMF-28 fibre, using the phase mask fabrication technique (figure 4.5). The phase mask has a pitch of 1083nm and dimensions of 30mm by 13mm respectively. Figure 4.6 shows the transmission loss profiles of the fabricated small angle TFGs.

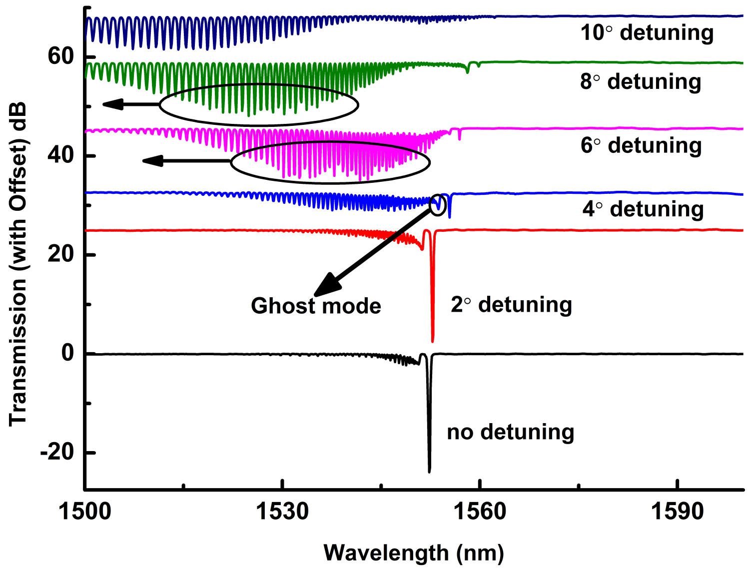

Figure 4.6: Transmission-loss spectra of TFGs with small tilted angles varying tilted angles from 0° to 10° (2° increment) fabricated on standard SMF-28 fibre, measured when the TFG fibres were exposed in air.

It can be seen from Figure 4.6 that the tilt angle strongly affects the transmission-loss profile of small angle TFG. When the tilt angle increases from 0° to 10° (2° increment), the Bragg peak (the single peak on the long wavelength side) shows a red shift (shift to a longer wavelength), while its strength decreases until it finally disappears at 10° when the light is completely coupled into the cladding modes. The reduced cladding mode resonance feature observed at 10° is due to the total internal reflection (TIR) as explained by Figure 4.1. Figure 4.6 also shows when the tilt angle increases, the whole coupled cladding modes spectrum blue-shift (shift to a shorter wavelength), with increasing dynamic range and strength (except at 10°). It is clear that when the tilted angle increases, the coupling to cladding modes becomes strong, especially for tilted angle more than 6°, whereas the red shift Bragg resonance strength decreases and eventually disappears as the tilt angle reaches 10°. Figure 4.7(a) shows the plotted relationship between the tilted angle and the central wavelength of transmission loss profile of cladding modes, and Figure 4.7(b) shows the relationship between the tilted angle and Bragg wavelength.

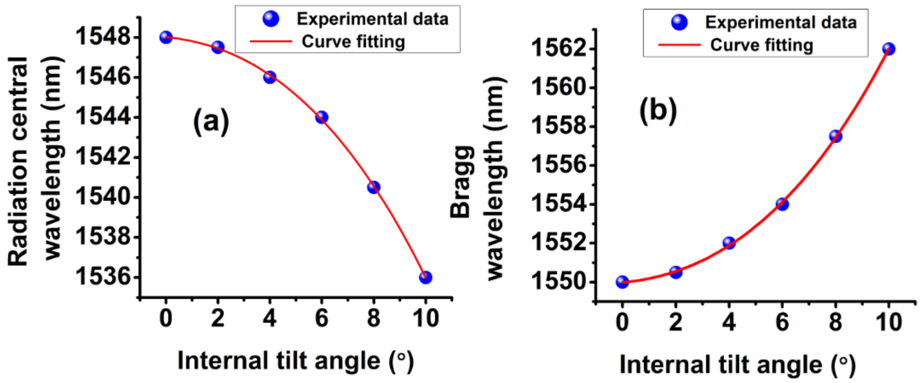

Figure 4.7: (a) Plot showing the relationship between cladding modes profile central wavelength Vs the internal tilt angle and (b) the relationship between the Bragg wavelength Vs the internal tilt angle.

By substituting Equation 4.11 into $\lambda_B = 2n\Lambda$ (where λ_B is the Bragg wavelength), the relationship between the Bragg wavelength of the TFG and the tilted angle is given by:

$$\lambda_B = \frac{n\Lambda_g}{\cos\theta_{int}} \tag{4.13}$$

The relationship shown in Figure 4.7(b) is non-linear and shows that as the internal tilt angle increases, the Bragg wavelength increases, which agree with Equation 4.13.

On the left hand side of the main Bragg feature in Figure 4.6, a well defined small loss peak called a 'Ghost Peak' is found [9]. This is a result of the conversion of the core mode of the fibre to a group of low order cladding modes; it often has a distinguished coupling strength and spectral position in comparison to the other cladding modes. Some applications have made use of ghost peaks for sensing; fibre optic laser-ultrasound [10], macro-bending sensor [11], TFG accelerometer [12] and directional bend sensor [13].

It was noticed during the fabrication process that high strength of cladding mode coupling requires longer exposure at a certain laser power. This could be due to the reduction in the UV beam interference area as more tilt is applied to the phase mask.

In order to remove the resonant features caused by the cladding-mode coupling effect in the transmission spectrum, the grating was immersed in index-matching gel which mimics an infinite cladding layer, then resulting in a more smooth radiation profile as seen in Figure 4.8. When the grating tilt angle increases, the light is continuously coupled to the backward-propagating cladding modes by the TFG and not to the backward-propagating core mode; hence the reduction in the strength of the Bragg reflection and the Bragg peak eventually completely disappeared (see TFG with titled angle at 10° in Figure 4.6).

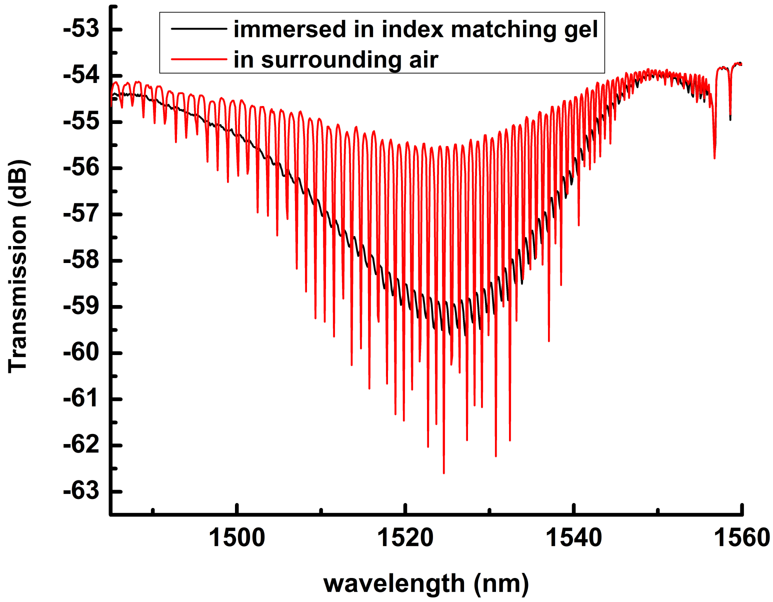

Figure 4.8: The spectral profile of a 4°-TFG with a resonance feature when the grating is surrounded by air and the smooth spectral profile when the grating is immersed in an index matching gel.

4.4.1 Polarisation Characteristics Of Small Angle Tilted Fibre Gratings

Further analysis was carried out on the transmission loss profiles of the fabricated small angle TFGs to investigate the response to different polarisation states. The set up used is shown in Figure 4.9. The broadband source from Agilent HP 83437A was used to launch light into a 1550nm polariser and the polarisation controller (PC), connected by pigtails. The PC is used to change the two orthogonal polarisation states (S-polarisation state or P-polarisation state) of the light incident on the TFG. The optical spectrum analyser (OSA) is then used to capture the TFG spectral change.

Figure 4.9: The set up for characterising the polarisation responses of small angle TFGs, with a BBS, a polariser, polarisation controller, the 8°-TFG, the OSA and a LabView capture programme.

An 8°-TFG was selected for the investigation; its whole resonance feature was divided into four wavelength sections of 9nm (i.e. 1500nmm – 1509nm, 1511nm – 1520nm, 1522nm – 1531nm and 15533nm – 1542nm), as shown in Figure 4.10 (a-d). When the position of the polarisation controller was changed, the light launched to the 8°-TFG may change the status of polarization, and two sets of orthogonal polarised mode profiles were obtained. As seen in Figure 4.10(a), the wavelength separation between the two sets of polarisation (P1 and P2) modes is the largest in this short wavelength section compared to the other three sections in Figure 4.10(b-d), with separations of ~0.21nm, 0.14nm, 0.7nm and 0.3nm respectively. The wavelength separation reduces as we go towards the higher wavelength section. However, the transmission losses of both P1 and P2 polarisations are small, with an average of 5dB in this shortest wavelength range (Figure 4.10(a)), but increases to an average of 9dB and 10dB respectively for the mid-wavelength sections (Figure 4.10(b-c)) and reduces (Figure 4.10(d)) as the wavelength gets close to the Bragg peak.

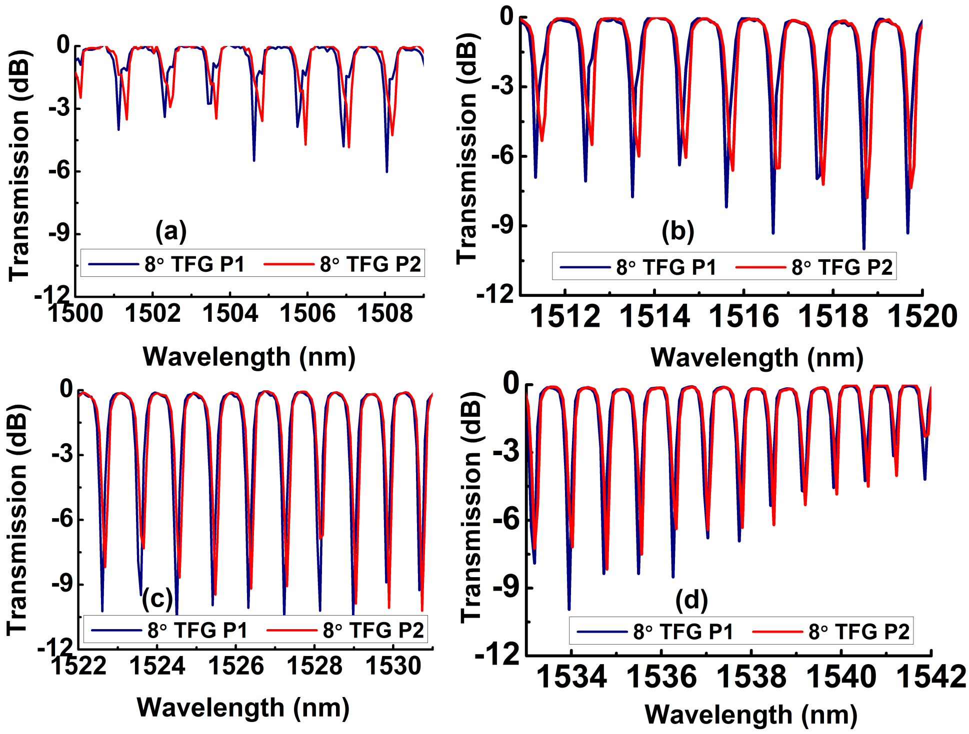

Figure 4.10: The transmission spectra of an 8°-TFG, showing the two sets of cladding modes of orthogonal polarisation states (P1 and P2) in four different wavelength ranges: (a)1500nm – 1509nm, (b)1511nm – 1520nm,(c)1522nm – 1531nm and (d)1533 – 1542nm.

Figure 4.10(a-d) shows that as the polarisation controller is changed, the propagating light is been switched between the P1 and P2 polarisation states, with one of the resonances growing to its full length while the other almost disappears. The number of resonance peaks in each 9nm wavelength range division also varies, as the wavelength increases, 8 resonances in the 1500nm – 1509nm range, 9 resonances in the 1511nm – 1520nm range, 10 resonances in the 1522nm – 1531nm range and 13 resonances in the 1533nm – 1542nm range.

Another two small angle TFGs (4°-TFG and 10°-TFG) were selected and the effect of polarisation changes on them were monitored and compared. However, it can be deduced that there is no noticeable polarisation dependency of the 4°-TFG (Figure 4.11(a) and (c)) but a much more noticeable polarisation dependency seen in the response of the 10°-TFG as shown in Figure 4.11(b) and (d).

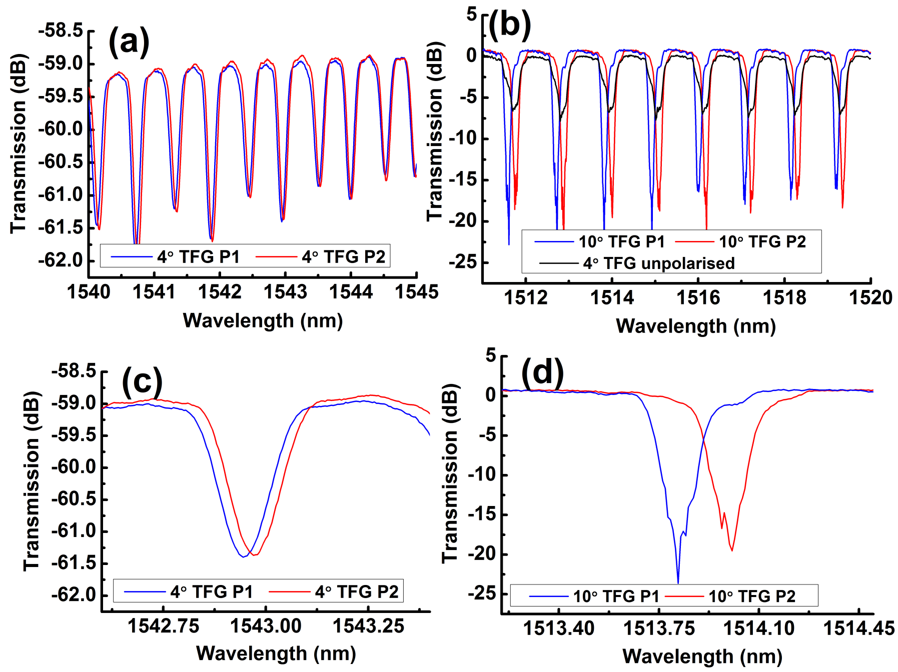

Figure 4.11: The transmission spectra of (a) a 4°-TFG and (b) a 10°-TFG with two orthogonal polarisation states; zoomed transmission spectra of (c) a 4°-TFG and (d) a 10°-TFG with two orthogonal polarisation (P1 in blue and P2 in red).

It can be observed that when the PC was adjusted for tilt angle 4°-TFG and 10°-TFG, their wavelength separation of the P1 and P2 polarisation states are 0.05nm and 0.15nm respectively (Figure 4.11(c) and (d)), the latter is 3 times more than the former. It can then be concluded that the larger the tilt angle is, the birefringence induced cladding mode splitting is more pronounced. For the 10°-TFG in Figure 4.11(b), when the light incident on the TFG is un-polarised, the transmission profile shows broad peaks (black line) of ~0.5dB strength and ~0.5nm width, but when the light incident passed through the 1550nm polarizer, the transmission loss strength increases for each polarisation states to ~20dB and peak width narrowed to ~0.23nm, compared to the transmission resonance of the un-polarised incident light.

4.4.2 Small Angle TFG Thermal Response

The thermal responses of the fabricated small angles (0°, 4°, 8°and 10°) tilted gratings were investigated by subjecting the TFGs to increasing thermal conditions from 10°C to 90°C with an increment of 10°C. The cladding modes of P1 and P2 polarised states were measured for each temperature. In Figure 4.12(a), the thermal sensitivity of a normal FBG with 0° tilt showed a sensitivity of ~10.9pm/°C. P1 and P2 polarisation cladding mode peaks at 1500.01nm and 1535nm of 4°-TFG, 8°-TFG and 10°-TFG were subjected to thermal response measurement and showed thermal sensitivities of 9.12pm/°C and 10.20pm/°C (Figure 4.12(b)), 9.81pm/°C and 10.81pm/°C (Figure 4.12(c)) and 9.88pm/°C and 10.97pm/°C (Figure 4.12(d)) for the two wavelengths peaks, respectively

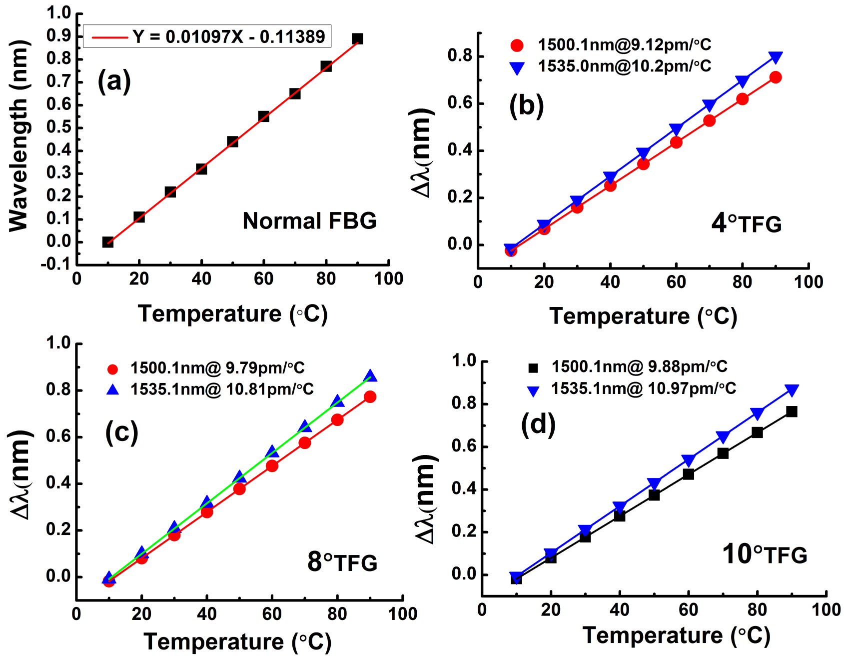

Figure 4.12: (a) The thermal response of a normal FBG (0°-TFG) at 1550nm; The thermal response of P1 polarisation state peaks at wavelengths 1500.1nm and 1535nm for (b) 4°-TFG, (c) 8°-TFG and (d) 10°-TFG.

The thermal sensitivity trend of the selected P1 polarisation modes seen in Figure 4.12(b)-(d) is summarised in table 4.1 below:

Peak 1 (P1 polarisation state)	Peak 2 (P1 polarisation state)	
4°-TFG	1500.1nm	1535.0nm
	Thermal Sensitivity	Thermal Sensitivity
	9.12pm/°C	10.20pm/°C
8°-TFG	1500.1nm	1535.1nm
	Thermal Sensitivity	Thermal Sensitivity
	9.79pm/°C	10.81pm/°C
10°-TFG	1500.1nm	1535.1nm
	Thermal Sensitivity	Thermal Sensitivity
	9.88pm/°C	10.97pm/°C

Table 4.1: The table showing the thermal sensitivity result comparison for the 4°-TFG, 8°-TFG and 10°-TFG:

It can be seen from Figure 4.12 and Table 4.1 that the thermal sensitivities of small angle TFGs are slightly lower than the thermal sensitivity of a normal FBG. Also, comparing peak 1 at 1500nm and peak 2 at about 1535.1nm shows that the thermal sensitivity of small angle TFG is also wavelength dependent, with a thermal sensitivity difference (P2 – P1) of 1.08pm/°C, 1.02pm/°C and 1.09pm/°C for the 4°-TFG, 8°-TFG and 10°-TFG respectively.

4.5 *FABRICATION AND CHARACTERISATION OF LARGE ANGLE TFGS*

4.5.1 Fabrication and Set Up

The large angle TFGs were UV-inscribed in hydrogenated standard SMF-28 fibre by the scanning amplitude mask technique using the same frequency doubled CW Ar^+ Sabre Fred laser. The amplitude mask used has a normal period of 6.6μm purchased from Edmund Optics Ltd. In order to achieve the internal tilt angles of ~76° and ~83°, the amplitude mask was tilted at approximately 69.5° and 79.2° respectively with respect to the fibre axis using the set up shown in Figure 4.5 and equation 4.10. In this fabrication, there was a limitation to the overall grating length to 12mm due to the length of the amplitude mask used. There was less index fringes created in the fibre core due to the large pitch size of the mask, yielding weaker grating. Hence, multiple scanning is employed during the fabrication process to increase the strength of the grating. The simulated relationship between the internal and the external tilt angle using equation 4.10 is shown in Figure 4.13(a) and the diffraction pattern displayed on the screen during fabrication is shown in Figure 4.13(b), clearly indicating the mask is at a tilted angle. The screen is usually placed after the fibre to ensure that the fibre axis is accurately aligned with the mask, the UV beam and to confirm the tilt angle. The simulation result from Figure 4.13(a) shows that the internal tilt angle increases as the external tilt angle increases with a slightly non-linear feature.

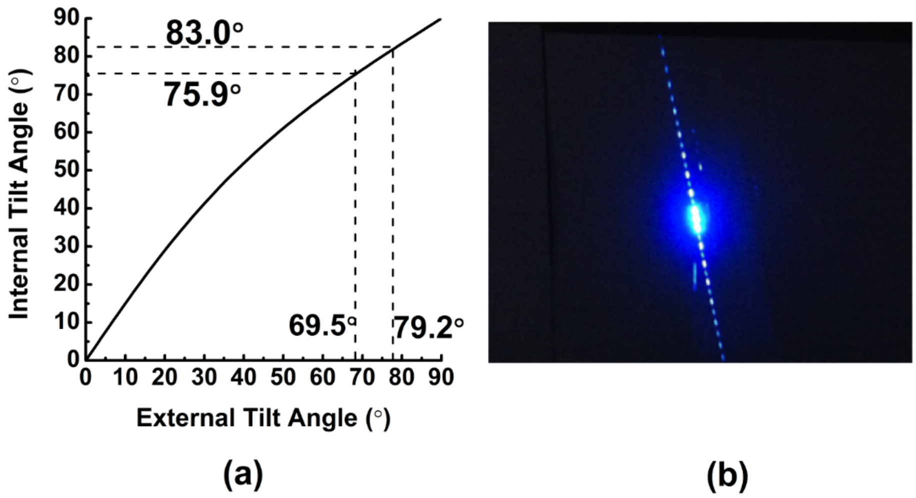

Figure 4.13: (a) Simulation showing the internal tilt angle (θ_{int}) Vs the external tilt angle (θ_{ext}) for TFGs fabricated by the phase mask technique using equation 4.10, (b) The diffraction pattern after the tilted amplitude mask captured on a screen during the fabrication.

The two inscribed large angle TFGs were then inspected under a high magnifying microscope with a 40x objective lens and the images are shown in Figure 4.14(a) and (b).

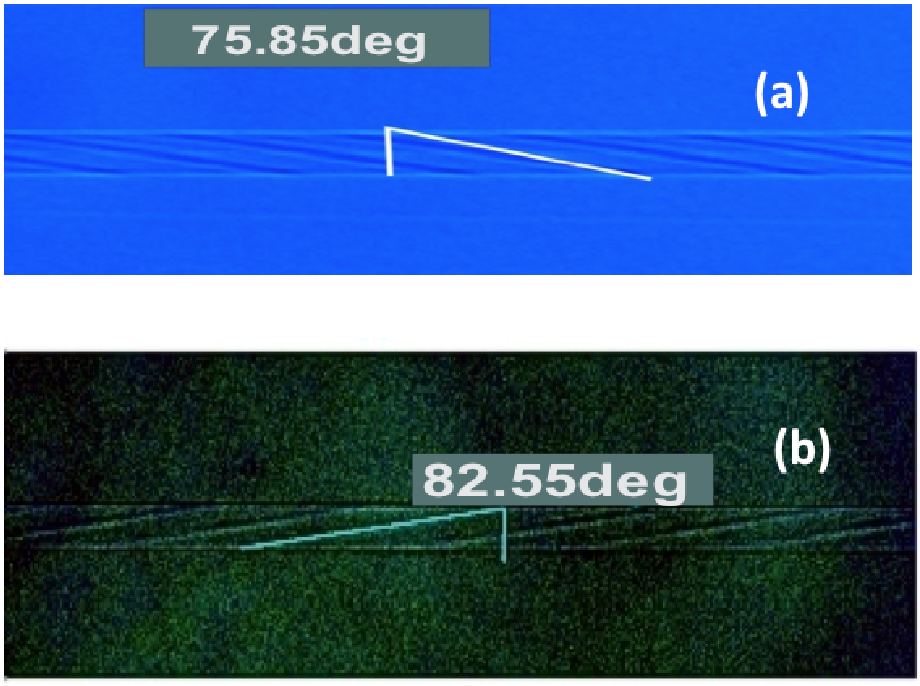

Figure 4.14: Magnified microscopic images of the fringe of the TFGs with internal angles (a) 75.85° i.e. the θ_{ext} is ~69.5° and (b) 82.55° i.e. the θ_{ext} is ~79.2°, captured with a 40x objective lens.

From Figure 4.14(a) and (b), we can see that the tilt angles of the fringes of the captured microscopic images are at 75.85° and 82.55°, which agree well with the target designed tilt angles of 76° and

83° respectively.

Figure 4.15(a) and (b) show clearly a series of dual-peak resonance for the 76°-TFG and 83°-TFG, which corresponds to two sets of cladding modes with orthogonal polarisation states when randomly polarised light was lunched into the fibre. The strength of these dual peaks is about 3dB, as for random polarized light the coupled light will be more evenly (50:50) split to the two sets of modes. Figure 4.15 (c) and (d) shows series of orthogonal polarised dual peaks labelled P1 and P2, when single polarization light was launched into the fibre. Figure 4.15 (e) and (f) shows zoomed spectra of the two TFGs for one paired polarisation loss peaks. As can be clearly seen from Figure 4.15 (c-f), when the single polarization light launched to the large angle TFG, one set of the dual peaks grows to its maximum while the other set almost vanished.

Apart from the dual-peak feature, the mode coupling mechanism is the same for large angle TFGs and LPG, their transmission spectra are distinctively different, as the large angle TFGs have a much denser mode spacing, i.e. the transmission peaks are much closer, and polarization mode splitting of all transmission peaks have dual-peak feature due to birefringence induced by excessively tilted structure.

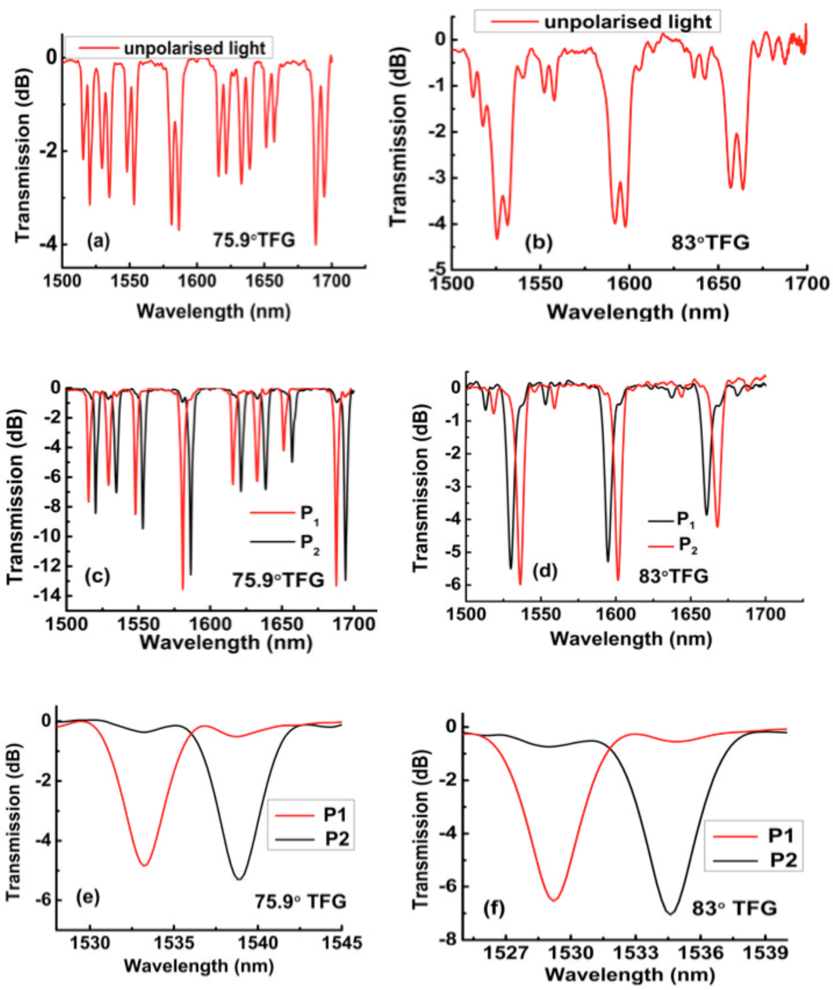

Figure 4.15: Transmission spectra of (a) 75.9°-TFG and (b) 83°-TFG across a wavelength range of 1500nm – 1700nm probed with un-polarised light, showing distinctive dual-peak feature. Transmission spectra of (c) 75.9°-TFG and (d) 83°-TFG across a wavelength range of 1500nm – 1700nm probed with polarised lights (P1 and P2). Zoomed transmission spectra of (e) 75.9°-TFG at ~1535nm and (f) 83°-TFG at ~1532nm.

The transmission loss dual peaks as seen in Figure 4.15 (e) and (f) are broader (~3nm width for the 75.9°-TFG and ~5nm width for the 83°-TFG) than that of the small angled TFG and the wavelength separations for the polarised peaks (P1 and P2) are of ~5nm for the 75.9°-TFG and ~6nm for the 83°-TFG, showing an increased birefringence for the 83°-TFG.

Similar to the analysis of the small angle TFGs (Figure 4.8), the 83°-TFG was immersed in an index matching gel; the spectrum profile almost disappeared, as shown by the black curve in Figure 4.16. This is due to the index gel inducing an infinite cladding size on the 83°-TFG, thus all cladding modes evolving into radiation modes and the light is coupled out of the fibre.

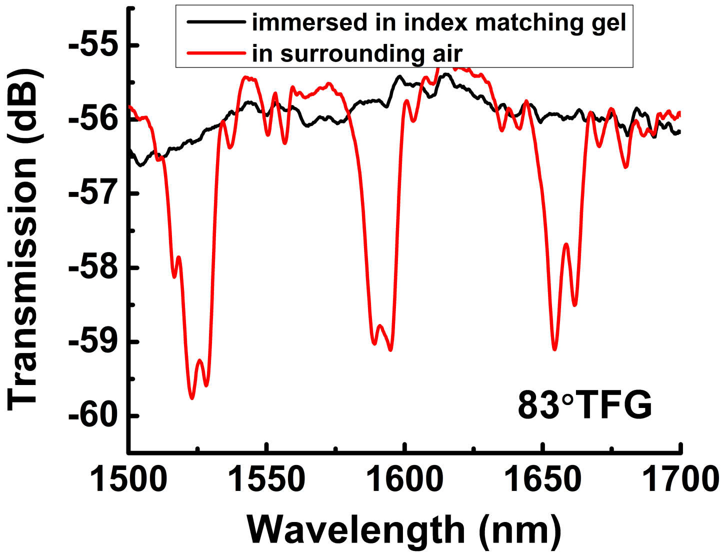

Figure 4.16: Transmission resonances with dual-peaks for an 83°-TFG in air (red line) and immersed in index matching gel (black line) across a wavelength range of 1500nm – 1700nm.

4.5.2 Large Angle TFG Thermal Response

The thermal responses of the two fabricated large angle TFGs were also characterised. Since all transmission resonances have dual-peak feature when probed with un-polarized light, only two P1 peaks, one at shorter and one at longer wavelength sides, were selected for the thermal response measurement. For the 75.9°-TFG, selected two P1 peaks at 1526.1nm and 1638.2 nm and for the 83°-TFG, selected two P1 peaks at 1524.2nm and 1690.1nm were chosen. The two TFGs were subjected to temperature measurement while the temperature was rising gradually in the range of 10°C to 90°C with an increment of 5°C and the thermal sensitivities of the two P1 peaks were measured and evaluated as presented in Figure 4.17 (a) and (b). The thermal sensitivities of the 75.9°-TFG and the 83°-TFG were measured as the transmitted resonance bands shifted from the shorter to the longer wavelengths, and results are presented in table 4.2.

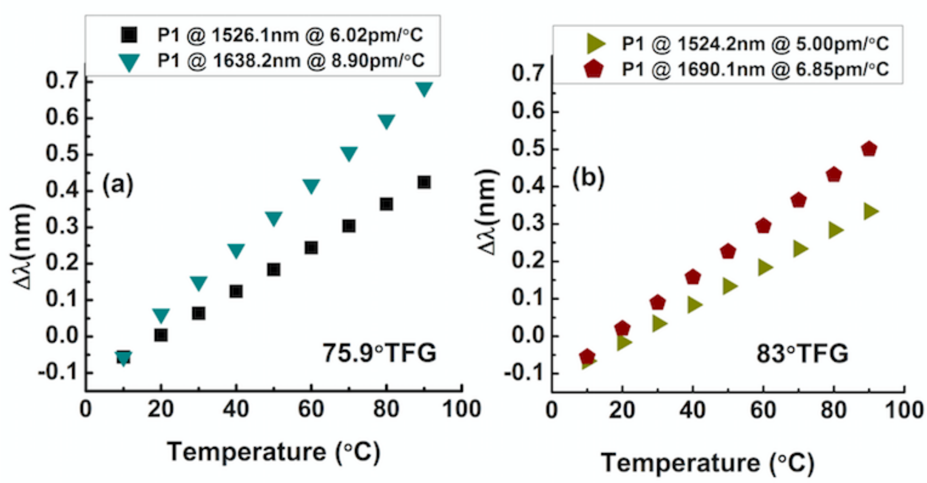

Figure 4.17: Thermal responses of the selected P1 polarised peaks from the dual polarisation states at (a) 1526.1nm and 1638.2 nm for the 75.9°-TFG, and (b) at 1524.2nm and 1690.1 nm for the 83°-TFG

	Peak 1 (P1 polarisation state)	**Peak 2 (P1 polarisation state)**
75.9°-TFG	1526.1nm	1638.2nm
	Thermal Sensitivity	**Thermal Sensitivity**
	6.02pm/°C	8.90pm/°C
83.0°-TFG	1524.2nm	1690.1nm
	Thermal Sensitivity	**Thermal Sensitivity**
	5.00pm/°C	6.85pm/°C

Table 4.2: The table showing the thermal sensitivity result comparison for the 75.9°-TFG and 83.0°-TFG:

Table 4.2 and Figure 4.17 (a) and (b) show the measured thermal sensitivities of the selected P1 polarised peaks from the dual polarisation states for the 75.9°-TFG at 1526.1nm and 1638.2nm as 6.02 pm/°C and 8.90pm/°C respectively; and for the 83°-TFG selected P1 polarised peaks from the dual polarisation states at 1524.2nm and 1690.1nm as 5.00pm/°C and 6.85pm/°C respectively. It can also be seen that the thermal sensitivity of the 75.9°-TFG is larger than the 83.0°-TFG, but the thermal sensitivities of both large angle TFGs are noticeably lower than that of normal FBGs (~12pm/°C) and small angle TFGs, and much lower (one order of magnitude lower) than that of LPG (~100pm/°C). The results also show that the selected P1 polarised peaks at the higher wavelength (Peak 2 in table 4.2) are more thermally sensitive than those at the lower wavelength (Peak 1 in table 4.2). This low thermal sensitivity of large angle TFGs makes them a good candidate for applications where thermal cross-sensitivity is an issue.

4.6 *SENSING APPLICATIONS OF LARGE ANGLE TFGS*

4.6.1 Twist Sensor Based On 81°TFG

TFG structures with relatively large tilt angle have shown not only the forward mode coupling characteristics but also a strong polarisation dependent spectral response and low thermal response. These properties have been utilised to achieve in-fibre polarimeters [14, 15], strain, refractive-index and torsion sensor [16, 17]. A twist sensor based on large angle TFGs have been proposed by Chen et al [18], which is based on a commercial polariser and an 81°-TFG. Wang et al in 2004 reported a twist sensor that used an LPG structure that had been induced using high frequency CO_2 laser pulses [19]. This section will present the results of exploring the use of the 81°-TFG as an all fibre optical twist sensor together with a 45°-TFG as an in-fiber polarizer ensuring single polarization measurement.

4.6.1.1 *Experimental set up and measurements*

When a fibre is twisted, the polarisation direction of the light propagating in the fibre changes; the encoded relationship between the coupled power into the cladding modes and twist (or rotation) can therefore be explored to implement an optical fibre twist or torsion sensor.

Aston University

Illustration removed for copyright restrictions

Figure 4.18: The experimental set up of the spectral interrogation for the implementation of the all-fibre twist sensor based on a 45°-TFG and an 81°-TFG.

The experimental setup of optical twist sensing system is illustrated in Figure. 4.18. A 15mm long 81°-TFG was inscribed in a 1.5m long SMF-28 fibre and a 45°-TFG was inscribed in front of 81°-TFG in the same fibre. This hybrid structure involving a 45°-TFG and an 81°-TFG will make a compact and low loss sensor structure as the use of a commercial polarizer is eliminated. As seen in Figure 4.18, the 45°-TFG is set between the broadband light source and the 81°-TFG, thus the light after 45°-TFG is linearly polarised, ensuring the 81°-TFG is measured at a single polarization. In the experiment, the 81°-TFG was fixed by a clamp on the incident light side and the output light side was mounted on a fibre rotator in order to apply twist (rotation) to the TFG. The length (L) between clamp and rotator was 95mm. In order to eliminate measurement errors from axial-strain and bending effects, a small axial tension was applied to the fibre maintaining it straight. Figure 4.19 shows the transmission spectra with a set of dual peaks, corresponding to two coupled modes with orthogonal polarisation states for the 81°-TFG used.

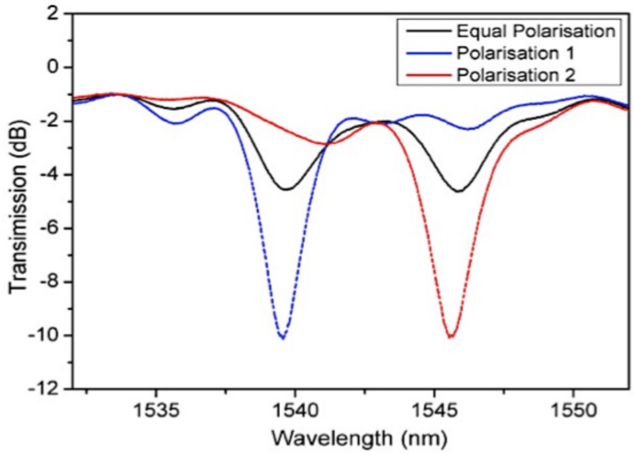

Figure 4.19: The transmission spectra of an 81°-TFG when lunched with randomly and orthogonally polarised light.

It can also be seen in Figure 4.19 that when the grating was lunched with randomly polarised light, the two peaks are coupled with almost the same strength, thus showing a 3-dB transmission loss, whilst when it is lunched with orthogonally polarised lights (P1 and P2), one peak is fully excited and the other almost diminished. This polarisation mechanism will further enable us to measure twist/torsion.

Before the measurement was started, the twist position of zero degree was firstly calibrated by adjusting the rotator to set the pre-polarisation state at P1. Then, the twist was applied to the fibre in the clockwise direction from 0° to 180° with 10° increments. The transmission spectrum for each applied twist was recorded and shown in Figure 4.20. It is clear that when the fibre was twisted, the coupled power transferred from P1 to P2, as the intensity of P1 decreased there was a noticeable increase in the polarisation peak of P2. When the twisted angle reached 180°, the P1 completely vanished and P2 reached its maximum (~11dB). The above measurement was then repeated by applying twist in an anticlockwise direction and the vice versa power exchange between P1 and P2 was observed.

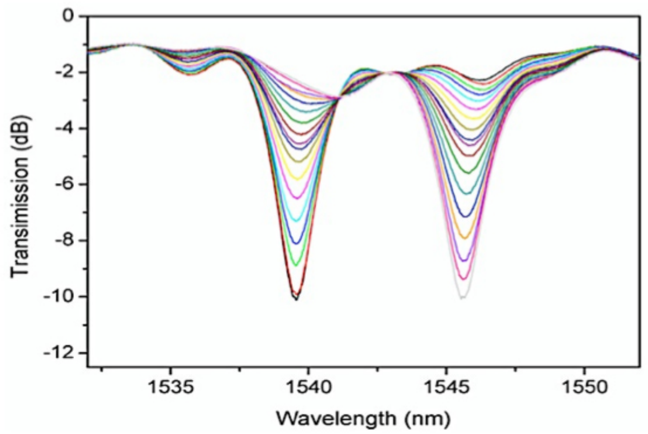

Figure 4.20: Spectrum evolution of 81°-TFG under twist in clockwise direction from 0° to 180° and in the anticlockwise direction.

4.6.1.2 *Power based measurements*

Based on the above experimental results, the directional polarisation mode coupling behaviour exhibited by the hybrid 45°-TFG and 81°-TFG in-fibre structure may be explored for the implementation of an all-fibre twist sensor based on optical power measurement. In real applications, it is desirable to use low-cost and compact-size wavelength source and power detector. To this end, the BBS and OSA (Figure 4.18) were replaced with a single wavelength laser (SWL) and a power detector (although in the experiment, a tunable laser was used). The schematic diagram of this all fibre system is shown in Figure 4.21

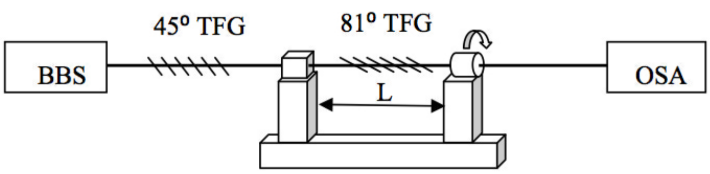

Figure 4.21: The schematic diagram of the all fibre twist sensor system using a single wavelength laser and a power detector.

Using the low cost power detecting interrogation method, a twist measurement on the same 45°-TFG in-fibre polariser and 81°-TFG was carried out. The selected dual peaks of the 81°-TFG are at 1539.62nm and 1545.74nm and by adjusting the rotator, the zero position of the sensor was calibrated to set the pre-polarisation state to the minimum power. The twist was then applied from 0° to 180° with 10° increments and the optical power from a power meter was measured for the P1 peak at 1539.62nm. Then, the measurement was repeated by changing the laser wavelength to 1545.74nm to measure the P2 peak, seen in Figure 4.22.

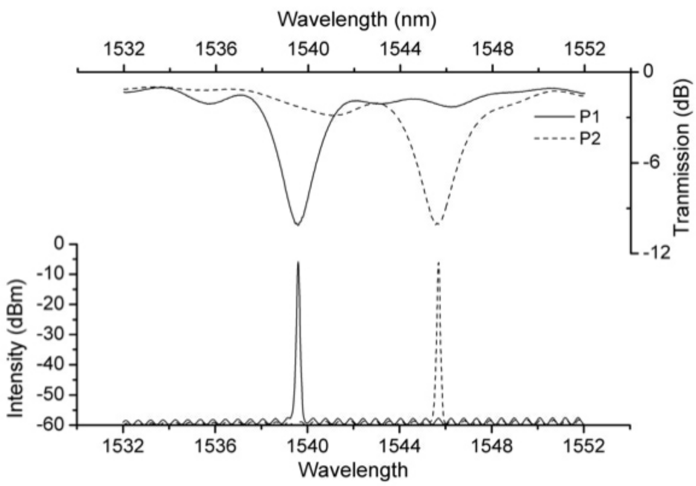

Figure 4.22: The upper plot is the transmission of spectra of dual peaks of the 81°-TFG; the wavelength of P1 is at 1539.62nm and that of the P2 is at 1545.74nm. The lower one is the output spectra of a tuneable laser set at the wavelength 1539.62nm and 1545.74nm.

The power measurement was first carried out using a power meter and then a photo-detector respectively and the results are shown in Figure 4.23 (a) and (b).

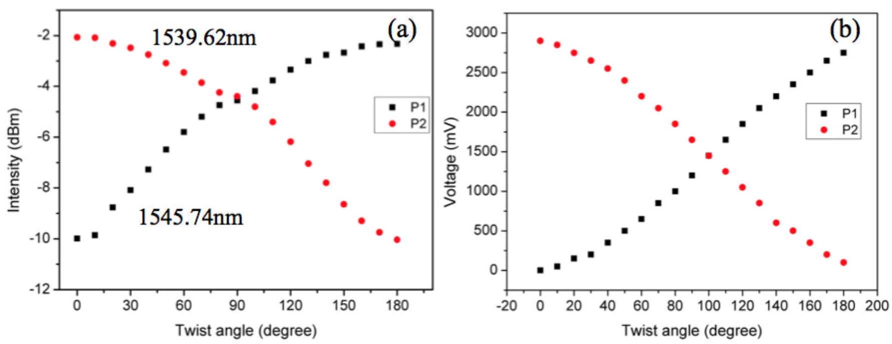

Figure 4.23: Transmission powers for the two orthogonal polarisation modes (Red dots – 1539.62nm and Black dots – 1545.74nm) measured by using a low-cost power detection method: (a) using a power meter and (b) using a photo-detector.

The power measurement reveals that the transmission power of P1 is increasing from -10dB to -2dB when the fibre was twisted from 0° to 180°, while the transmission power of P2 is decreasing from -2dB to -10dB. However, in Figure 4.23 (b), similar results were observed by changing the power meter to a photo-detector showing a voltage change between 0mV and 3000mV for the twist changing from 0° to 180°. This can provide a mechanism in which the sensing signal may be transmitted wirelessly for remote control sensing and monitoring.

4.6.2 Large Angle TFG Based Mach-Zehnder Interferometer

Over the years there has been increasing interest in the implementation of optical biosensors, by exploiting the response of fibre gratings to the change in the refractive index of the surrounding medium [20–23]. The use of an appropriate fibre type can make way for intrinsic or enhanced surrounding medium refractive index (RI) sensitivity of the grating structure. Bioactive materials can also be coated on fibre grating based RI sensors, which make it interact with certain biological agents, and thus becoming a real highly sensitive and selective biosensor.

Few scientists have claimed that the use of LPG pair-based Mach-Zehnder interferometer (MZI) [24], fibre-taper seeded LPG pair [25] and microfibre-based MZI [26] improved the measurement scheme and sensitivity. This section will report the investigation of large angle TFG based in-fibre MZI formed by a pair of 81°-TFGs for measurement of sugar solution concentrations with enhanced sensitivity and high resolution. As discussed earlier that the mode coupling of large angle TFGs is highly polarization dependent as the largely tilted structure increases the birefringence of the fibre, resulting in the light coupling to the two sets of orthogonal polarized modes (P1 and P2), the MZI response will be investigated for lights with different polarization states.

4.6.2.1 *Fabrication and spectral characteristics*

The two 81°-TFGs used to form the in-fibre MZI were fabricated in a hydrogenated SMF-28 fibre separated by a designed cavity length. The schematic of the fabricated structure is shown in Figure 4.24.

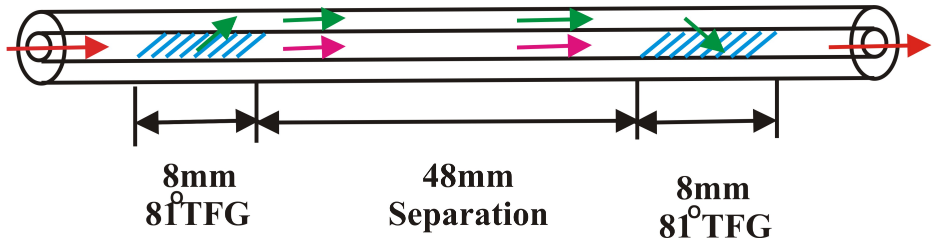

Figure 4.24: The schematic of an in-fibre Mach-Zehnder interferometer implemented with a pair of large angle tilted fibre gratings.

The spectral characteristics for this implemented in-fibre Mach-Zehnder consisting a pair of 81°-TFGs (Figure 4.24) was analysed by examining its spectrum on an optical spectrum analyser (OSA). The Mach-Zehnder structure shown in Figure 4.24 has two identical 81°-TFG which act as 3-dB couplers, for dividing and combining the optical signal between fibre core and cladding. Part of the input beam is first forward-coupled to the cladding modes by the first 81°-TFG and then guided through the cladding whereas the rest of the incident light is remained and guided along the core. Hence, the fibre core and the cladding create two optical paths. The light travelling along the cladding arm (green arrow) that later meets the second identical 81°-TFG is recoupled back into the core and finally interferes with the core mode light (pink arrow) generating the interference fringes, which can be useful for high resolution measurement.

Figure 4.25 shows the plot of the transmission spectra of the MZI formed by a pair of 8mm long 81°-TFGs with 48mm separation, showing multi-peak resonances at 1523nm region. With the selected polarization mode, the core light can be coupled to either P1 (red line) or P2 (blue line) polarized cladding modes, respectively, with a separation of 6.33 nm giving an estimated birefringence of $2{\times}10^4$.

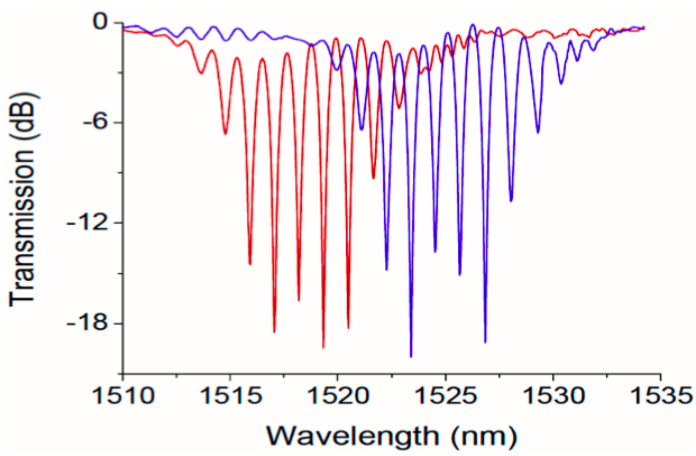

Figure 4.25: Interference fringes of the MZI formed by a pair of 81°-TFGs with 48mm separation (Red and blue curves: core mode coupled to P1 and P2 orthogonal polarised cladding modes respectively)

The fringe spacing can be approximated by [24]:

$$\Delta\lambda = \frac{\lambda^2}{\Delta n_g L} \tag{4.14}$$

where Δn_g is the group index difference between the core and cladding modes and L is the grating separation length. A series of 81°-TFG pairs were later fabricated to investigate the variation of the fringe spacing of the MZIs in terms of grating separation (16mm, 24mm, 32mm, 40mm, and 48mm, respectively). The result (Figure 4.26) shows that the fringe spacing decreases dramatically and nonlinearly when the grating separation is increased. In comparison, Gu et al in 1998 obtained 1.55nm fringe spacing at 1530nm wavelength region with an LPG pair of 410mm total length [27], this experiment produced the same fringe spacing using large angle TFG pair with 40mm total length, which is only $\frac{1}{10}th$ of the former, showing a much more compact size.

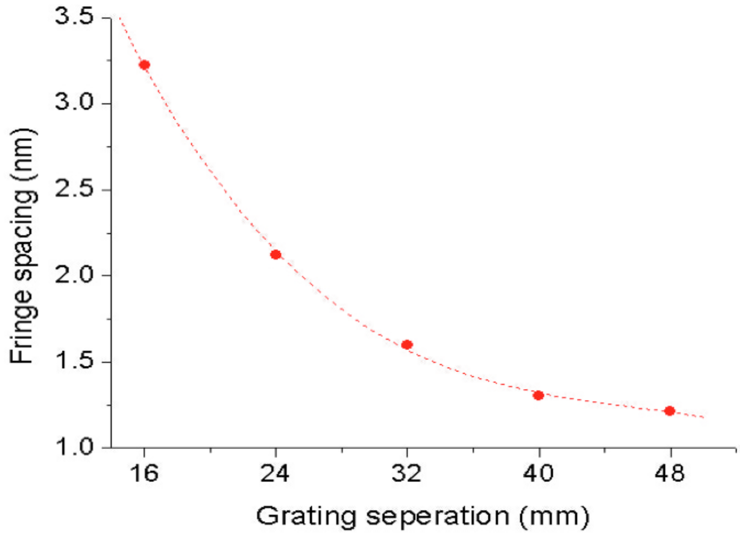

Figure 4.26: Fringe spacing against the grating separation with individual grating length of 8mm.

4.6.2.2 *Refractive index sensing and sugar concentration measurement*

The MZI sensor based on a pair of 81°-TFGs was first calibrated using a set of commercial index matching gels. The experimental set up is similar to that used in Figure 3.22 in Chapter 3. The index measurement result is shown in Figure 4.27.

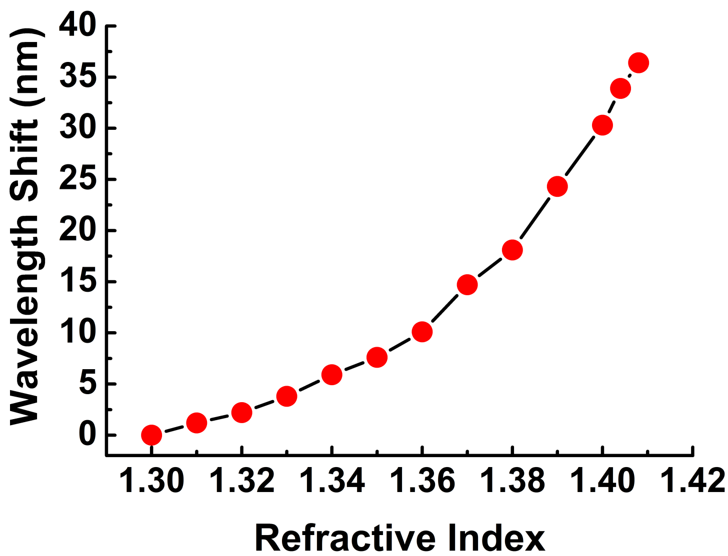

Figure 4.27: The graph of the wavelength shift Vs the change in index matching gel ranging from 1.30 to 1.42 RIU.

The outcome in Figure 4.27 shows that as the refractive index increases, the resonances of the MZI shift to longer wavelength. The rate of wavelength shift is slow to start with (RIU 1.30 – 1.36) and later increases faster as the index change exceeds RIU 1.36. This calibration with index gel now forms the basis for the sugar concentration sensing experiment. For this experiment, an unrefined cane sugar was purchased from Tesco (Figure 4.28(a)) and diluted to give different concentrations. It can also be noted in Figure 4.28(c) that as the sugar concentration increases the colour of the sugar solution gets darker. The first measurement is water (Figure4.29(a)) and this was then used as a reference on the OSA when monitoring the wavelength shift due to RI change.

Figure 4.28: (a) The unrefined cane sugar used for the experiment, (b) the digital weighting scale used to measure the sugar and (c) the cylindrical glass holding the diluted sugar of different sugar concentration.

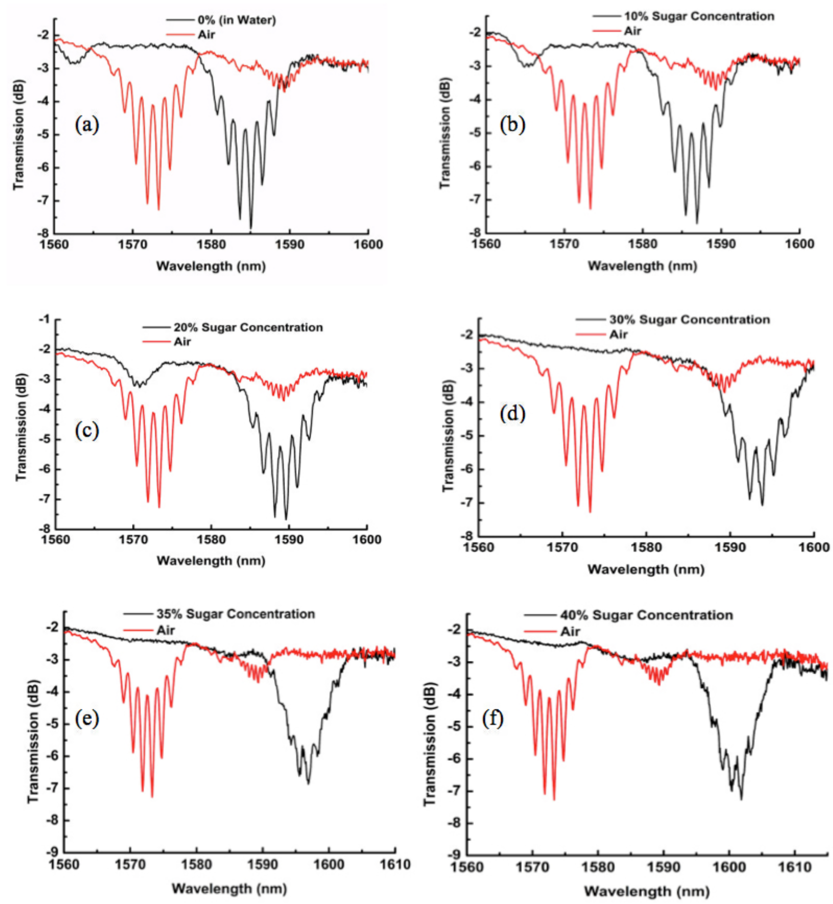

Figure 4.29: (a) MZI wavelength shifts at (a) 0% (b) 10%, (c) 20%, (d) 30%, (e) 35% and (f) 40% sugar concentrations. Red curve (in air) and black curve in different sugar concentrations.

The results shown in Figure 4.29 (a-f) clearly indicate that as the MZI sensing device was placed in the 10% sugar solution, the separation between the resonances with two orthogonal states began to increase, and then further increases with increasing of sugar concentration. It can also be seen from the figures that the visibility of comb-like resonances decreases with increasing sugar concentration, indicating the light coupled into the cladding modes experienced increasing loss.

The relationship between sugar concentration and RI has been calibrated and plotted as shown in Figure 4.30, showing a near linear trend from 1.33 to 1.42. The measured wavelength shift against sugar concentration is plotted in Figure 4.30 (b) showing that the MZI wavelength red shifts nonlinearly with increasing sugar concentration, especially, it is more sensitive in sugar concentration range 30%-40% (RI range 1.381-1.400). If one defines $\frac{\Delta\lambda}{\Delta n_{sur}}$ as RI sensitivity, this device can offer RI sensitivity as high as 719nm/RIU (1.37nm/1%). Thus, the sugar concentration change as small as 0.07% can readily be detected by this device using a standard interrogation system with 0.1-nm spectral resolution.

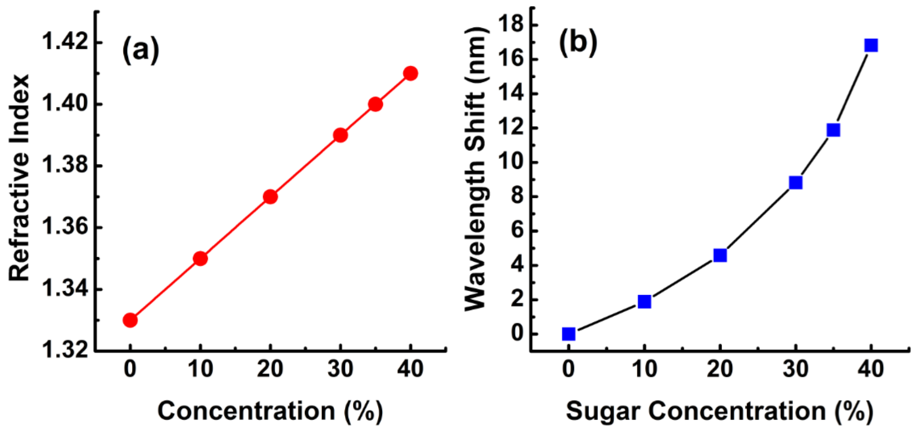

Figure 4.30: (a) Wavelength shift against the concentration of sugar and (b) Graph showing correlation calibration between RI and sugar concentration for the paired 81°-TFGs based MZI.

4.6.2.3 *Bio sensing application – HgB measurement*

Over the years, biosensors have been applied in genomics, proteomics and also in the food industry, homeland security and environmental monitoring systems [28–32]. In addition to these, there have also been increased interest in research aimed at the implementation of optical biosensors by exploring the response of optical fibre gratings to changes in bio solutions. Previous work carried out in this area includes biosensors that make the use of normal FBGs, small angle TFGs, and LPGs in single mode, multimode and D-shape fibres [33][34][35, 36].

In order to extend this work, the MZI interferometer was then used to measure the concentration of Haemoglobin (HgB) in sugar and phosphate solutions. The red blood cell gets its colour from HgB and HgB is the most important respiratory protein of vertebrates with the ability to transport oxygen from the lungs to the body tissues and also to facilitate the return transport of carbon dioxide. Production of the HgB concentrations was carried out in the same way as the sugar concentration experiment (section 4.6.2.2), but unlike sugar, the HgB was dissolved in a phosphate buffer solution. The phosphate buffer maintains the pH of the protein in HgB, since they require a certain pH range to maintain neutrality (otherwise the protein structure becomes deformed). The HgB lyophilized powder was purchased from Sigma Life Science and was obtained from a cow, with a storage temperature of 2-8°C.

The MZI was used to measure the concentration of HgB in phosphate buffer solution mixed with 20% sugar solution. The 20% sugar solution value was chosen as a result of the sugar sensitivity experimental result in Figure 4.30 (a), which shows significant wavelength shift (~4nm) occurred at about 20%. Thus the changes in the HgB concentration may be easily detectable by the MZI. The centre peak of the MZI at ~1572nm was monitored for this experiment. A set of HgB solutions with concentrations ranging from 0.0% to 1% with a step of 0.2% was prepared by adding HgB to the phosphate buffer and also to 20% of sugar solution. 5ml of each solution was then placed in 6 beakers (similar to Figure 4.28 (c)); each beaker contains 20% of 30g aqueous sugar solution.

The whole MZI grating area was immersed into solutions with different HgB concentrations one at a time; while the grating area was cleaned with ethanol in between the different concentration measurements in order to remove residual HgB or buffer before the next measurement. During the experiment, the polarization controller was used to maximise the MZI transmission peaks (meaning that the propagating core modes are fully coupled out of the fibre) and also to ensure that a single polarisation state (P1) is used for the measurements.

Figure 4.31 (a) shows the MZI centre peak wavelength shift under different concentrations of HgB in phosphate buffer solution; Figure 4.31 (b) plots the MZI central peak wavelength shift against changes in HgB concentration in 20% sugar concentration.

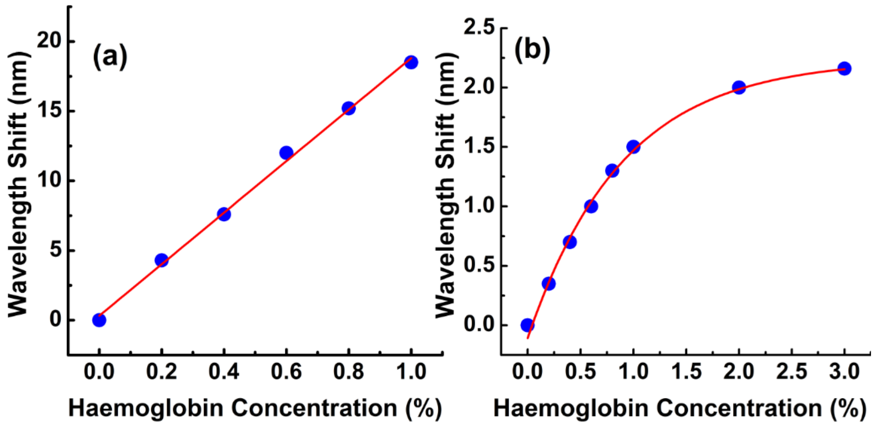

Figure 4.31: (a) Graph showing the wavelength shift of resonant peaks against the concentration of HgB in phosphate buffer solution, (b) Graph showing the wavelength shift of resonant peaks against the concentration of HgB in 20% sugar solution.

The experimental result shows that the wavelength shift of resonance peaks is linear to the increase in the concentration of HgB in phosphate buffer solution, as quantitatively we measured wavelength shifts of 0nm, 5nm, 7nm, 12nm, 16nm and 18nm for 0.0%, 0.2%, 0.4%, 0.6%, 0.8% and 1.0% HgB concentrations, respectively. But the relationship is non-linear between the wavelength shift and the concentration of HgB in 20% sugar solution, as we measured the wavelength shifts of 0nm, 0.4nm, 0.6nm, 1.0nm, 1.2nm, 1.5nm, 2.0nm and 2.5nm for 0.0%, 0.2%, 0.5%, 0.6%, 0.8%, 1.0%, 2.0% and 3.0% HgB concentrations, respectively. From the latter, we may deduce the maximum HgB concentration change from 0.0% to 3.0% gives a peak red shifts of 2.5nm, demonstrating a sensitivity of ~2.5 nm/1%.

4.7 *CHAPTER CONCLUSION*

This chapter presents a full investigation of fibre gratings with tilted structures at small (< 45°) and large (>45°) angles. A theoretical analysis of phase match condition for forward and backward cladding mode coupling has been conducted, showing the relationship between the radiation angle, the central wavelength and the Bragg resonance of the tilted structures respectively. The structures have been fabricated in a hydrogenated fibre using the phase and amplitude mask fabrication techniques. The systematic investigation of the structures, spectral responses, polarisation dependence, thermal, RI and bio responses were systematically carried out, showing distinctive characteristics and functions of small and large angle tilted fibre gratings. Large angle TFGs has the capability of coupling light from the core mode to the co-propagating cladding modes and due to its asymmetrical index fringe structure, two sets of birefringence cladding modes occur making it highly polarisation dependent. There low thermal sensitivity also makes them suitable for applications that require low thermal cross-sensitivity.

For the twist sensing, a highly sensitive twist sensor system based on a 45°and an 81°tilted fibre grating (TFG) has been experimentally demonstrated. The 81°-TFG has a set of dual-peaks that are due to the birefringence induced by its extremely tilted structure. When the 81°-TFG is subjected to twist, the coupling of light to the two peaks would interchange from each other, providing a mechanism to measure and monitor the twist. The performance of the sensor system by three interrogation methods (spectral-measurement, power-measurement and voltage-measurement) has also been investigated. The experimental results clearly show that the 81°-TFG and the 45°-TFG could be combined forming an all-fibre twist sensor system capable of not just measuring the magnitude but also recognising the direction of the applied twist. The advantages of an all-fibre and power measurement of this system provide potential for twist/torsion sensing applications using low-cost interrogation method and remote control and monitoring.

Finally for the chemical and bio sensing, the mode coupling and spectral characteristics of a pair of 81°-TFGs based MZI have been studied and presented, which shows the advantages of extremely enhanced RI sensitivity, higher resolution and more compact size. This device has been used for the detection of sugar concentrations and Haemoglobin concentrations, demonstrating an RI sensitivity as high as 719nm/RIU and ~2.5nm/1% for Haemoglobin detection.

4.8 References

[1] Y. C. Lu, W. P. Huang, and S. S. Jian, "Full vector complex coupled mode theory for tilted fiber gratings.," *Optics Express*, vol. 18, no. 2, pp. 713–726, 2010.

[2] P. S. Westbrook, T. A. Strasser, and T. Erdogan, "In-Line Polarimeter Using Blazed Fiber Gratings," *IEEE Photonics Technology Letters*, vol. 12, pp. 1352–1354, 2000.

[3] S. J. Mihailov, R. B. Walker, T. J. Stocki, and D. C. Johnson, "Fabrication of tilted fibre-grating polarisation-dependent loss equaliser," *Electronics Letters*, vol. 37, no. 5, pp. 284–286, 2001.

[4] K. Zhou, G. Simpson, X. Chen, L. Zhang, and I. Bennion, "High extinction ratio in-fiber polarizers based on 45 degree tilted fiber Bragg gratings," *Optics Letters*, vol. 30, no. 11, pp. 1285–1287, 2005.

[5] T. Erdogan and J. Sipe, "Tilted fiber phase gratings," *Journal of the Optical Society of America A-Optics Image Science and Vision*, vol. 13, pp. 296–313, 1996.

[6] K. S. Lee and T. Erdogan, "Fiber mode coupling in transmissive and reflective tilted fiber gratings.," *Applied Optics*, vol. 39, no. 9, pp. 1394–1404, 2000.

[7] K. Zhou, A. G. Simpson, L. Zhang, and I. Bennion, "Side detection of strong radiation-mode out-coupling from blazed FBGs in single-mode and multimode fibers," *Photonics Technology Letters, IEEE*, vol. 15, no. 7, pp. 936–938, 2003.

[8] C. Mou, "Fabrication and Characterisation of 45° of Ex 45°- Tilted Fibre Gratings and Their Applications in Fibre Lasers and Sensors," no. December, 2010.

[9] P. Westbrook, K. Feder, P. Reyes, P. Steinvurzel, B. Eggleton, R. Ernst, L. Reith, and D. Gill, "Application of fiber Bragg grating filter/tap module to a wavelength-locked low-chirp directly-modulated 10 Gb/s RZ transmitter," *Optical Fiber Communication Conference and Exhibit*, vol. 2002, pp. 680–682, 2002.

[10] J. Tian, Q. Zhang, and M. Han, "Distributed fiber-optic laser-ultrasound generation based on ghost-mode of tilted fiber Bragg gratings," *Optics Express*, vol. 21, no. 5, pp. 6109–6114, 2013.

[11] S. Baek, Y. Jeong, and B. Lee, "Characteristics of short-period blazed fiber Bragg gratings for use as macro-bending sensors," *Applied Optics*, vol. 41, no. 4, pp. 631–636, 2002.

[12] T. Guo, L. Shao, H.-Y. Tam, P. A. Krug, and J. Albert, "Tilted fiber grating accelerometer incorporating an abrupt biconical taper for cladding to core recoupling," *Optics Express*, vol. 17, no. 23, pp. 20651–20660, 2009.

[13] L. Y. Shao, L. Xiong, C. Chen, A. Laronche, and J. Albert, "Directional bend sensor based on re-grown tilted fiber bragg grating," *Journal of Lightwave Technology*, vol. 28, pp. 2681–2687, 2010.

[14] X. Shu, L. Zhang, and I. Bennion, "Sensitivity characteristics near the dispersion turning points of long-period fiber gratings in B/Ge codoped fiber.," *Optics Letters*, vol. 26, no. 22, pp. 1755–1757, 2001.

[15] X. Shu, L. Zhang, and I. Bennion, "Sensitivity characteristics of long-period fiber gratings," *Journal of Lightwave Technology*, vol. 20, no. 2, p. 255, 2002.

[16] Z. Zhang and J. S. Sirkis, "Temperature-compensated long period grating chemical sensor," in *Optical Fiber Sensors*, p. OWC38, Optical Society of America, 1997.

[17] H. H. J. Patrick, a. A. D. Kersey, and F. Bucholtz, "Analysis of the response of long period fiber gratings to external index of refraction," *Journal of Lightwave Technology*, vol. 16, no. 9, pp. 1606–1612, 1998.

[18] X. F. Chen, K. Zhou, L. Zhang, and I. Bennion, "In-fibre twist sensor based on a fibre Bragg grating with 81° tilted structure," *IEEE Photonics Technology Letters*, vol. 18, pp. 2596–2598, 2006.

[19] R. Yun Jiang, W. Yi Ping, R. Zeng Ling, and Z. Tao, "Novel fiber-optic sensors based on long-period fiber gratings written by high-frequency CO2 laser pulses," *Journal of Lightwave Technology*, vol. 21, 2003.

[20] B. H. Lee and J. Nishii, "Dependence of fringe spacing on the grating separation in a long-period fiber grating pair.," *Applied Optics*, vol. 38, no. 16, pp. 3450–3459, 1999.

[21] P. Lu, L. Men, K. Sooley, and Q. Chen, "Tapered fiber Mach–Zehnder interferometer for simultaneous measurement of refractive index and temperature," *Applied Physics Letters*, vol. 94, no. 13, p. 131110, 2009.

[22] J. Wo, G. Wang, Y. Cui, Q. Sun, R. Liang, P. P. Shum, and D. Liu, "Refractive index sensor using microfiber-based Mach–Zehnder interferometer," *Optics Letters*, vol. 37, no. 2012, p. 2221–2793, 2012.

[23] K. Zhou, L. Zhang, X. Chen, and I. Bennion, "Optic sensors of high refractive-index responsivity and low thermal cross sensitivity that use fiber Bragg gratings of> 80 tilted structures," *Optics Letters*, vol. 31, no. 9, pp. 1193–1195, 2006.

[24] J. Dakin and B. Culshaw, "Optical Fiber Sensors, vol. 4," *Artech House, Boston*, p. 315, 1997.

[25] O. S. Wolfbeis, "Fiber-optic chemical sensors and biosensors.," *Analytical Chemistry*, vol. 72, no. 12, pp. 81R–89R, 2000.

[26] X. Chen, K. Zhou, L. Zhang, and I. Bennion, "Simultaneous measurement of temperature and external refractive index by use of a hybrid grating in D fiber with enhanced sensitivity by HF etching.," *Applied Optics*, vol. 44, no. 2, pp. 178–182, 2005.

[27] X. Chen, K. Zhou, L. Zhang, and I. Bennion, "Optical chemsensor based on etched tilted Bragg grating structures in multimode fiber," *Photonics Technology Letters, IEEE*, vol. 17, no. 4, pp. 864–866, 2005.

[28] P. N. Prasad, *Introduction to Biophotonics.* John Wiley & Sons, 2004.

[29] G. Murugaboopathi, V. Parthasarathy, C. Chellaram, T. P. Anand, and S. Vinurajkumar, "Applications of Biosensors in Food Industry," *Biosciences Biotechnology Research Asia*, pp. 711–714, 2013.

[30] L. D. Mello and L. T. Kubota, "Review of the use of biosensors as analytical tools in the food and drink industries," *Food Chemistry*, vol. 77, no. 2, pp. 237–256, 2002.

[31] N. Hu, M.-h. Zhao, J.-l. Chuang, and L. Li, "The application study of biosensors in environmental monitoring," in *Cross Strait Quad-Regional Radio Science and Wireless Technology Conference (CSQRWC), 2011*, vol. 2, pp. 976–979, IEEE, 2011.

[32] K. R. Rogers, "Recent advances in biosensor techniques for environmental monitoring," *Analytica Chimica Acta*, vol. 568, no. 1, pp. 222–231, 2006.

[33] M. E. Bosch, A. J. R. Sánchez, F. S. Rojas, and C. B. Ojeda, "Recent development in optical fiber biosensors," *Sensors*, vol. 7, no. 6, pp. 797–859, 2007.

[34] O. S. Wolfbeis, "Fiber-optic chemical sensors and biosensors," *Analytical Chemistry*, vol. 76, no. 12, pp. 3269–3284, 2004.

[35] X. Chen, K. Zhou, L. Zhang, and I. Bennion, "High sensitivity biosensor based on dual-peak LPG sensitised by light cladding etching," in *Bruges, Belgium-Deadline Past*, pp. 383–386, International Society for Optics and Photonics, 2005.

[36] T. Allsop, H. Dobb, V. Mezentsev, T. Earthgrowl, A. Gillooly, D. J. Webb, and I. Bennion, "The spectral sensitivity of long period gratings fabricated in elliptical core D-shaped optical fibre," *Optics Communications*, vol. 259, no. 2, pp. 537–544, 2006.

5 45°TILTED FIBRE GRATINGS AT 800NM RANGE

5.1 *INTRODUCTION*

Tilted fibre gratings (TFGs), also known as slanted or blazed fibre gratings, are a type of fibre gratings with refractive index modulation structure tilted at a certain angle that is capable of coupling the light from a forward-propagating core mode to backward-propagating core and cladding, or radiation or forward-propagating cladding modes, depending on the degree of the tilt angle. In 1996, Erdogan demonstrated the first TFG [1] and advanced work on TFGs has been carried out since then by many researchers [2–4]. Li et al reported the first theoretical description of the power radiation property of TFGs in 2001 [2], which were based on the volume current method (VCM) to explain the scattering of out-coupled light from a TFG. TFG's at 45° will couple out the S-polarization component of light and leave the P-polarization part propagating in the fibre core, functioning as a polarizer. In 2005, Zhou et al [5] used an advanced UV-inscription technique to fabricate a 45°-TFG (a TFG with the structure tilted at 45°), showing in-fibre polarizer function with Polarization Extinction Ratio (PER) as high as 33dB. Later in 2011, Yan et al [6] systematically investigated the polarization dependent loss (PDL) and thermal characteristics of 45°-TFGs at 1550nm wavelength range.

This chapter is focused on 45°-TFGs specifically designed and fabricated with function response and applications in 800nm region. 800nm falls in the near infrared region of the light spectrum, which has made it possible to use this wavelength for applications in scientific, industrial and medical applications. Example of devices that operates in the near-infrared are: night vision goggles, thermal imaging cameras, telescopes, remote temperature sensors and spectroscopes. This wavelength region is of great interest in this report due to its various applications and its cost effectiveness in design. It is suffice to say that this it is the first time 45°-TFGs in this wavelength range have been carefully investigated and systematically characterized. Furthermore, the fabrication and characterization of 45°-TFG based in-fibre polarizers and power tappers working at a shorter wavelength range of 800nm is reported in this section.

5.2 *STRUCTURE AND MODE COUPLING MECHANISM*

Compared to a normal fibre Bragg grating (FBG), a TFG has a grating wave vector with a certain angle to the fibre axis. In 1969, Kogelink [7] describe the diffraction of the TFGs using the coupled wave theory. Since Kogelink theory is one dimensional, it is not fully suitable for analyzing 45°-TFG; it assumes the grating is infinite in two dimensions and doesn't account for the light propagation in the z direction. The coupled wave theory also assumes that a grating is either transmitive or reflective, which is not completely valid for 45°-TFG. When a grating structure is tilted at exactly 45°, it can be verified that the structure is at Brewster's angle, thus nulling (couples out) the S-polarized (TE-polarization) light component and leaves the P-polarized (TM-polarization) light transmitting through the fibre. For a UV-inscribed TFG, the Brewster angle can be expressed as:

$$\theta_{Brewster} = \tan^{-1} \frac{n_{core}}{(n_{core} + \delta n)} \tag{5.1}$$

Where n_{core} is the refractive index of fibre core and δn is the UV-induced index modulation. The index change through the single photon absorption of UV light is in general very small (10^{-5} to 10^{-3}). From equation 5.1, it can be seen that the Brewster angle for a UV-inscribed tilted grating is at 45°; this clearly explains why 45°-TFG can function as a polarizer as it couples out the TE-polarization component of light and leaves the TM-polarization to propagate through the fibre. Figure 5.1 shows the result of a simulation carried out by Zhou et al, which shows that the transmission loss of the TM-polarized light is almost zero and the transmission loss of the TE-polarized light is significantly high when the tilt angle is at 45°.

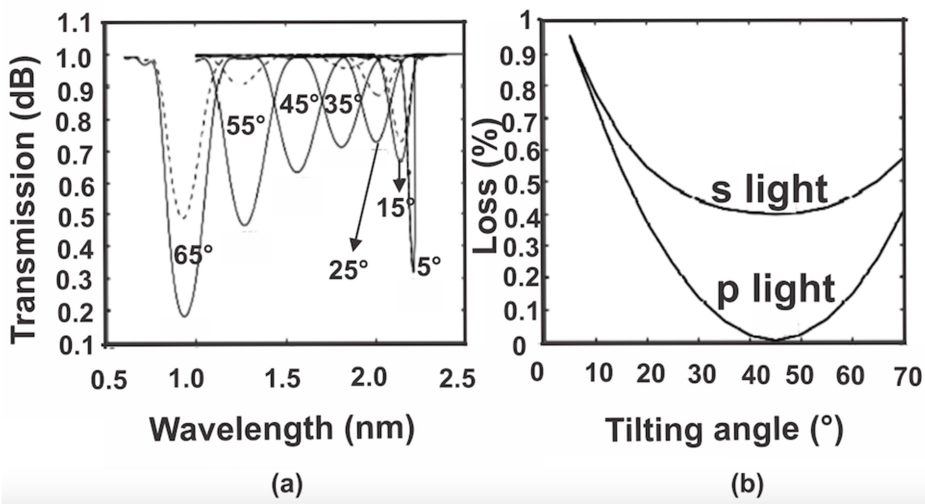

Figure 5.1: (a) The Transmission spectra of TFGs with 5°C, 15°C, 25°C, 35°C, 45°C, 55°C and 65°C tilted angles; showing the dashed lines (P-polarised light) and solid curves (S-polarised light). (b) Plot showing the percentage transmission losses of TFGs versus the S-polarized and P-polarised light for a 45°C tilt angle[8].

The mode coupling mechanism of a TFG works by coupling the forward-propagating core mode to the counter or the co-propagating modes or radiation modes [9, 10]. Zhou et al [11] confirmed that the strongest coupling wavelength condition occurs when this phase matching condition is established:

$$\vec{K}_R = \vec{K}_{core} + \vec{K}_G \tag{5.2}$$

where $\vec{K}_R$, $\vec{K}_{core}$ and $\vec{K}_G$ represents the light radiated, core mode and the grating wave vectors. As reviewed in [11], there are three tilted angle ranges (as shown in Figure 5.2 (a) – (c)) defined by the total internal reflection. When the tilted angle θT < θ_{1C} (23.1°), the light is coupled to backward-propagating core and cladding modes; when θT > θ_{2C} (66.9°), the light is coupled to forward-propagating cladding modes; when θ_{1C} < θT < θ_{2C}, the light is radiated out from the side of the fibre.

Aston University

Illustration removed for copyright restrictions

Figure 5.2: (a) The phase matching of TFG < 45° (b) The phase matching of TFG = 45° (c) The phase matching of TFG > 45° (d) The Schematic of 45°-TFG structure showing the three mode coupling range.

Therefore, the strongest coupling wavelength for a 45°-TFG can be described as:

$$\lambda_{strongest} = \frac{n\Lambda_G}{\cos 45^0} \tag{5.3}$$

where n is the refractive index of the fibre core and Λ_G is grating period. At 45°, the light is taped out at normal direction with the fibre axis. The tilt angle of the grating plane and the index modulation strength will determine the radiation coupling efficiency of the light that is tapped out.

5.3 *FABRICATION OF 800NM 45°- TILTED FIBRE GRATING*

5.3.1 Introduction

The limitations of fibre photosensitivity and fabrication techniques have limited the research of early researchers to FBGs, until when Meltz et al [12] discovered that the mode coupling in phase gratings could be enhanced by tilting the angle of the grating (i.e. the angle between the wave vector and the axis), hence the name Tilted Fibre Grating (TFG). They are also called; Slanted gratings or Blazed Fibre Grating. The grating tilt structures can be achieved either by using the phase mask inscription technique or by the two beam holographic technique; by rotating the fibre at an angle with respect the interference beam (figure 4.4 in chapter 4).

In TFGs, any beam incident on the tilted structure radiates out of the fibre core in various directions with different strengths. Fresnel's Law [9] states that a partial reflection and refraction occurs when a beam of light shines on an interface with different dielectrics (i.e. the interface reflectivity or refractivity depends on the refractive indexes of the dielectric). When a grating is 45° tilted, the S-polarised light component is coupled out of the fibre core and the P-polarised light component transmits through the fibre.

The phase-mask technique for fabricating FBGs was first demonstrated by Hill et al. [13] and Anderson et al. [14]. It has been widely reported as the most effective grating inscription technique for TFGs due to the simplicity of the optical system and its stability compared to the two-beam holographic technique [15]. The beam incident on the mask is diffracted into several orders, and for a standard phase mask, the light energy of 0_{th} order is suppressed and the energy in the ± 1 order maximized. The laboratory set-up for this technique is shown in Figure 2.9 in chapter 2. In the work reported in this chapter, the phase mask used was from Ibsen with a mask pitch of 922.46nm (giving central response at around 800nm), external tilted at 33.7°and is 0_{th} order suppressed. The theoretical explanation of the relationship between the internal and the external tilt angle of the 45°-TFG has been explained in chapter 4, section 4.2.3. The simulation derived from equation 4.1 (chapter 4); with n given as 1.52 (the refractive index of Silica at UV wavelength) showing this relationship is shown in Figure 5.4. The result shows that the internal tilt angle increases as the external tilt angle increases. For instance, the Ibsen phase mask used in this research to fabricate a 45°-TFG has an external tilted fringe of 33.7°. It can be seen that when the tilt angle is less than 10°, the curve is almost linear and non-linearity begins to show as the tilt angle increases.

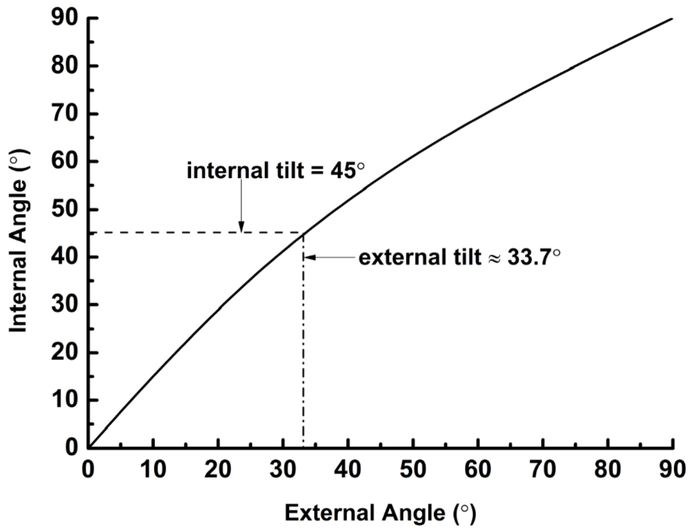

Figure 5.3: Simulation showing the internal tilt angle (θ_{int}) Vs the external tilt angle (θ_{ext}) for TFGs fabricated by the phase mask technique using Equation 4.10.

5.3.2 Fabrication Set-Up and Configuration

As discussed in chapter 4, the fabrication of fibre gratings depends on the size of the UV interfering area after the phase mask. The fabrication set up includes: a 244nm UV continuous wavelength (CW) frequency double Argon ion laser (with a beam size of 268μm at the x-axis and 240μm at the y-axis), a cylindrical lens, an air-bearing stage and a phase mask. The use of the cylindrical lens makes the incident beam on the phase mask rectangular in shape. The inference of the beam occurs after the phase mask and the index modulation of the fibre core only takes place in the effective interference area of the ± 1 diffracted order with the 0 order suppressed.

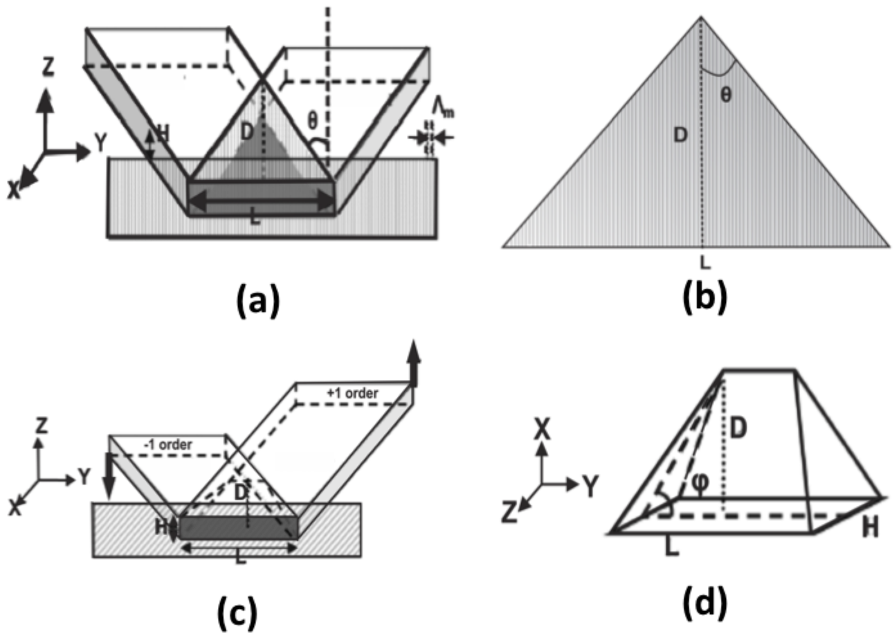

Figure 5.4: (a) 3-D schematic diagram showing the interference area of the ± 1 UV diffraction order after a normal phase mask; the dark area represents the interference area in the xy plane (b) 2-D diagram of the UV interference region with θ = angle between the ± 1 order diffraction beam, D is area of the depth of interference and L is the UV beam in the y-axis (c) 3-D schematic diagram showing the interference area of the ± 1 UV diffraction order after a tilted phase mask (d) 3-D diagram of the volume after the tilted phase mask; with φ = tilt angle of the phase mask, H is the height of the UV beam in the z-axis and D is the distance between the interference area and the phase mask. [6]

To increase D in Figure 5.5(d), the beam can be defocused (by adjusting the focal length of the focusing lens before the phase mask), but this will also weaken the UV beam intensity. A weakened UV beam can be ideal for fabricating gratings in large core fibres, as the defocus beam ensures all the fringes cover the entire area of the fibre core. There is however a fundamental limit to the fabrication of 45°-TFG using tilted phase mask because it doesn't only diffract beam in the x-z plane but also in the y-z plane; meaning that the effective $\pm$ 1 order overlap area becomes smaller in comparison to the normal FBG phase mask. For all the 45°-TFG fabricated in this chapter, the UV beam was defocused to 1.5mm as seen below:

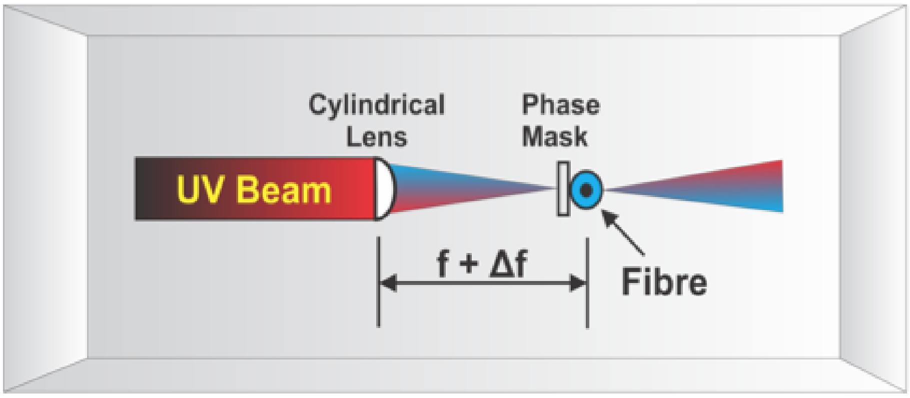

Figure 5.5: The fabrication set up showing how the change in the focal length of the cylindrical lens is used to defocus the beam by 1.5mm; yielding a UV beam spot size of about 0.5mm.

5.3.3 Phase Mask Efficienncy

Another analysis was carried out before the 45°-TFGs were fabricated; the diffraction efficiency of the $\pm$ 1 order of the commercial tilted phase mask (TPM) used in this report (by Ibsen Photonics) was compared to a set of three custom made TPMs. The schematic of the tilted phase mask is shown in Figure 5.7:

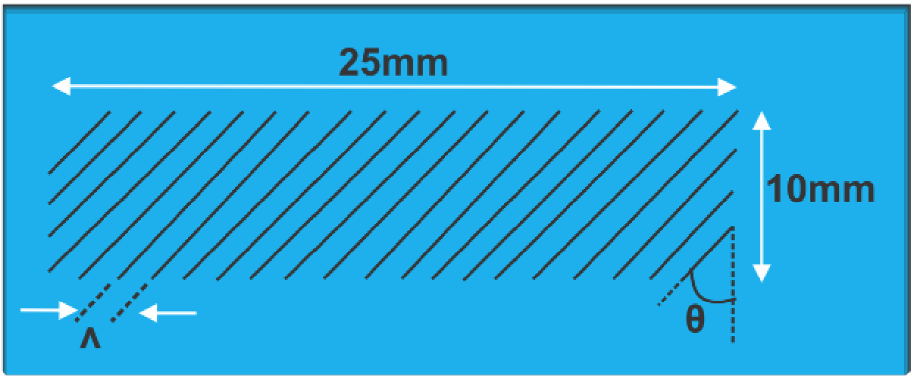

Figure 5.6: Schematic of a tilted phase mask of length 25mm and a height of 10mm

The specifications of the aforementioned three TPMs are:

SKR003C- 1 (in-house):

Grating area: 25mm×10mm; θ=33.7°; Period of mask: 1563.762nm;

SKR003C- 2 (in-house):

Grating area: 25mm×10mm; θ=33.7°; Period of mask: 1563.772nm;

Ibsen Phase Mask:

Grating area: 25mm×10mm; θ=33.7°; Period of mask: 1800.0nm.

A diffraction efficiency experiment (Figure 5.8 (a) and (b) was carried out by lunching an incident UV beam (Frequency doubled argon ion laser at 244nm wavelength) with a spot size of approximately 0.5 mm to the phase mask. The mask structure results in diffraction beams of 0, $\pm$1, $\pm$2 orders which were viewed clearly on a screen placed behind the mask. The intensity of three other beams (0 order,$\pm$ 1 order) were measured using a UV detector. Five points across the mask grating area at 2mm, 7mm, 12mm, 17mm and 22mm (Figure 5.8 (b)) were selected for the diffraction efficiency measurement. The diffraction efficiency was calculated using the following definition:

Diffraction Efficiency = Diffracted power / Incident UV beam power

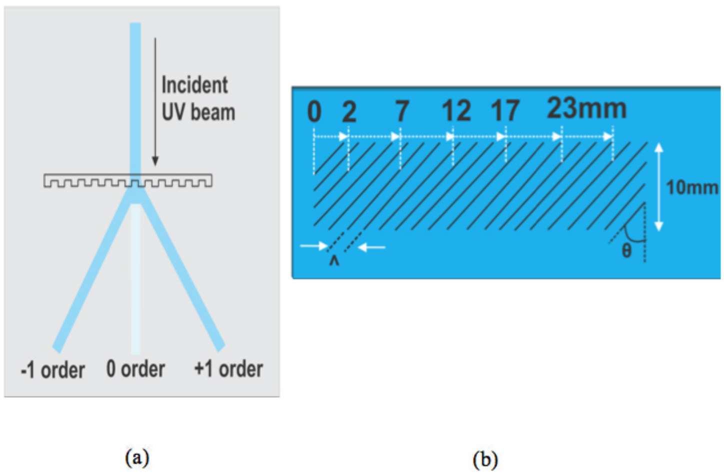

Figure 5.7: Schematic of UV diffraction beams by phase mask (a) and five selected points of phase mask for measurement (b).

Point Location (mm)	Diffraction Efficiency (%)		
	-1 order	0 order	+1 order
2	12.7	50.1	12.2
7	12.4	48.8	12.2
12	12.2	48.1	12.3
17	12.8	48.2	12.5
22	12.7	48.7	12.8

Table 5.1: Tilted phase mask diffraction efficiency of SKR003C-1

Point Location (mm)	Diffraction Efficiency (%)		
	-1 order	0 order	+1 order
2	12.7	47.8	14.9
7	13.1	47.2	15.1
12	13.5	47.7	15.3
17	13.5	47.7	15.4
22	13.4	47.6	15.5

Table 5.2: Tilted phase mask diffraction efficiency of SKR003C-2

Point Location (mm)	Diffraction Efficiency (%)		
	-1 order	0 order	+1 order
2	37.5	1.1	37.0
7	37.7	0.1	37.8
12	39.0	0.1	39.4
17	39.7	0.1	40.6
22	37.4	0.1	38.8

Table 5.3: Tilted phase mask diffraction of Ibsen Phase Mask

It is clear from the Tables 5.1- 5.3 that all three TPMs exhibit the uniformity for the region from 0mm to 25mm, and the symmetry characteristics in diffraction efficiency of the same order beam (e.g. +1 order and -1 order). But, for both of SKR003C-1 and SKR003C-2 phase masks, the diffraction efficiencies of 0 order show as high as 48% whilst ± 1 order show only around 13%. For the Ibsen phase mask, the 0 order diffraction efficiency has been suppressed to less than required 5%, even less than 0.5% (measured value). Below are the diffraction patterns observed on the screen;

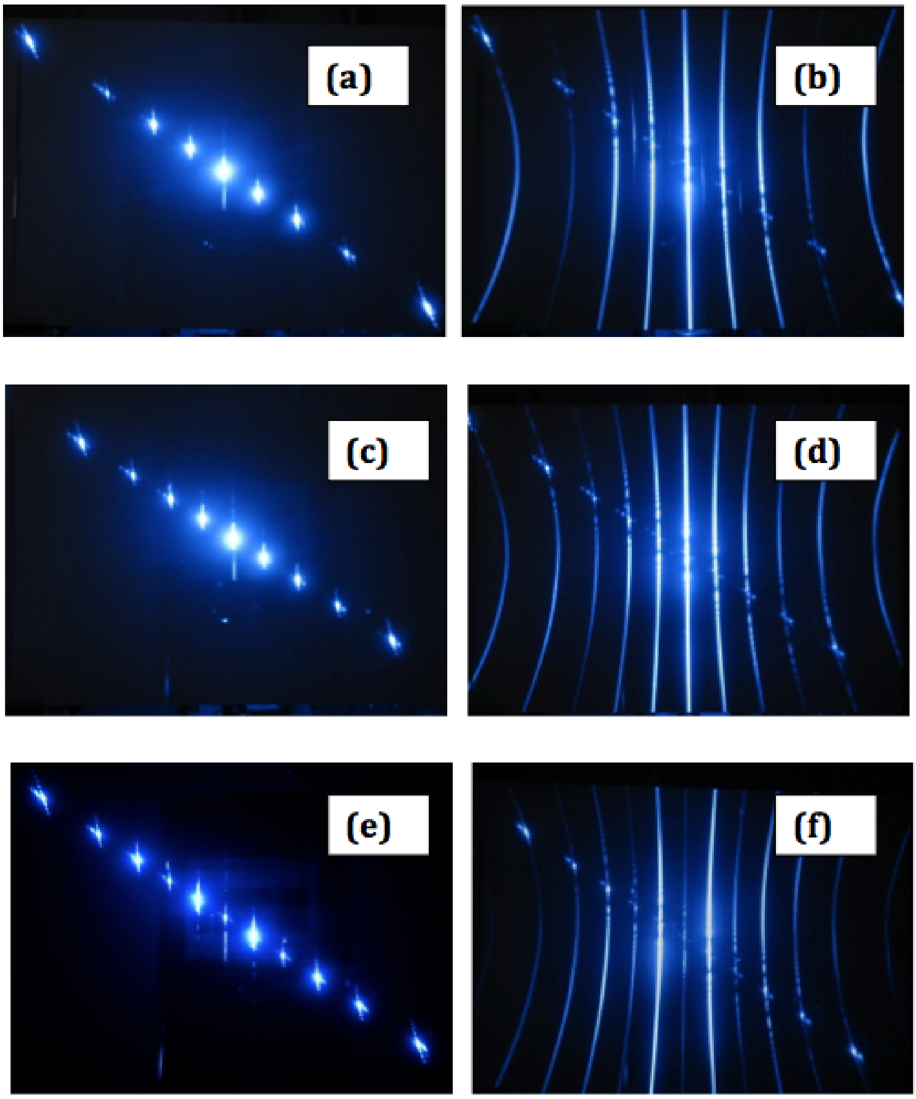

Figure 5.8: Image of UV diffraction pattern by SRK003C-1 phase mask. (a) with bare phase mask and (b) with phase mask and optical fibre; Image of UV diffraction pattern by SRK003C-2 phase mask.(c) with bare phase mask and (d) with phase mask and optical fibre; Image of UV diffraction pattern by Ibsen phase mask.(e) with bare phase mask and (f) with phase mask and optical fibre.

For both of the SKR003C-1 and SKR003C-2, most of the incident UV beam power has been diffracted to the first several orders (0, ±1, ±2 order) whilst the 0 order is significantly strong indicating a low suppression effect. For the commercial Ibsen phase mask, the ±1 orders have the highest diffraction efficiency. For fibre grating fabrication with a phase mask, usually ±1 order diffraction beams are employed to generate the interference pattern area for grating inscription. Normally, ±1 orders have efficiency higher than 35% whilst 0 order is being suppressed less than 5%. (The strong 0 order will erase the grating fringes induced by +/-1 order diffraction.). The 0 order diffraction efficiency of SKR003C-1 and SKR003C-2 phase masks has not been suppressed less than 5%, and the ±1 order diffraction efficiencies are only 13%, these two phase masks would be unsuitable for tilted fibre grating fabrication.

5.3.4 800NM 45°- TFG Fabrication

The 800nm 45°-TFG used in this chapter was UV inscribed into the photosensitive fibre (PS750 single mode fibre) using the phase mask scanning technique. The UV laser is a 244nm, CW frequency doubled Argon ion laser (Coherent Sabre Fred®). The PS750 fibre was hydrogen loaded under 150 bar at 80°C for 48 hours pre-fabrication to enhance photosensitivity. The UV Laser was focused through the phase mask unto the fibre by the cylindrical lens, which was carefully aligned along the fibre axis. The computer controlled air-bearing stage is then used to scan the UV beam over the fibre in the fibre holder to inscribe the grating structure. The phase mask from Ibsen photonics has a total length of 25mm, a pitch of 1059.7nm, a chirp of 1.3nm/cm and an external tilt angle of 33.7°. Figure 5.10 shows the grating fabrication layout used in our photonics lab.

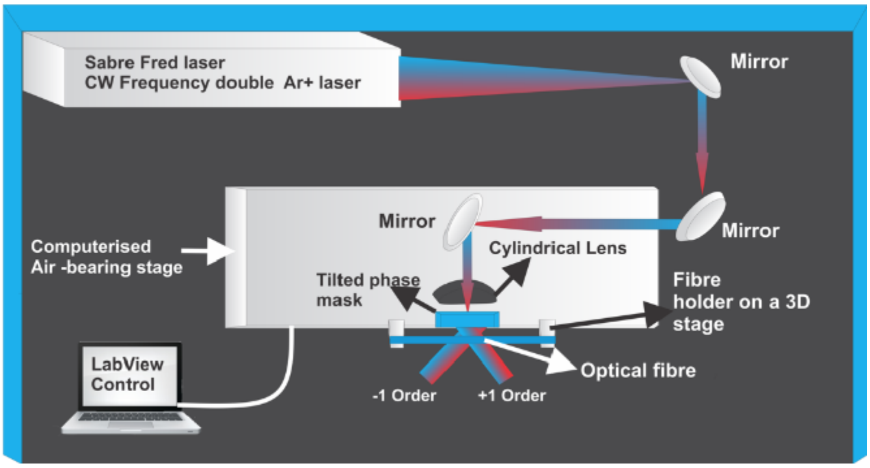

Figure 5.9: The grating fabrication set up used in the laboratory; with a LabView programme controlling the air-bearing stage.

TFGs usually require a minimum of 10^{-3} refractive index modulation for an inscription to take place; this depends on the photosensitivity of the fibre and the UV exposure condition. In order to achieve this level of index modulation, the laser power was set to 95mW and the UV beam scanning speed set to 0.08mm/s. The inspection of the inscribed tilted grating took place post-fabrication using the Zeis Axioskop microscope system. In other to see the grating structures, a 100x oil immersion microscopic lens was used as seen in Figure 5.11. The microscopic image shows an approximate measured diameter of the fibre core as 4.08μm and the measured tilted angle of 45°.

Figure 5.10: The microscopic image captured from the Zeiss Axioskop 2 mot plus showing the grating structure of the 45°-TFG inscribed in the fibre core

5.4 *SPECTRAL CHARACTERISTICS OF 800NM 45°- TFGS*

5.4.1 The Entire PER Profile

Polarisation extinction ratio (PER), also known as polarisation dependent loss (PDL) is the difference between the maximum and minimum loss with respect to all possible polarization states. Noutsios et al in 2001 [16] and Kim et al in 2002 [17] explained the importance of PER on the system performance of optical communication systems. There are two main methods used in analyzing the PER of passive optical devices: the polarization scanning technique and the Mueller Matrix method, but this report will only show the polarization scanning technique as a way of measuring the PER of the fabricated TFGs. The measure of this peak-to-peak difference of the transmission between the maximum and minimum can be calculated as:

$$PER = 10 \times \left(\frac{T_{max}}{T_{min}} \right) \tag{5.4}$$

where T_{max} is the maximum transmission loss and T_{min} is the minimum transmission loss. The set up used for this measurement is similar to that used in Figure 4.8 (Chapter 4), but with polarizer replaced with a commercial grade polarizer working at 800nm. The PER (maximum and minimum transmission spectra) of the 45°-TFG can then be obtained by changing the PC paddles, which then adjusts the two polarization states of the light lunched into the fibre. The normalized PER (in dB) is then obtained by subtracting the maximum spectra from the minimum spectra. As seen in Figure 5.12 (a) , the entire profile of a 45°-TFG is a near-Gaussian distribution, and can be measured using a tunable laser or a broadband light source (BBS) covering the whole wavelength range. The PER distribution of the UV-inscribed 800nm 45°-TFGs over almost 200nm range has been evaluated.

To carry out the PER measurement at different central wavelengths, the central wavelength of the OSA was set from 690nm to 870nm with an increment of 10nm for each measurement. Once the central wavelength was fixed, the OSA resolution was set to 0.06nm, sensitivity to -75dB and a span of 0nm (in order to measure at the exact central wavelength). The 15mm long 45°-TFG was selected for this measurement. With the use of the polarization controller, the PER was measured at different wavelengths (690nm – 870nm). The results are plotted in Figure 5.12 (a) showing a near-Gaussian profile and the maximum PER of ~16dB at approximately 770nm and the PER values greater than 10dB cover over 70nm span. The PER value at 802.7nm from the plot is approximately 11dB, which agrees well with the PER result using a single wavelength laser diode shown in Figure 5.12 (b).

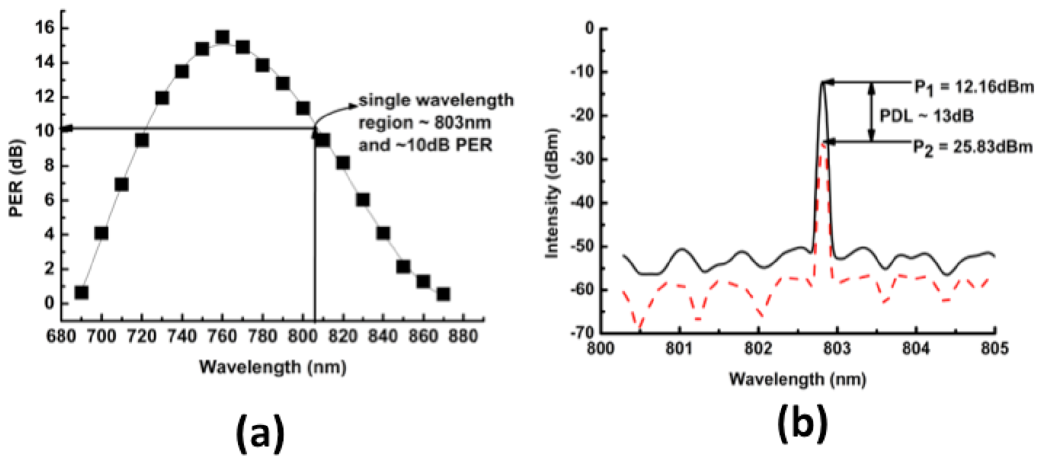

Figure 5.11: (a) The broadband PER profile of a 15mm long 45°-TFG over a 180nm span using HP83437A broadband source, (b) PER measurement of a 15mm long 45°-TFG using a single wavelength laser diode

5.4.2 The Annealing Effect and Effect of Temperature on Grating Profile

The annealing treatment of hydrogen-loaded grating fibre needs to be carried out after UV inscription to remove un-reacted hydrogen from the fibre, as the presence of this un-reacted gas causes instability of the grating structure. The 45°-TFGs reported in this thesis have been annealed at 80°C for 48 hours. For investigation on stability, a 15mm 45°-TFG was annealed at 80°C for 48 hours in an oven. Figure 5.13 shows the comparison of the PER distribution over a wavelength range from 770nm to 830nm before and after annealing. It can be seen clearly from the figure that after annealing treatment, the overall PER values are not significantly affected and reduced by less than 2dB for the whole 60nm range.

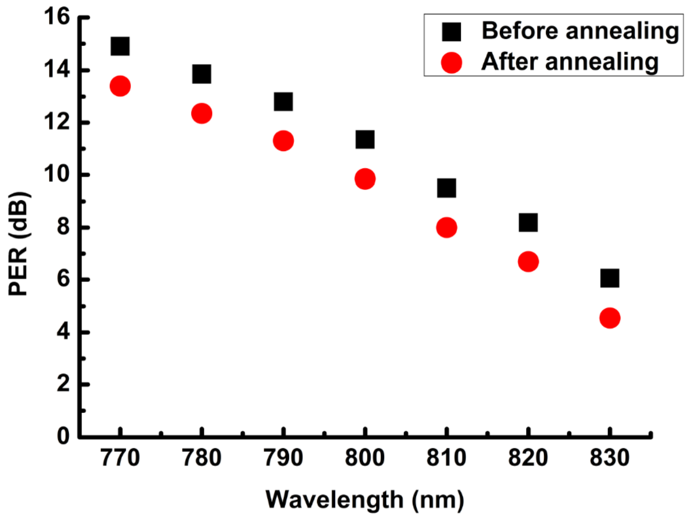

Figure 5.12: The PER profile of a 15mm long 45°-TFG before and after annealing over 60nm span

To further investigate the grating stability, five 800nm 45°-TFGs of different lengths (15mm, 12mm, 9mm, 5mm and 3mm) were fabricated under the same inscription condition (the same power level and scanning speed of the UV beam) showing PER values of 13dB, 10dB, 7dB, 3dB and 1dB at this wavelength, respectively, using a single wavelength laser at 802.7nm. The annealed 45°-TFGs were then subjected to a temperature elevation process from 10°C to 80°C (using the set up described by Yan et al in 2011 [6]) and the PER values at 802.7nm for all five 45°-TFGs with different lengths were monitored. The PER values versus temperature are plotted in Figure 5.14, showing almost no change with increasing temperature. This clearly indicates that all gratings are stable in structure and there is no effect from thermal environment condition changes on the devices.

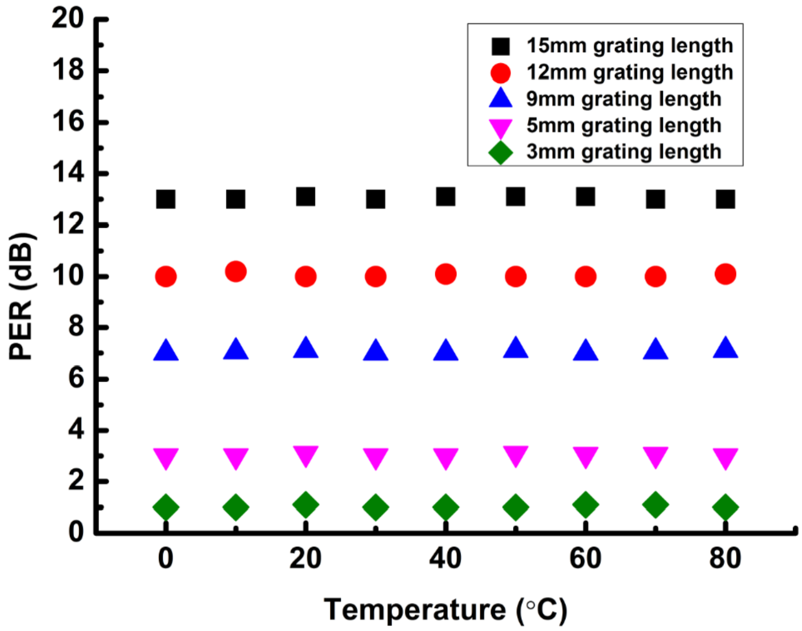

Figure 5.13: (a) Experimental measurement of the PER thermal response of the post- annealed five 45°-TFGs, showing no change with increasing temperature.

5.4.3 Effect of Grating Length On PER

The transmission loss of a 45°-TFG can be expressed as:

$$T = Exp(-\alpha l) \tag{5.5}$$

where l is the grating length and α is the loss coefficient. Equation 5.6 shows that a linear relationship occurs between PER and the grating length. To verify this, the previous five 45°-TFGs of different lengths (15mm, 12mm, 9mm, 5mm and 3mm) in section 5.4.2 were used. The PER result for the individual TFGs is plotted in Figure 5.15:

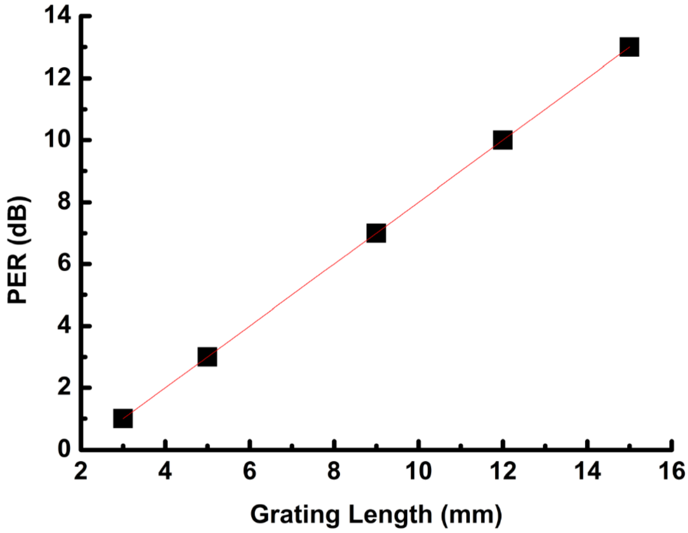

Figure 5.14: The linear relationship between 45°-TFG grating lengths and its PER.

The linear relationship (by combining Equation 5.5 and 5.6) has been verified by measuring the PER values at 802.7nm (Figure 5.15). The plot shows a linear fit with a correlation rate of ~1dB/mm. This linear correlation gives a simple design rule to 45°-TFG based in-fibre polarizer achieving a desirable PER value. Another method used to increase the PER is by concatenating. This helps to overcome the grating length limitation due to the phase mask length (25mm). Figure 5.16 (a) and (b) shows the PER result of concatenating two 15mm 45°-TFGs:

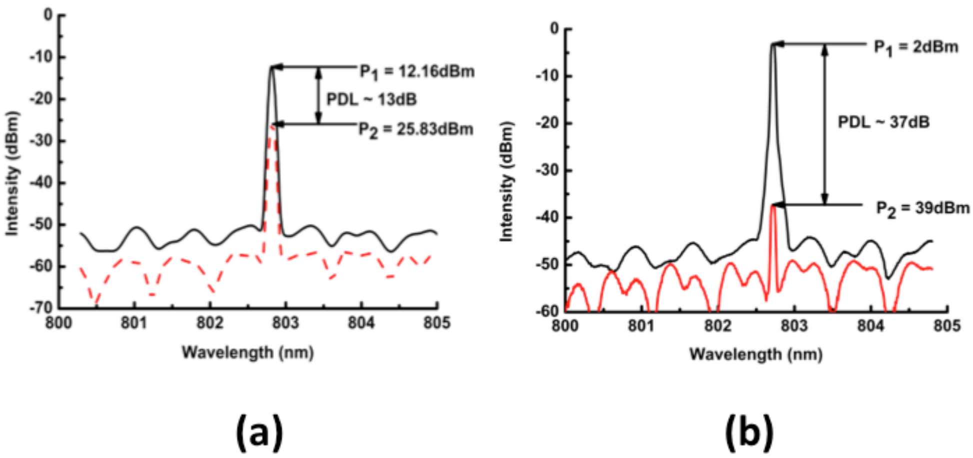

Figure 5.15: (a) PER of a 15mm 45°-TFG at approximately 802nm wavelength showing a PER of ~13dB and (b) the PER of a concatenated 30mm long 45°-TFGs at approximately 802nm wavelength showing a PER of about 37dB.

Figure 5.16 (a) shows the max and min output spectrum of a 15mm long 45°-TFG at 802.7nm; the difference of the two outputs gives the grating PER value as ~13dB. Figure 5.16 (b) shows the measured max and min output spectrum by concatenating two 15mm long 45°-TFGs, doubling the PER value to ~37dB.

5.4.4 Ultra Broadband PER By Concatenating Detuned 45°-TFGs

From Equation 5.4 and 5.5 and the results shown in Figure 5.15, it can be clearly seen and verified that the PER of the 45°-TFG increases linearly with the grating length. Thus, it should be possible to achieve ultra-high PER by concatenating several 45°-TFGs with the same response. However, if the gratings are offset accordingly in central PER response, an in-fibre polarizer with high PERs covering an ultra-broadband should be possible. For this purpose, we have UV-inscribed a standard 22mm long 45°-TFG and another four with structures detuned by +4°, +2°, -2° and -4°, simply by tilting the phase mask using the goniometer on the mounting base. The four detuned 45°-TFGs were measured for PER distribution from 600nm to 950nm using a SuperK Continuum light source (SC450-6 Femto-power 1060 Super-continuum source 450nm 6 Watt).

The six TFGs were fabricated under the same conditions with a grating length of 22mm and a writing speed of 0.2m/s. The first TFG was fabricated with phase mask external tilt angle of 33.7°(without detuning) with the highest PER of ~25dB at 770nm wavelength . The phase mask was then detuned anti-clockwise with an increment of +2° and +4°, meaning the external tilt changed from 33.7° to 35.7° and 37.7°. The actual detuned angles are: 29.7°, 31.7°, 35.7°and 37.7°-TFGs, which has been calculated from the relationship (Equation 5.7) between the external angle (θ_{ext}) and the internal tilted angle in the fibre core (θ_{int}).

$$\theta_{int} = \left(\frac{\pi}{2} - \tan^{-1} \left[\frac{1}{n \tan(\theta_{ext})} \right] \right) \tag{5.6}$$

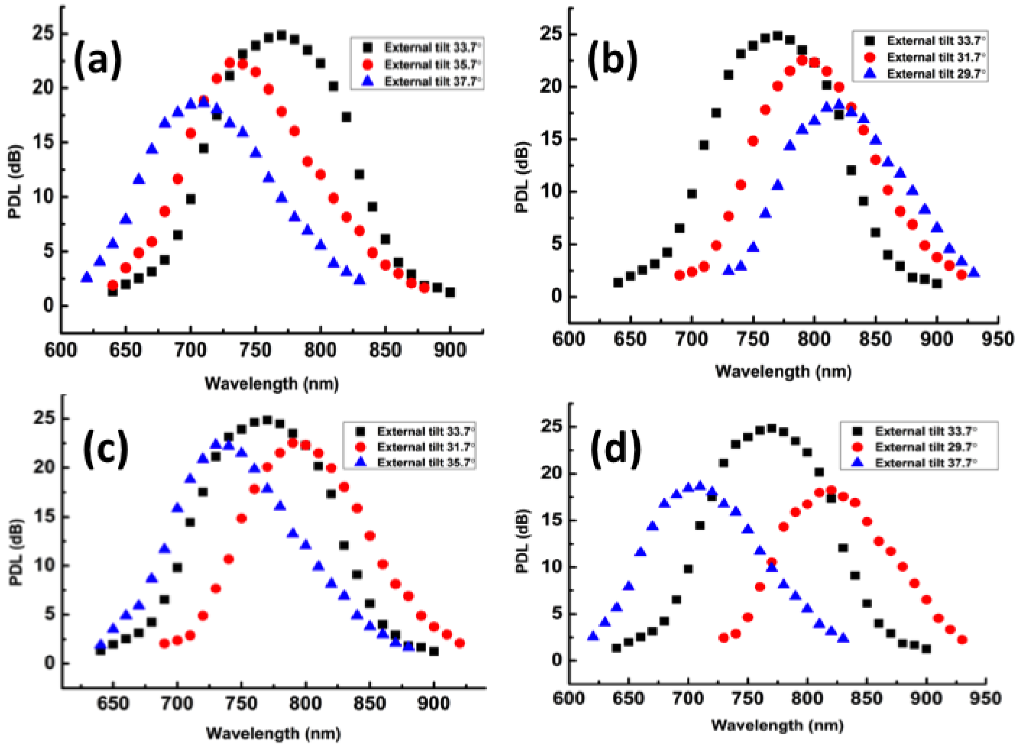

Figure 5.16: (a) The PER profile of a 22mm long 45°-TFG detuned at +2° and +4° to the phase mask tilt angle of 33.7°, (b) the PER profile of a 22mm long 45°-TFG detuned at -2° and -4° to the phase mask tilt angle of 33.7°, (c) The PER profile of a 22mm long 45°-TFG detuned at -2° and +2° to the phase mask tilt angle 33.7°, (d) the PER profile of a 22mm long 45°-TFG detuned at -4° and +4° to the phase mask tilt angle of 33.7°.

The experimental result in Figure 5.17 (a) shows that the central wavelength of the highest PER (un-detuned profile in black) shift to a shorter wavelength (from 770nm to 730nm to 710nm) when the external tilt angle is detuned by +2° and +4°. Likewise, in Figure 5.17 (b), the central wavelength of the highest PER (un-detuned profile in black) shift to a longer wavelength (from 770nm to 790nm to 820nm) when the external tilt angle is detuned by -2° and -4°. It can also be observed all through Figure 5.17 (a)-(d) that the maximum PER reduces due to the detuning of the external tilt angle; this could be due to the reduced interference area after the phase mask as it is been detuned.

Two detuned gratings at angles 31.7°and 35.7° (-2° and +2° respectively) were concatenated; with the grating length of each detuned TFG as 12mm, making an overall grating length of 24mm. The PER profile achieved by concatenating gave an overall PER of about 20.20dB and covers a wavelength range of approximately 300nm as seen in Figure 5.18.

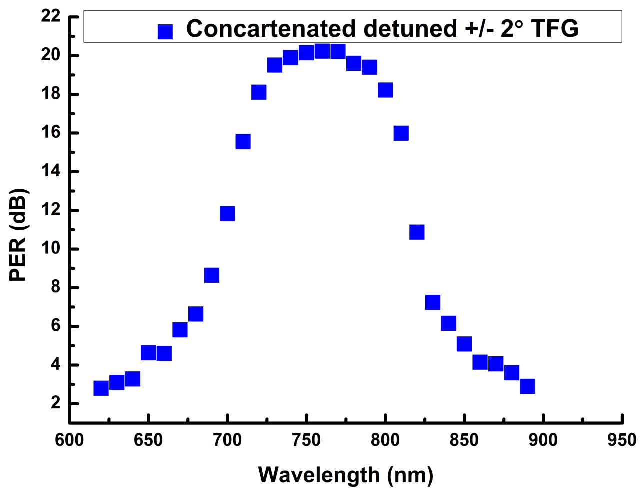

Figure 5.17: The PER profile of a 24mm long 45°-TFG (concatenated 12mm TFGs) detuned at +2°and -2°to the phase mask tilt angle 33.7°, showing a very broad PER spectrum.

To be more specific, such an in-fibre polarizer can have >20dB PER over 100nm. This result is of great significance as it gives a simple method to implement in-fibre polarizers with high PER over ultra-broadband wavelength range.

5.4.5 Polarisation Distribution Measurement

The 45°-TFG, as described earlier, works by coupling out the S-polarized light and propagating the P-polarized light through the tilted grating, giving a linearly polarized response. If the linearly polarized output from the 45°-TFG is coupled into either the slow or fast axis of a polarization maintaining (PM) fibre, the output will show a minimum and a maximum power. The polarization distribution of a UV-inscribed 800nm 45°-TFG with ~13dB PDL has been examined using the set-up shown in Figure 5.19. The two outputs of the polarization beam splitter (PBS) are PM fibres, which means the output light is linearly polarized with orthogonal polarization states. This set-up enables polarized light to be coupled into the fibre with different alignment (rotation) by means of the fibre rotator (rotated from 0° to 360°) [6].

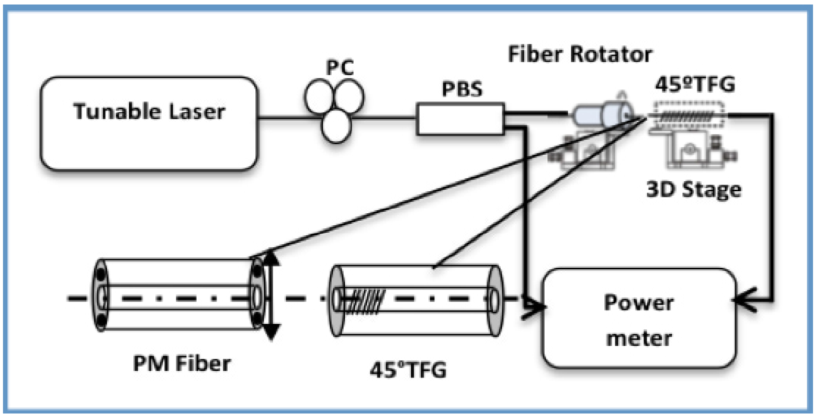

Figure 5.18: Experimental set-up for measuring the polarization distribution of 45°-TFG

The set up in Figure 5.19 consists of a tunable laser, PC, fibre polarisation beam splitter (PBS), a fibre rotator, a 3D stage, a dual channel power meter and polarisation maintaining (PM) fibre. The PBS has two output ports (using PM fibres) which produces linearly polarised light with orthogonal polarisation states. One of the output polarised light goes to one channel of the power meter as a reference and the other output from the PBS goes to through the fibre rotator which is butt-coupled to the 45°-TFG. The second chanel of the power meter is then connected to the output of the 45°-TFG. By rotating the PBS output through the fibre rotator, the polarisation distribution of a 15mm 45°-TFG was measured and compared to the polarisation distribution of a bare optical fibre. The transmission distribution shows a uniform power distribution from a fibre without a TFG (Figure 5.20 (a)) as it has no polarizing function and a figure-8 shape from a 15mm long 45°-TFG with ~13dB PER (Figure 5.20 (b)). The closeness of the figure-8 clearly indicates the strength of polarizing function of the grating.

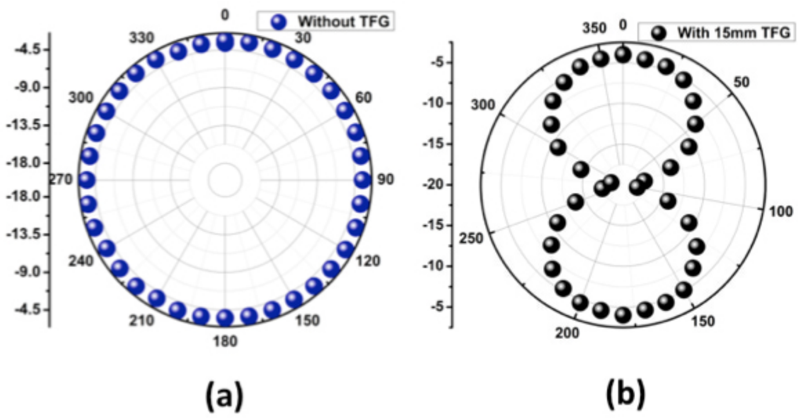

Figure 5.19: (a) The Polarization distribution in a plain fibre with 0dB PER; (b) the polarization distribution of an 800nm 45°-TFG (15mm in length) with ~13dB PER.

5.5 *POWER TAPPING FUNCTION AND MEASUREMENT*

5.5.1 Introduction

Power tapping, also known as optical tapping, is the process of monitoring and measuring the average signal intensity through an optical fibre via a fractional power tapped out from the side of the fibre. It is a concept that exploits the propagation of light in optical fibres through total internal reflection, i.e. the light radiates out of the cladding when the angle of incidence is less than the critical angle [18]. Over the years different methods have been used to tap light out of a fibre; fibre bending, evanescent coupling and scattering [19]. The complete analyses of TFG structures using the volume current method and the coupled mode theory method have been explored in previous literatures [2][20]. The 45°-TFG also acts as a reflector which is wavelength dependent [21]. This however causes the reflected light to leave the fibre core at an angle that depends on a resonance condition between the wavelengths, blaze angle and period of the fringes. The relationship between the period and tilt angle can be expressed as [22]:

$$\Lambda \cos(\theta) = \frac{\lambda}{2n} \tag{5.7}$$

The angle dispersion of a grating can be expressed as: [22]

$$\frac{\partial \beta}{\partial \lambda} = -\frac{n \sin(\theta) \Lambda}{n^2 \Lambda^2 - 2n\lambda\Lambda \cos(\theta) + \lambda^2} \tag{5.8}$$

Equation 5.9 shows that for a given λ_0, the maximum angle of dispersion occurs when θ = 45°. The conventional tapping devices in this category are the fused coupler, which is used to tap light into another fibre for monitoring signals. A power tapper would be ideal for applications like network monitoring, fibre laser systems, fibre optic sensors, real time in-line test and measurement and optical amplifier gain monitoring. Since the side-tapped light is highly directional, it can also be used to measure return losses instead of transmitted power. According to its unique polarization property, a 45°-TFG is a natural side power tapper, as S-polarization light is coupled out from the grating fibre and the amount of the out-coupled light depends on the grating strength. For this function and application, the side power tapping property of 800nm 45°-TFGs has been systematically investigated.

5.5.2 Side Tapped Power Distribution Measurement

The experimental set-up used to measure the side-tapped and transmitted power from a 45°-TFG fibre is shown in Figure 5.20. For the measurement, the single wavelength light source used is a 802.7nm laser diode from LUMICS. An InGaAS amplified detector (700nm -1800nm) from Thorlabs connected to an oscilloscope was used to measure the power from the side of the 45°-TFG. The other end of the grating fibre was connected into a power-meter to measure the transmitted light.

Figure 5.20: Experimental set-up used for the power tapping measurement; comprising of an 800nm butterfly laser diode, power meter, polarization controller, silicon photo-detector, an oscilloscope, fibre holder, a 3D stage and a 45°-TFG at 800nm

By replacing the 800nm laser diode in Figure 5.20, the first side-tapped experiment was carried out by lunching a BBS (SuperK light source from 450nm to 2400nm) and a red light source at 633nm into the device using the set up in Figure 5.20; the image of the out-coupled light was captured using a digital camera; images observed are shown in Figure 5.21 (b) and (c). In Figure 5.21 (b), different wavelengths (colours – green, yellow, red) are seen and, with the appropriate filter, a single wavelength can be selected; Figure 5.21 (c) shows the image of the red light lunched out coupling from the grating area of the fibre. Using the set up in Figure 5.20, the side tapped power was measured for 800nm 45°-TFGs of five different PERs, this was performed to analyse the effect of PER on the side tapped power measured. The grating PERs are 1dB, 3dB, 7dB, 10dB and 13dB respectively. As the 800nm laser diode was launched into the fibre; it can be seen that as the PDL of the grating increases, the side tapped power increases and the transmitted power decreases. Therefore the amount of transmitted power can be carefully controlled to suit a specific application.

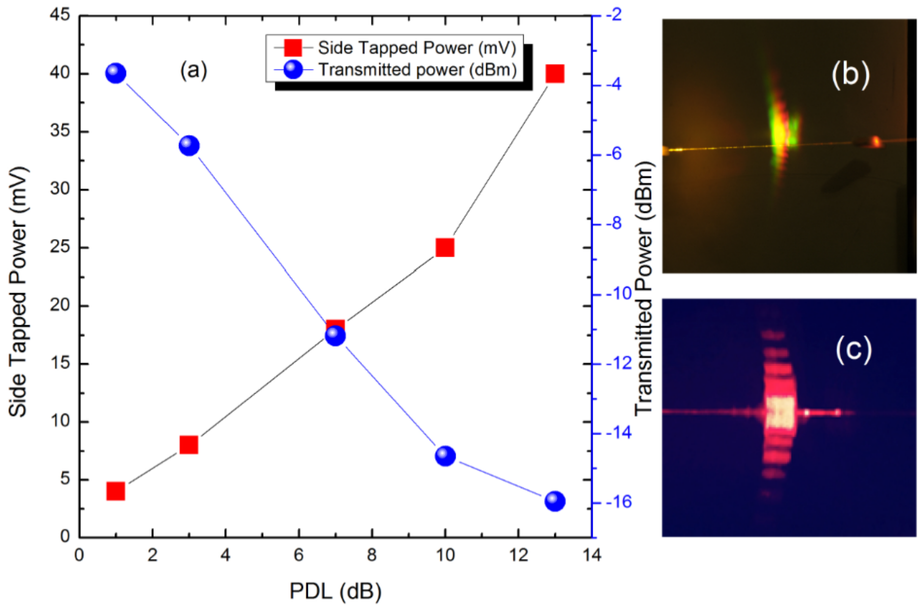

Figure 5.21: (a) the relationship showing the amount of side tapped power and PDL (b) Captured image of white light through the 45°-TFG grating and (c) captured image of red light through the 45°-TFG grating.

To further investigate the side tapped diffraction pattern, the power distribution over the entire grating length (9mm long 45°-TFG) was measured by mounting the photodiode unto a translation stage, moving in 1mm steps. The result (Figure 5.22 (a)) shows the power is highest at the start of the grating, but reduces as the photodiode scans close to the end of the grating length.

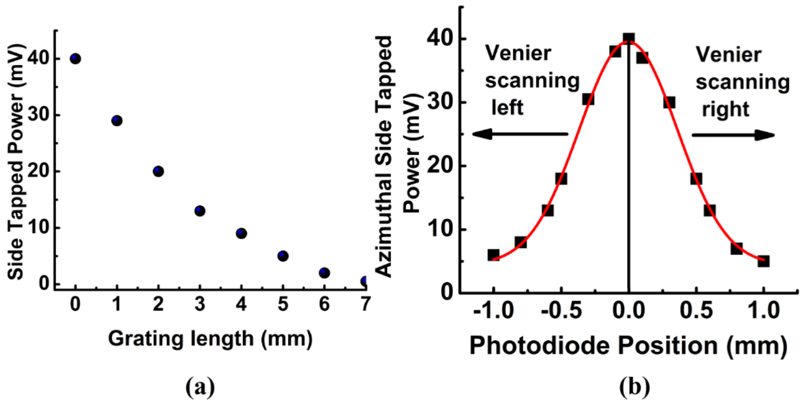

Figure 5.22: (a) Side tapped power distribution along the TFG length (b) measured power distribution in azimuthal direction along a 9mm 45°-TFG, showing a Gaussian profile

The 9mm long grating sample, which has a modest PER, was analysed by scanning the detector along the 45°-TFG. The side-tapped power distribution along the grating length (azimuthal direction by moving the photodiode in the lateral dimension) is plotted in Figure 5.22 (b) and Figure 5.23. A Gaussian fit was applied to Figure 5.22 (b) to generated Figure 5.23.

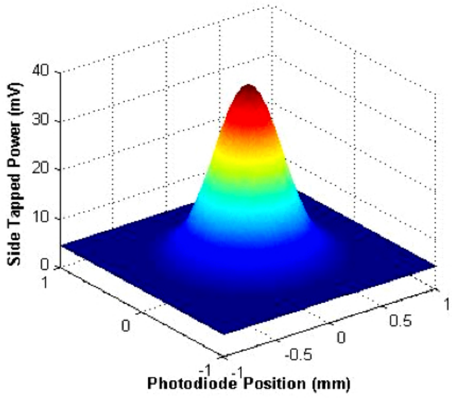

Figure 5.23: Gaussian profile generated from the measurement seen in Figure 5.22 (b) using Matlab

5.5.3 Side Tapped Beam Characterisation And Dispersion Measurement

To be able to effectively use this device as a power tapper, the side-tapped beam size from the 45°-TFG was measured using the set-up shown in Figure 5.24.

Aston University

Illustration removed for copyright restrictions

Figure 5.24: Schematic diagram of the experimental set-up for the side tapped beam characterizing and dispersion measurement.

A LC100 CCD-array from Thorlabs with a 14μm pixel size was used to view the radiation beam size from the 45°-TFG via the LabView program used to capture the CCD-array data. The set-up is such that the CCD camera is moved close (<0.5mm) to the 45°-TFG, which is mounted on a 3D stage. A 2mm diameter cylindrical rod is placed almost touching the 45°-TFG to focus the radiated beam in the x-direction and the CCD-array is placed at approximately 100mm from the cylindrical rod. This set-up was essential to enable easy alignment of the side-tapped beam to the CCD-array. The CCD was mounted on a motorized stage and placed in the plane of the side-tapped beam. The initial alignment of the side tapped beam to confirm its direction was carried out using a He-Ne red light source.

After the alignment, the light source was changed to a single wavelength laser diode operating at 802.7nm. The CCD array was then scanned across the radiation beam profile to measure the side tapped beam width. For this experiment, a short (1mm) 45°-TFG and a medium length (10mm) 45°-TFG were examined. For the 1mm 45°-TFG, the CCD measurement confirms the length of the 45°-TFG under test, as 100 pixels (Figure 5.25 (a)) of high intensity were shown, giving 100x14μm = 1.4mm, which is broader than the actual grating length of 1mm due to the edge illusion effect.

For the 10mm long 45°-TFG, as shown in Figure 5.25 (b), 750 pixels of high intensity were measured, giving 750×14μm = 10.5mm, which verified the grating length more accurately. It can be observed from the side tapped beam width measurement for both the 1mm 45°-TFG and 10mm 45°-TFG that there was a difference of 0.4mm and 0.5mm respectively, in comparison to the calculation. This difference is due to systematic errors in the measurement.

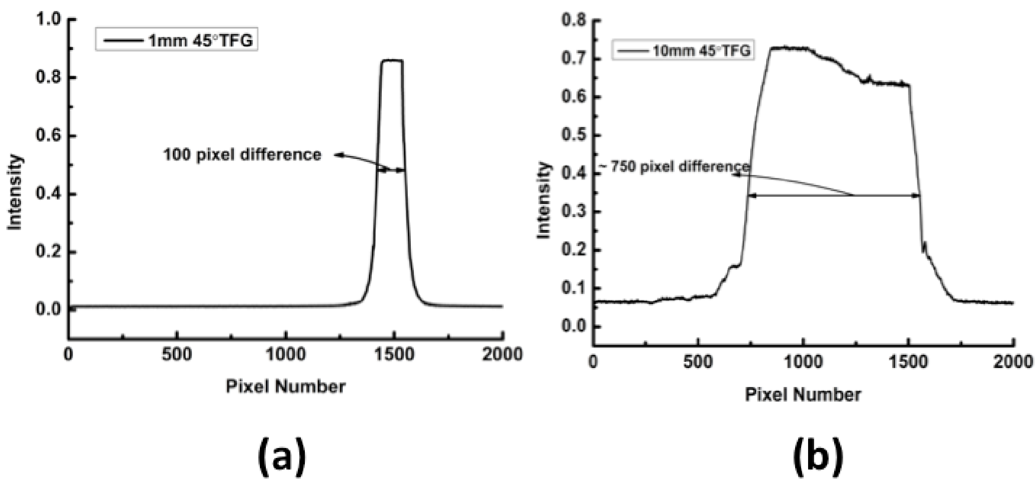

Figure 5.25: (a) Measurement of the side tapped beam width of a 1mm 45°-TFG, (b) measurement of the side tapped beam width of a 10mm 45°-TFG

The outcome of this measurement means that we are able to select the right grating length that will give the right side tapped beam size for the appropriate silicon photo-detector, hence improving the efficiency of the device. It also means that it is possible to measure the whole size and intensity distribution of the side tapped beam from a 45°-TFG, which would be suitable for applications of a power-tapping device. The side tapped beam was also analysed with a 2D camera to observe the dispersion of the side tapped light by moving the 2D camera (on a motorized stage) at various distances from the 10mm 45°-TFG, without the use of the 2mm diameter cylindrical rod. The result (Figure 5.26 (a)-(d)) shows that the intensity of side tapped light was highest and sharp when the 10mm 45°-TFG was 1mm away from the 2D camera, but as the 2D camera moves in 5mm steps away from the 10mm 45°-TFG, the side tapped light became weaker and less focused. Its is important to understand this in order to ensure all the side-tapped power is efficiently captured by the detector.

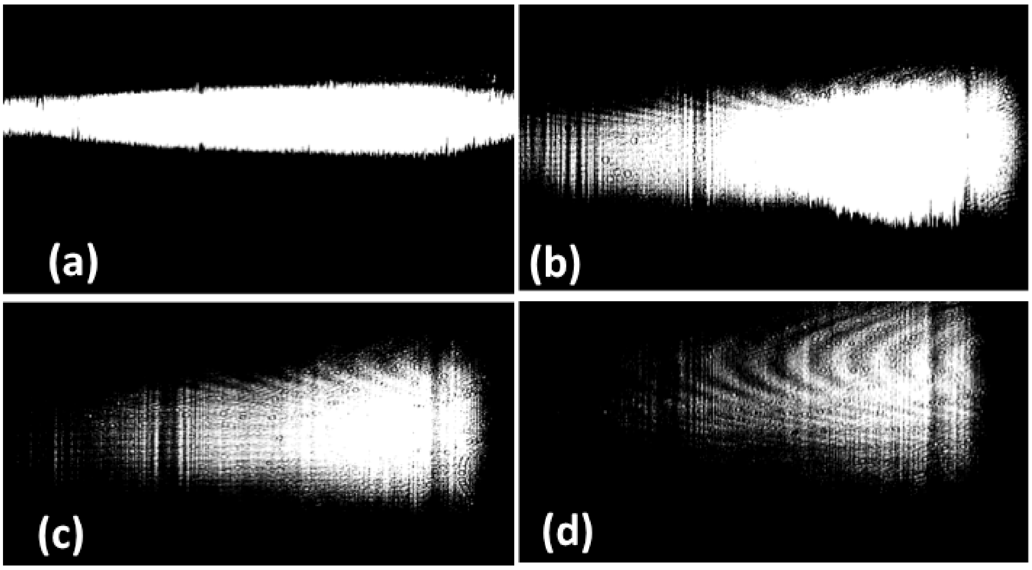

Figure 5.26: (a) Measurement of the side tapped beam dispersion of a 10mm 45°-TFG with 2D camera at 1mm from TFG, (b) measurement of the side tapped beam dispersion of a 10mm 45°-TFG with 2D camera at 5mm from TFG, (c) measurement of the side tapped beam dispersion of a 10mm 45°-TFG with 2D camera at 10mm from TFG and (d) measurement of the side tapped beam dispersion of a 10mm 45°-TFG with 2D camera at 15mm from TFG.

Thus, for a real device, a suitable grating length must be chosen in order to maximize the efficiency of the power-tapping device.

Another factor that needs considering is the azimuthal dispersion of the side tapped beam at various distances between the CCD camera and the 45°-TFG; in this investigation it was realized that the dispersion only occurs in the azimuthal direction, but the horizontal section of the beam remains unchanged at various distances between the CCD and the 45°-TFG. This experiment was carried out for both the 1mm and 10mm grating 45°-TFG. The results are shown in Figure 5.27 (a) and Figure 5.27 (b) shows the dispersion in the azimuthal direction as the distance between the

CCD camera and the 45°-TFG increases for a 1mm and 10mm long 45°-TFG respectively.

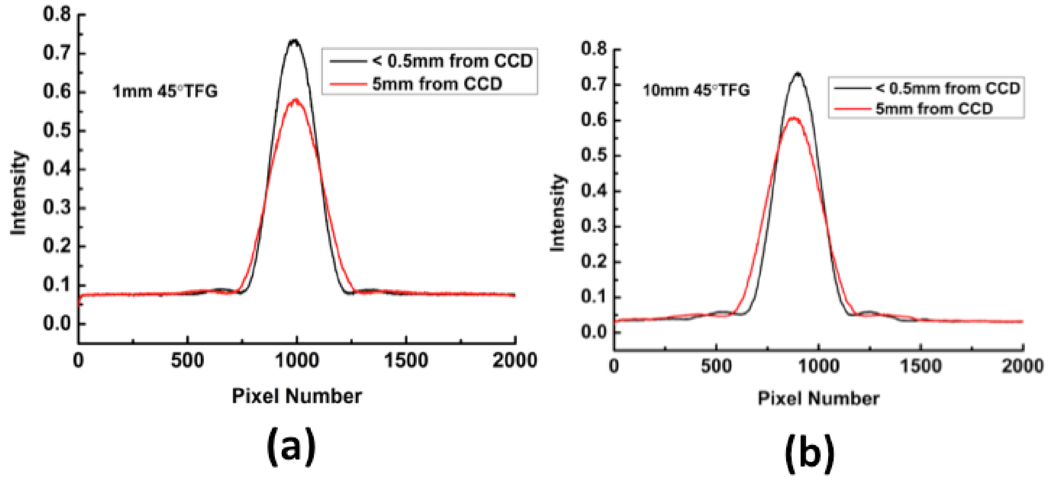

Figure 5.27: (a) Azimuthal dispersion measurement of the 1mm 45°-TFG sample, (b) Azimuthal dispersion measurement of the 10mm 45°-TFG sample

The spectral width of the CCD spectrum increases (pixel number difference) as the distance between the CCD and 45°-TFG increases. It should also be noted that the intensity of the detected side tapped power by the CCD camera decreases (from 0.75 to 0.57 for the 1mm 45°-TFG and from 0.75 to 0.62 for the 10mm 45°-TFG) as the distance between the CCD camera and the 45°-TFG increases.

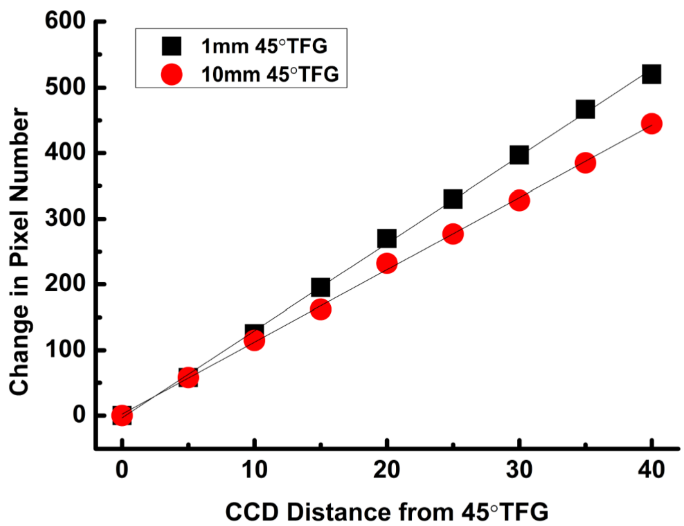

Figure 5.28: Dispersion rate comparison between the 1mm 45°-TFG and the 10mm 45°-TFG.

Further analysis shows that the result in Figure 5.28 reflects a linear relationship between the dispersion rates of the side tapped beam and the CCD camera distance from the 45°-TFG; it also shows a slight difference in the rate of dispersion between the 1mm and 10mm 45°-TFG. The rate of dispersion of the 1mm 45°-TFGs is slightly higher than that of the 10mm 45°-TFG, which could be as a result of the length of the 45°-TFG. So a short grating length 45°-TFG is most desirable for fibre tapping applications, as the silicon photo detector is able to capture all the out-coupled light with minimal loss due to dispersion.

5.6 *CHAPTER CONCLUSION*

This chapter was introduced by mentioning the developments in TFGs and its applications in recent years; and concludes that the 45°-TFGs ability to couple out the S-polarisation component of light and leave the P-polarisation component propagating has made it a good candidate for in-line polarisers and power tapping device.

The structure and mode coupling of 45°-TFGs is such that the TE polarization component of light is coupled out of the fibre while the TM polarization state transmits through the fibre. A simulation by Zhou et al also confirms that the strongest coupling wavelength condition occurs when the phase matching condition (tilt angle = 45°) is established. The radiation coupling efficiency is however determined by the index modulation (~10^{-3}) strength and the tilt angle of the grating.

The phase mask fabrication technique was used for the inscription of the TFGs structures. This technique is the most effective method of fabricating TFGs owing to its simplicity, stability repeatability. When the UV beam shines on the phase mask (pitch of 922.46nm and internal tilt of 33.7°), the light is diffracted into different orders (0,± 1,± 2); the TFGs are therefore inscribed using the ± 1 (>40%) orders with the 0 order suppressed (<5%). The hydrogenated PS750 fibre (clamped in place by a fibre holder mounted on a 3D stage) is then placed at the beam interference region after the phase mask. The grating length and speed of fabrication is set by a LabView programme. Also changing (defocusing) the focal length of the cylindrical lens to 1.5mm increases the interference region of the UV beam, at the expense of intensity.

Further analysis of four phase masks was then carried out to analyse the diffraction efficiency of the 0 and the ± 1 orders. One of the four was a commercially made phase masks from Ibsen photonics and the other three was custom made. The outcome of this analysis showed that the phase mask from Ibsen is well suited (with the efficiency of the ± 1 >45% and the 0 order suppressed to <5%) than the custom-made phase masks.

The entire PER profile of the 800nm of the 45°-TFG is near Gaussian in nature, covering almost 200nm. This was measured by using both a BBS and a single wavelength laser diode. The PER measurement shows a linear correlation with the grating length and after post-inscription annealing (at 80°C for 48 hours), the PER variation observed is <2dB. The effect of elevated temperatures on five 800nm 45°-TFG of different grating lengths was also examined and the result shows that the effect of elevated temperature is negligible. The different grating lengths also show different PER values (i.e. the PER increases linearly with grating length). Due to limitation of the phase mask length in inscribing long length gratings with higher PERs, two 15mm gratings were concatenated together (making a grating length of 30mm) yielding a PER of ~37dB.

In order to achieve an ultra broadband PER, a 22mm 800nm 45°-TFG was detuned to give external tilt angles of 35.7°, 37.7° (for the +2 and +4 detuning) and external tilt angles of 31.7°, 29.7° (for the -2 and -4 detuning). The detuned +2 and -2 were concatenated together to give a very broad PER spectrum in comparison to the measured individual PER spectrum. A 15mm 800nm 45°-TFG was selected in comparison to a bare fibre for polarization distribution measurement; the result shows an almost figure 8 for the fibre with the TFG and a complete circle for the bare fibre when the fibre was rotated through 0-360°

Finally, the power tapping application of this device was then examined. The ratio of the transmitted power to the radiated power of 800nm 45°-TFGs with different PERs was first analysed to investigate the effect the PER on the transmitted and radiated power. The result shows that as the PER (PDL) increases the radiated (side tapped power) increases and the transmitted power reduces; meaning that both the transmitted and the side tapped power shows an inverse relationship as the PER increases. The side tapped power distribution across the length of a 9mm TFG was then examined, showing the highest side tapped power at the beginning of the grating and reduces towards the end of the grating length. The azimuthal side tapped power was also measured showing a near Gaussian power distribution. In order to ensure the efficiency of this device, the dispersion of the side tapped light was analysed. The result shows that dispersion increases as the detector moves away from the out-coupled light, but noticed that there is minimal dispersion in the horizontal direction but most dispersion takes place in the azimuthal direction of the TFGs. This analysis means that we are able to select the appropriate grating length and detector for this device. The side-tapped power vs. PDL shows that using this device, it is possible to tap power as small as 1% out of the fibre guided mode, which can be useful in optical communication systems.

5.7 References

[1] T. Erdogan and J. Sipe, "Tilted fiber phase gratings," *Journal of the Optical Society of America A-Optics Image Science and Vision*, vol. 13, pp. 296–313, 1996.

[2] Y. Li, M. Froggatt, and T. Erdogan, "Volume current method for analysis of tilted fiber gratings," *Journal of Lightwave Technology*, vol. 19, no. 10, pp. 1580–1591, 2001.

[3] Y. Li and T. G. Brown, "Radiation modes and tilted fiber gratings," *Journal of the Optical Society of America B*, vol. 23, no. 8, pp. 1544-1555, 2006.

[4] S. Lu, O. Xu, S. Feng, and S. Jian, "Analysis of radiation-mode coupling in reflective and transmissive tilted fiber Bragg gratings.," *Journal of the Optical Society of America. A, Optics, image science, and vision*, vol. 26, no. 1, pp. 91–98, 2009.

[5] K. Zhou, X. Chen, L. Zhang, and I. Bennion, "High extinction ratio in-fiber polarizer based on a 45deg-tilted fiber bragg grating," *OFC/NFOEC Technical Digest. Optical Fiber Communication Conference, 2005.*, vol. 1, 2005.

[6] Z. Yan, C. Mou, K. Zhou, X. Chen, and L. Zhang, "UV-Inscription, Polarization-Dependant Loss Characteristics and Applications of 45{\textdegree}Tilted Fiber Gratings," *J. Lightwave Technol.*, vol. 29, pp. 2715–2724, Sept. 2011.

[7] H. Kogelnik, "Coupled Wave Theory for Thick Hologram Gratings," *Bell System Technical Journal*, vol. 48, no. 9, pp. 2909–2947, 1969.

[8] Z. Yan, *Advanced tilted fiber gratings and their applications.* PhD thesis, Aston University, 2013.

[9] M. J. Adams, *An introduction to optical waveguides.* UMI Books on Demand, 1981.

[10] K. S. Lee and T. Erdogan, "Fiber mode coupling in transmissive and reflective tilted fiber gratings.," *Applied Optics*, vol. 39, no. 9, pp. 1394–1404, 2000.

[11] K. Zhou, L. Zhang, X. Chen, and I. Bennion, "Low thermal sensitivity grating devices based on ex-45?? tilting structure capable of forward-propagating cladding modes coupling," *Journal of Lightwave Technology*, vol. 24, no. 12, pp. 5087–5094, 2006.

[12] G. Meltz, W. Morey, and W. Glenn, "In-fiber Bragg grating tap," in *Optical Fiber Communication Conference*, vol. 1169, p. 6108, 1990.

[13] K. O. Hill, B. Malo, F. Bilodeau, D. C. Johnson, J. Albert, and K. Hill, "Bragg gratings fabricated in monomode photosensitive optical fiber by UV exposure through a phase mask Bragg gratings fabricated in monomode by UV exposure through a phase mask photosensitive optical fiber," *Albert Appl Phys Lett*, vol. 1035, pp. 1035–1037, 2005.

[14] D. Z. Anderson, V. Mizrahi, T. Erdogan, and A. E. White, "Production of in-fibre gratings using a diffractive optical element," *Electronics Letters*, vol. 29, no. 6, pp. 566–568, 1993.

[15] G. Meltz, W. W. Morey, and W. H. Glenn, "Formation of Bragg gratings in optical fibers by a transverse holographic method.," *Optics Letters*, vol. 14, no. 15, pp. 823–825, 1989.

[16] P. Noutsios and S. Poirier, "PMD assessment of installed fiber plant for 40 Gbit/s transmission," in *Proceedings of the National Fiber Optics Engineers Conference 2001*, pp. 1342–1347, 2001.

[17] N. Y. Kim, D. Lee, H. Yoon, J. Park, and N. Park, "Limitation of PMD compensation due to polarization-dependent loss in high-speed optical transmission links," *IEEE Photonics Technology Letters*, vol. 14, no. 1, pp. 104–106, 2002.

[18] M. Z. Iqbal, H. Fathallah, and N. Belhadj, "Optical fiber tapping: Methods and precautions," in *High Capacity Optical Networks and Enabling Technologies (HONET), 2011*, pp. 164–168, IEEE, 2011.

[19] K. Shaneman and S. Gray, "Optical network security: technical analysis of fiber tapping mechanisms and methods for detection & prevention," *IEEE MILCOM 2004. Military Communications Conference, 2004.*, vol. 2, pp. 711–716, 2004.

[20] H. F. A. Ab-Rahman, "New Design of Wavelength Demultiplexer Based on Tilted Grating in Glass Waveguide for First Window Operating wavelength," *Australian Journal of Basic and Applied Sciences*, vol. 3, no. 3, pp. 2602–2607, 2009.

[21] M. J. Holmes, R. Kashyap, and R. Wyatt, "Physical properties of optical fiber sidetap grating filters: Free-space model," *IEEE Journal on Selected Topics in Quantum Electronics*, vol. 5, pp. 1353–1365, 1999.

[22] K. Zhou, X. Chen, Z. Yan, A. Adebayo, and L. Zhang, "Optical Spectrum Analyzer using a 45° tilted fiber grating," *Optical Society of America*, pp. BW2E–7, 2012.

6 45°TFB BASED SPECTROMETER

6.1 *INTRODUCTION*

Optical taps using TFGs as a side detection system was reported by Meltz [1] and in 1991, Meltz et al filed the first TFG patent [2] and since then Koeppen et al and Perez et al later filed another patent. In 1997, Wagner et al designed a spectrometer based on blazed fibre Bragg grating (BFBG), using a 256-element InGaAs detector array and an index-matching prism (to remove cladding – air gaps). Due to these advancements, researchers have devised several new detection systems based on TFGs, including TFG based interrogation system with three photo-detectors [3], spectrometer (using a chirped TFG and a detector array) [4] and a demodulation device (using a TFG, CCD array and a convex lens) [5]. In 2004, Simpson et al developed a 1550nm-interrogation system based on a TFG-Convex lens-CCD structure, but the design reported in this section would be working at 800nm wavelength range. There are advantages to build spectrometer in this wavelength range, because most commercial CCD-arrays are cheap and sensitive in this wavelength range, light sources at 800nm is cheaper than light sources at 1550nm, compact interrogation systems can be designed at 800nm wavelength range and 800nm interrogation systems can be used to detect biochemical samples, making them viable in the medical, life sciences and environmental applications.

Based on the discussion in Chapter 5 about the spectral characteristics of 45°-TFGs power tapping capabilities, this Chapter, however, explains the design and development of a 45°-TFG based interrogation system working at 800nm capable of true spectral measurement by utilising a CCD linear array and a 45°-TFG. In the second part, we will demonstrate the use of this interrogation system as an optical coherence tomography (OCT) for bio-sensing application.

6.2 45°- TFG BASED INTERROGATION SYSTEM

6.2.1 Principle And System Set-Up Of The Interrogation System

An important application of TFGs is its use as a dispersive grating; coupling light from the forward propagating core mode to radiation modes. These radiation modes are then focused unto a CCD linear array. However, from equation 6.1 the spatial position of the illuminated pixel on a CCD is a function of the wavelength since the radiation angle θ is wavelength dependent.

$$\cos(\theta) = \frac{\frac{\lambda}{\Lambda}\cos(\xi) - n_{eff}k_0}{n_2 k_0} \tag{6.1}$$

where k_0= $\frac{2\pi}{\lambda}$, the equation 6.1 now becomes:

$$\cos(\theta) = \frac{\frac{\lambda}{\Lambda}\cos(\xi) - n_{eff}}{n_2} \tag{6.2}$$

The 800nm interrogation system is made from a TFG (at 800nm), a cylindrical rod, a convex lens and a CCD. The schematic of the laboratory setup for the interrogation system is shown in Figure 6.1. A white-light super-continuum light source (SC450-M, 80 MHz rep. rate, 4ps pulse width, 450-2400nm), by Fianium LTD is used as the broadband light source.

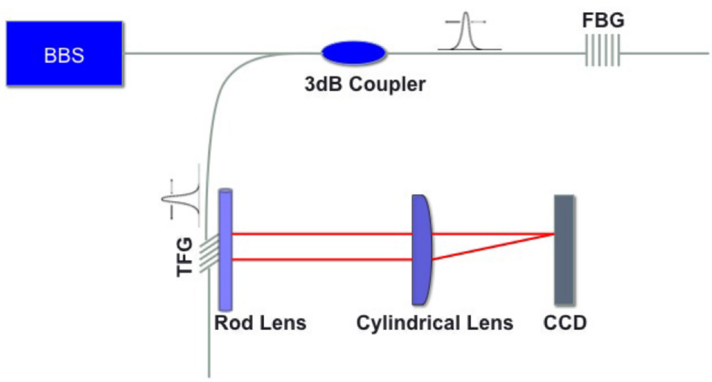

Figure 6.1: Schematic showing the 800nm TFG-CCD interrogation system

The transmission spectrum of the Super-continuum Fianium broadband light source is shown in

Figure 6.2 and it was measured using an optical spectrum analyser (OSA) with an optical resolution of 0.06nm; and also measured with the CCD device (within the wavelength specification of the CCD), showing a full optical bandwidth of 450nm (600nm – 1050nm) and an output power greater than -40dB.

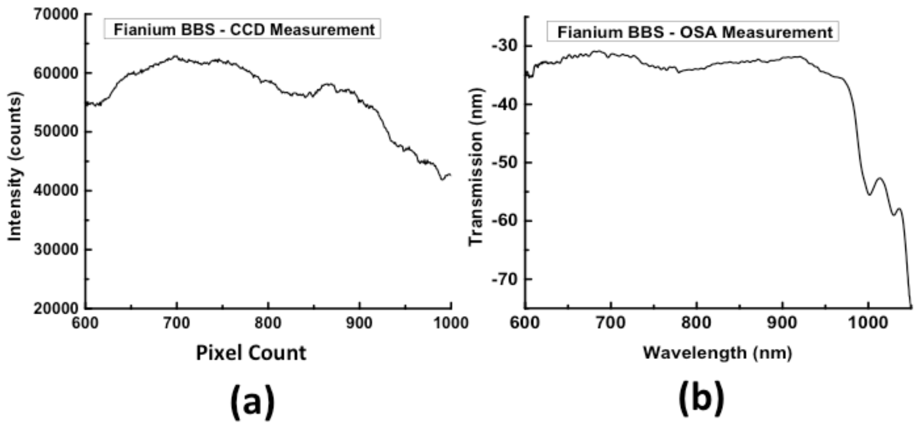

Figure 6.2: Transmission spectrum of the white-light continuum laser by Fianium, measured from 600nm to 1050nm.

The interrogation system has an overall dimension of 210mm length and 150mm width, with an arrangement of: a 2mm diameter cylindrical rod is < 0.5mm from the TFG, the cylindrical lens is placed 45mm from the cylindrical rod and the CCD is placed at the focal point (155mm) of the cylindrical lens. A schematic of this system is shown in Figure 6.3

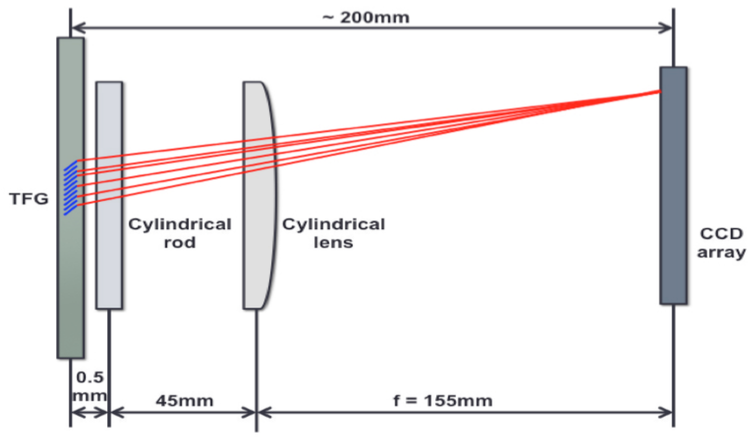

Figure 6.3: The dimensions and arrangement of the 800nm TFG interrogation system as used in the set up shown in Figure 6.1.

The light is lunched into the sensing gratings via a 3dB coupler; with port 1 connecting to the BBS, port 2 connecting to the Bragg gratings and port 3 connecting to the 800nm TFG (passing through the light reflected back from the FBGs), which then radiates to the linear CCD. As mentioned above in Equation 6.2, the direction of radiation is wavelength dependent and it also depends on the fibre used and TFG parameters. To know the wavelength radiated is crucial to correctly analyse the CCD detection and decoding. The CCD-array records the far field radiated light focused by the convex lens, which is related to the wavelength change of the FBG sensor. The reflected signal from the FBG can then be captured by the CCD signal through its spectral spatial transformation function.

6.2.1.1 *Spectral property of the sensing FBG and 45°-TFGs*

The 800nm 45°-TFG used for out-coupling the light was fabricated in hydrogen loaded photosensitive PS750 single mode fibre using the scanning phase mask technique. The transmission spectra of the sensing TFG and FBG are shown in Figure 6.4 (a) and (b). The transmission spectrum of the 800nm 45°-TFG is near Gaussian in nature (Figure 5.12 in Chapter 5), with a radiation range of about 180nm (690nm – 870nm) as seen from Figure 6.4 (a).

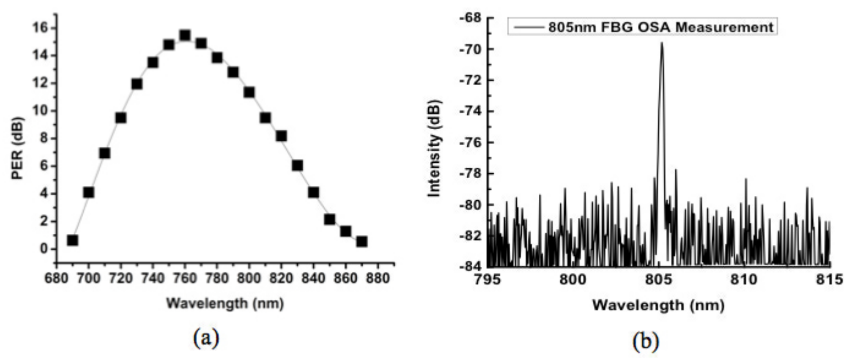

Figure 6.4: (a) The transmission spectrum of an 800nm 45°-TFG, measured in air. (b) The reflection spectrum of the sensing FBG sensor.

A FBG sensor with the Bragg resonance in the TFG radiation range by UV inscription using the two-beam holographic technique; Figure 6.4 (b) shows the reflection spectra of the fabricated FBG, with resonance at 805nm.

6.2.1.2 *Set-up of the 800nm TFG-CCD interrogation system*

Figure 6.5 shows the actual evaluation system set on the laboratory optical table. In this system, the TFG is clamped on both sides to a 3D stage; this helps to keep the grating area straight. Immediately after the grating is a cylindrical rod of about 2mm in diameter. This is glued to a surface mounted on a 3D stage; this makes the alignment of the radiated light from the TFG to the CCD accurate and also focuses the radiated beam in the x-axis in relation to the fibre. The cylindrical lens is placed on a temporal surface for the purpose of this experiment to focus the light in the y-axis and the CCD placed at the focal point of the cylindrical lens. The cylindrical rod is the master lens by which the bandwidth and resolution of the spectrometer system are defined; the cylindrical lens is then used to increase the intensity of the radiated light.

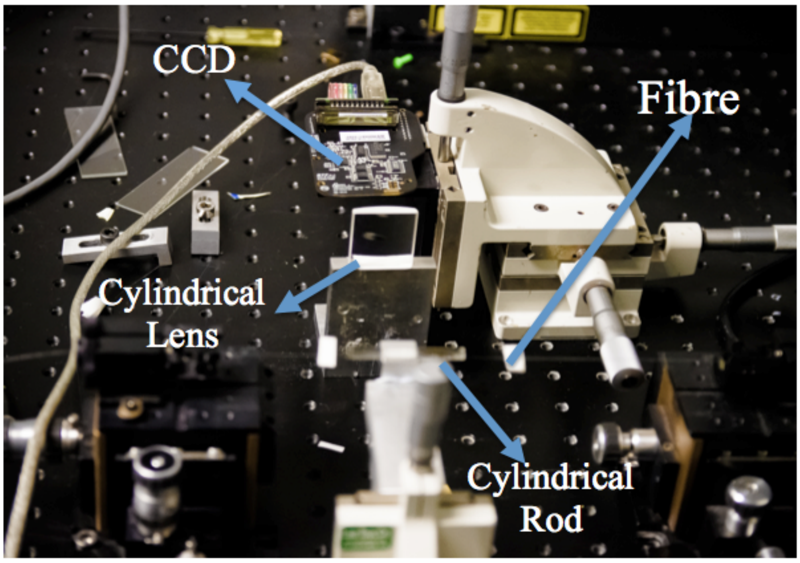

Figure 6.5: The photograph of the experimental setup using the CCD, cylindrical lens, cylindrical rod and TFG.

The Sony ILX511 linear CCD, coated with Y2O2S:Er,Yb (to make it responsive to infra-red (IR) radiation since it was originally made to respond to wavelengths between 400nm and 1000nm) was employed in capturing the out-coupled radiation from the TFG. The CCD device has 2048 pixels with a pixel size of 14µm in length, which makes it low cost and gives it improved sensitivity. The choice of CCD arrays over photodiode arrays is due to the possibility of smaller pixel size, longer arrays and low cost. The spectral sensitivity given by the manufacturer (Figure 6.6) shows that this CCD is intrinsically sensitive to illumination from an 800nm source. The CCD is positioned at a certain distance along the x-axis in the focal plane of the cylindrical lens in the y-axis.

Aston University

Illustration removed for copyright restrictions

Figure 6.6: The manufacturers stated relative sensitivity from 400nm to 1000nm radiation range (Sony ILX511 datasheet).

6.2.1.3 *System alignment*

The initial alignment of the CCD to the out-coupled light from the 45°-TFG was carried out using a 5mW, 633nm red He-Ne laser Source. A screen is placed in front of the light radiated outwards by the TFG, covering the x-y plane of radiation. The visible output is used to set the orientation of the TFG and CCD array. Figure 6.7 (a) shows the image projected from the 633nm He-Ne red laser on the screen without the cylindrical rod and also without cylindrical lens; Figure 6.7 (b) shows the image projected from the 633nm He-Ne red laser on the screen without the cylindrical rod and with cylindrical lens placed before the screen; Figure 6.7 (c) shows the image projected from the Fianium super continuum BBS on the screen without the cylindrical rod and cylindrical lens; Figure 6.7 (d) shows the image projected from the 633nm He-Ne red laser on the screen with the cylindrical rod and without the cylindrical lens placed before the screen; Figure 6.7 (e) shows the image projected from the 633nm He-Ne red laser on the screen with the cylindrical rod and with the cylindrical lens placed before the screen.

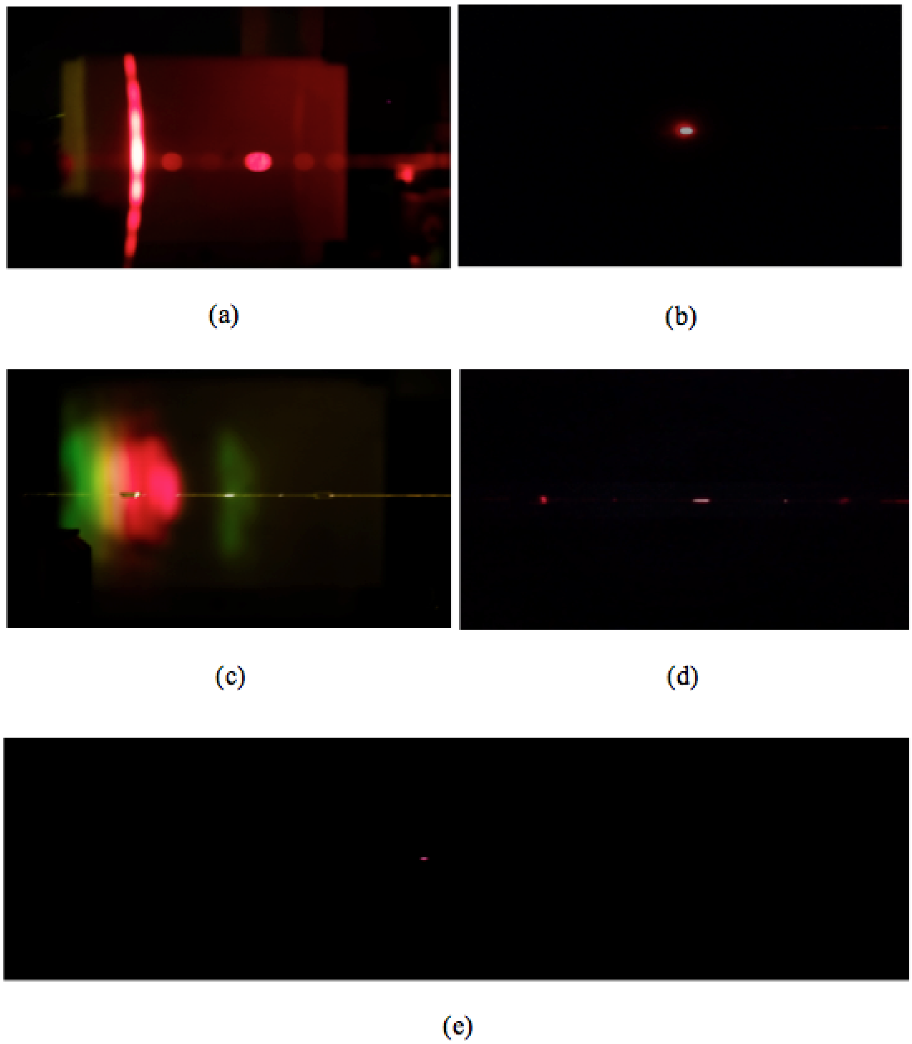

Figure 6.7: The photographic images projected on the screen from the 633nm He-Ne laser; (a) without the cylindrical rod and cylindrical lens, (b) without the cylindrical rod and with the cylindrical lens, (c) using Fianium BBS without cylindrical lens and rod, (d) with the cylindrical rod and without the cylindrical lens and (e) with both the cylindrical rod and cylindrical lens.

It is clear to see that without both the cylindrical rod and lens (Figure 6.7 (a)), the radiation captured on the screen is elongated in the y-axis and there is increase in x-axis. But when the cylindrical lens was placed in the set up, without the cylindrical rod (Figure 6.7 (b)), the radiated light was focused in the y-plane; when a Fianium super continuum BBS was lunched into the fibre, the radiated light shows a series of colours (green, yellow, orange and red) relating to the radiation at different wavelengths (Figure 6.7 (c)); the cylindrical rod was then placed after the fibre at a distance of about 0.5mm without the cylindrical lens, the projected image (Figure 6.7 (d)), shows the focusing of the radiated light in the x-plane; for the full system, both the cylindrical rod and the cylindrical lens were placed before the screen, showing the radiated light been focused both in the x-y plane on a point (Figure6.7 (e)), which will make the CCD detection efficient. The different colours in

Figure 6.7 (c) were then separated into individual colours (Figure 6.8) using a smart phone camera (8MP with 1.5μ pixel and f/2.2 aperture). The colours of green, yellow, orange and red correspond to wavelengths 530nm, 600nm, 630nm and 670nm respectively.

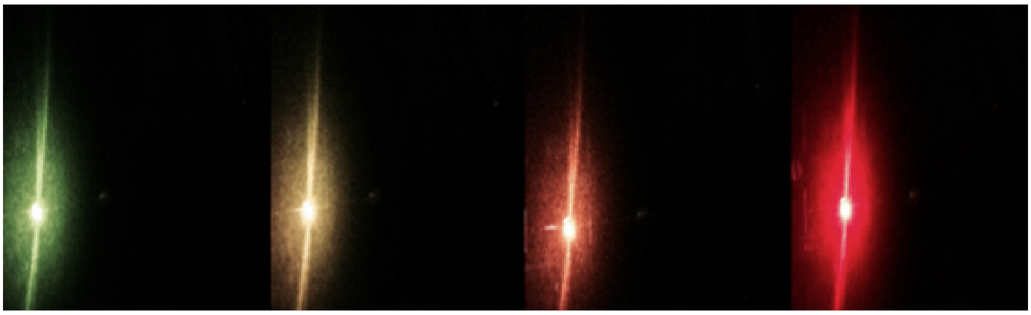

Figure 6.8: The separated colours from Figure 6.7 (c), showing individual colours green, yellow, orange and red corresponding to wavelengths 530nm, 600nm, 630nm and 670nm respectively.

Once a good alignment is achieved using the 633nm He-Ne laser, the different components of the set up are then put in place; with the radiation pattern distributed symmetrically and shift along the screen when the experimental factors (the temperature and strain of the FBG sensor) change.

6.2.1.4 *CCD detected signal – bandwidth and resolution*

Once the CCD–array is in place right at the centre of the radiated light, examples of radiation signals using 800nm laser diode and He-Ne red laser were captured and compared to the measured signal using the OSA, as seen Figure 6.9 (a)-(d).

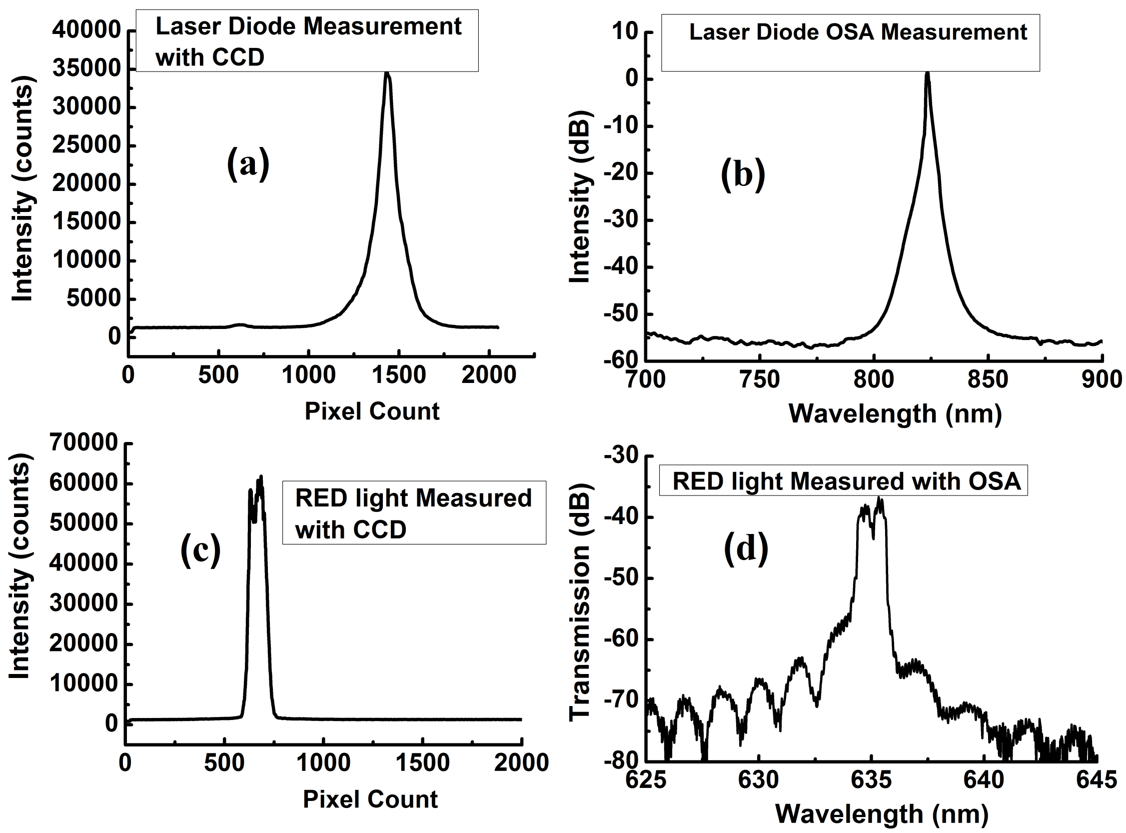

Figure 6.9: (a) Signal captured from an 800nm laser diode by the CCD-array, (b) Signal captured from an 800nm laser diode by an OSA, (c) Signal captured from a 633nm He-Ne laser by the CCD-array and (d) Signal captured from a 633nm He-Ne laser by an OSA.

The captured signals from the laser diode using the CCD and an OSA are almost similar in intensity and width; this is also the same when the 633nm He-Ne laser was measured using the CCD-array and an OSA. Figure 6.9 (c) and (d) possess similar features, but not as identical in comparison to Figure 6.9 (a) and (b).

Due to the finite width of the CCD pixels size (14μm), a consequence of pixilation occurs as the maximum physical resolution of the CCD-array is reached. In order to correct this possible pixilation effect, a function is needed to transfer the signal profile to radiation wavelength. Since this affects the resolution of the system, different algorithms can be applied to improve the resolution [6]. However, the centroid detection algorithm provides a minimal computation time; by taking the amplitude weighted mean of the data using equation 6.3:

$$\hat{x} = \frac{\sum_{1}^{2048} x_i . y_i (> y_{min})}{\sum_{1}^{2048} y_i} \tag{6.3}$$

where $\hat{x}$ is the centroid fitted peak value, x_i is the wavelength of the *ith* element and $y_i(> y_{min})$ is the amplitude of the ith element greater than the noise floor y_{min} .

Bandwidth and resolution are always a trade off that needs to be balanced in this system; as the bandwidth becomes wider, the resolution becomes reduced. The factor that affects the bandwidth of this system is the detection length of the CCD-array, the focal length of the cylindrical lens and the range of radiation of the TFG. In this system, the bandwidth is calculated by multiplying the spectral resolution and the number of pixels. The focal length of the cylindrical lens used in this system is 155mm. Through calculation, a bandwidth of 26nm and a physical resolution of 12.7pm/pixel were deduced. These two parameters then enable the usage of the full length of the CCD array and increases its efficiency.

With the cylindrical lens of 155mm focal length selected, the intensity counts of the CCD-array captured image was analysed, (a) when the focal length of the cylindrical lens was changed by $\pm$ 10mm (in 1mm steps) using the 3D stage and (b) when the focal length stays the same but the 802nm laser diode current was increased from 30mA to 50mA, the results are displayed in Figure 6.10 (a) and (b) below:

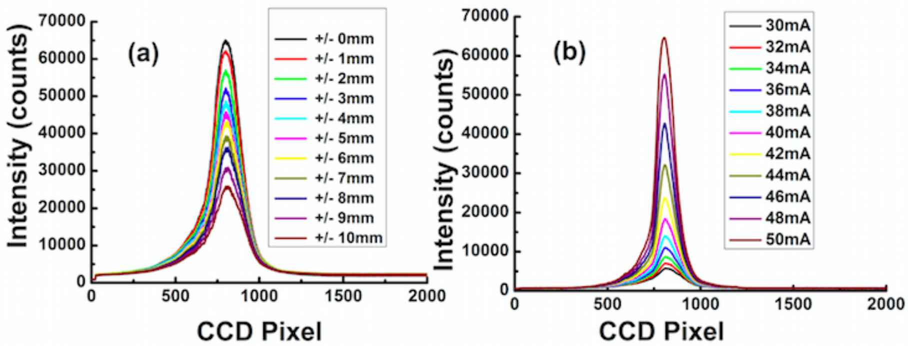

Figure 6.10: (a) The CCD array captured signal when the focal length of the cylindrical lens was changed by $\pm$10mm in steps of 1mm, (b) The CCD array captured signal when the focal length of the cylindrical lens was kept at 155mm and the 800nm laser diode current changed from 30mA to 50mA in steps of 2mA.

The result shown in Figure 6.10 (a) when launched with an 800nm pigtailed laser diode shows that the optimum intensity of the 800nm interrogation system is at the focal point (155mm) of the cylindrical lens, outside this focal point the radiated signal received by the CCD array becomes weaker and not well resolved. Figure 6.10 (b) shows that another factor that can affect the power of radiated signal received by the CCD array is the source power, showing that at the cylindrical lens focal point, the more the laser diode power increases from 30mA to 50mA, the stronger the intensity of the captured signal.

6.2.1.5 *Transfer function of the interrogation system*

Since the CCD measurement is encoded in pixel counts, it is important to correlate the wavelength shift and the CCD pixel by carefully calibrating the spectral-spatial encoding function of the 45°-TFG-CCD system. The reflection signal of the FBG (at 805nm) in Figure 6.4 (b) was used to carry out a strain sensing and the result was used to generate a transfer function for the system. Tension was applied to the FBG sensor (Figure 6.1) and the wavelength shift was monitored on an OSA and the CCD based interrogation system simultaneously. The result in Figure 6.11 shows a linear correlation between CCD reading and the Bragg wavelength shift recorded by the OSA. The conversion coefficient is therefore 11.3pm/pixel for a 155mm focal length, meaning this interrogation system has a resolution of about 11.3pm.

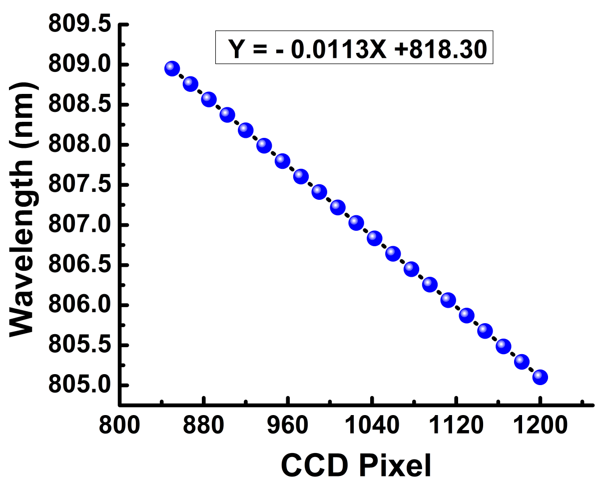

Figure 6.11: The relationship between the CCD pixel reading and the Bragg wavelength shift of the 800nm interrogation system; showing a linear correlation.

6.3 *APPLICATION OF 45°- TFG BASED INTERROGATION SYSTEM*

6.3.1 Temperature Sensing

In order to demonstrate a practical application of the system, a sensor interrogation system employing a WDM sensor array, which was fabricated in SMF with Bragg resonances to coincide with the near Gaussian fitted profile of the 800nm 45°-TFG (Figure 6.4 (a)). The central wavelength of the FBG sensor is at 805nm (Figure 6.4 (b)) and with a strength of ~10dB. This central wavelength was chosen because its around a PER region of 12dB on the 800nm 45°-TFG PER profile, meaning that the TFG will couple out most of the FBG sensor reflected signal changes.

6.3.1.1 *Experimental set up*

The experimental arrangement for using 45°-TFG interrogation units to monitor FBG temperature sensing is shown in Figure 6.12. The FBG sensor is carefully placed in a peltier heating unit connected to a temperature controller, which is used to increase the temperature applied to the FBG sensor, while capturing the wavelength shift with the CCD array. The temperature was elevated from 10°C to 70°C with 10°C intervals; the temperature controller reading was allowed to settle for 10mins between each temperature change to ensure an equilibrium temperature reading. By inserting a 2mm cylindrical rod and a cylindrical lens of 155mm focal length between the 45°-TFG and the CCD array, the losses surrounding the coupling of the radiation modes from the 45°-TFG to the CCD array was reduced. The high power Fianium Super continuum BBS was chosen, with the sensing FBG connected to the output of the 3dB coupler and the return port of the coupler connect to the 45°-TFG; enabling the FBG sensors reflected signal to be radiated onto the CCD array which enables a data capture through a software system.

Figure 6.12: The schematics of the 800nm interrogation system based on 45°- TFG and CCD for temperature sensitivity.

6.3.1.2 *Experiment result and discussion*

The FBG sensor was monitored in varying temperarute environments. Figure 6.13 (a)-(g) show a series of 7 intensity profiles captured using the CCD array at elevated temperatures of 10°C to 70°C. Observed is a red shift in the CCD pixel and the data were converted to wavelength shifts against temperature change as shown in Figure 6.13 (h). From this plot we estimate the temperature sensitivity is ~5pm/°C; which is in a similar order with the temperature results of 6.8pm/°C reported by [7]. The intensity was maintained throughout all the temperature measurements, owing to a stable set up.

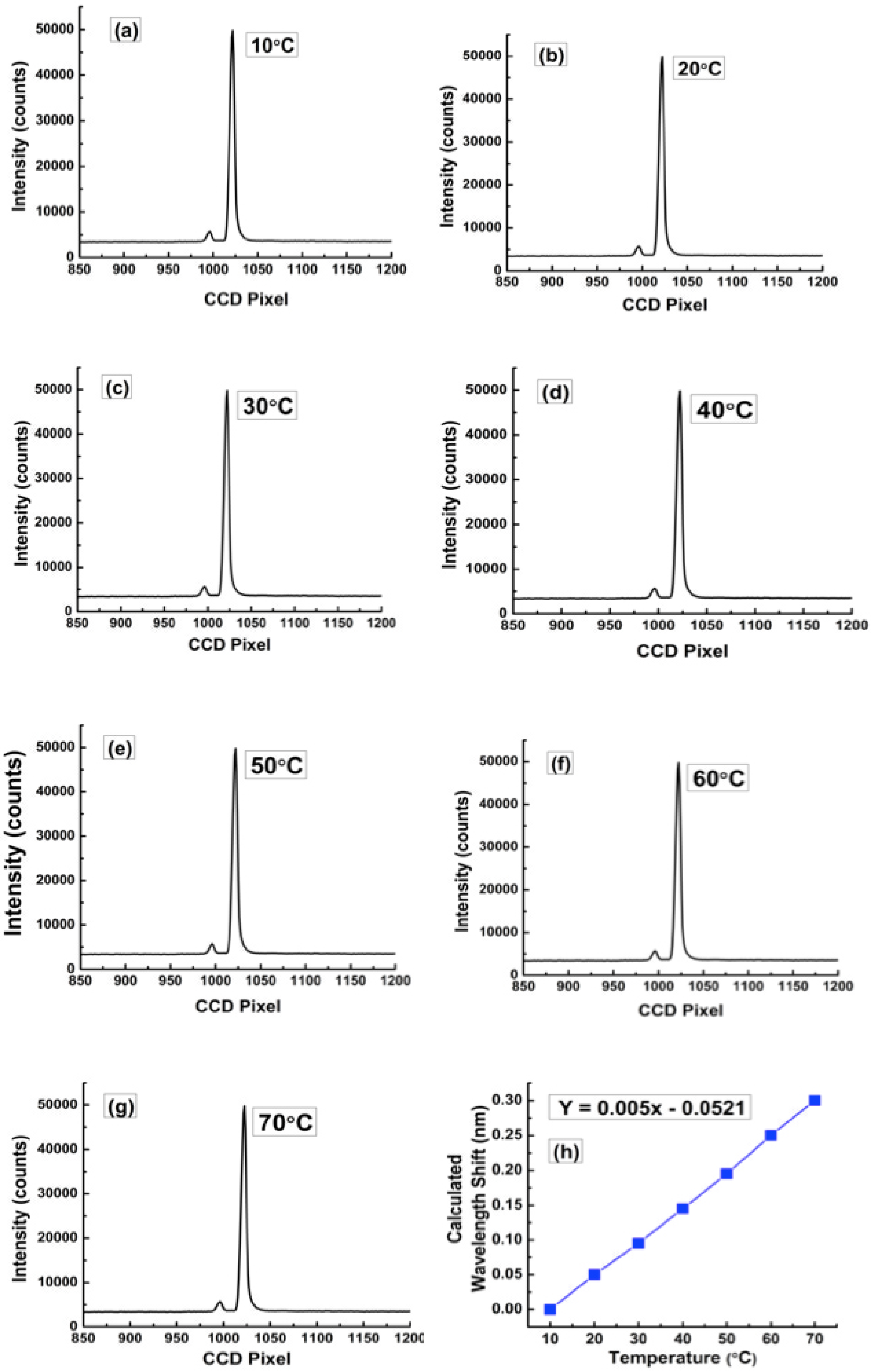

Figure 6.13: (a)-(g) The intensity profiles of FBG captured by the 800nm 45°- TFG and CCD based interrogation unit under temperature change from 10°C to 70°C; (h) Converted wavelength shift against temperature for the FBG sensor.

In order to confirm this result, an OSA interrogated the same FBG sensor and the captured spectrum for each temperature is shown in Figure 6.14 (a) and the wavelength shift against temperature is plotted in Figure 6.14 (b)

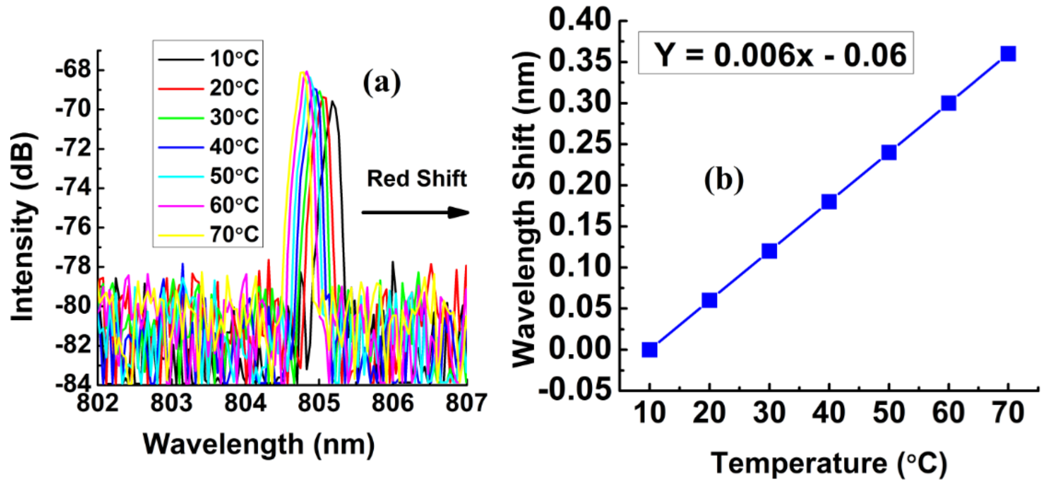

Figure 6.14: (a) The reflection spectra for all temperatures captured by the OSA system; (b) the plot of wavelength shift against temperature.

In Figure 6.14 (a), the reflection signal from the FBG sensor operating at 805nm shifts to the longer wavelength as the temperature of the heating unit is elevated from 10°C to 70°C. The wavelength shift for this temperature change is recorded as 6pm/°C. This is very close with a 1pm/°C difference to the temperature sensitivity measured using the 800nm 45°-TFG and CCD interrogator (Figure 6.13 (h)). This clearly demonstrated the proposed and developed 45°-TFG and CCD based interrogation unit is capable of monitoring FBG temperature sensing, which is a low-cost and much more compact interrogation system than an OSA and should be suitable for real applications in the field.

6.4 *BIOLOGICAL APPLICATION*

6.4.1 Application In Optical Coherence Tomography (OCT)

Building spectrometers with diffraction gratings is common practice. Though such spectrometers can show high performance, the miniaturization of these devices is restricted by the diffraction limit that necessitates expansion and focusing of the beam. Furthermore, the number of components and the long-term alignment drives the costs for low maintenance and high-resolution instruments. An approach to miniaturize devices and thereby increase their stability is to combine functionalities of different optical components into one, such as with classic concave gratings that integrate the grating with the focusing element [8] or arrayed waveguide gratings that found examples of applications in spectrometers for biomedical imaging [9]. These approaches suffer from high complexity of the manufacturing process. A tilted fiber grating acting as the dispersive element can be integrated via a rather simple inscription process directly into the optical fibre, which is already an intrinsic component of the optical set-up. The principle realization of a high resolution tilted fibre Bragg-grating (TFBG) Optical Spectrum Analyzer (OSA) was demonstrated [4], [10]. Its simplicity and high potential for efficient light collection makes it appealing for low-cost high-resolution spectrometry, and spectral imaging techniques like Spectral Domain Optical Coherence Tomography SD-OCT. OCT is a well-established technology to generate non-invasive cross-sectional depth resolved 2-dimensional and 3-dimensional tomograms of biological tissue by measuring the backscattered and back-reflected light [11–13] that encodes depth information in a spectral interference signal.

A compact, fibre-based spectrometer for biomedical application utilising a tilted fibre grating (TFG) as an integrated dispersive element is demonstrated via collaborative work between Bern University of Applied Sciences, Bangor University, Jiangnan University and Aston University. Based on a 45° UV-written in PS750 TFG, a refractive spectrometer with 2.06 radians/µm dispersion and a numerical aperture of 0.1 was set-up and tested as an integrated detector for an OCT system. Featuring a 23mm long active region in the fibre, the spectrum is projected via a cylindrical lens for vertical beam collimation and focused by an achromatic doublet onto the detector array. Covering 740nm to 860 nm, the spectrometer was optically connected to a broadband white light interferometer, a wide field scan head and electronically to an acquisition and control computer. Tomograms of ophthalmic and dermal samples obtained by the frequency domain OCT-system were obtained achieving 2.84µm axial and 10.2µm lateral resolution.

Integration of the spectrometer's dispersive element (i.e. 45°-TFG) into the fibre eliminates the need for an external diffraction grating and the collimation optics. The reduction of the bulk optical elements increases stability. Together with simple broadband light sources the miniaturization and simplification results in cost reduction for OCT-devices. This opens new fields of potential applications such as portable OCT devices for flexible and long term monitoring of diseases.

6.4.1.1 *System design*

A TFG alters the propagation direction and causes partial coupling out of the fibre by reflection. The angle of the out-coupled light is strongly wavelength dependent. In other words, adjacent wavelengths, separated by $\delta\lambda$ are separated by the angle $\delta\theta$. The dispersion can be formulated as:

$$D = \frac{\delta\theta}{\delta\lambda} \tag{6.4}$$

Figure 6.15: Simplified sketch of a TFBG displaying the emission geometry. Left: Divergence output characteristics in the radial plane of the fiber. Right: Wavelength dependent refraction of the tilted Bragg grating in the axio-lateral plane.

The refraction in the axial direction leads to a diverging light bundle coupling out at angle α in the radial direction, according to the numerical aperture as displayed in Figure 6.15.

$$N_A = \sin(\alpha) \tag{6.5}$$

However, only a small portion of the inserted light is de-coupled by the TFG. Therefore, a part of the light is not refracted and is further guided towards the end of the fibre. The transmitted light depends on the polarization [14], [15] of the incoming light and the length of the TFG. As expected, the emitted intensity profile in the axial direction follows an exponential decay in the propagation direction [16]. After quantifying the spectral and intensity characteristics of the TFG in a first stage, a simple two-element imaging system was realized, consisting of a cylindrical and a spherical lens of suitable focal lengths. Connected to a high-resolution 2D-camera with standard data acquisition and a Michelson interferometer with a motor-driven sample arm, the spectral resolution and the corresponding depth dependent fringe loss could be specified as -16dB/0.4mm. Since the sensitivity of this device was limited by the chromatic error of the cylindrical lens, the size of the focusing lens and the instability of the fibre mount, a second spectrometer with a USB line-camera (3648 pixels, 8μm pixel pitch) was devised to span a 6.4mm depth scan range in air. To optimize the performance of this low-cost configuration the optical concept was revised based on the specifications of the TFG.

6.4.1.2 *OCT system*

A PS750 fibre with an UV-inscribed 45°-TFG providing a dispersion of 2.06 radians/μm, a grating length of 23mm and a numerical aperture of 0.1 was used to build a spectrometer. For horizontal beam collimation a cylindrical lens 69-747 from Edmund Optics with a focal length of 20mm was inserted. The spectral focusing was achieved by an objective consisting of two achromatic doublets AC508-150-B from Thorlabs with focal lengths of 150mm using an additional field flattener lens with a focal length of 86mm for reducing internal reflections to a low-cost USB CCD Line from Mightex with 3648 pixels of the size of 8μm pitch and 200μm height. The field flattener lens was not optimized for this spectrometer design; however, it was inserted to reduce the reflection on the uncoated camera glass. The spectrometer was designed for a super luminescence diode laser source (SLED) EBS8000 from Exalos with a central wavelength of 800nm the FWHM broadband of 120nm, which was mapped on approximately 2000 pixels. Since the orthogonally emitted wavelength of the TFG was 776nm, the TFG and the cylindrical lens had to be tilted with respect to the CCD line array. The arrangement of the elements was optimized with the ray trace software Zemax. Figure 6.16 shows the two different planes as 2D Layout printouts.

Figure 6.16: Optical design illustrated in different planes as a printout of the Zemax simulation.

Figure 6.17: The opto-mechanical design of the TFG spectrometer.

Figure 6.18: Schematic overview of the OCT system with the implemented TFG spectrometer: SLED - superluminescence diode, FC – 50:50 fibre coupler, PC1-PC3 – Polarization controller, Ref – reference arm, L1-L6 – lenses, Dim – screw to dim the reference signal, Mirr – silver mirror, Sam – Sample arm, Galvo – galvanometric scanner, Spec – TFG Spectrometer, TFG – tilted fibre grating, CCD – CCD line camera, USB – USB interface, Comp – computer, DAQ – data acquisition card.

The element positions were numerically optimized for broadband operation to maximize throughput and minimize chromatic error. The 280×80×70mm set-up (including the camera) was realized as a cage system supporting the necessary degrees of freedom for the alignment (Figure 6.17). The spectrometer with the TFBG was connected with a common fibre optical Michelson Interferometer OCT set-up as schematically shown in Figure 6.18. The broadband laser light of the SLED (λ_C = 800nm, $\Delta\lambda_{FWHM}$ = 120nm) is guided in a single mode fibre trough a FC APC plug to a 50:50 fibre coupler where the light is split into reference- and sample arm.

The backscattered and reflected light interferes in the fibre coupler before it is analyzed by the TFG spectrometer. Since the coupling efficiency of the TFG is highly polarization sensitive, in the reference arm, the sample arm and before the spectrometer, polarization controllers were inserted to adjust the polarization.

6.4.1.3 *OCT sensitivity measurement*

The performance of the spectrometer was specified with the OCT system described above. In a first step a sensitivity characterization of the spectrometer was done. In a second step B-Scans of different biological samples were acquired. All measurements were done with an integration time for the CCD Line Camera of 100µs. The spectrometer sensitivity can be determined by measuring an extremely low back-reflected signal from the sample arm, calculating the SNR and adding the losses in the sample and the common mode losses from sample arm to the entrance of the spectrometer as Grulkowski et al. describes in [12]. Therefore the sensitivity can be calculated as follow:

$$\sum = SNR + 20.log\left(\sqrt{R_{Samp}}.\sqrt{T_{CM}}.T_{ND}\right) \tag{6.6}$$

Where R_{Samp} is the reflection of the sample, T_{ND} is the transmission of the ND filter inserted in the sample arm to attenuate the signal and T_{CM} is the common mode transmission of the sample signal to the spectrometer. The sensitivity and the fall-off of the TFG spectrometer implemented into the OCT set-up are shown in Figure 6.19. The fall-off of -34dB is caused by the mean RMS (waist) spot size, which is the 2.5 amount of the pixel pitch.

Aston University

Illustration removed for copyright restrictions

Figure 6.19: Measured sensitivity over the half depth range acquired with an integration time of 100µs and an optical power of 0.98 mW on the sample. The maximum sensitivity reaches 108 dB and falls-off by -34 dB over 3.23 mm.

To evaluate the imaging performance of the TFG spectrometer 2-dimensional OCT, imaging on a lemon slice shown in Figure 6.20 (a) was performed. The low scattering and high contrast of the sample's cellular structures underlines the high resolution of the device.

Human in-vivo measurements of dermal tissue were obtained by a telecentric 2-D galvanometric scanhead with an effective focal length of 47mm and a minimal spot waist of 10.2µm, Figure 6.20 (b) shows a 2-dimensional OCT image of a fingertip. Furthermore ophthalmological cross-sectional OCT images from an anterior segment of a pig eye were performed (Figure 6.20 (c) and (d)). All measurements were performed at an optical power of 0.98mW on the sample.

Aston University

Illustration removed for copyright restrictions

Figure 6.20: (a) Single tomogram of lemon pulp: lateral scan range of 18 mm, acquired at 100µs integration time sampled at 1024×4096 pixels. (b) In-vivo OCT image of a fingertip with 400×1200 pixels from a volunteer acquired on an integration time of 100µs over a scan range of 11 mm. (c) Anterior segment images of a pig-eye made with an integration time of 100µs; cross-sectional OCT image of the cornea, scan range of 12.5 mm, 1024×1400 pixels (d) averaging of 18 frames shows lens and the iris, scan range 11.5 mm, 667×1096 pixels.

6.5 *CHAPTER CONCLUSION*

The use of a 45°-TFG to construct a spectrometer working at 800nm has been investigated and the design, principle and laboratory implementation are described in this chapter. The set up for this interrogation system includes BBS or laser diode, 3dB coupler, 45°-TFG, a 2mm cylindrical rod, a cylindrical lens, CCD array and a software to capture the signal. The CCD array records the spatial position of the illuminated pixel and through calibration; a correlation is made between the pixel number and wavelength. The spectral for the 800nm 45°-TFG signal (near Gaussian in nature) and the FBG sensor reflection signal were captured and used for the interrogation. The interrogation bandwidth of this system is 120nm with a resolution of 11.3pm.

After careful system alignment using the 633nm He-Ne laser, this system was then used to measure the temperature sensitivity of an FBG sensor, showing a sensitivity of 5pm/°C and was also confirmed by using an OSA to measure the reflected signal, given a thermal sensitivity of 6pm/°C, which is in close agreement with the former. However, this system is capable of WDM interrogation by detecting multiple signals from FBG sensors array operating within the TFG dynamic range.

In collaboration Bern University of Applied Sciences, Bangor University and Jiangnan University, the feasibility of a TFG-spectrometer for SD-OCT was successfully demonstrated. The maximum sensitivity of the prototype reaches 108dB at 100μs integration time and an overall sensitivity fall-off of 34dB across 6.4mm detection length. Cross-sectional 2-D OCT images of a fruit, a human fingertip and the anterior segment from a pig-eye were demonstrated and depict a reasonable image quality for this preliminary low-cost system that is well comparable to competing devices.

Further improvements of the optical design and the TFG fabrication process have the potential to optimize the TFG spectrometer towards smaller size and higher efficiency to achieve better optical performance and higher imaging speed.

6.6 References

[1] G. Meltz, W. Morey, and W. Glenn, "In-fiber Bragg grating tap," in *Optical Fiber Communication Conference*, vol. 1169, p. 6108, 1990.

[2] G. Meltz, W. W. Morey, and A. L. Wilson, "Optical waveguide embedded light redirecting and focusing Bragg grating arrangement," *Google Patents*, 1991.

[3] P. Westbrook, K. Feder, P. Reyes, P. Steinvurzel, B. Eggleton, R. Ernst, L. Reith, and D. Gill, "Application of fiber Bragg grating filter/tap module to a wavelength-locked low-chirp directly-modulated 10 Gb/s RZ transmitter," *Optical Fiber Communication Conference and Exhibit*, vol. 2002, pp. 680–682, 2002.

[4] J. Wagener and T. Strasser, "Fiber grating optical spectrum analyzer tap," *ECOC 97*, vol. 1997, pp. 65–68, 1997.

[5] A. G. Simpson, K. Zhou, L. Zhang, L. Everall, and I. Bennion, "Optical sensor interrogation with a blazed fiber Bragg grating and a charge-coupled device linear array," *Applied Optics*, vol. 43, no. 1, pp. 33–40, 2004.

[6] W. H. Press, B. P. Flannery, S. A. Teukolsky, and W. T. Vetterling, "Numerical Recipes: The art of scientific computing (Cambridge," *Cambridge Univ. Press*, 1986.

[7] Y.-J. Rao, "In-fibre Bragg grating sensors," *Measurement Science and Technology*, vol. 8, no. 4, pp. 355–375, 1999.

[8] E. G. Loewen and E. Popov, *Diffraction Gratings and Applications.* CRC Press, May 1997.

[9] B. I. Akca, B. Považay, A. Alex, K. Wörhoff, R. M. de Ridder, W. Drexler, and M. Pollnau, "Miniature spectrometer and beam splitter for an optical coherence tomography on a silicon chip," *Optics Express*, vol. 21, no. 14, pp. 16648–16656, 2013.

[10] K. Zhou, X. Cheng, Z. Yan, A. Adedotun, and L. Zhang, "Optical Spectrum Analyzer using a 45° tilted fiber grating," in *Advanced Photonics Congress*, OSA Technical Digest (online), p. BW2E.7, Optical Society of America, June 2012.

[11] D. Huang, E. A. Swanson, C. P. Lin, J. S. Schuman, W. G. Stinson, W. Chang, M. R. Hee, T. Flotte, K. Gregory, and C. A. Puliafito, "Optical coherence tomography," *Science (New York, N.Y.)*, vol. 254, no. 5035, pp. 1178–1181, 1991.

[12] I. Grulkowski, M. Gora, M. Szkulmowski, I. Gorczynska, D. Szlag, S. Marcos, A. Kowalczyk, and M. Wojtkowski, "Anterior segment imaging with Spectral OCT system using a high-speed CMOS camera," *Optics express*, vol. 17, no. 6, pp. 4842–4858, 2009.

[13] A. F. Fercher, "Optical coherence tomography - development, principles, applications," *Zeitschrift fur medizinische Physik*, vol. 20, no. 4, pp. 251–276, 2010.

[14] T. Erdogan and J. Sipe, "Tilted fiber phase gratings," *Journal of the optical society of America A-Optics Image Science and Vision*, vol. 13, pp. 296–313, 1996.

[15] K. Zhou, G. Simpson, X. Chen, L. Zhang, and I. Bennion, "High extinction ratio in-fiber polarizers based on 45 degree tilted fiber Bragg gratings," *Optics Letters*, vol. 30, no. 11, pp. 1285–1287, 2005.

[16] A. Adebayo, Z. Yan, K. Zhou, L. Zhang, H. Fu, and D. Robinson, "Power Tapping Function in Near Infra-Red Region Based on 45° Tilted Fiber Gratings," *Optics and Photonics Journal*, vol. 03, pp. 158–162, 2013.

7 THESIS CONCLUSION, FUTURE WORK AND PUBLICATIONS

7.1 *THESIS CONCLUSION*

7.1.1 Theoretical, Literature Review And Fabrication Techniques

The work presented in this thesis started with the review of the history of photosensitivity mechanism in optical fibres and the various photosensitisation techniques were discussed. A brief overview of the mode coupling theory and phase matching conditions for FBG, LPG and TFG structures were also included in this thesis.

The fibre grating structures reported in this thesis has been fabricated using one of the UV inscription techniques: two-beam holographic technique, phase mask scanning technique and the point-by-point technique. The two beam holographic technique was employed for the fabrication of FBGs at arbitrary wavelengths due to its low cost and flexible system set up. The phase mask scanning technique was used for fabricating high quality and complex grating structures, including normal FBGs and TFGs (small, large and 45°-TFGs). The fundamental limitation of the phase mask when tilted due to the effective inscription area (EIA) was also discussed and a defocus technique during the inscription process, which can increase the EIA, was introduced. In order to ensure UV-inscription efficiency during the fabrication, the power distribution of the diffraction order from the phase mask (normal and tilted) were analysed and the relationship between the internal and external tilt angle for TFGs was clearly revealed. The point-by-point technique, in which the hydrogenated standard fibre is exposed to a scanning UV beam, was used for fabricating the LPGs reported in this thesis.

7.1.2 Spectral Characteristics Of Normal Periodic Structure Gratings And Their Applications

The light weight, in-fibre and highly sensitive nature of normal periodic structures including FBGs and LPGs have made them ideal candidates for optical fibre sensors with applications in thermal, refractive index, chemical and bio sensing. FBGs with operating wavelengths from near-IR to mid-IR were fabricated and subject to elevated temperatures, showing that the temperature sensitivities of FBGs and their operating wavelengths are linearly related. Due to the unique core-to-cladding mode coupling properties of LPG, the refractive index and thermal sensitivities of LPGs were investigated and reported, showing a much higher thermal response compared to the FBGs. The LPGs were further investigated for monitoring the protein degradation in Fetal Bovine Serum (FBS). The measured sensitivity results have shown the capability of these grating structures and their potential benefit in a wide range of applications.

7.1.3 Spectral Characteristics Of Small And Large Angle Tilted Grating Structures And Their Applications

In this thesis, the results from the theoretical and practical investigations of the small and large angle TFGs, including inscription methods, spectral characteristics, thermal and refractive index change effects and polarisation dependences, were presented. Small and large angle TFGs have been fabricated in hydrogenated standard fibre for the purpose of this investigation. The mode coupling regimes of these TFGs were also reported, showing three main coupling regimes corresponding to backward cladding mode coupling, radiation mode out coupling and forward cladding mode coupling. Further investigation was then carried out on the effect of change in polarisation on the dual peaks of large angle TFGs, showing that the polarization mode splitting effect is much more pronounced on the large angle TFGs compared to the small angle ones. A Mach-Zehnder interferometer making use of cascaded large angle TFG pair for chemical sensing was then developed. A twist sensors was also implemented using a combination of 45°-TFG and a large angle TFG, with the 45°-TFG replacing a bulk commercial polariser in Chapter 4.

7.1.4 45°-TFG Structures In Near-IR 800nm And Their Applications

Based on the coupled mode theory and their unique radiation mode coupling properties, the 45°-TFGs were fabricated in a hydrogenated 800nm single mode fibre, showing high PER and a near Gaussian PER spectral profile. The polarisation characteristics of these 800nm 45°-TFGs were fully investigated, showing a linear correlation between the measured PER and grating length. To achieve high value PER, 45°-TFGs were concatenated during fabrication to increase the effective grating length and overall response bandwidth. A power tapping device was then developed using a short 45°-TFG, showing a possibility of tapping out 2% of the transmitting power which could be a useful way to monitor the power in a fibre laser system. Further development were carried out in collaboration with Bern University of Applied Sciences and Bangor University to develop an OCT spectrometer based on the 45°-TFG UV-written in PS750 fibre. The system was used to measure the tomograms of ophthalmic and dermal samples, achieving 2.84μm axial and 10.2μm lateral resolution. Also, a spectrometer system specifically designed to work at 800nm was developed for a WDM interrogation system. The system involves the use of focussing lenses and a CCD array. This TFG-CCD spectrometer was then used for temperature sensing experiment and found to have a measurement resolution of 12pm/pixel.

7.2 *SUGGESTED FUTURE WORK*

7.2.1 Dual Parameter Grating Sensor

The temperature sensing using FBG based sensors have been discussed in this thesis and also FBGs for applications in strain sensing and micro bending have been widely reported. But an issue of thermal cross-sensitivity has made measuring both the temperature and strain simultaneously using FBGs difficult. Ranges of solutions have been provided in the past but with a poor discrimination resolution [1–3]. By fabricating a tilted chirped fibre grating (TCFG) with a small tilt angle, both the Bragg peak and the cladding mode resonance peaks can be used. For example, due to the possibility of coupling light in both the backward core and cladding modes, the cladding resonance peaks may be used to sense the changes in refractive index change while the Bragg peak will only be sensitive to temperature.

7.2.2 LPG In 2µm Region For Chemical And Bio Sensing

The LPG work reported in this thesis shows that the higher order cladding modes have higher sensitivity to changes in surrounding medium and also LPG sensitivity increases as wavelength increases. Since these were all carried out in the 1550nm wavelength range, LPG with operating wavelength in the mid-infrared region (2µm) will have enhanced sensitivity and can be used for applications in the mid-infrared region such as: in medical and bio sensing, fibre lasers and spectroscopy. The only foreseen obstacle will be the expensive high power BBS required to carry out the characterisation and the high absorption of standard fibre at about 1970nm. However, as more R&D activities extends to mid-IR region, the low-cost light sources, other components and better fibres will become available in future. The point-by-point set up in our laboratory can be optimised for scanning speed, cylindrical lens defocus, and laser beam power to produce high quality LPGs in 2µm region.

7.2.3 OCT Spectrometer Optimisation

Further improvement of the optical design and the TFG fabrication process has potential to optimize the TFG spectrometer towards smaller size and higher efficiency to achieve better optical performance and higher imaging speed. In the current setup the detection probe is the limiting component rather than the detection side. Even without further optical optimization the device can be fitted into a 200×60×10 mm format after removal of unnecessary optical surfaces using only standard components. To reduce the depth dependent signal loss that is caused by the limited spectral resolution, an increase of the numerical aperture is necessary. This is usually associated with enlarged optics. A more efficient grating with shorter emission length but higher coupling ratio can help reduce the physical size of the device, so that the radii of curvature can be reduced. The relatively simple design and dense integration of a fiber-optic adapter to an existing cheap optical-electronic infrastructure overcomes mechanic limitations of bulk systems, enables miniaturization at reduced costs and has the potential to extend the field of application for OCT-systems in biology, medicine and technology.

7.2.4 Dual Wavelength 45°-TFG Based Spectrometer

The ability of 45°-TFGs to tap light out of the fibre core and its use in side detection spectrometers are reported in Chapter 6 of this thesis; several spectrometer involving the use of small angle TFGs have also been reported [4–7], but are all limited to a narrow radiation mode profile (about 30nm for a 10°-TFG) and the fibre has to be immersed in an index matching gel, making the system complex and inflexible. The use of a 45°-TFG instead of a small angle as reported in Chapter 6 provides a wider wavelength range of almost 200nm and giving a broader dynamic range for the spectrometer without the need for an index matching gel. However, the present system is only working at 800nm and by changing the system arrangement, there is a possibility of dual wavelength range spectrometer using a single CCD array. The Sony ILX511 CCD array has sensitivity ranging from 400-1000nm, so by fabricating another FBG sensor working at 980nm, the FBG sensors combined can then be used to sense different parameters at the same time. One of the issues that could arise will be the cross talk between the reflected signals from the FBG sensors and the accurate discrimination between the signals detected by the CCD camera.

7.3 PUBLICATIONS

Journal Papers:

[1] **A. Adebayo**, Z. Yan, K. Zhou, L. Zhang, H. Fu, and D. Robinson, ‘Power Tapping Function in Near Infra-Red Region Based on 45° Tilted Fiber Gratings", Optics and Photonics Journal, vol 3, no. 2, 2013.

[2] P. Saffari, T. Allsop, **A. Adebayo**, D. Webb, R. Haynes, and M. M. Roth, ‘Long period grating in multicore optical fibre: an ultra-sensitive vector bending sensor for low curvatures’, Optics Letters, vol 39, no. 12, pp. 3508 - 3511, 2014.

Conference Papers:

[1] **A. Adebayo**, Z. Yan, L. Zhang, and D. Robinson, "45°-TFG based in-fibre polarizer at 800nm by UV inscription", in Asia Communications and Photonics Conference, 2012.

[2] **A. Adebayo**, Z. Yan, L. Zhang, and D. Robinson,"45°-TFG based in-fibre polarizer at 800nm by UV inscription", in OSA Technical Digest (online) (Optical Society of America, 2012), ATh2A.4.

[3] **A. Adebayo**, Z. Yan, L. Zhang, D. Robinson, P. Li, and J. Leng, "Optical fibre gratings with response to 2μm and their sensing capabilities", Proc. SPIE 8421, OFS2012 22nd International Conference on Optical Fiber Sensors, 842141 (2011).

[4] Z. Yan, **A. Adebayo**, K. Zhou and L. Zhang, "Highly sensitive temperature and strain sensors based on all-fiber 45°-TFG Lyot filter", Proc. SPIE 8439, Optical Sensing and Detection II, 843905 (2012).

[5] Z. Yan, **A. Adebayo**, K. Zhou, L. Zhang, and D. Webb, "All-fibre twist sensor system based on 45°and 81°tilted fibre gratings", in 21st International Conference on Optical Fibre Sensors (OFS21), , 77538E-77538E-77534.

[6] Z. Yan, K. Zhou, **A. Adebayo**, and L. Zhang, "All-fibre Lyot filters based on 45°tilted gratings UV-inscribed in PM fibre", in Bragg Gratings, Photosensitivity, and Poling in Glass Waveguides,

(Optical Society of America, 2012).

[7] X. Chen, K. Zhou, **A. Adebayo**, and L. Zhang, "Chemical sensor using Mach-Zehnder interferometer based on a pair of largely tilted fibre gratings", in Advanced Photonics Congress, 2012, p. JTu5A.51.

[8] Z. Yan, P. Saffari, K. Zhou, **A. Adebayo**, and L. Zhang, "Optical RI sensor based on an in-fibre Bragg grating Fabry-Perot cavity embedded with a micro-channel", Proc. of SPIE Vol 8426, 842609-842601 (2012).

[9] K. Zhou, X. Cheng, Z. Yan, **A. Adebayo**, and L. Zhang, "Optical Spectrum Analyzer using a 45°tilted fibre grating", in Bragg Gratings, Photosensitivity, and Poling in Glass Waveguides, (Optical Society of America, 2012).

[10] G. C. B. Lee, K. Kalli, C. Koutsides, Z. Yan, **A. Adebayo**, M. Komodromos, and K. Sugden, "Femtosecond laser inscribed phase masks for fibre Bragg grating sensor inscription", Proc. of SPIE Vol 8421, 84214V-84211 (2012).

[11] S. Remund, A. Bossen, X. Chen, L. Wang, **A. Adebayo**, L. Zhang, B. Povasay, and C. Meier, "Cost-effective optical coherence tomography spectrometer based on a tilted fibre Bragg grating", Proc. of SPIE BiOS, 2014, p. 89381E–89381E.

Preparing Papers:

[1] **A. Adebayo**, Z. Yan, K. Zhou, D. Robinson, L. Zhang, " In-fibre polarizer and power tapper at 800nm based on 45°- Tilted Fiber Gratings", Journal of Lightwave Technology.

[2] Z. Yan, **A. Adebayo**, Z. Sun, K. Zhou, H. Fu, L. Zhang, "Polarization Switchable single/multi-wavelength fibre ring laser with an intra-cavity all fibre Lyot filter" to be submitted to Laser physics Letters.

7.4 References

[1] P. M. Cavaleiro, F. M. Araujo, L. A. Ferreira, J. L. Santos, and F. Farahi, "Simultaneous measurement of strain and temperature using Bragg gratings written in germanosilicate and boron-codoped germanosilicate fibers," *Photonics Technology Letters, IEEE*, vol. 11, no. 12, pp. 1635–1637, 1999.

[2] O. Frazao, R. Romero, F. M. Araujo, L. A. Ferreira, and J. L. Santos, "Strain-temperature discrimination using a step spectrum profile fibre Bragg grating arrangement," *Sensors and Actuators A: Physical*, vol. 120, no. 2, pp. 490–493, 2005.

[3] K. Zhou, X. Chen, D. Webb, L. Zhang, and I. Bennion, "Simultaneous temperature and strain measurement with enhanced resolution up to 20 times by using a compact hybrid optical waveguide Bragg grating," in *Asia Optical Fiber Communication and Optoelectronic Exposition and Conference*, p. SuR1, Optical Society of America, 2008.

[4] K. S. Feder, P. S. Westbrook, J. Ging, P. I. Reyes, and G. E. Carver, "In-fiber spectrometer using tilted fiber gratings," *Photonics Technology Letters, IEEE*, vol. 15, no. 7, pp. 933–935, 2003.

[5] A. G. Simpson, K. Zhou, L. Zhang, L. Everall, and I. Bennion, "Optical sensor interrogation with a blazed fiber Bragg grating and a charge-coupled device linear array," *Applied Optics*, vol. 43, no. 1, pp. 33–40, 2004.

[6] G. Meltz, W. Morey, and W. Glenn, "In-fiber Bragg grating tap," in *Optical Fiber Communication Conference*, vol. 1169, p. 6108, 1990.

[7] J. Wagener, T. Strasser, J. Pedrazzani, J. DeMarco, and D. DiGiovanni, "Fiber grating optical spectrum analyzer tap," in *Integrated Optics and Optical Fibre Communications, 11th International Conference on, and 23rd European Conference on Optical Communications (Conf. Publ. No.: 448)*, vol. 5, pp. 65–68 vol.5, 1997.